SOME APPLICATIONS OF ELIASHBERG THEORY

By

Richard Akis, B.Sc., M.Sc.

A Thesis

Submitted to the Faculty of Graduate Studies

in Partial Fulfilment of the Requirements

for the Degree

Doctor of Philosophy

McMaster University

November 1991

SOME APPLICATIONS OF ELIASHBERG THEORY

DOCTOR OF PHILOSOPHY(1991) McMASTER UNIVERSITY

(Physics) Hamilton, Ontario

TITLE: Some Applications of Eliashberg Theory

AUTHOR: Richard Akis, B.Sc. (Lakehead University)

M.Sc. (McMaster University)

SUPERVISOR: Dr. Jules P. Carbotte

NUMBER OF PAGES: viii, 219

ABSTRACT

Eliashberg theory, which was formulated assuming that the electron-phonon interaction is the mechanism for superconductivity, has been very successful in explaining the physical properties of most superconductors. Eliashberg theory is an extension of BCS theory, the original microscopic theory of superconductivity. BCS theory is recovered from Eliashberg theory in the weak electron-boson coupling limit. Recently, a new challenge to Eliashberg theory has been brought forth by the discovery of a new class of superconductors known as the high T_c oxides. As of this writing, the question of what is the the superconducting mechanism for these materials is still unanswered.

In this thesis, many superconducting properties have been calculated mainly in an effort to see if Eliashberg theory may still be applicable to these materials. The approach of this effort has depended on the property being studied. In the case of the critical temperature and the isotope effect, a great deal of work has been put in to fit actual experimental results, particularly for the isotope effect. We shall show that two distinct models, one with an additional electronic mechanism along with the phonons and the other with a very large coulomb repulsion, may be able to explain the experimental results. For the electronic specific heat, maxima that should not be exceeded by an Eliashberg superconductor are established for several quantities associated with this physical property. Unfortunately, some experimental values for these quantities appear to exceed these maxima. In the case of the the nuclear spin relaxation, which has not been very extensively studied in the past, we shall look at how the coherence peak in the relaxation rate can be

reduced as a function of coupling strength and draw conclusions that are applicable to conventional superconductors. The behaviour of this property in the oxides is not ignored however, and some fitting of experiment including anisotropy as well as antiferromagnetic Fermi liquid corrections is done. For the conductivity, we examine how one may extract the superconducting gap from this property, mainly as a theoretical exercise but inspired by the efforts of experimentalists who have tried to do this using optical data for the oxides. The low frequency conductivity, like the nuclear spin relaxation, should show a coherence peak in the BCS limit. We study this as a function of coupling strength, frequency and impurity concentration. The conductivity results here are contrasted with those obtained experimentally for the oxides. There are indications that a strong coupling mechanism may have difficulty explaining these experiments. Finally, we examine the phonon self-energy, mainly using a newly derived formula for this quantity written on the real frequency axis. Results from this new formula are compared with a previous formula written on the imaginary axis. In this case, the main concern here was theoretical and the experiments results for this quantity are only briefly touched on.

ACKNOWLEDGEMENTS

There are several people who I wish to thank for contributing to my development while at McMaster. First of all, Frank Marsiglio must be acknowledged as the person who laid the foundation that enabled most of the work in thesis to be done. I would also like to thank Jules Carbotte, "the mad genius of superconductivity", for his supervision and for laughing at my jokes. I also acknowledge Ewald Schachinger, for his programming expertise, and Elisabeth Nicol, who was helpful in several areas during the course of my Ph.D work. Finally, I thank Tom Szeredi and Matt Greeson who, through their friendship, have helped me grow as a human being.

As to financial support, I wish to acknowledge the Natural Sciences and Engineering Research Council (NSERC) of Canada. I have also benefited from the Harry Lyman Hooker scholarship.

Table of Contents

Chapter 1

Introduction

1.1 IN THE BEGINNING-EXPERIMENT

Superconductivity was first observed by Kamerlingh Onnes[1] in 1911 when he discovered mercury (Hg) went through a superconducting transition around a temperature of 4 K. In his experiment, this transition manifested itself by a drop in the D.C. electrical resistivity to immeasurably small values.

While this drop in resistance is an important sign of superconductivity, it is by no means the only one. More than twenty years later Meissner and Ochsenfeld[2] discovered what is now known as the Meissner effect. What they found is that applied magnetic flux is expelled from a superconductor when it makes the transition into the superconducting state. However, this phenomena does not occur for all magnetic field strengths. If the applied magnetic field is strong enough it will finally penetrate the sample completely. At this point, the superconductivity is destroyed.

The entrance into the superconducting state also effects many other physical properties of the material. How some of these properties are affected will be explored in various chapters of this thesis. It should be noted that how some of these changes manifest themselves is greatly tied in to the nature of the superconducting mechanism. However, the drop in the resistivity and the Meissner effect should occur regardless of the mechanism. For this reason, it is considered sufficient in order to confirm that a material is a superconductor to observe just these two effects.

The practical benefits of superconductivity were recognized right from Onnes' time. However, the superconducting transition temperatures of the early known superconductors were only accessible by use of liquid helium technology. This placed severe limitations on the potential applications of these materials as liquid helium is expensive to produce and the cooling apparatus bulky. This of course has lead to a search for materials with higher transition temperatures. The earliest known superconductors were monoatomic metals such as Hg, Pb as well as many others. The highest critical temperature for a simple metal is 9.2 K in the case of Nb[3]. As time progressed, more complicated classes of materials were found to be superconducting, some of which have higher transition temperatures than the monatomic metals. By 1973, the material with the highest known critical temperature or T_c for short was Nb_3Ge with $T_c = 23.2$ K[4]. This material is one of a class of compounds known as the A-15's, each with the general chemical formula A_3B. So, in approximately 60 years, the maximum critical temperature was raised by a mere ~ 18 K and was still quite far away from the range accessible to the more practical liquid nitrogen cooling technology. For liquid nitrogen, the important temperature is the boiling point, 77 K.

Between 1973 and 1986 there was no further progress in raising T_c. In 1986 however, the situation changed radically with the discovery of the high-T_c oxide superconductors.

1.2 IN THE BEGINNING -THEORY

The earliest theories of superconductivity were phenomenological and macroscopic in nature. Chief among these was the two-fluid model[5], developed in the 1930's, where the electrons in the material are separated into superconducting and non-superconducting fractions. This concept turned out to be highly useful in describing quantitatively the behavior of some of the thermodynamic and electrodynamic properties of superconductors, including the Meissner effect.

Progress towards an effective microscopic theory was somewhat slower. Early on it was realized that only the electronic properties of the superconductors were being profoundly affected[6]. What was required was an appropriate description of the electrons in the superconducting state. It was also recognized that it was interactions between the electrons themselves that gave rise to this new state. So what was also required was knowledge of the nature of these interactions.

In 1957, progress toward a successful microscopic theory finally experienced fruition. In that year an explanation was proposed by Bardeen, Cooper and Schreiffer[7] which has since been referred to as BCS theory. In the framework of BCS theory, the energy of the normal state can be lowered by having the electrons in the Fermi sea "condense" into a superconducting state where the superconducting electrons form pairs in momentum space. In real space, it is impossible to pick out specific paired electrons. If one

calculates the average size of a Cooper pair, given by the coherence distance ξ, one finds that for a typical superconductor ξ is of the order of thousands of Angstroms. In the meantime, the inter-electron distance is more like 1 Anstrom. Obviously, there must be a great deal of overlap of the pairs in real space.

Pairing requires an attractive potential between electrons. BCS theory assumes that this potential takes the form:

$$\langle k,\sigma|V(q)|k',\sigma'\rangle = -V\delta_{k,-k'}\delta_{\sigma,-\sigma'} \ . \tag{1.1}$$

Here, k and k' are the momenta and σ and σ' are the spin indices of the electrons (note: if $\sigma = \uparrow$, then $-\sigma = \downarrow$). This potential applies for a rim of thickness $2\hbar\omega_D$ centered about the Fermi surface, where ω_D is the Debye frequency.

Doing the quantum mechanical problem with this sort of potential is relatively simple for a single pair of electrons. Unfortunately, doing it for a situation where all the electrons in the system are participating is much more complicated. One of the major breakthroughs of BCS theory was the choice of wave function. The BCS wave function has the form of a product:

$$|G>=\prod_{\vec{k}}(u_{\vec{k}} + v_{\vec{k}}C^{\dagger}_{\vec{k}\uparrow}C^{\dagger}_{-\vec{k}\downarrow})|0> \ . \tag{1.2}$$

In this equation, $|0>$ refers to the vacuum state and the $C^{\dagger}$'s are electron creation operators. The factors $u_{\vec{k}}$ and $v_{\vec{k}}$ are related to probabilities of occupation. Here, $v^2_{\vec{k}} \equiv$ probability of occupation of state $\vec{k}$ while $u^2_{\vec{k}} = 1 - v^2_{\vec{k}}$. As it turns out, these factors are also closely related to an energy gap that is predicted by the theory to occur in the superconducting state and deriving

an equation to solve for the factors $u_{\vec{k}}$ and $v_{\vec{k}}$ leads eventually to the famous BCS gap equation. At zero temperature, this equation is given

$$\Delta_o = 2\hbar\omega_D \exp\left(-\frac{1}{N(0)V}\right) . \tag{1.3}$$

In obtaining this equation, it has been assumed that the system is isotropic and that the electronic density of states is essentially constant in the rim where the potential acts. This accounts for the appearance of the electronic density of states at the Fermi energy, N(0), appearing in this formula.

The V which gives the attractive potential is a positive constant that is usually fitted to an experimental T_c. This can be done since the theory also predicts the relation

$$k_B T_c = 1.13\hbar\omega_D \exp\left(-\frac{1}{N(0)V}\right) , \tag{1.4}$$

This can be combined with the relation for Δ_o to give the ratio

$$\frac{2\Delta_o}{k_B T_c} = 3.53 . \tag{1.5}$$

This ratio is independent of any material dependent quantities and thus should be obeyed by all superconductors. This is just one of the many universal relationships involving the physical properties of superconductors that have been derived from BCS theory.

BCS theory has been highly successful in a qualitative sense. Unfortunately it fails in most cases quantitatively as evidenced by the fact that most materials deviate from the supposedly universal BCS predictions. The degree of this failure varies from material to material. For example, a material such as Al yields quite good agreement with the BCS results. Pb on the other hand, is famous for being a bad "actor". In most cases, the failure

of BCS can be directly traced back to the model being oversimplified. The constant potential must be replaced by the full details of the interactions in order to get accurate results.

For most materials it was apparent that the attractive potential was due to an electron-phonon interaction. Bardeen, Cooper, and Schreiffer of course recognized this. It is for this reason that their constant pairing potential is cutoff by ω_D. This is the only phonon related frequency that appears in the theory. As a result, BCS theory only very roughly takes into account the fact that an attractive interaction mediated by phonons is retarded in time. Why time retardation effects are important can be understood by thinking of this simple picture[8]: an electron moving through a lattice will create an electronic polarization (i.e. a phonon) by attracting the positive ions. If the ions obey simple harmonic motion with a frequency ω equal to the typical phonon frequency then it will take a finite time, $t = \frac{\pi}{2\omega}$, for a maximum polarization to occur. A second electron feels the effect of the polarization and becomes attracted to the region where the first used to be. As it turns out, BCS only correctly accounts for this situation quantitatively, provided that the characteristic phonon energy, $\hbar\omega$, is much higher than the typical superconducting energy, $k_B T_c$.

In 1960, Eliashberg[9] used a formal Green's function approach to incorporate the details of the electron-phonon interaction into the theory of superconductivity. The result was a theory that could explain the deviations from BCS theory for most materials. In fact, the level of agreement with experiment is usually within a few percent, making Eliashberg theory one of the most successful theories in physics. The important microscopic parameters that enter into Eliashberg theory are a spectral function $\alpha^2 F(\omega)$

and a Coulomb pseudopotential μ^*. In the function $\alpha^2F(\omega)$ is contained the electron-phonon coupling, $\alpha^2(\omega)$ (it is squared since two electrons are coupled), and the phonon frequency distribution $F(\omega)$. The parameter μ^* represents the effective Coulomb repulsion between the coupled electrons. The stronger the coupling between the electrons and phonons, the greater the deviations from BCS theory. For this reason, Eliashberg theory is often referred to as strong coupling theory. In a strong coupling superconductor, the characteristic phonon energies tend to be within an order of magnitude or so of k_BT_c.

It should be noted that while Eliashberg theory was formulated with phonons in mind, any mechanism that involves the exchange of virtual bosons can be cast within the Eliashberg framework, at least as a first approximation.

While Eliashberg theory has been successful in giving quantitative answers, its added complexity meant that these answers could not be obtained by exact analytic solutions. While there have been advancements in making the theory more workable since 1960, we are still faced with the same situation today.

With the success of Eliashberg theory, the field of theoretical superconductivity over the years became relatively stagnant. This situation was to change profoundly with advent of the oxide superconductors.

1.3 THE OXIDES- A NEW ERA

The high-T_c revolution began in 1986 when Bednorz and Müller[10] observed evidence of a superconducting transition with $T_c \sim 30$ K in a sample of Ba-La-Cu-O. The particular phase that resulted in the superconductivity

was later identified as $La_{2-x}Ba_xCu_2O_{4-y}$. After that, it was discovered that the T_c could be raised to nearly 40 K by substituting such elements as Sr and Ca for Ba[11,12].

This turned out only to be the beginning. The group headed by Chu at the University of Houston discovered[13] a material later identified[14,15] as $YBa_2Cu_3O_{7-y}$, which had a critical temperature above 90 K. Thus, with this material the liquid nitrogen barrier had been broken. The critical temperature was raised further by the discovery[16] of the Bi-Sr-Ca-Cu-O system which has a two step transition at 110 K and 85 K. The current record holder[17–19] however is the Tl-Ca-Ba-Cu-O system with $T_c \sim 120$ K, depending on the phase. These only represent a few of the materials discovered since 1986 that fall into the category of the high-T_c oxides. By high-T_c it is implied that T_c is significantly higher than 23 K, the pre-1986 record.

While it was Ba-La-Cu-O that started all the excitement, the field of oxide superconductivity actually began in 1964 with the discovery of $SrTiO_3$ by Schooley *et al.* [20]. This material had a $T_c \sim 0.3$ K. It has perovskite structure, which can be described in terms of a unit cell in the form of a cube with the Sr atom at the very center, Ti atoms at the corners and O atoms at the centers of each face of the cube. The structures of the later oxides have been found to be closely related variations of this basic type of structure. For example, $YBa_2Cu_3O_7$ has a unit cell that can be derived from three perovskite units cells by shifting some atoms around while removing others[21]. The exact structure of a material like $YBa_2Cu_3O_{7-y}$ depends strongly on the oxygen deficiency, y. Changing y causes a range of distortions from ideal cubic structure. Similar comments can be made about the structure of the various other types of high-T_c oxides.

While not all oxide superconductors contain the element Cu, the materials with the highest T_c's all appear to contain it. A distinct feature of these materials is the occurrence of layers consisting exclusively of Cu and O. Usually, the crystal axes of the material are defined such that these Cu-O sheets lie in the a-b plane, with the c direction perpendicular. One finds for the Cu oxides a large degree of anisotropy for various physical properties when comparing the a-b planes with the c direction. For example, if one measures the resistivity of a Cu oxide above T_c, one finds metallic behavior in the a-b planes, while the resistivity in the c direction tends to be much higher and non-metallic[22,23]. This metallic behavior appears to be tied to the Cu-O sheets. Anisotropy is also indicated in the superconducting state. A gauge of this anisotropy can be obtained by using a parameter[22,24] that involves the upper critical field as measured in the a-b plane ($||$) and c ($\perp$) direction :

$$\epsilon = (dH_{c2||}/dT)/(dH_{c2\perp}/dT) \,, \tag{1.6}$$

where the temperature derivative is taken at T_c. In Y-Ba-Cu-O, ϵ is of the order 10, which indicates very large anisotropy indeed. This parameter is even larger in the Tl and Bi oxides. In comparison, for materials that are known to follow Eliashberg theory, anisotropy tends to be relatively unimportant.

This anisotropy is also reflected in the coherence distance. The coherence distance in the a-b plane tends to be significantly larger than that in the c direction[22,24,25]. Beyond the anisotropy, the values of ξ_{a-b} one obtains for the various oxides tend to be of the order of tens of Angstroms[22,24-26], which is 2 orders of magnitude smaller than the values of ξ typically seen in BCS-Eliashberg superconductors.

Thus, the high-T_c oxides differ substantially from the typical BCS-Eliashberg superconductors in terms of their critical temperatures, anisotropy and their coherence distances. There are many other physical properties of these materials that are also unusual. Some of these will be encountered as this thesis unfolds.

1.4 SCOPE AND OUTLINE OF THESIS

The discovery of the high-T_c oxides has been the primary motivation for most of the work presented in this thesis. While it is quite possible or even likely that some exotic mechanism may be the ultimate cause of the superconductivity in these materials, the strong coupling framework so well developed in the past is what has been mainly exploited to obtain the results shown in the remaining chapters of this thesis. The reason for this is twofold. First of all, there is some evidence that a strong coupling model can explain at least some of the experiments performed on the oxides and so it can not be ruled out completely. The second reason is the fact that several of the physical properties that are studied in this thesis have never been examined very extensively in the past even within the strong coupling framework. So, looking at what occurs within a strong coupling model is a logical starting point.

In chapter 2, the derivation of the Eliashberg equations is sketched out. A point that is emphasized is that these equations can be recast in several different forms. The form that one uses depends mainly on which physical property one wishs to calculate.

In chapter 3, the critical temperature, T_c, and the isotope effect, which is closely related to T_c, are examined. The oxides of course differ from conventional superconductors in that their T_c's are so large. By a conventional superconductor, we imply that the material has $T_c < 23.2$ K and is known to follow the predictions of Eliashberg theory. Unlike most conventional materials, the isotope effects obtained for the oxides for the most part have been comparatively quite small. Theoretical attempts are made to formulate models which can predict correct values for both properties at the same time. As it turns out, this can be done with a very strong coupling model with a large coulomb repulsion. It can also be done by combining phonons with a high energy boson mechanism. Comments shall also be made on some recent experiments where some very large isotope effects have also been observed.

In chapter 4, several quantities associated with the electronic specific heat in superconductors are discussed. Using functional derivative techniques, maxima are established for these quantities. These maxima should not be violated by any strong coupling superconductor. A comparison with some experiments for the oxides show that these materials may indeed exceed these maxima.

Chapter 5 is concerned with nuclear magnetic resonance in the superconducting state. The chapter focuses mainly on the nuclear spin relaxation rate as well as the Yosida function. As well as examining these quantities as a function of coupling strength, the effect of including anisotropy in an approximate way is also studied. It is shown how both strong coupling and anisotropy remove the coherence peak in the spin-lattice relaxation rate expected in BCS theory. There is also some comparison with experiment, at which point the inclusion of the antiferromagnetic Fermi liquid introduced

by Monien and Pines to help explain the anomalous NMR behavior of the oxides is also discussed.

In chapter 6, the focus shifts to the conductivity. While there is some comparison with experiment, the primary concern of this chapter shall be a theoretical exercise in seeing how easily the superconducting gap can be extracted in a strong coupling superconductor for different impurity concentrations and choices for $\alpha^2F(\omega)$. As with the nuclear spin relaxation, BCS also predicts a coherence peak in the low frequency conductivity. The appearance of such a peak or the lack of one is examined theoretically as a function coupling strength, impurity concentration and frequency.

In chapter 7, the effect of entering the superconducting state on the phonon self-energy is examined in the Eliashberg framework. Several formula for calculating the phonon self-energy are discussed and a new one is derived. Results from these various formulations are compared with each other. Beyond this, the phonon self-energy is calculated using the new formula for various coupling strengths, temperatures and impurity concentrations. Some recent experiments are discussed as well.

A brief summary is found in Chapter 8.

1.5 SOME NOTES ABOUT CONVENTIONS

In the course of this thesis, units such that $\hbar = k_B = 1$ shall be used. Since this is the case, quantities such as k_BT_c and $\hbar\omega$ can be used interchangeably with T_c and ω respectively. It is traditional that the constants of proportionality are left in when discussing BCS quantities. However, it seems just as traditional to leave them out when discussing Eliashberg theory. In this thesis, both traditions shall be maintained for the most part.

Very frequently in this thesis, experimental results for the oxide superconductors $YBa_2Cu_3O_{7-x}$ and $La_{2-x}Sr_xCuO_4$ shall be discussed. When this does occur, the short forms YBCO and LSCO respectively will be used to represent these two materials.

A quantity that comes up quite frequently is the superconducting gap edge or gap for short. When this is referred to using the symbol Δ, it is implied that it applies for some finite temperature. The zero temperature gap is always represented by Δ_o.

Chapter 2

Eliashberg Theory

2.1 INTRODUCTION

In the opening chapter, the notion that electrons being paired in momentum space leads to superconductivity was discussed. As was mentioned earlier, the BCS theory of superconductivity achieves this pairing by assuming a constant interaction potential between the paired electrons. Of course, the actual physical picture is much more complicated than this and, if one wants to obtain truly accurate results in most cases, one must put in the full details of the interactions. In this chapter, the goal is to sketch out some of the details of how this is done in Eliashberg theory. For this theory, a Green's function approach is required. The reader is referred to several excellent books for background on the Green's function technique[6,27–29].

In the next section, the Nambu formalism, whereby the pairing Hamiltonian is rewritten in terms of matrices, is discussed. In the final section of

this chapter, the Eliashberg equations are introduced. As we shall see, these equations can take several different forms. Which form one chooses depends greatly on the superconducting property that is to be studied.

2.2 THE NAMBU FORMALISM

Schrieffer[27] explained the Nambu formalism starting from a basic pairing Hamiltonian:

$$H_o' = H_o + H_{HF} + H_\phi \ , \tag{2.1}$$

where H_o is simply the free electron Hamiltonian, H_{HF} are the Hartree and Fock terms, which end up providing only a simple shift in the energy, and H_ϕ is the all important pairing term. This pairing term is given by

$$H_\phi = \sum_{\vec{k}} \left\{ \phi_{\vec{k}}^* C_{\vec{k},\uparrow}^\dagger C_{-\vec{k},\downarrow}^\dagger + \text{hermitian conjugate} \right\} . \tag{2.2}$$

The Hamiltonian H_o' is to the superconducting state what H_o is to the normal state. Typically with a problem involving Green's functions, one wants to set things up so that all the terms of any perturbation expansions can be expressed using non-interacting **one body** Green's functions. However, because the pairing term of the superconducting Hamiltonian contains two body operators, this appears on the surface to be impossible. Nambu[30] and Gorkov[31] independently discovered the means by which this difficulty could be overcome. They introduced a two component spinor field

$$\psi_{\vec{k}} = \begin{pmatrix} C_{\vec{k}\uparrow}^\dagger \\ C_{-\vec{k}\downarrow}^\dagger \end{pmatrix} \tag{2.3}$$

and

$$\psi_{\vec{k}}^\dagger = (C_{\vec{k}\uparrow}^\dagger, C_{-\vec{k}\downarrow}^\dagger) \ . \tag{2.4}$$

These operators obey the anticommutation relations

$$\{\psi_{\vec{k}}, \psi^{\dagger}_{\vec{k}'}\} = \delta_{\vec{k},\vec{k}'}\mathrm{I} \tag{2.5}$$

and

$$\{\psi_{\vec{k}}, \psi_{\vec{k}'}\} = \{\psi^{\dagger}_{\vec{k}}, \psi^{\dagger}_{\vec{k}'}\} = 0 \ , \tag{2.6}$$

where I is just the 2×2 unit matrix. The Hamiltonian $H'_{\circ}$ can be rewritten in terms of the spinors with the help of the Pauli matrices

$$\tau_1 = \begin{pmatrix} 0 & 1 \\ 1 & 0 \end{pmatrix}$$

and

$$\tau_3 = \begin{pmatrix} 1 & 0 \\ 0 & -1 \end{pmatrix} \ . \tag{2.6}$$

The resulting Hamiltonian has the form (with $\epsilon_{\vec{k}}$ reset to compensate for the Hartree-Fock contribution) :

$$H'_{\circ} = \sum_{\vec{k}} \{\psi^{\dagger}_{\vec{k}}[\bar{\epsilon}_{\vec{k}}\tau_3 + \phi_{\vec{k}}\tau_1]\psi_{\vec{k}} + \bar{\epsilon}_{\vec{k}}\} \ . \tag{2.7}$$

Thus, $H'_{\circ}$ now has the appearance of a one-body Hamiltonian which is desired to make the perturbation expansion possible. The resulting zeroth order one particle Green's function now becomes a 2×2 matrix :

$$G^{\alpha\beta}_{\circ}(\vec{k}, t) = -i < T\{\psi_{\vec{k}\alpha}(t)\psi^{\dagger}_{\vec{k}\beta}(0)\} > \ , \tag{2.8}$$

where T is the Wick's time ordering operator and, for zero temperature, <> denotes a matrix element with an N body ground state. At this point, one wishs to Fourier transform from t to ω and solve Dyson's equation, which will give the fully interacting Green's function, $G(\vec{k}, \omega)$:

$$G^{-1}(\vec{k}, \omega) = G^{-1}_{\circ}(\vec{k}, \omega) - \Sigma(\vec{k}, \omega) \ , \tag{2.9}$$

where $\Sigma(\vec{k},\omega)$ is the electron self-energy. The reader should note that this is a matrix equation. The non-interacting Green's function in ω space that enters here can be written as

$$G_o(\vec{k},\omega) = \frac{\omega + \epsilon_{\vec{k}}\tau_3}{\omega^2 - \epsilon_{\vec{k}}^2 + i\delta} , \tag{2.10}$$

where δ is a positive infinitesimal. As it turns out, when all the interactions are actually included, the most general form for the electron self-energy can be written as[27,32]

$$\Sigma(\vec{k},\omega) = [1 - Z(\vec{k},\omega)]\omega + \epsilon_{HF}\tau_3 + \phi(\vec{k},\omega)\tau_1 . \tag{2.11}$$

The corresponding form for the fully interacting Green's function becomes

$$G(\vec{k},\omega) = \frac{\tilde{\omega} + \bar{\epsilon}_{\vec{k}}\tau_3 + \phi(\vec{k},\omega)\tau_1}{\tilde{\omega}^2 - (\bar{\epsilon}_{\vec{k}}^2 + \phi^2(\vec{k},\omega)) + i\delta} , \tag{2.12}$$

where $\tilde{\omega} = Z(\vec{k},\omega)\omega$ and $\bar{\epsilon}_{\vec{k}} = \epsilon_{\vec{k}} + \epsilon_{HF}$. In solving Dyson's equation for a superconductor one thus obtains the renormalization function, $Z(\vec{k},\omega)$, and the pairing function $\phi(\vec{k},\omega)$. Both these functions are complex. Of course, in order to do this one must know what the important physical processes are that enter into the electron self-energy. At that point, the Eliashberg equations can then be derived.

2.3 THE ELIASHBERG EQUATIONS

In Eliashberg theory, there are two important contributions to the electron self-energy. The first is the Coulomb interactions between the paired electrons which is usually repulsive. This is represented by $V_c(\vec{k} - \vec{k}')$, which is simply the screened coulomb potential in momentum space. The second is

due to the electron-phonon interaction which provides the attraction between the electrons that causes superconductivity in the first place.

In Fig. 2.1, the diagrams due to virtual phonon exchange that contribute to the electron self-energy are displayed. In this figure, the double line represents the fully interacting electron Green's function, the single lines non-interacting electron Green's functions and the wavy lines the Green's functions for the phonons. The phonon Green's function takes the form:

$$D_{o\sigma}(\vec{q},\omega) = \frac{2\omega_{\vec{q}\sigma}}{\omega^2 - \omega^2_{\vec{q}\sigma} + i\delta} , \tag{2.13}$$

where σ is the phonon branch index and $\omega_{\vec{q}\sigma}$ is the phonon frequency for wave vector $\vec{q}$ and index σ. Generally speaking, one should also consider self-energy corrections to the phonons as well as to the electrons as the phonons will obey their own Dyson's equation. This usually is not done formally because of the added difficulty and the fact that the phonon information that is usually used as input into the Eliashberg equations has been obtained experimentally - thus, the phonon frequencies have essentially already been renormalized. Of course, one concern might be what happens to the phonons when the material goes from the normal to the superconducting state. This concern shall be addressed in the seventh chapter of this thesis. The point where a phonon line meets an electron line is referred to as the electron-phonon vertex and in the Nambu formalism is represented mathematically by $\tau_3 g_{\vec{k}\vec{k}'\sigma}$. The term $g_{\vec{k}\vec{k}'\sigma}$ is the electron-phonon matrix element which depends not only on the phonons but also on the electronic wave functions and electronic potential as well. Evaluating such a matrix element gives the coupling strength of a process whereby an electron with momentum $\vec{k}$ emits a virtual phonon with momentum $\vec{q}$, branch index σ and energy $\omega_{\vec{q}\sigma}$ and then

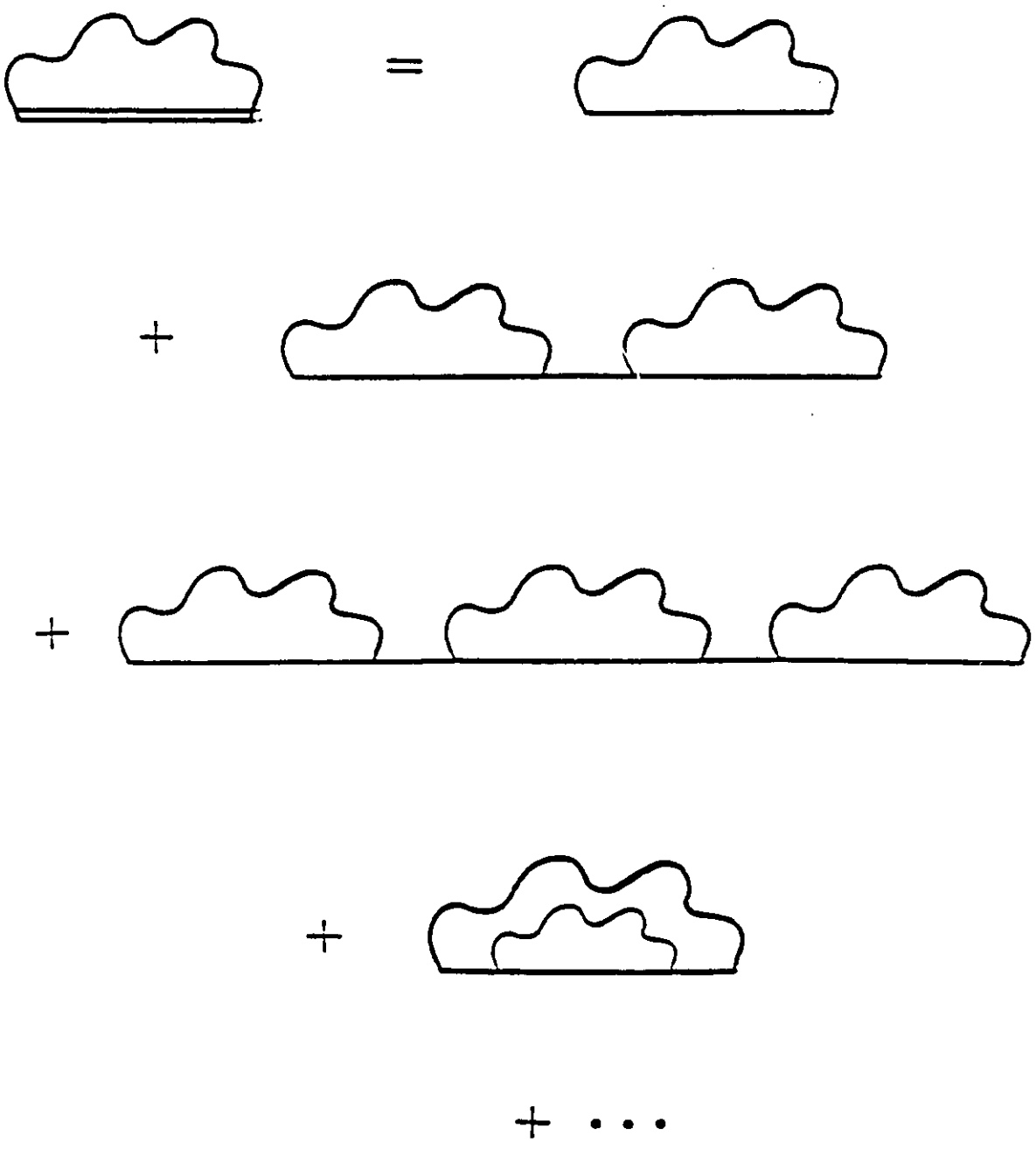

Figure 2.1 The Feynman diagrams that illustrate the contribution to the electron self-energy from virtual phonon exchange.

scatters off with momentum $\vec{k}'$. The phonon momentum $\vec{q}$ is related to $\vec{k}$ and $\vec{k}'$ through $\vec{k} - \vec{k}' = \pm\vec{q} + \vec{G}$, where $\vec{G}$ is a reciprocal lattice vector. Luckily, more complicated diagrams - ones where the phonon lines cross, which would constitute vertex corrections, are not required. This is because of Migdal's theorem[33] which states that these vertex corrections will be smaller than a factor of $\sim (\omega_{ph}/E_F)^{\frac{1}{2}}$, where ω_{ph} is a typical phonon energy and E_F is the Fermi energy. Generally, this ratio is of the order of 10^{-2} for conventional superconductors.

Combining the coulomb and electron-phonon contributions, one can write the electron self-energy in the form

$$\Sigma(\vec{k},\omega) = i\int \frac{d^3k'}{(2\pi)^3}\frac{d\omega'}{2\pi}\tau_3 G(\vec{k}',\omega')\tau_3\left[\sum_\sigma |g_{\vec{k}\vec{k}'\sigma}|^2 D_{\sigma\sigma}(\vec{k}-\vec{k}',\omega-\omega') + V_c(\vec{k}-\vec{k}')\right] . \tag{2.14}$$

For this equation one can substitute the form of equation (2.11) for $\Sigma(\vec{k},\omega)$ on the left side and substitute the form of equation (2.12) for $G(\vec{k},\omega)$ on the left side. In this manner, one can obtain self-consistent equations for the functions $Z(\vec{k},\omega)$ and $\phi(\vec{k},\omega)$ which are the Eliashberg equations. Something that is particularly helpful in deriving these equations is expressing $D_{\sigma\sigma}(\vec{q},\omega)$ in terms of it's spectral function $B_\sigma(\vec{q},\omega)$:

$$D_{\sigma\sigma}(\vec{q},\omega) = \int_0^\infty d\omega' B_\sigma(\vec{q},\omega')\left(\frac{1}{\omega-\omega'+i\delta} - \frac{1}{\omega'+\omega'-i\delta}\right) , \tag{2.15}$$

where

$$B_\sigma(\vec{q},\omega) = \delta(\omega - \omega_{\vec{q},\sigma}) . \tag{2.16}$$

Another important point is that the pairing function $\phi(\vec{k},\omega)$ is related to another important function - the gap function :

$$\Delta(\vec{k},\omega) = \phi(\vec{k},\omega)/Z(\vec{k},\omega) . \tag{2.17}$$

This function happens to be the energy dependent Eliashberg generalization of the BCS gap.

The Eliashberg equations can be written in many different forms. If for example one chooses the isotropic case, where the momentum dependence can be integrated out, and writes them down at zero temperature for real electronic frequencies, they become[27,34]

$$\Delta(\omega) = \frac{1}{Z(\omega)} \int_0^{\omega_c} d\nu Re\left\{ \frac{\Delta(\nu)}{\sqrt{\nu^2 - \Delta^2(\nu)}} \right\} [K_+(\omega,\nu) - \mu^*] \tag{2.18}$$

and

$$[1 - Z(\omega)]\omega = \int_0^{\omega_c} d\nu Re\left\{ \frac{\nu}{\sqrt{\nu^2 - \Delta^2(\nu)}} \right\} K_-(\omega,\nu) \ , \tag{2.19}$$

where

$$K_\pm(\omega,\nu) = \int_0^\infty d\omega' \alpha^2 F(\omega') \left(\frac{1}{\omega + \omega' + \nu + i\delta} \pm \frac{1}{\omega - \omega' - \nu + i\delta} \right) . \tag{2.20}$$

Strictly speaking, the variable ω that appears in $\Delta(\omega)$ and $Z(\omega)$ should have an $i\delta$ added to it to denote we are in the upper-half of the complex frequency plane. It has been left out here for convenience.

Entering into the kernel $K_\pm(\omega,\nu)$ is the electron-phonon spectral density[34]:

$$\alpha^2 F(\omega) = \frac{\Omega}{(2\pi)^3} \sum_\sigma \frac{\int_{S_F} \frac{dS_{k'}}{|v_{k'}|} \int_{S_F} \frac{dS_k}{|v_k|} |g_{\vec{k}\vec{k}'\sigma}|^2 \, \delta\left(\omega - \omega(\vec{q},\sigma)\right)}{\int_{S_F} \frac{dS_{k'}}{|v_{k'}|}} \ . \tag{2.21}$$

In this relation, Ω is the cell volume, v_k and $v_{k'}$ are Fermi velocities and S_F denotes integration over the Fermi surface. The factor α^2 is closely related to $|g_{\vec{k}\vec{k}'\sigma}|^2$. How equation (2.21) incorporates $F(\omega)$, the phonon density of states, becomes more evident when we note that $F(\omega)$ is given by the relation :

$$F(\omega) = \frac{1}{N} \sum_{\vec{q},\sigma} \delta(\omega - \omega_{\vec{q},\sigma}) \ , \tag{2.22}$$

where N is the number of atoms in the crystal and $\vec{q}$ is restricted to the first Brillouin zone. The cut off ω_c that appears in these Eliashberg equations technically should be infinite but in practice is usually set to $\omega_c \sim 10\omega_{max}$, where ω_{max} is the maximum phonon energy. This is possible because the phonon contribution to these equations is fairly rapidly convergent. The Coulomb contribution, rather than using a full expression for the screened potential, is instead modeled by single parameter μ^*. This is possible since electronic energies are usually much higher than phonon energies (recall Migdal's theorem) and so the Coulomb interaction can be taken to be instantaneous and thus have no frequency dependence. It does however depend on the cut-off frequency ω_c. Strictly speaking, the cut-off for the Coulomb interaction should be of the same order as the Fermi energy, E_F, but Morel and Anderson[35] have shown that this cut-off can be scaled down to ω_c, with the potential renormalized according to the formula :

$$\mu^*(\omega_c) = \frac{\mu(E_F)}{1 + \mu(E_F)\ln(\frac{E_F}{\omega_c})} \ . \tag{2.23}$$

Now, if one wishes to write down the Eliashberg equations at finite temperature one must use the Matsubara formalism, where the Green's functions become expressed in terms of Fourier series that are written on the imaginary frequency axis. If one carries through the entire derivation remaining on the imaginary frequency axis, the Eliashberg equations then take the form[36]:

$$\Delta(i\omega_n)Z(i\omega_n) = \pi T \sum_{m=-\infty}^{\infty} \left[\lambda(i\omega_m - i\omega_n) - \mu^*(\omega_c)\theta(\omega_c - |\omega_m|)\right] \frac{\Delta(i\omega_m)}{\sqrt{\omega_m^2 + \Delta^2(i\omega_m)}} \tag{2.24}$$

and

$$Z(i\omega_n) = 1 + \frac{\pi T}{\omega_n} \sum_{m=-\infty}^{\infty} \lambda(i\omega_n - i\omega_n) \frac{\omega_m}{\sqrt{\omega_m^2 + \Delta^2(i\omega_m)}} . \tag{2.25}$$

Here, $i\omega_n = i\pi T(2n-1)$, $n = 0, \pm 1, \pm 2, \ldots$ are the Matsubara frequencies as defined for fermions. The factors $\Delta(i\omega_n)$ and $Z(i\omega_n)$ are the Matsubara gaps and mass renormalization functions respectively, defined at each discrete frequency. Unlike their real axis counterparts, these are purely real. The function $\theta(x)$ is defined by

$$\theta(x) = \begin{cases} 1 & \text{if } x < 1; \\ 0 & \text{if } x > 1; \end{cases} \tag{2.26}$$

The electron-phonon spectral density $\alpha^2 F(\omega)$ enters into equations (2.24) and (2.25) in this case through the relation :

$$\lambda(z) = \int_0^\infty \frac{2\nu \, d\nu \, \alpha^2 F(\nu)}{\nu^2 - z^2} . \tag{2.27}$$

Using similar justification as for the zero temperature equations, the sums that appear in these Eliashberg equations are likewise cut off in practice. The parameter μ^* here again obeys the Morel-Anderson formula.

One can also write the Eliashberg equations on the real frequency axis at finite temperature. This can be done two ways. The original way of accomplishing this was to simply sum over the Matsubara frequencies using a residue technique. This can be done at a stage in the derivation where the Matsubara frequencies correspond to points on the complex plane where there are simple poles. In this manner, one obtains a set of Eliashberg equations quite similar to the zero temperature equations (2.18) and (2.19), except that they are modified by some thermal factors which enter the integrals[32,34]. A more recent way of doing this was developed by Marsiglio, Schossmann

and Carbotte[37,38] essentially by pushing the calculation a little further. Examining the zero temperature Eliashberg equations, it is obvious that these equations through the inclusion of the kernels $K_{\pm}(\omega,\nu)$ actually involve double integrals. What Marsiglio *et al.* realized was that one of these integrals could actually be performed analytically after some manipulation. The final result is a set of equations that is, in a sense, a hybrid between the imaginary axis and original real axis formulations. These Eliashberg equations are given by:

$$\tilde{\omega}(\omega) = \omega + i\pi T \sum_{m=0}^{\infty} \frac{\tilde{\omega}_m}{\sqrt{\tilde{\omega}_m^2 - \tilde{\Delta}_m^2}} [\lambda(\omega - i\omega_m) - \lambda(\omega + i\omega_m)]$$

$$+i\pi \int_{-\infty}^{+\infty} dz \frac{\tilde{\omega}(\omega - z)}{\sqrt{\tilde{\omega}^2(\omega - z) + \tilde{\Delta}^2(\omega - z)}} \alpha^2 F(z)[N(z) + f(z - \omega)] \tag{2.28}$$

and

$$\tilde{\Delta}(\omega) = i\pi T \sum_{m=0}^{\infty} \frac{\tilde{\Delta}_m}{\sqrt{\tilde{\omega}_m^2 - \tilde{\Delta}_m^2}} [\lambda(\omega - i\omega_m) + \lambda(\omega + i\omega_m) - 2\mu^*]$$

$$+ i\pi \int_{-\infty}^{+\infty} dz \frac{\tilde{\Delta}(\omega - z)}{\sqrt{\tilde{\omega}^2(\omega - z) - \tilde{\Delta}^2(\omega - z)}} \alpha^2 F(z)[N(z) + f(z - \omega)] \tag{2.29}$$

where $\tilde{\Delta}(\omega) = Z(\omega)\Delta(\omega)$ and $\tilde{\omega}(\omega) = Z(\omega)\omega$. Also,

$$N(z) = \frac{1}{e^{\beta z} - 1} \tag{2.30}$$

is the boson occupation and

$$f(z) = \frac{1}{e^{\beta z} + 1} \tag{2.31}$$

is the fermion occupation. As with the original real axis equations, ω here should be understood to contain a infinitesimal complex part. Note that in order to solve these equations, one must already have solved the imaginary axis equations (2.24) and (2.25) so that the renormalized frequencies, $\tilde{\omega}_n$ =

$\omega_n Z(i\omega_n)$, and gaps, $\tilde{\Delta}_n = \Delta(i\omega_n)Z(i\omega_n)$, can be used as input. This set of equations, unlike the original real axis formulas, do not require evaluation of principle part integrals which are cumbersome to do numerically. The result is that these equations have a great advantage in terms of computation time. Marsiglio *et al.* [37] estimated that this advantage is in the range of two orders of magnitude. This means that calculations that may not have been attempted in the past because they were too time consuming are now within reach. In fact, some of the superconducting properties that are discussed in the latter chapters of this thesis fall in this category.

While Marsiglio *et al.* 's version of the Eliashberg equations are relatively quick to solve on a computer, the imaginary axis equations can still be solved much more rapidly as they involve sums rather than integrals and all quantities are real. Many superconducting properties can be expressed directly in terms of sums over the discrete solutions to these equations. Chief among the these are thermodynamic properties such as the specific heat, which is the subject of the fourth chapter of this thesis. The critical temperature can also be determined using the imaginary axis equations - this shall be discussed in the next chapter. Many more examples can be cited. On the other hand, there are some properties where at least at some point we must have some contact with the real frequency axis. A good example of this would be a transport property such as the optical conductivity, which in order to be physical meaningful must be known for real frequencies. The last three chapters of this thesis are devoted to properties that fall into this category - the nuclear spin relaxation, the conductivity and the phonon self-energy. On a more basic level, another quantity that must be obtained on the real frequency axis is the gap edge - this is the value of the real part of the gap

function $\Delta(\omega)$ that is the true analog of the BCS gap. The gap edge or gap for short is given in Eliashberg theory by the condition:

$$\Delta = Re\{\Delta(\omega = \Delta)\} \ . \tag{2.32}$$

There is a means by which $\Delta(i\omega_n)$ and $Z(i\omega_n)$ can be analytically continued to the real axis to give $\Delta(\omega)$ and $Z(\omega)$ without having to solve the real axis equations. The technique is to use Padé approximants[39,40]. The N-point Padé approximant, $C_N(z)$, to a complex function $u(z)$ which has N known values u_i $(i = 1...N)$ for N points on the complex plane z_i $(i = 1...N)$ is given by the continued fraction

$$C_N(z) = \cfrac{a_1}{1 + \cfrac{a_2(z - z_1)}{1 + \cfrac{a_3(z - z_2)}{\ddots \\ 1 + \cfrac{a_N(z - z_{N-1})}{1}}}} \ . \tag{2.33}$$

This continued fraction is constructed so that

$$C_N(z_i) = u_i, i = 1...N \ . \tag{2.34}$$

For our purpose here, the z_i are purely complex and are given by the Matsubara frequencies. The coefficients a_i that enter $C_N(z)$ are in turn given by a recursion formula

$$a_i = g_i(z_i),$$

where

$$g_1(z_i) = u_i, i = 1...N$$

and

$$g_p(z) = \frac{g_{p-1}(z_{p-1}) - g_{p-1}(z)}{(z - z_{p-1})g_{p-1}(z)}, p \geq 2 \ . \tag{2.35}$$

It can also be shown that

$$C_N(z) = \frac{A_N(z)}{B_N(z)} , \tag{2.36}$$

where A_N and B_N are polynomials given by the recursion

$$A_{n+1}(z) = A_n(z) + (z - z_n)a_{n+1}A_{n-1}(z), n = 1...N-1$$

and

$$B_{n+1}(z) = B_n(z) + (z - z_n)a_{n+1}B_{n-1}(z), n = 1...N-1 , \tag{2.37}$$

where $A_0 = 0$, $A_1 = a_1$ and $B_0 = B_1 = 1$. Using this latter formulation for $C_N(z)$ turns out to quite efficient numerically. Using this algorithm, one can obtain $\Delta(\omega)$ from the imaginary axis solutions accurately enough so that one can get values for the gap that compare extremely well with those obtained when $\Delta(\omega)$ is calculated directly on the real axis. Unfortunately, there are still problems. For example, if the function that is being analytically continued has fine structure such as sharp peaks or valleys, these details can be smeared by the Padé technique. The algorithm is also only truly accurate at low frequency[38]. Perhaps the biggest drawback to the technique is it's apparent sensitivity to temperature. It appears to work well at low temperature, but at higher temperatures, such as those near the critical temperature, it seems to break down. The reason for this is probably related to the problems at higher frequency. Recall that the Matsubara frequencies are proportional to temperature so that the higher the temperature the larger the imaginary frequencies become. It should be noted that work on

improving the effectiveness of the technique at higher temperature has been performed[41,42].

The Padé techniques difficulties with fine detail prove to be fatal when applied to the process known as tunneling inversion and a real axis formulation is required[43]. From tunnel junction experiments on superconductors, say from a superconductor-insulator-superconductor sandwich, one can obtain I-V data which can in turn give the tunneling density of states[44,45],

$$N(\omega)/N(0) = \left(\frac{dI}{dV}\right)_S / \left(\frac{dI}{dV}\right)_N , \tag{2.38}$$

where $S \equiv$ superconducting and $N \equiv$ normal. In Eliashberg theory, this density of states is related to the gap function $\Delta(\omega)$ through

$$N(\omega)/N(0) = \mathrm{Re}[\frac{\omega}{\sqrt{\omega^2 - \Delta^2(\omega)}}] . \tag{2.39}$$

Note that the gap defined by equation (2.32) corresponds to the frequency where the density of states experiences a sharp peak. The density of states for the superconductor lead is displayed in Fig. 2.2. Besides the sharp peak, the other features to notice are the wiggles at approximately $\sim$ 5 meV and $\sim$ 10 meV. These wiggles reflect the phonon structure in the material as they are a direct result of the electron-phonon interaction. In a truly BCS superconductor these wiggles would not occur since BCS does not contain any of the details of the phonon structure. From the previous discussion of the Eliashberg equations, we know that information about the phonons enters into these equations through the electron-phonon spectral density,$\alpha^2F(\omega)$. This tunneling data thus makes it possible to obtain $\alpha^2F(\omega)$ experimentally. To obtain $\alpha^2F(\omega)$ from the tunneling density of states is a trial and error

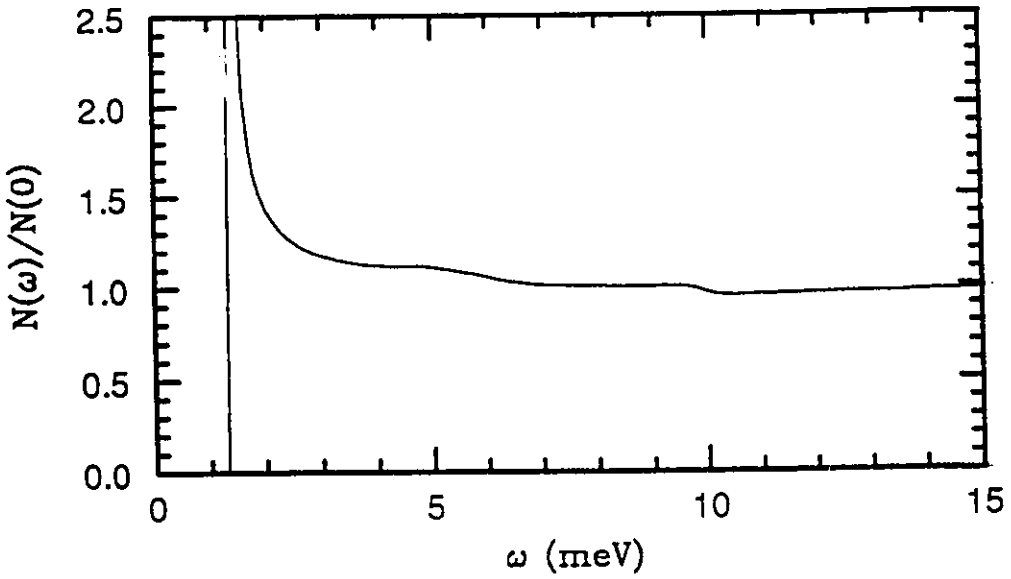

Figure 2.2 The electronic density of states, $N(\omega)/N(0)$, is plotted for the superconductor lead. The temperature is $T/T_c = 0.1$.

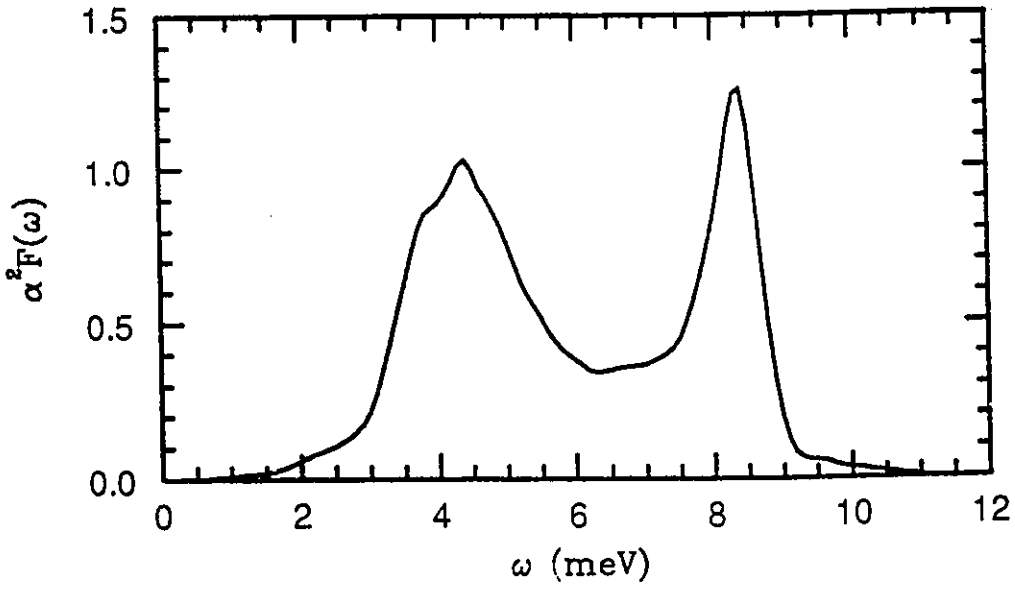

Figure 2.3 The $\alpha^2 F(\omega)$ of lead as obtained by tunneling.

process. One makes an appropriate guess for $\alpha^2F(\omega)$ and μ^* and the Eliashberg equations are solved for $\Delta(\omega)$ and $Z(\omega)$. The obtained $\Delta(\omega)$ is used to calculate a theoretical $\frac{N(\omega)}{N(0)}$ curve and this is compared with the experimentally obtained function. If the agreement is not good, $\alpha^2F(\omega)$ and μ^* are adjusted and the whole procedure repeated until the experimental and theoretical tunneling densities of states are in good agreement. The validity of the procedure can be tested by using the tunneling data up to the maximum phonon energy, ω_{max}, to obtain $\alpha^2F(\omega)$ and μ^*. Once they have been obtained, they can be used to predict what the experimental $\frac{N(\omega)}{N(0)}$ should be above ω_{max}. It should be noted that there are other methods for obtaining $\alpha^2F(\omega)$. The agreement with the tunneling results is usually reasonably good in the cases where comparison is possible[43].

In Fig. 2.3, the $\alpha^2F(\omega)$ of lead obtained from such a procedure is displayed[44]. It is this function along with the coulomb repulsion μ^* that are at the heart of Eliashberg theory. Once they are known for a given material, practically every superconducting property imaginable can then be calculated theoretically. What all superconducting properties essentially become are functionals of the electron-phonon spectral density and μ^*.

This situation is somewhat problematic in that in order to solve the Eliashberg equations we effectively must deal with an infinite number of variables. This problem can sidestepped numerically by decomposing $\alpha^2F(\omega)$ into a series of delta function bins such that it can be expressed in the form: $\alpha^2F(\omega) = \sum_{i=1}^{N} a_i\delta(\omega - \omega_i)$. Here, N is the number of bins. Typically, N must be fairly large ($N \sim 100$) in order that the actual spectrum be well reproduced. The frequencies, ω_i, are where the bins are centered and the a_i are the coupling strengths for each bin. Thus a problem involving an infinite

number of variables is reduced to one involving ~ 100 variables and in this way is made manageable numerically. We are still left with a problem, however. While we can obtain the physical properties by solving the equations in this manner, it is a "black-box" approach that makes it difficult to gain an intuitive insight into the physics.

Ideally, one wishes to break away from pure numerics and be able to obtain analytic solutions for the various superconducting properties just as can be done in BCS theory. Unfortunately, there are no exact analytic solutions to the Eliashberg equations. However, much work has been done to find approximate analytic solutions for the physical properties, especially for T_c. These solutions are usually expressed in terms of a few parameters that are themselves simple functionals of $\alpha^2F(\omega)$. Typically, the functional form is that of an integral which contains $\alpha^2F(\omega)$ as part of the integrand. In this way, the details of the electron-phonon interaction are condensed into these parameters and thus a well chosen parameter will reflect the important features of the $\alpha^2F(\omega)$ spectrum. In fact, for this reason the significance of these parameters goes well beyond just being useful in some approximate equation.

Two such parameters that are well worth mentioning are

$$\lambda = 2\int_0^\infty \frac{d\nu}{\nu}\alpha^2F(\nu) \tag{2.40}$$

and

$$\omega_{ln} = \exp\left\{\frac{2}{\lambda}\int_0^\infty \frac{d\nu}{\nu}\alpha^2F(\nu)\ln\nu\right\} \tag{2.41}$$

The parameter λ in equation (2.40) is a dimensionless measure of the strength of $\alpha^2F(\omega)$. The larger λ is the stronger the electron-phonon coupling . Conventional superconductors have λ values which reach as large as 2.5[38,43]. This

parameter has played a prominent role in approximate equations for T_c [46–48], as we shall see in the next chapter. It is also quite important physically from the standpoint that the quantity, $1+\lambda$, plays the role of the electron-phonon mass enhancement factor which renormalizes certain physical quantities such as the specific heat. One significant feature of λ is that, by the way it is defined, the low frequency range of the $\alpha^2F(\omega)$ spectrum is heavily weighted in determining its value. From this, one concludes that the low frequency phonons are very important in determining the electron-phonon coupling strength. One can recover BCS theory from Eliashberg theory in the limit $\lambda \rightarrow 0$. This is the so-called weak coupling limit. This implies that if the phonon frequencies tend to be high relative to T_c then the more likely a superconductor is to follow BCS theory.

The parameter, ω_{ln}, defined by equation (2.41) was first introduced by Allen and Dynes[48]. This parameter can be taken as an average phonon frequency characteristic of the given $\alpha^2F(\omega)$ spectrum. It's effectiveness as an average can be demonstrated by replacing the $\alpha^2F(\omega)$ spectrum of lead (Pb) shown in Fig. 2.3 with a delta function spectrum placed at the ω_{ln} value of Pb (4.829 meV) and giving it the same area as the original spectrum. What one finds is that numerical values for the physical properties are obtained that compare quite closely with those obtained with the original Pb spectrum. The Allen and Dynes parameter, like λ, places an emphasis on what occurs at lower frequencies.

Combining ω_{ln} with T_c, one can create a new parameter T_c/ω_{ln}. As was the case with λ, T_c/ω_{ln} is useful as gauge of electron-phonon coupling strength. It is so useful in fact that a great many approximate formulas for strong coupling corrections to BCS quantities have been derived using T_c/ω_{ln}

as sole input parameter[38,49,50]. These approximate formulas have been very successful in reproducing the results of the full numerical solution of the Eliashberg equations for real crystalline materials. Some of these formulas shall be discussed later in this thesis. In all the chapters that follow, very extensive use of T_c/ω_{ln} as a strong coupling parameter shall be made.

Chapter 3

The Critical Temperature and the Isotope Effect

3.1 INTRODUCTION

In this chapter, we shall focus on two main issues which are closely related. Since the goal is to account for the behavior of the high-T_c oxides, we must answer the question of how one can achieve temperatures of order 100 K within the context of the Eliashberg formalism. As we shall see from the extensive discussion of the critical temperature following in the second section of this chapter, there are several ways within the theory that these high critical temperatures can be achieved. While this is true, one must also be concerned having that the explanation be consistent with other experimental data. One type of experiment that is particularly important in this regard involves changing of the isotopic mass of the atoms in the superconductor to see if there is a shift in T_c. This shift in T_c is identified as the isotope effect. The sort of isotope effects that have been measured in the oxides are in most

cases much smaller than what one usually expects for an Eliashberg superconductor. This has been taken as evidence by some that Eliashberg theory can not be applied to these materials. It will be shown in the third section of this chapter that this need not be the case as small isotope effects can be easily accommodated by the theory. Conclusions are drawn in the closing section of this chapter as well as some comments on some recent dramatic experimental developments.

3.2 THE CRITICAL TEMPERATURE

As mentioned previously, the critical temperature is of course the temperature at which the superconductor turns normal. This constitutes a phase transition. One can consider the superconducting phase as being more ordered as the normal phase since as, has been outlined earlier, electrons with equal and opposite momentum are correlated and the system forms a many-body condensate. One way one can quantify an ordered phase is by introducing what is called an order parameter which vanishes at the transition temperature. Not surprisingly, different systems will have different order parameters. For a ferromagnet, it is the magnetization, M. In the case of a BCS-Eliashberg superconductor, the appropriate order parameter is the superconducting gap function. So, in order to determine the critical temperature, one must calculate the temperature at which the gap function vanishes. In BCS theory, this is fairly easy to do and one can get after some approximations the analytic expression first discussed in chapter 1:

$$k_B T_c = 1.13\,\hbar\omega_D \exp\left(-\frac{1}{N(0)V}\right), \tag{3.1}$$

where again N(0) is the electronic density of states at the Fermi energy and V is the BCS pairing potential.

This equation is beautiful in it's simplicity. Unfortunately, it is also limited in it's applicability. Of course, in order to calculate the critical temperature accurately for an electron-boson superconductor one must use Eliashberg theory. At T_c, the Eliashberg equations introduced in chapter 2 take on the form

$$\Delta(i\omega_n)Z(i\omega_n) = \pi T \sum_{m=-\infty}^{\infty} \left[\lambda(i\omega_m - i\omega_n) - \mu^*(\omega_c)\theta(\omega_c - |\omega_m|)\right] \frac{\Delta(i\omega_m)}{|\omega_m|} \qquad (3.2)$$

and

$$Z(i\omega_n) = 1 + \frac{\pi T}{\omega_n} \sum_{m=-\infty}^{\infty} \lambda(i\omega_m - i\omega_n) sgn(\omega_m) \; . \qquad (3.3)$$

Essentially the only difference between these equations and those in the last chapter is that the Matsubara gaps that appeared in the denominators of the original equations have been set to zero. Despite this simplification, these equations must still be solved numerically in order to determine T_c. While this can be done quite quickly on a computer, much effort has been put into trying to derive approximate analytic expressions for T_c which will be applicable beyond the BCS weak coupling limit.

Probably the most popular T_c equation that has been derived is the one given by McMillan[46]. This equation is given by

$$k_B T_c = \frac{\hbar\omega_{ln}}{1.2} \exp\left(-\frac{1.04\,(1+\lambda)}{\lambda - \mu^*\,(1+0.62\lambda)}\right) \; . \qquad (3.4)$$

This equation has a similar form to the BCS formula but contains factors one associates with Eliashberg theory- λ, μ^* and the Allen and Dynes parameter ω_{ln}. It should be noted that there are different variations of this formula. How they vary is in the prefactor as there are several ways one may choose

to define an average boson frequency. The Allen-Dynes parameter is just one possible choice. The McMillan formula represents an improvement over the BCS expression but it still has some important limitations. First of all, it still is not particularly accurate. As an example[43], Pb has $\lambda = 1.55$, $\omega_{ln} = 4.829$ meV and $\mu^*(\omega_c = 66\text{meV}) = 0.144$, for which the McMillan equation gives a $T_c = 5.76K$. The full equations (3.2) and (3.3) on the other hand yield $T_c = 7.2K$ which is about twenty percent larger. In the case of the full equations, the value of μ^* that we use depends on the cut-off ω_c. In the case of the McMillan equation, which was derived from the full equations, the choice is no longer clear as it is ω_{ln} that appears in the equation and not ω_c. For our purposes here, the μ^* we shall use whenever we use the McMillan equation is that appropriate to a cut-off $\omega_c = \omega_{ln}$. This is the obvious choice to make, but does not fall out of the mathematics of the derivation. In fact, how one should treat μ^* here is not precisely known.

One important aspect of both the BCS formula and the McMillan equation is that both predict a saturation of T_c if one keeps ω_D or ω_{ln} fixed while increasing $N(0)V$ or λ. It should be noted here that $\frac{\lambda-\mu^*}{1+\lambda}$ in Eliashberg theory can be thought of as being essentially equivalent to the BCS $N(0)V$. In the case of the McMillan formula the maximum is given by[43]

$$(k_B T_c)^{max} = \frac{\hbar\omega_{ln}}{1.2} \exp(-1.04) \; . \tag{3.5}$$

This formula is obtained by taking the limit $\lambda \to \infty$. From this result, it appears that the theory puts intrinsic limitations on T_c which is an important consideration if one is trying to obtain a high T_c. However, this is a spurious conclusion. This is well illustrated by Fig. 3.1. In this figure, we plot T_c/ω_{ln} vs. λ for the McMillan equation with $\mu^* = 0.1$. Also plotted on

this figure are the results of the full equations obtained using several different $\alpha^2F(\omega)$ spectra: Pb, Hg, Nb and Nb_3Sn . Different values of T_c/ω_{ln} were obtained by scaling the spectra ie. introducing scaling factors B and b such that $\alpha^2F(\omega) \rightarrow B\alpha^2F(b\omega)$. It has been shown by Coombes and Carbotte[51,52] that shifting b has an effect both on T_c and ω_{ln}: $T_c \rightarrow \frac{T_c}{b}$ and $\omega_{ln} \rightarrow \frac{\omega_{ln}}{b}$. For reasons that shall become clearer later, changing the B factor influences the T_c that can be obtained. Using this scaling technique, any value of T_c/ω_{ln} can be obtained from any $\alpha^2F(\omega)$. Throughout this thesis, this type of scaling will be used to evaluate various superconducting properties as a function of T_c/ω_{ln}. Importantly, the quantities that shall be examined in this manner (typically a ratio of some sort) can be shown, for a given base spectrum, to be independent of how the spectrum was scaled - only T_c/ω_{ln} is important.

In Fig. 3.1, the McMillan equation gives us a saturation for large λ as expected. The results using the full equations for the various scaled spectra tell a different story. While the different spectral shapes yield different quantitative results, the qualitative trend is clear - T_c/ω_{ln} continues to increase with λ and there is no saturation.

After careful consideration, it has been determined by Leavens and Carbotte[53,54] that it is the area under the $\alpha^2F(\omega)$, $A = \int_0^\infty d\nu\, \alpha^2F(\nu)$ that plays perhaps the most important role in determining T_c. For any spectral shape at all, they derived the following inequality

$$T_c \leq C(\mu^*)\, A\ , \tag{3.6}$$

where $C(\mu^*)$ is a function only of μ^*. Roughly speaking then, a larger area, A, will usually give a higher T_c. Of course, we can increase A indefinitely by increasing our scaling factor B.

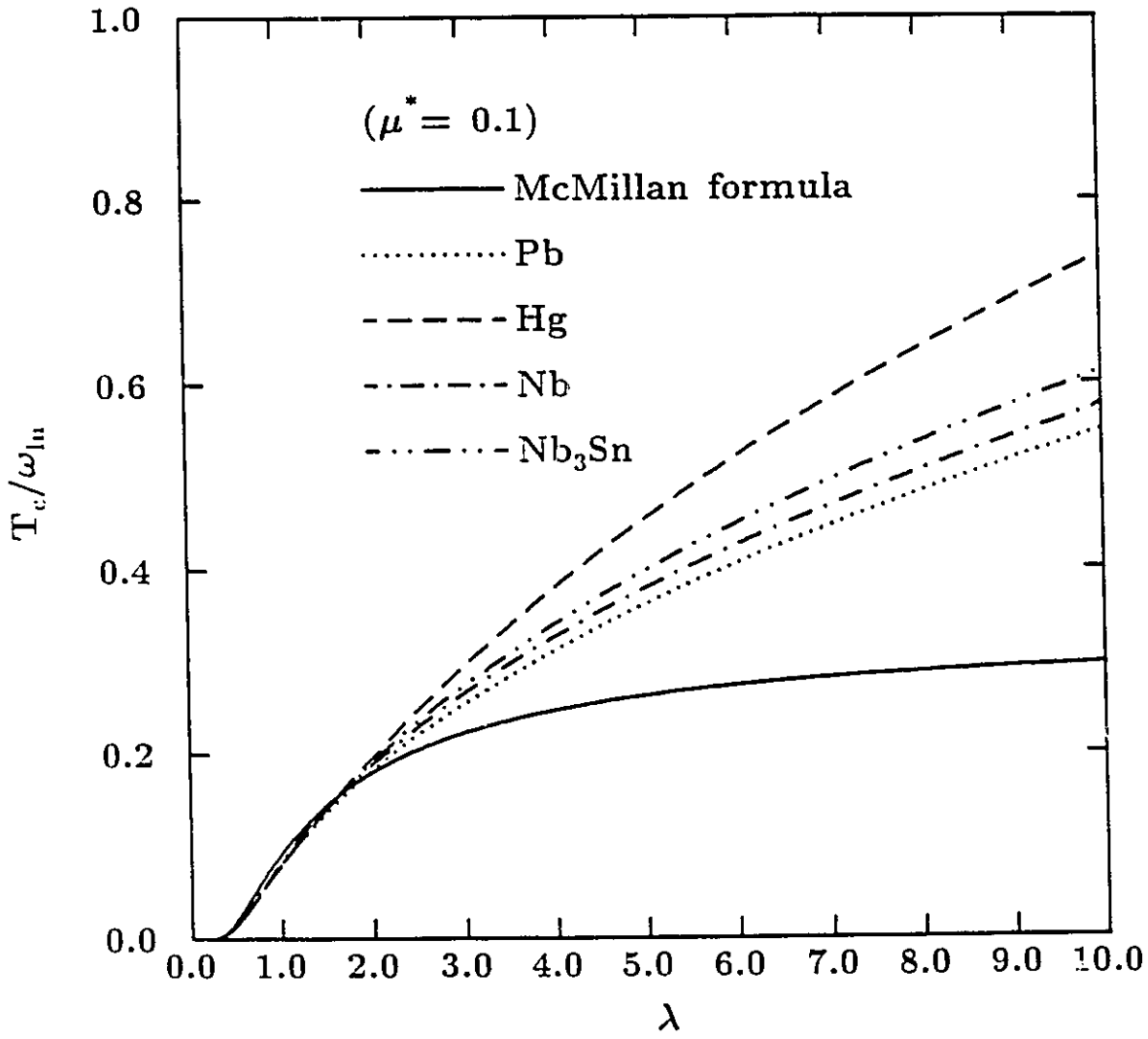

Figure 3.1 T_c/ω_{ln} vs. λ is plotted for the McMillan formula as well as for the full solution of the Eliashberg equations using the scaled $\alpha^2 F(\omega)$ of the materials Pb, Hg, Nb and Nb_3Sn.

From using the full equations it is evident the mathematics of the theory by itself does not put a limitation on T_c. Instead, one must apply physical arguments that are external to the theory. One such argument which applies to the phonon mechanism involves lattice stability. It is believed[55,56] that, if the electron-phonon coupling becomes too strong, the lattice will become unstable and a structural phase transition will ensue. Just when this will occur can only be roughly estimated. Now in conventional materials $\lambda \leq 2.5$. Referring back to Fig. 3.1, data for λ as large as 10 has been plotted. If we fix $T_c = 100K$, this translates to an $\omega_{ln} \sim 15$ meV, depending on the spectral shape that is considered. While one can not be sure when the instability will occur, it seems likely that a $\lambda = 10$ due to phonons may not be physically plausible. In the meantime, an $\omega_{ln} = 15$ meV would represent a typical value of this parameter for conventional materials. The value $\mu^* = 0.1$ that has been used is also what one would consider typical.

There are reasons other than lattice stability for rejecting a pure phonon mechanism for the high-T_c oxides. Some of these will be encountered later on in this thesis.

Of course, the most direct means to avoid the problems posed by phonons is to invoke a different mechanism for the superconductivity. Indeed, a countless number of new theories involving many different mechanisms have been developed to try to account for the high-T_c oxides. For our own purposes, rather than start from scratch and try to develop a new formalism, we shall consider only mechanisms for which Eliashberg theory can be directly applied. This still leaves us with many possibilities, as Eliashberg theory would be applicable to any mechanism that involves the exchange of virtual bosons. Two such possible exchange bosons are plasmons[57,58] and

excitons[59–62]. Bosons that are electronic in nature being intrinsically high in frequency are particularly attractive with respect to getting large transition temperatures. That this should be the case is obvious from the BCS T_c equation where the frequency appears as part of the prefactor. Much work has been done trying to work out the underlying physics behind these potential mechanisms. In the end however, when one wants to see the implications on the superconducting state that these mechanisms would have, what is required are appropriate choices for the $\alpha^2F(\omega)$ and μ^*. In the case of an electronic boson-exchange mechanism where the characteristic energies are much higher than one expects for phonons the situation is made relatively simple. If this is the case and one looks at a strong-coupling parameter such as T_c/ω_{ln} the BCS limit is approached. In this limit, the actual shape of the $\alpha^2F(\omega)$ spectra becomes less and less important[63,64]. Given this, we can use the simpliest $\alpha^2F(\omega)$ possible, a delta function, in order to represent the electronic mechanism. Of course, the frequency where this delta function is placed will be high enough to be appropriate to the mechanism one is trying to model. In the past, such models were used with a phonon contribution also included to calculate many superconducting properties[38,61,62]. A phonon contribution is still required in order to account for the finite isotope effects observed in the oxides.

One potential problem with a high-energy boson mechanism is a violation of Migdal's theorem, which was discussed briefly in the last chapter. With a high energy mechanism, ω_{boson} becomes much more comparable with E_F, indicating that vertex corrections should perhaps be included. However, some work by Marsiglio[65,66] has indicated that the inclusion of vertex corrections may not be too important, even in a situation such as this.

There is another means by which an electronic mechanism can be introduced into Eliashberg theory. If the high energy mechanism puts us in the BCS limit, then it can be modeled by a constant BCS pairing interaction $N(0)V$. This interaction is included into the equations by combining it with the coulomb repulsion parameter μ^* to form an effective attractive Coulomb pseudopotential:

$$\mu^*_{eff} = -N(0)V + \mu^* \ . \tag{3.6}$$

Of course, for μ^*_{eff} to represent an attractive interaction, $N(0)V$ has to be large enough to overcome μ^* so that $\mu^*_{eff} < 0$. If this is the case, then one can define a critical temperature associated with this high energy mechanism by itself:

$$T_{c0} = 1.13\,\hbar\omega_c \exp\left(\frac{1}{\mu^*_{eff}(\omega_c)}\right) \ . \tag{3.7}$$

This equation is essentially a restatement of the BCS equation. However, it is important to point out that it is the cut-off that we apply to the equations, ω_c, that appears here and not the actual frequency of the boson. In this equation we emphasize the fact that μ^*_{eff} is a function of ω_c as it obeys the Morel-Anderson formula given in the previous chapter. Since we need not specify the frequency of the mechanism as we would using delta functions,this means that this type of model is quite general when applied to an electronic mechanism and we in fact need not identify which type of boson is the mediator for the superconductivity.

Using this sort of model, since it is so general, is intrinsically less accurate than the previous work involving the delta function models. However, since we are near the BCS limit it is not expected that truly significant differences between the two methods should occur. Indeed, what has been

found is confirmation of the previous results[67]. Given this, we can apply the μ^*_{eff} model with confidence and exploit the advantage it gives us by being so general.

To include phonons with the electronic mechanism is as simple as including an $\alpha^2F(\omega)$. When both contributions are combined one obtains a $T_c > T_{c0}$. This is not surprising. What perhaps is surprising is how the two contributions act together to give the net T_c. One can define the phonon contribution to the T_c as

$$\Delta T_c = T_c - T_{c0} \; . \tag{3.8}$$

In Fig. 3.2, we plot $\Delta T_c/\omega_{ln}$ vs. T_{c0}/ω_{ln}. The parameters, $\Delta T_c/\omega_{ln}$ and T_{c0}/ω_{ln}, can be shown to follow the same scaling as T_c/ω_{ln}. To produce this figure, we have used the Pb $\alpha^2F(\omega)$ which was scaled so that we could obtain three different values for the mass enhancement parameter λ: $\lambda = 1.55$ (solid line), $\lambda = 3.10$ (dotted) and $\lambda = 4.55$ (dashed). For each of these values of λ, we see that the phonon contribution to the net T_c/ω_{ln} initially increases rapidly as we turn on the electronic contribution at $T_{c0}/\omega_{ln} = 0$, passes through a maximum as we continue to increase T_{c0}/ω_{ln}, and then drops off quite gradually. From this figure, it is obvious that for each value of λ, there is an optimum phonon contribution to T_c/ω_{ln}, $(\Delta T_c/\omega_E)_{max}$.

In Fig. 3.3, we plot $(\Delta T_c/\omega_E)_{max}$ vs. λ. In this case we have used delta functions to represent the phonon contribution and ω_E is the delta function frequency. For comparison, we also plot T_c/ω_E as well. This is just the critical temperature given by the phonons in the absence of the electronic contribution - $\mu^*_{eff} = 0$. For all values of λ displayed $(\Delta T_c/\omega_E)_{max} > T_c/\omega_E$. From this figure and the previous one it is apparent that not only does

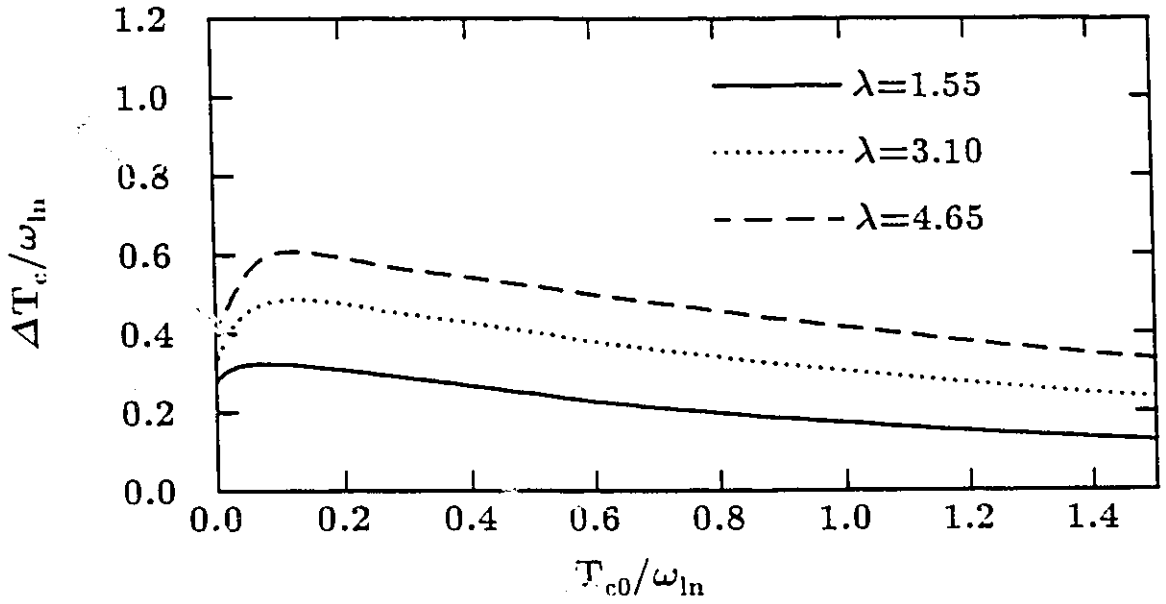

Figure 3.2 $\Delta T_c/\omega_{ln}$ vs. T_{c0}/ω_{ln} is plotted using results obtained from a scaled Pb $\alpha^2F(\omega)$ spectrum.

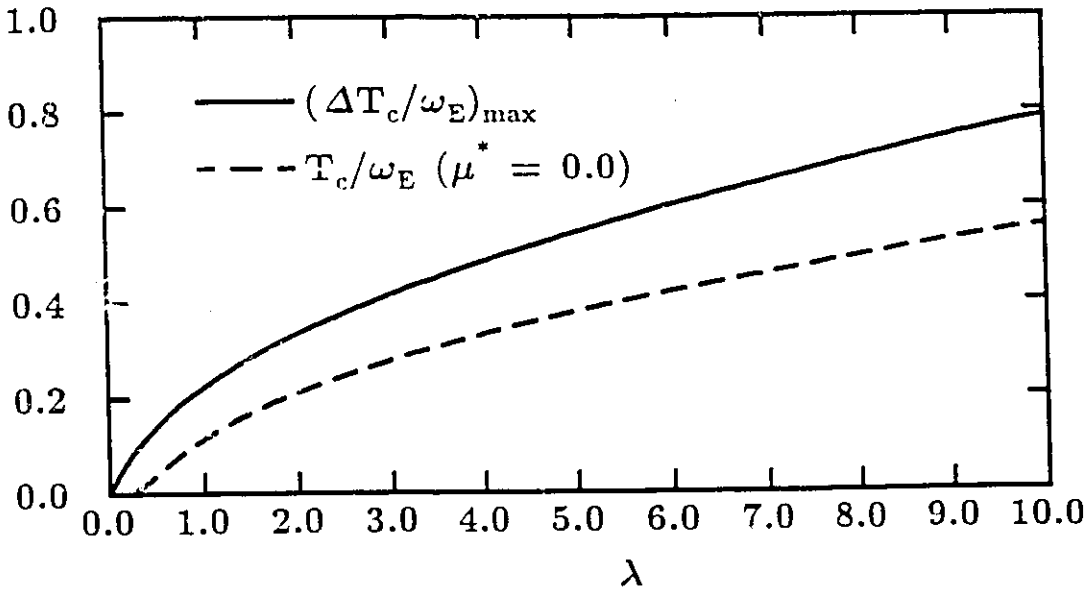

Figure 3.3 $(\Delta T_c/\omega_E)_{max}$ and T_c/ω_E are plotted against λ.

including an electronic contribution increase the T_c but it has a strong effect on how the phonons themselves contribute to the T_c and in fact can enhance their effectiveness if the electronic and phonon contributions are in the proper balance.

The appropriate question to ask at this point is, given that such a combined phonon-high energy boson mechanism is applicable, how does one determine the relative contributions of the two mechanisms. The question can be answered at least in part by appealing to the isotope effect. which is the topic of the next section of this chapter. Beyond answerering this question, we shall also see how having a pure phonon mechanism may not be out of the realm of possibility provided certained special conditions are met.

3.3 THE ISOTOPE EFFECT

In the introduction to this chapter, the isotope effect was described in terms of shifting T_c by changing the atomic masses of the ions in the superconducting crystal. These shifts can be quantified by introducing an isotope effect coefficient, β:

$$\beta = \frac{-d\,ln\,T_c}{d\,ln\,M} \ , \tag{3.9}$$

where here M is the ion mass. In the case of BCS, the fact that $\omega_D \sim 1/\sqrt{M}$ can be used to obtain the result that $\beta = \frac{1}{2}$. As is common in BCS, this result is a universal prediction. In reality, almost all superconductors deviate from this result. Some by relatively small[68] amounts e.g, $\beta_{Pb} = 0.48$, others much more dramatically[68] e.g., $\beta_{Ru} \sim 0.0$. It can be shown that the deviations from $\beta_{BCS} = \frac{1}{2}$ stem primarily from the Coulomb interactions which enter through μ^*. This can be most easily seen by applying equation (3.9) to the McMillan

T_c equation. When this is done one obtains the following equation for the isotope effect[69]:

$$\beta = \frac{1}{2}\left[1 - \frac{1.04(1+\lambda)(1+0.62\lambda)}{(\lambda - \mu^*(1.0+.62\lambda))^2}\,\mu^{*2}\right] . \tag{3.10}$$

where

$$-\frac{1}{2}\,\mu^{*2} = \frac{d\,ln\,\mu^*}{d\,ln\,M} . \tag{3.11}$$

The relationship given in equation (3.11) stems directly from the Morel-Anderson formula. Equation (3.10) reduces to $\frac{1}{2}$ in the case where $\mu^* = 0.0$.

In Fig. 3.4. we plot β vs. λ using the McMillan isotope equation. We show results for three different μ^*'s: $\mu^* = 0.10$ (solid line), $\mu^* = 0.13$ (dotted) and $\mu^* = 0.2$ (dashed). For the larger values of λ. The values of β appear to be trending toward $\frac{1}{2}$ with the results for $\mu^* = 0.2$ lagging far behind the other two curves in this regard. What is more interesting is the sudden plunge that all the curves show toward $\beta = 0.0$ for the smaller values of λ. In fact, though we have not shown them here, equation (3.10) quite readily yields $\beta < 0.0$. The point where $\beta = 0.0$ is given by

$$\mu^* = \frac{\lambda}{1 + 0.62\lambda + \sqrt{1.04(1+\lambda)(1+0.62\lambda)}} . \tag{3.12}$$

For $\lambda = 0.4$, $\mu^* \simeq 0.154$ for $\beta = 0.0$. Such a value of μ^* would be considered large for a conventional superconductor. Putting these parameters into the McMillan T_c equation, one obtains a small T_c. Indeed, those conventional superconductors where small isotope effects have been observed generally have low T_c's[68,70]. What is occurring is that λ in these cases is of the same order as μ^* and the result of this competition is reflected in T_c and β. In the case of Pb, λ is much larger than μ^* so that the effect of it's inclusion amounts to only a tiny correction.

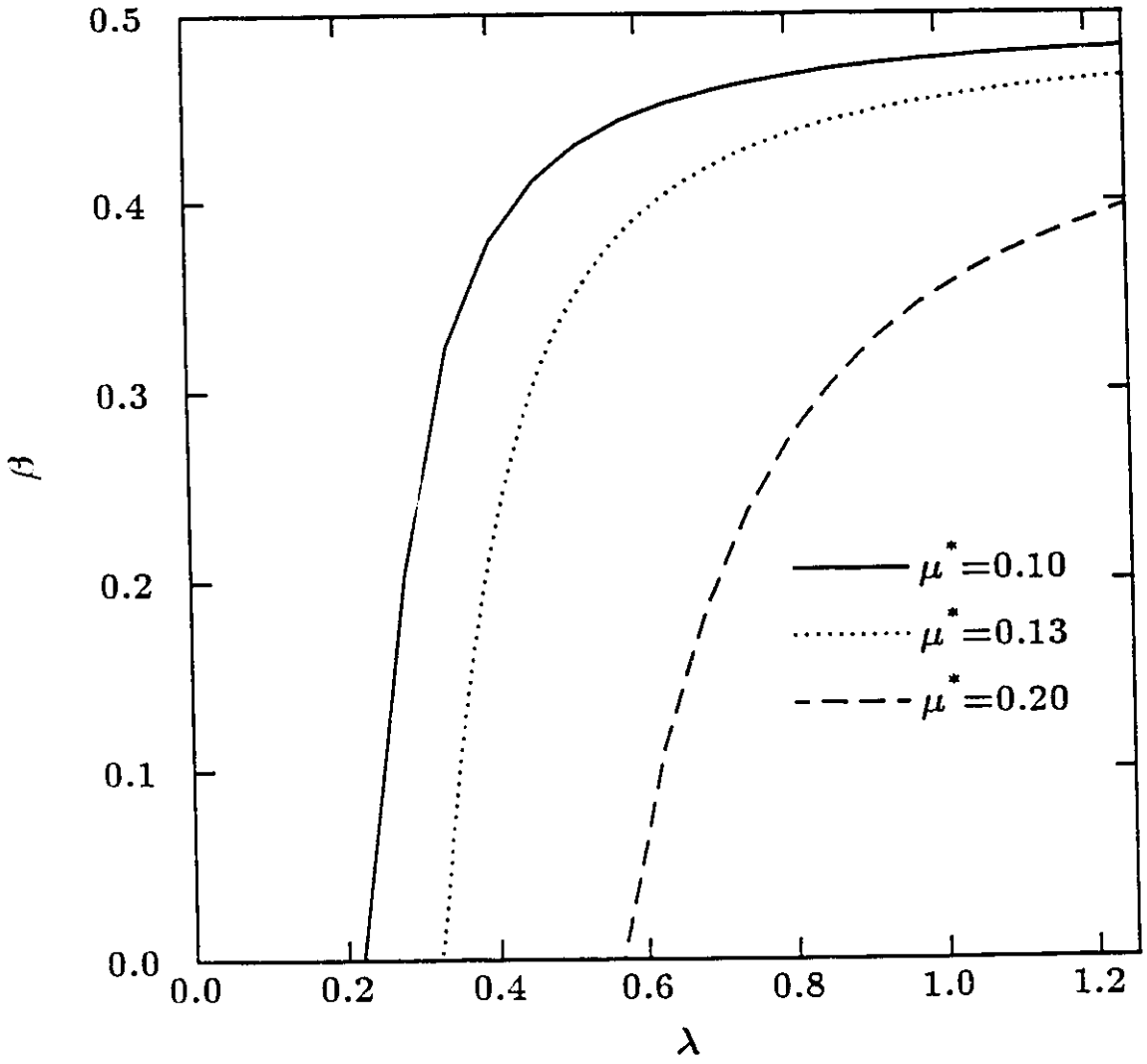

Figure 3.4 β vs. λ is plotted using results obtained using the McMillan equation.

From Fig. 3.4, and equation (3.12) it is apparent that the value of λ that is permissible for $\beta \sim 0.0$ increases with μ^*. The larger λ is the higher T_c. This seems to suggest the possibility that one may be able to get a substantial T_c and yet at the same time get $\beta \sim 0.0$. These are the sorts of conditions one is required to deal with in the high-T_c oxides.

In the case of YBCO, several groups have measured the oxygen isotope effect[71-76]. Now since this is a compound one must deal with isotope effects due to the different kinds of ions. It turns out that partial isotope effects can be defined for each M_i according to

$$\beta_i = \frac{-d\ln T_c}{d\ln M_i} \ . \tag{3.13}$$

and a total isotope effect given by

$$\beta_{tot} = \sum_i \beta_i \ . \tag{3.14}$$

In the case where $\mu^* = 0.0$, β_{tot} must satisfy $\beta_{tot} = \frac{1}{2}$. While this may be the case, in general each individual partial isotope effect can be quite different. For YBCO, it has been discovered that $0.0 \leq \beta_{ox} \leq 0.1$, with β_{ox} being typically ~ 0.05[69]. From this fact alone, one cannot conclude very much about the participation of the electron-phonon interaction. Importantly, the isotope effects of Ba and Cu have also been measured[77-81] and appear to be zero within the experimental error. This seems to suggest that the *total* isotope coefficient is of order $\beta_{tot} \sim 0.05$. This is a very significant result as it places strong constraints on the theory. Obviously, using a large λ with a small μ^* may give a large T_c but it would also give $\beta \sim \frac{1}{2}$ and so must be rejected.

We return now to the conjecture that combining a large μ^* with a large λ may give the desired results. One can justify the possibility of these conditions existing in the oxides simply by noting that the carrier concentration of these materials is low, particularly in comparison with metals. Since this is the case, it is reasonable to expect that the effect of screening is reduced. This in turn will have two effects. The first is that the electron-phonon interaction is enhanced, leading to larger λ's. The second is that the coulomb repulsions represented by μ^* will also be larger. It was mentioned earlier that the McMillan equation has limited validity. This implies that any conclusions drawn from it must be viewed with some skepticism. Obviously, one must use the full equations in order to test our conjecture[82].

In fig. 3.5, we plot β vs λ for results obtained using both the McMillan β formula and the full Eliashberg equations using $\alpha^2F(\omega) = \frac{\lambda\omega_E}{2}\delta(\omega - \omega_E)$. The curves represent the McMillan results for the following values of μ^*: 0.1 (solid), 0.2 (dotted), 0.3 (dashed) and 0.45 (dash-dotted). The data points represent the results of the full calculations for $\mu^* = 0.2$ (circles), $\mu^* = 0.45$ (crosses) and $\mu^* = 0.50$ (triangles). It is important to note that these μ^*'s are meant to apply to the delta function frequency ω_E and are related to those that one actually uses in the calculations, which are appropriate to ω_c, through the Morel-Anderson formula. As mentioned in the previous chapter, ω_c needs to be several times larger than the maximum boson frequency in order for the equations to converge. First of all, we see that the results of the full calculations appear to agree with the qualitative trend set by the McMillan formula, with a drop toward $\beta \sim 0.0$ in the lower λ range. The quantitative agreement between the full calculation and the McMillan equation is particularly good for $\mu^* = 0.2$. However, in the case of $\mu^* = 0.45$

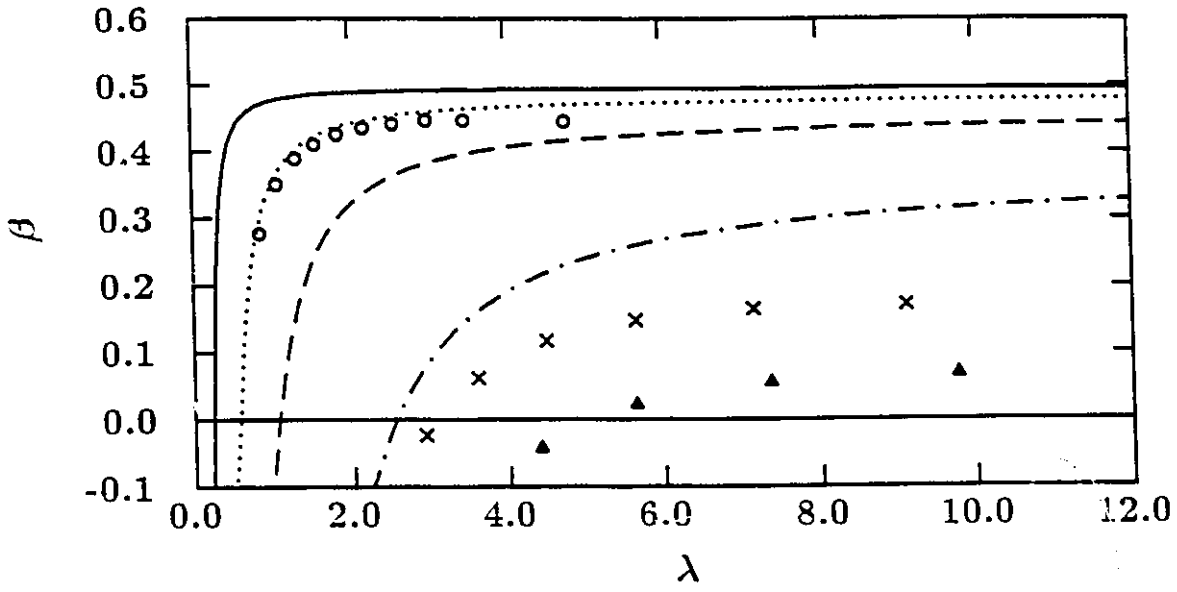

Figure 3.5 β vs. λ is plotted using results obtained using the McMillan equation for $\mu^* = 0.1$ (solid line), $\mu^* = 0.2$ (dotted), $\mu^* = 0.3$ (dashed) and $\mu^* = 0.45$ (dash-dotted). Results for the full Eliashberg equations are also depicted for $\mu^* = 0.2$ (circles), $\mu^* = 0.45$ (crosses) and $\mu^* = 0.50$ (triangles).

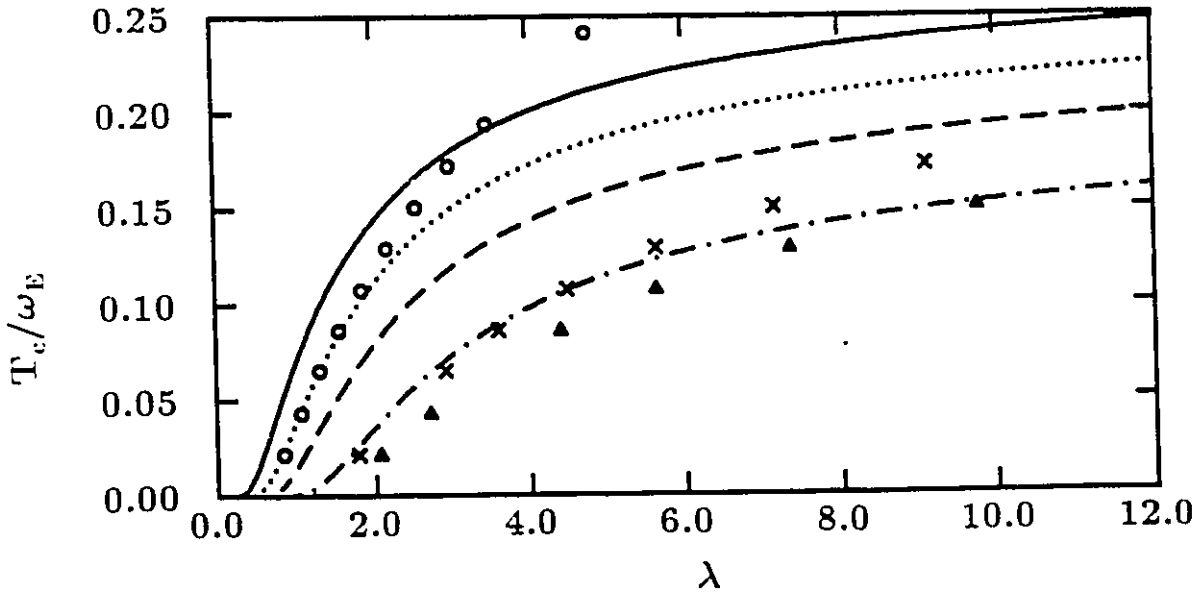

Figure 3.6 T_c/ω_E vs. λ is depicted for results obtained using the Mcmillan equation as well the full Eliashberg equations. For the meanings of the symbols and curves, refer to the previous figure.

the results differ substantially, with the McMillan formula over estimating β. Of particular interest is the point where β crosses zero. For $\mu^* = 0.45$, the full calculation yields $\lambda \sim 3.0$ for $\beta = 0.0$. This is just slightly larger than the maximum for the conventional range for λ. For $\mu^* = 0.5$, the required λ is of the order of 5.0. This is about twice the conventional maximum value, but not so large as to be totally out of the realm of possibility, particularly since the electron-phonon effects may be enhanced by reduced screening.

To see what critical temperatures these values of λ translate into, T_c/ω_E vs λ is plotted in Fig. 3.6. Again, we are comparing the McMillan results with the full calculations and the curves and symbols apply to the same cases as the previous figure. Comparing the McMillan results with the full calculations for $\mu^* = 0.2$, we see the same trend as was shown in Fig. 3.1, the McMillan formula showing an apparent saturation while the full calculation continues to increase. On the other hand, for $\mu^* = 0.45$, the exact results no longer grow as quickly and the McMillan formula appears to hold fairly well up to $\lambda \sim 6.0$. This is somewhat surprising considering how poorly the McMillan formula reproduces the isotope effect in this case. For the two larger values of μ^*, it appears from the exact calculations that having $\lambda \sim 5.0$ means that $T_c/\omega_E \sim 0.1$. For $\lambda \sim 3.0$, T_c/ω_E, is more of the order of 0.05.

This gives us quite stringent conditions under which one may see a small isotope effect for a high T_c superconductor. If one takes $T_c = 100K$, then $T_c/\omega_E = 0.1$ translates into $\omega_E \simeq 90$ meV. This is quite high but not out of the question. Indeed, the results of neutron scattering experiments indicate that the phonon spectrum of YBCO does extend up to these high frequencies[83,84]. So it appears that the case $\mu^* = 0.5$, $T_c = 100K$ and $\omega_E \simeq 90$ meV and $\beta \sim 0.0$ may be in the realm of physical possibility. The $\mu^* = 0.45$ case can be ruled

out as the required phonon frequencies would be too high. However, even in the optimistic case we have outlined, there are still difficulties in that the electron-phonon coupling would have to be almost exclusively to these high frequencies. In the course of the calculations displayed here we have been using delta functions for $\alpha^2F(\omega)$. One should recall from the previous chapter that a delta function can act as a good approximation for a full $\alpha^2F(\omega)$ provided we set $\omega_E = \omega_{ln}$. From the way that ω_{ln} is defined, it is apparent that if an $\alpha^2F(\omega)$ spectrum has any significant weight at lower frequencies then ω_{ln} is reduced drastically. In order to obtain a small β in a case where the phonons that are being coupling to are lower in energy requires that a larger μ^* be employed. As in the case of λ, there must be some point where the size of μ^* must be considered unphysical but this is difficult to determine.

Before closing this discussion on large μ^*'s, it should be mentioned that there has been some previous work done on this type of model by Bourne *et al.* [77] and also by Hoen *et al.* [85]. In these papers, the basic result was that one required λ of the order of 30 even with a large μ^* in order to obtain $\beta \sim 0.0$. In these calculations a full spectrum was employed rather than delta functions. To be more specific, the $\alpha^2F(\omega)$ was simulated by using an experimentally obtained phonon density of states of YBCO. The electron-phonon coupling, α^2, was taken to be independent of ω. Thus, in this earlier work the average phonon frequency was fixed at a fairly low frequency in comparison to those we have been talking about here. The T_c they used was also fixed so that the only parameters left to vary were λ and μ^*. Obviously, in both these papers a much more restricted region of parameter space is considered.

The goal of achieving a small isotope effect while also obtaining a high T_c can also be accomplished by employing the sort of joint electronic-phonon mechanism discussed in the previous section. In this situation, shifting the phonon frequencies by changing the isotope effect only directly alters ΔT_c and not T_{c0}. Thus, the smaller the phonon contribution to the net T_c the smaller the isotope effect will be. For the purposes of the calculations shown here, we shall again employ delta functions.

In Fig. 3.7, we plot β vs. T_c/ω_E for several different values of T_{c0}/ω_E, namely 0.022 (solid), 0.173 (long-dashed), 0.348 (dash-dotted), 0.521 (dash-double dotted) and 0.696 (dash-triple dotted). For $\beta = 0.0$, all curves start at their given values of T_{c0}/ω_E. When the phonon contribution is first turned on and then increased, the T_c/ω_E value increases as well as the isotope effect. As is apparent in this figure, how quickly the isotope effect increases depends on how large T_{c0}/ω_E is. It should be noted that even for the largest value of T_{c0}/ω_E, the rise of β is still fairly rapid. If one wishes a $\beta < 0.1$ in this case, this means that the phonon contribution to T_c would have to be less than about one eighth of the total T_c from reading off the figure.

While in this model it appears that the phonon contribution to T_c must be small in order to obtain a small isotope effect, this does not necessarily imply that the mass enhancement parameter λ is small. This is demonstrated in Fig. 3.8 where λ vs. T_c/ω_E is plotted. For the curves in this figure, the phonon and electronic contributions have been adjusted to keep the the isotope effect fixed. The following values of β are considered: 0.05 (solid), 0.1 (dotted), 0.2 (dashed), 0.3 (dot-dashed), 0.4 (double-dot-dashed) and 0.5 (triple-dot-dashed). This last curve applies for a case where $\mu^*_{eff} = 0.0$ or in other words, pure electron-phonon. In this case, the rise in λ with T_c/ω_E is

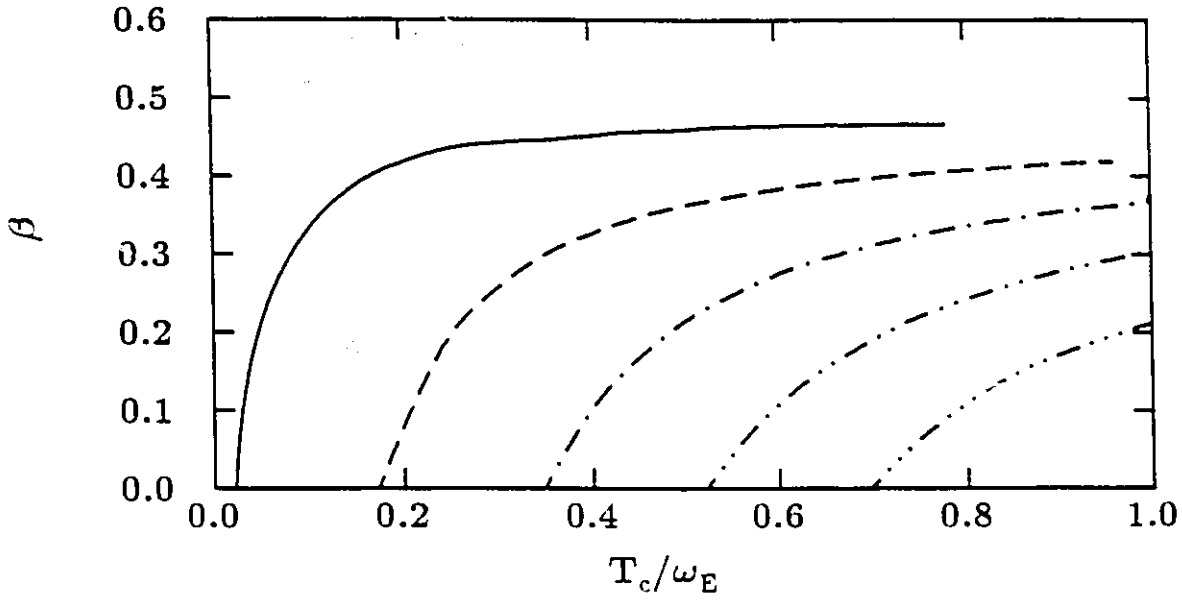

Figure 3.7 β vs. T_c/ω_E shown for several different values of T_{c0}/ω_E : 0.022 (solid line), 0.173 (long-dashed), 0.348 (dash-dotted), 0.521 (dash-double dotted) and 0.696 (dash-triple dotted).

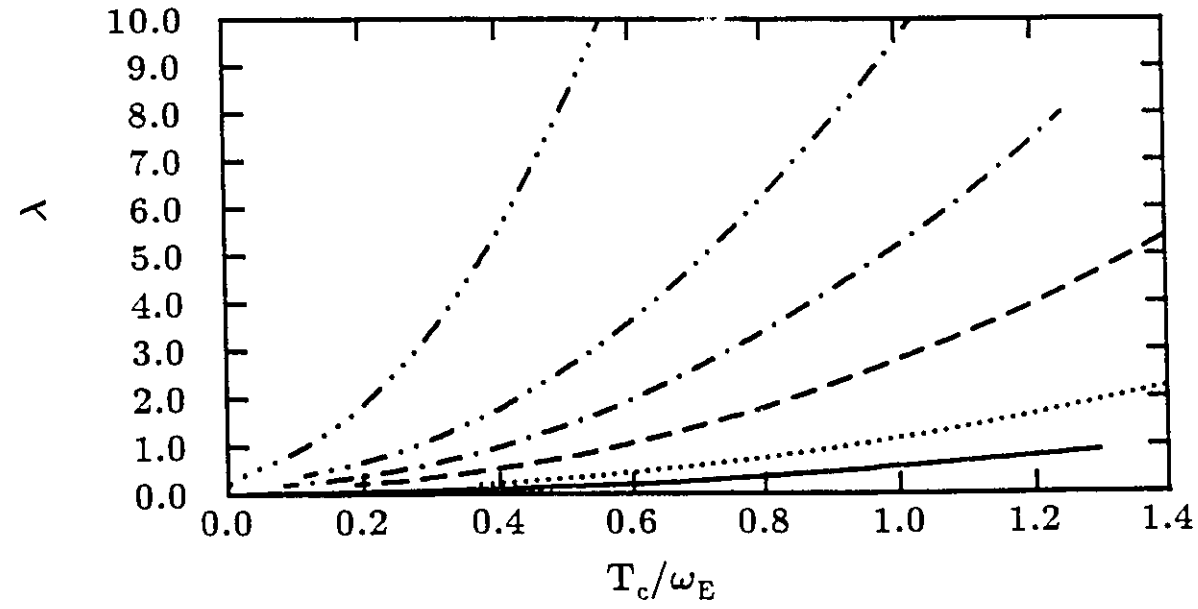

Figure 3.8 λ vs. T_c/ω_E is plotted for several fixed values of β, these being 0.05 (solid line), 0.1 (dotted), 0.2 (dashed), 0.3 (dot-dashed), 0.4 (double-dot-dashed) and 0.5 (triple-dot-dashed).

quite rapid. As the isotope effect is reduced, the rise in λ becomes markedly less rapid. For the case where $\beta = 0.05$, $\lambda \sim 0.6$ for $T_c/\omega_E = 1.0$, which is only a tiny fraction of what it would be for the $\beta = 0.5$ case. However, this value of λ is still quite considerable particularly when one compares with the results of Pattnaik and Newns[86]. They concluded that for $\beta \sim 0.05$ that the electron-phonon coupling would necessarily have be very nearly zero. Unfortunately, they only considered situations where the phonons were placed fairly high in frequency, thus putting them in a regime where T_c/ω_E was quite small. As a result, they obtained values of λ which were correspondingly small. If one uses $T_c = 100K$, then $T_c/\omega_E = 1.0$, which gives $\lambda \sim 0.6$ for $\beta = 0.05$, corresponds to $\omega_E = 8.6$ meV. So, if there is coupling to low frequency phonons one can still have a fair sized value of λ and still have a small isotope effect.

In the discussion for both the combined mechanism as well as the large μ^* model the significance of which phonons the electrons are most greatly coupled to, has been mentioned. A strong argument can be made that it is the higher frequency phonons that are being coupled to just from the fact that only the oxygen shows any significant isotope effect in YBCO. The oxygen atoms, being the lightest in this compound, are primarily responsible for the higher frequency phonons. The other constituents such as Ba and Cu contribute most strongly to lower frequency modes. It is of interest therefore to be able to quantify how different parts of an $\alpha^2F(\omega)$ are contributing to the total isotope effect.

Rainer and Culetto[87] have provided a powerful technique by which this can be achieved. Using functional derivative techniques, they were able to derive a differential isotope effect $\beta(\omega)$ given by

$$\beta(\omega) = R(\omega)\,\alpha^2F(\omega)\ , \tag{3.14}$$

where the weighting function $R(\omega)$ is

$$R(\omega) = \frac{d}{d\omega}[\frac{\omega}{2T_c}\frac{\delta T_c}{\delta\alpha^2F(\omega)}] \ . \tag{3.15}$$

The total isotope effect, β is related to the differential isotope effect $\beta(\omega)$ through the formula

$$\beta = \int_0^\infty d\nu\, \beta(\nu) \ . \tag{3.16}$$

In equation (3.15), the factor $\frac{\delta T_c}{\delta\alpha^2F(\omega)}$ is the functional derivative of T_c with respect to $\alpha^2F(\omega)$. What functional derivatives tell us is how each part of the $\alpha^2F(\omega)$ spectrum is contributing to the quantity being studied. To be general, let us say Q represents some physical quantity. It's functional derivative with respect to $\alpha^2F(\Omega)$ at the frequency Ω is then given by :

$$\frac{\delta Q}{\delta\alpha^2F(\Omega)} = \lim_{\epsilon\to 0}\frac{Q\left[\alpha^2F(\omega)+\epsilon\delta(\omega-\Omega)\right]-Q\left[\alpha^2F(\omega)\right]}{\epsilon} \tag{3.17}$$

where $\delta(\omega-\Omega)$ is a delta function used to enhance the $\alpha^2F(\omega)$ spectrum. If $\alpha^2F(\omega)$ is changed by a small amount, $\Delta\alpha^2F(\Omega)$, then the corresponding change in Q, ΔQ, is given by :

$$\Delta Q = \int_0^\infty d\Omega\frac{\delta Q}{\delta\alpha^2F(\Omega)}\Delta\alpha^2F(\Omega) \ . \tag{3.18}$$

For T_c as well as with most other properties, the functional derivative when plotted as a function of frequency has a generic shape that is independent of the choice of $\alpha^2F(\omega)$ or μ^*. In the case of T_c[43], the generic $\frac{\delta T_c}{\delta\alpha^2F(\omega)}$ curve rises linearly with ω for small ω, passes through a broad maximum at $\omega\sim 7k_BT_c$ and then falls off like ω^{-1}. The fact that functional derivatives have generic shapes such as this make them particularly useful for finding extrema in superconducting properties. In fact, the Leavens and Carbotte inequality for

T_c given in equation (3.6) was established using functional derivative techniques. Functional derivatives shall be used to establish extrema for several quantities associated with the specific heat in the next chapter.

Before discussing the actual results, it should be noted that the functional derivatives of T_c used to determine $R(\omega)$ were calculated numerically by brute force using the definition the the functional derivative given by equation (3.17).

To give some feeling for how the Rainer and Culetto technique works, several examples are displayed in Fig. 3.9, where the weighting function $R(\omega)$ is plotted vs. ω for three different μ^*'s: 0.0 (solid line), 0.15 (dotted) and -0.15 (dashed). The cutoff has been set at $\omega_c = 800$ meV. The actual $\alpha^2F(\omega)$ shape that was used is also shown - it is just a box extending from 0 meV to 80 meV. In the figure, it has been subdivided into four regions labeled 1 to 4, each of equal size. In all three cases, T_c has been fixed at 96 K while the $\alpha^2F(\omega)$ was scaled vertically according to which μ^* that was used. Note that all three curves have essentially the same form. This is a reflection of the robustness of the form of $\frac{\delta T_c}{\delta \alpha^2 F(\omega)}$. All three curves appear to pass through a a very broad maximum at $\omega \sim 35$ meV. As $\omega \to \infty$ it is expected that $R(\omega) \to 0$. This is again due to the relationship to $\frac{\delta T_c}{\delta \alpha^2 F(\omega)}$. Since $R(\omega)$ is known, we can determine the contribution each $\alpha^2F(\omega)$ region has to the total isotope effect by simple integration.

Table 1 : Partial isotope effects for 96 K case

μ^*	λ	β_{tot}	β_1	β_2	β_3	β_4
-0.15	1.791	0.405	0.062	0.122	0.119	0.102
0.00	4.860	0.500	0.083	0.159	0.146	0.112
0.15	6.884	0.491	0.086	0.160	0.141	0.104

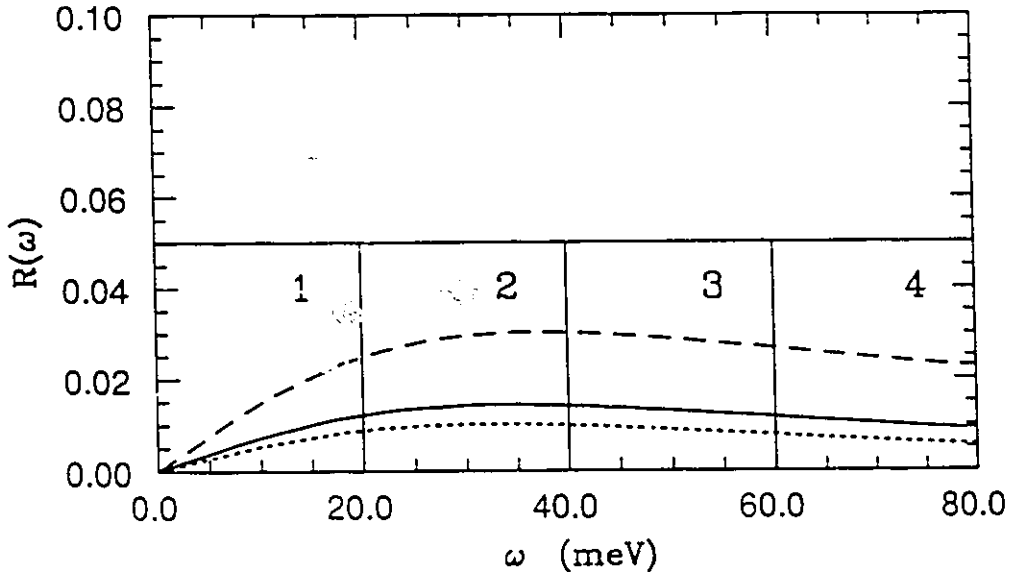

Figure 3.9 The weighting function $R(\omega)$ is displayed vs. ω for three different μ^*'s: 0.0 (solid line), 0.15 (dotted) and -0.15 (dashed). The $\alpha^2F(\omega)$, which takes the form of a box, is also depicted. To generate this data, T_c has been set at 96 K.

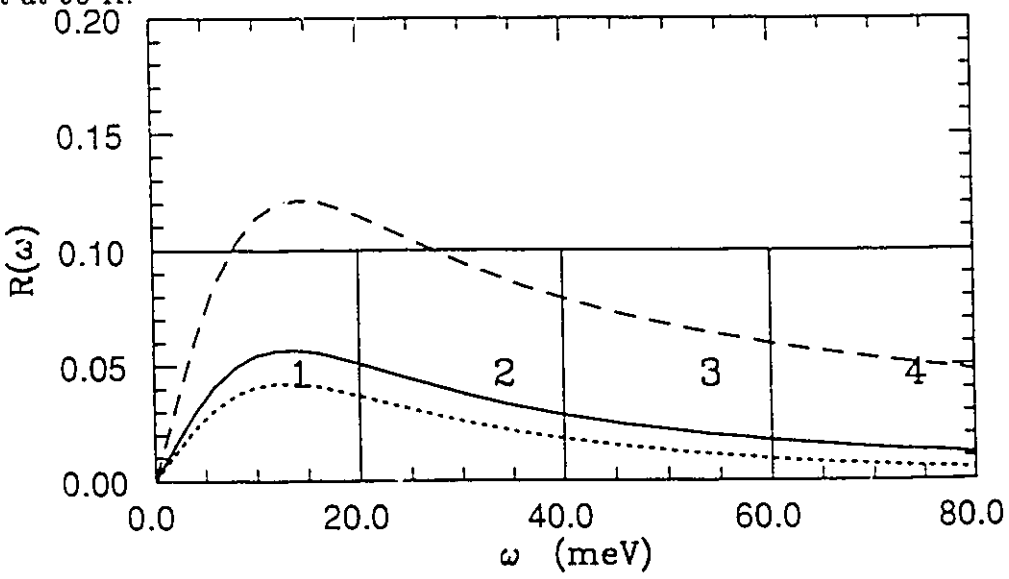

Figure 3.10 $R(\omega)$ is again plotted vs. ω for the same three μ^*'s: 0.0 (solid line), 0.15 (dotted) and -0.15 (dashed). However, in this case T_c has been set at 36 K.

The results of these calculations are summarized in Table 1. Note that the values of λ range from 1.791 for the $\mu^* = -0.15$ to 6.884 for $\mu^* = 0.15$. From the earlier discussion, we know that $\mu^* < 0$ enhances T_c so less λ is required. Of course, with a positive μ^*, the value of λ must be increased to overcome the coulomb repulsion. Not surprisingly, the smallest contributions come from the first region. The second region, where $R(\omega)$ reachs a maximum, gives the largest contribution. For all three values of μ^*, the contributions from the lower 2 $\alpha^2F(\omega)$ regions combined and the the upper two regions combined are fairly even. Now if the actual $\alpha^2F(\omega)$ of YBCO was similar to the model here or perhaps enhanced at lower frequencies this would seem to indicate that if β_x is significant then the isotope effects for Ba and Cu could be important as well. On the other hand, if the coupling to lower frequencies was significantly reduced with respect to what occurs at higher frequencies, then one should obtain appropriately small isotope effects for these elements. However, in either case the actual form of $R(\omega)$ would not have changed significantly since $\frac{\delta T_c}{\delta \alpha^2 F(\omega)}$ is relatively insensitive to spectral shape.

Up until now, we have been mainly concerned with modeling the isotope effect in YBCO. However, oxygen isotope effects have also been measured in LSCO. In this compound, which has $T_c \simeq 36$ K, the experiments done in the first year or so of high-T_c typically had $\beta_{ox} \sim 0.15$[70,88–90], which is quite considerable. In this case, none of the other partial isotope effects have been measured so no conclusions can be drawn on what the total isotope effect may be. This is an interesting compound to try and model. In Fig. 3.10, $R(\omega)$ is again plotted vs. ω. The same model $\alpha^2F(\omega)$ shape used in the previous case is again utilized as well as the same values of μ^*. The cutoff

is again fixed at ω_c = 800 meV. The curves correspond to: 0.0 (solid line), 0.15 (dotted) and -0.15 (dashed). As in the previous figure, the curves for the different μ^*'s have basically the same form. Note however that the peaks in $R(\omega)$ are more distinct in this figure and are shifted down to $\omega \sim 10 - 15$ meV. This is most likely a reflection of the change in energy scales. Recall that $\frac{\delta T_c}{\delta \alpha^2 F(\omega)}$ peaks at about $7k_BT_c$. Since T_c = 36 K is $\frac{3}{8}$ that of T_c = 96 K, the peak in the functional derivative curve should be shifted down by that fraction. This downward shift in the functional derivative leads to the downward shift in the peak in $R(\omega)$.

Table 2 : Partial isotope effects for 36 K case

μ^*	λ	β_{tot}	β_1	β_2	β_3	β_4
-0.15	0.369	0.267	0.083	0.080	0.058	0.045
0.00	1.792	0.500	0.188	0.157	0.092	0.063
0.15	2.586	0.474	0.202	0.155	0.077	0.040

The partial isotope effects for the four regions are summarized in table 2. The values of λ range from 0.369 for $\mu^* = -0.15$ to 2.586 for $\mu^* = 0.15$. Since the peaks in $R(\omega)$ now fall in the first region, this region now gives the largest contribution to the total isotope effect. The highest two regions fall in the tail of $R(\omega)$ and contribute a much smaller fraction than they do in the T_c = 96 K case. If one thinks of these two regions as representing in a rough sense the oxygen modes, it is apparent that for all three μ^*'s this particular spectral shape yields results that are not inconsistent with the experiments mentioned earlier.

Using a box shape for $\alpha^2 F(\omega)$, while it gives us a good idea of the trends that one should expect, is not a particularly good model for a electron-phonon spectral function. More physical shapes have been used to analyze

the isotope effect for LSCO[91]. Weber[92] has actually calculated a theoretical $\alpha^2F(\omega)$ for LSCO. As part of his calculations, he was able to obtain values for all the partial isotope effects. As was stated earlier, the lighter atoms contribute mainly to the higher frequency modes while the heavier atoms influence the lower frequency modes most strongly. However, changing one of the lighter isotopes will still effect the lower frequency modes to some extent. Weber, in his more detailed calculation is able to take this into account. To achieve T_c = 36 K with his spectrum required λ = 2.6 and μ^* = 0.12. The partial isotope effects were β_{ox} = 0.30, β_{La} = 0.02, β_{Ba} = 0.165 and the total β = 0.49, which is typical for a conventional superconductor. Note that the oxygen isotope effect is somewhat higher than the typical experimental value mentioned earlier. If one believes in Weber's spectrum being the appropriate shape, this would tend to suggest that an additional electronic mechanism may be accounting for part of the T_c and is reducing this value. Ashauer *et al.* [91] perform an analysis of the isotope effect based on the experimental phonon frequency distribution $F(\omega)$ obtained by Renker *et al.* [83]. They used several different models for $\alpha^2(\omega)$. For a case where all phonon modes are weighted equally, they obtained β_{ox} lower than experiment. This is without including any additional mechanism. Of course, increasing or decreasing $\alpha^2(\omega)$ at the appropriate frequencies can lead to an infinite number of values for the partial isotope effects. These results, along with the simple model displayed earlier, point to the difficultly in determining what contribution the phonons are making to the critical temperature of LSCO from using β_{ox} by itself.

3.4 CONCLUSIONS AND POSTSCRIPT

In this Chapter, we have shown that a large critical temperature combined with a small isotope effect need not be inconsistent with Eliashberg theory. This has been demonstrated by concentrating on two different regimes of μ^*. Having large positive values of μ^*, which are consistent with reduced screening, can, under the right conditions, give a small isotope effect and at the same time imply λ's that may be physically reasonable. Using a negative μ^*, which was labeled μ^*_{eff}, can be used to simulate an additional electronic mechanism. Of course, the larger the electronic contribution is the smaller the isotope effect should be.

These two regimes, along with the intermediate regime that is consistent with more conventional superconductivity, can be summarized in one figure. In Fig. 3.11, β (solid line) and $\mu^*(\omega_E)$ (dashed line) are plotted vs. λ. To produce this figure, a delta function $\alpha^2F(\omega)$ was fixed at ω_E = 40 meV. The critical temperature was fixed at T_c = 96 K. For small λ, a negative μ^* is required to obtain the desired T_c. The isotope effect is correspondingly small. This of course corresponds to a situation where an electronic mechanism is combined with the phonon contribution. As λ is increased, β and μ^* rise. At $\lambda \simeq 2.0$, the phonon contribution is enough to account for all the T_c and so μ^* = 0.0. At this point, β reaches a maximum at 0.5. This region corresponds to the usual situation in superconductors. As λ is increased further, an increasingly larger positive μ^* is required to hold down the T_c. In the meantime, β now is decreasing. This then represents the scenario with very large coulomb repulsion.

POSTSCRIPT

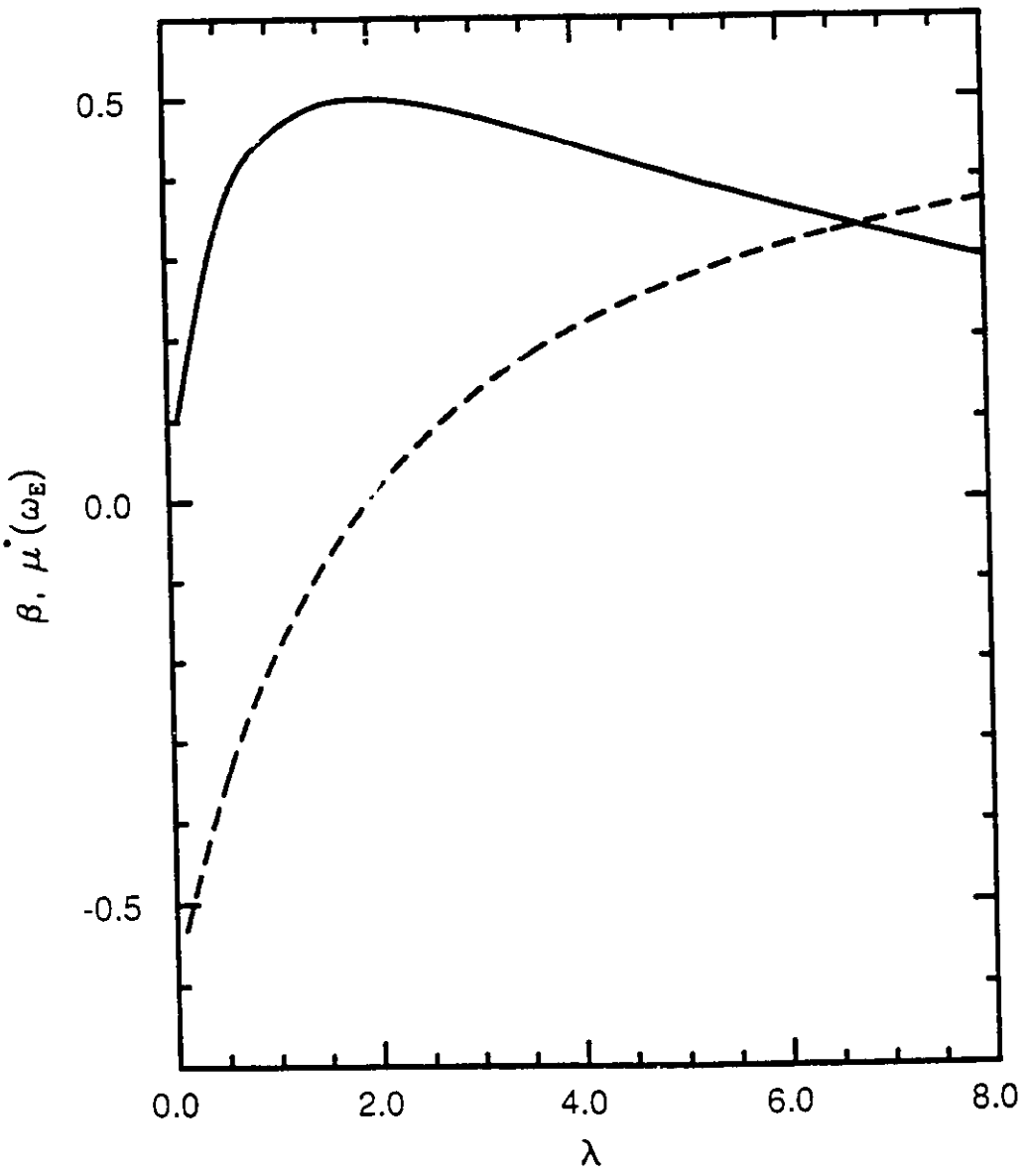

Figure 3.11 β (solid line) and $\mu^*(\omega_E)$ (dashed line) are plotted vs. λ for a T_c= 96 K superconductor. A delta function set at ω_E = 40 meV was used to produce this data.

Since most of the work shown in this chapter was done, several new and exciting experimental developments have occurred. In the work of Franck *et al.* [93], YBCO was doped with Pr, forming $Y_{1-x}Pr_xBa_2Cu_3O_7$. Increasing the level of Pr had two effects. The first was to reduce the critical temperature from $T_c \sim 90$ K for to $T_c \sim 30$ K . While this is occurring, the oxygen isotope effect appears to increase dramatically from the sort of values discussed earlier to $\beta_{ox} \sim 0.5$ for $T_c \sim 30$K. This result while striking may still be workable purely in the $\mu^*_{eff} < 0$ regime. What may be occurring is that the electronic mechanism is somehow being turned off by the presence of the Pr. However, to determine how this actually might be occurring would require a fully developed theory of whatever electronic mechanism one chooses to believe in.

There are of course several alternate ways to explain this behavior. There is speculation that the Pr may be acting to some degree like a paramagnetic impurity. This type of impurity causes the breaking of Cooper pairs. It has been found that including these impurities in the Eliashberg equations can enhance the calculated isotope effects dramatically[94], despite the fact that the greater part of the T_c in the pure case may be accounted for by a negative μ^*_{eff}. It should be noted that including paramagnetic impurities involves only a minor modification of the equations.

A more major modification of the equations involves the possibility of a rapidly varying electronic density of states. As part of the derivation of the Eliashberg equations shown in this thesis, the assumption was made that the density of electronic states was slowly varying close to the Fermi energy and so it's energy dependence could be ignored. Obviously, this need not be the case. Fortunately, the equations can be modified to take this into

account[95,96]. It has been recognized that including a nonconstant electronic density of states can have some profound effects on the isotope effect[97–99]. The scenario within the nonconstant DOS of states framework that would explain Franck *et al.* 's experiment would have a peak in the electronic DOS right at the Fermi energy in the pure compound. In this situation it has been found that the T_c is maximized and the isotope effect is minimized. When doping is introduced the idea is that the number of conducting holes in the system is changed and this shifts the Fermi energy away from the peak. When this occurs, the T_c drops and the isotope effect goes up as desired. Some authors[99] have concluded using a BCS type model that a pure phonon mechanism combined with a nonconstant DOS may be able to account for the oxides. Doing the calculation using a full Eliashberg formalism appears to indicate this is probably not the case[100,101] and that some additional electronic component is required in order to account for the small initial value of β_{ox}.

Another dramatic experiment that was done earlier was on LSCO. Crawford *et al.* [102] measured the isotope effect of $La_{2-x}Sr_xCuO_4$ while changing the Sr doping. Changing the Sr doping also alters T_c and the optimum compound with $T_c \sim 36$ K occurs for $x \simeq 0.15$. The experiments cited previously were probably performed on samples that had Sr concentrations in this region. As $x \simeq 0.15$ is deviated from on either side, the result is that T_c drops. The oxygen isotope effect on the other hand behaves in a most peculiar way. Going from $x \simeq 0.07$ to $x \simeq 0.12$, β_{ox} increases from 0.4, which is already quite large, to about 0.8, as T_c increases. Beyond this point, while T_c is still increasing, β_{ox} drops dramatically to ~ 0.15. As x is increased, T_c passes

through it's maximum and turns over while in the meantime β_{ox} remains relatively constant. These results are impossible to explain by simply choosing the right μ^* since the maximum β that can be obtained in this manner is 0.5. One can achieve $\beta > 0.8$ by using a nonconstant DOS or with paramagnetic impurities. Unfortunately, neither of these explanations would give the desired β_{ox} vs. T_c dependence - having β_{ox} increase with T_c or having β_{ox} remain fixed while T_c decreased is next to impossible if a nonconstant DOS model or paramagnetic impurity model is used individually. However, using both effects in combination may provide for some more unusual behaviour.

Several more explanations to these strong variations in the isotope effect have also been proposed. In the marginal Fermi liquid model, one has a temperature dependent $\alpha^2F(\omega)$, the form of which has been chosen to ensure that the correct behavior for normal state properties such as the resistivity drop out of the theory automatically. This phenomological $\alpha^2F(\omega)$, which becomes gapped below T_c, is assumed to arise from charge fluctuations. Spin fluctuations, which are assumed to follow an identical spectral function, are also included in the model. Like paramagnetic impurities, spin fluctuations tend to reduce T_c. Adding a small phonon contribution, it has been found that the behavior seen in the YBCO-Pr experiments can be mimicked by leaving the phonon contribution constant while reducing the MFL part[101]. This procedure is analogous to the switching off of μ^*_{eff} discussed earlier. Beyond this, it has also been suggested that the anomalous isotope effects may be due to such things as sample inhomogeneity[103] and anharmonic effects[104].

Chapter 4

The Electronic Specific Heat

4.1 INTRODUCTION

Measurements of the specific heat of the oxide materials have been carried out by many authors. In particular, the specific heat jump at T_c has been extensively documented[105,106]. Generally, one finds that there is a large degree of sample dependence. The size of the specific heat jump that is obtained depends on things such as how much of the sample is actually superconducting as well as disorder and inhomogeneity in the sample. Reproducibility of results is affected also by the fact that many of the oxide materials are notoriously unstable.

The quantity most often quoted in the experimental literature is $\Delta C(T_c)/T_c$. In Eliashberg theory, the preferred quantity to study is the normalized specific heat jump $\Delta C(T_c)/\gamma_o T_c$ where γ_o is the Sommerfeld constant

defined by

$$\gamma_o = \frac{2}{3}\pi^2 N(0)(1+\lambda) \; . \tag{4.1}$$

Note that the electronic density of states at the Fermi energy, $N(0)$, appears here. As it turns out, ΔC is also proportional to $N(0)$. This being the case, $N(0)$ becomes a parameter that need not be known in order to calculate the ratio $\Delta C(T_c)/\gamma_o T_c$, as it is canceled out. In order to form this ratio from experiments one must also measure γ_o as well as the actual jump. Many experimenters have attempted to extract γ_o from their data. Unfortunately, there is a great deal of uncertainty on the value of this quantity, so that studying the ratio is not advisable as one must deal with the combined uncertainty of the jump and the Sommerfeld constant. On the other hand, if one wants to study $\Delta C(T_c)/T_c$ theoretically, one must know N(0) and the mass enhancement parameter λ. While these quantities have been estimated for the oxides, they are by no means certain[38,105,106].

What one would like to study therefore are quantities that do not depend on any material dependent parameters that are unknown or uncertain and at the same time can be extracted from experimental results with a minimal number of assumptions. Recent experiments by Junod *et al.* [106,107] and others[108–112] have provided results that yield quantities that may be compared meaningfully with theory. In these experiments, the electronic specific heat difference between the normal and superconducting states $\Delta C(T)$ has been obtained as a function of T below T_c. From these results one can form the ratio $\Delta C(T)/\Delta C(T_c)$, a quantity which fits the desired requirements. Also of interest is the slope of the specific heat difference right at T_c. Finally, another significant property that one can extract from these experiments is

the temperature at which $\Delta C(T) = 0$, which will henceforth be referred to as the crossover temperature.

In the next section of this chapter, some important background material is provided. Following this is a theoretical study of the the quantities mentioned in the preceding paragraph. In particular, we shall study these quantities as a function of coupling strength as well as provide theoretical upper bounds for the slope in the specific heat difference and the crossover temperature. The fourth section of this chapter is concerned with a comparison with experiment. The chapter closes with a brief conclusion.

4.2 BACKGROUND MATERIAL

The specific heat of metals is a subject covered by every elementary text on solid state physics. At low temperatures, the specific heat has the form :

$$C(T) = \gamma_0 T + \beta T^3 \ . \tag{4.2}$$

The linear term applies to the electronic contribution to the specific heat. The T^3 term gives the contribution due to the phonons. At higher temperatures, the assumptions used to derive these two terms break down. In the case of the electronic contribution, γ_0 can be replaced by a temperature dependent $\gamma(T)$, as derived by Grimvall[34] by taking into account modifications due to the electron-phonon interaction. For the phonon part, higher order correction terms that take the form $\beta_{2n+1} T^{2n+1}$ have to be added on. At a sufficiently high temperature, one expects that the phonon contribution will saturate at the classical value given by Dulong and Petit.

The phase transition between the normal and superconducting states is of second order, and thus, the entropy, S, is continuous while the specific

heat, $C = T\left(\frac{dS}{dT}\right)_V$, is discontinuous at T_c. This leads to there being a jump in the electronic specific heat, $\Delta C(T_c) = C_S(T_c) - C_N(T_c)$, right at T_c. Within BCS theory, one can use the expression for the entropy of fermions to show that $\Delta C(T_c)$, is proportional to Δ_o and therefore to T_c since BCS also predicts the relationship $\frac{2\Delta_o}{k_B T_c} = 3.53$. Normalizing $\Delta C(T_c)$ by the denominator $\gamma_o T_c$ gives the B.C.S. ratio:

$$\frac{\Delta C(T_c)}{\gamma_o T_c} = 1.43 \ . \tag{4.4}$$

Here, γ_o is of course the Sommerfield constant as given by equation (4.1). Here however λ has been set to zero to correspond to the B.C.S. case. The factor $\gamma_o T_c$ gives the normal state specific heat at T_c provided T_c is not very large. This would usually be the case for a conventional superconductor.

According to BCS theory, just below T_c, the electronic specific heat in the superconducting state, $C_S(T)$, is larger than $C_N(T)$, the normal state specific heat. However, as the temperature is lowered, $C_S(T)$ drops more quickly than $C_N(T)$ and they eventually cross. At very low temperatures the gap in the excitation spectrum becomes reflected in the specific heat as $C_S \sim e^{-\Delta/k_B T}$. Rickayzen[6] states that this temperature dependence should hold for $T < \frac{T_c}{10}$. This behavior is illustrated beautifully in Fig. 4.1. In this figure experimental data for the specific heat of Al is plotted for both the normal and superconducting states[113,25]. Aluminum is probably the best example of a BCS superconductor. The solid curve in this picture is a fit to the exponential law. Features to note here are how well defined the transition is as well as the fact that the normal state specific heat does indeed follow a linear law. It should be noted that $T_c = 1.2K$ for Al.

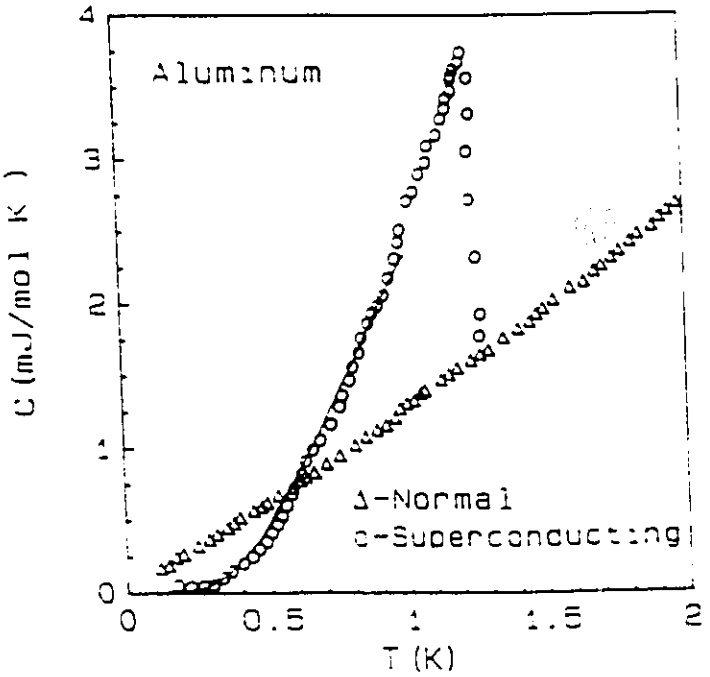

Figure 4.1 The electronic specific heat of Al in the normal and superconducting states. The data is from a paper by Phillips[113,25].

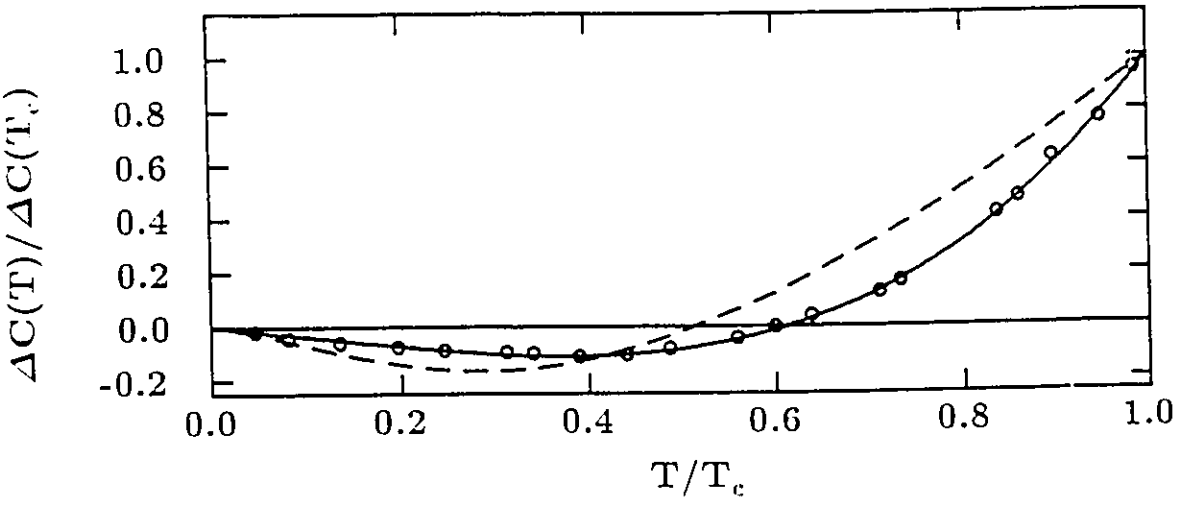

Figure 4.2 $\Delta C(T)/\Delta C(T_c)$ vs. T/T_c for the BCS limit (dashed line) and an Eliashberg calculation for Pb (solid line). The circles represent the experimental results of Chanin and Torre[114].

The specific heat jump, $\Delta C = C_S - C_N$ can also be determined by using the relation $S = -\frac{dF}{dT}$. In this case, one finds that the jump in the specific heat at T_c is related to the change in the free energy, $\Delta F = F_S - F_N$, by the formula:

$$\Delta C(T_c) = -T\frac{d^2\Delta F}{dT^2}\Big|_{T_c} . \tag{4.5}$$

Equations for the change in free energy have been derived within the framework of Eliashberg theory. One convenient form is the Bardeen-Stephen[115] formula:

$$\frac{\Delta F}{N(0)} = -\pi T \sum_{n=-\infty}^{\infty} \left[\sqrt{\omega_n^2 + \Delta_n^2} - |\omega_n|\right]\left[Z_S(n) - Z_N(n)\frac{\omega_n}{\sqrt{\omega_n^2 + \Delta_n^2}}\right] . \tag{4.6}$$

All the terms in this equation can be obtained by using the imaginary axis equations (2.24) and (2.25). This is true even for the $Z_N(n)$ factors which represent the normal state mass renormalization. To obtain these, the Matsubara gaps are simply set to zero in the equations. Thus, the analytic continuation to the real axis is unnecessary in this case.

In Fig. 4.2, $\Delta C(T)$ normalized by $\Delta C(T_c)$ is plotted as a function of reduced temperature, $t = T/T_c$. The dashed line in this picture is the BCS prediction. The solid line is the result of an Eliashberg calculation using the $\alpha^2F(\omega)$ of Pb obtained by tunneling. The circles are the experimental results of Chanin and Torre[114]. The correspondence between theory and experiment here is quite striking and provides strong confirmation of the validity of Eliashberg theory in this material. Another interesting feature of the figure is that, while the BCS curve is well above the Pb curve for the higher temperatures, it falls significantly lower than the Pb curve below the

crossover temperature. The reason this occurs is due to the concept of entropy conservation. As stated earlier, the entropy at T_c is continuous so that $S_S(T_c) = S_N(T_c)$ or

$$\Delta S(T_c) = \int_0^{T_c} dT\, \Delta C(T)/T = 0 \,. \tag{4.7}$$

So, what ever excess specific heat there is above the crossover temperature must be compensated for below it in order to maintain the entropy balance. This is a balance that can not be violated and provides an important check on the validity of any experiment.

The difference in free energy is also related to the thermodynamic critical field :

$$\Delta F(T) = -\frac{H_c^2(T)}{8\pi} \,. \tag{4.8}$$

This formula comes from the requirement that the total free energy in the normal and superconducting states be equal when the applied magnetic field reaches $H_c(T)$. In a type I superconductor, the Meissner effect and the superconductivity are destroyed at this point and the applied magnetic flux will fully penetrate into the superconductor. In type II superconductivity there is a perfect Meissner effect until the applied field reaches the lower critical field $H_{c1}(T)$. Beyond this, there is the occurrence of a mixed state where the applied magnetic flux penetrates the superconductor in filaments and thus creates normal regions in the sample. The superconductivity is finally destroyed and there is full flux penetration when the upper critical field $H_{c2}(T)$ is reached. The thermodynamic critical field $H_c(T)$ is not directly related to $H_{c1}(T)$ and $H_{c2}(T)$ in type II superconductors. The concept of a thermodynamic critical field is only meaningful through the definition given by equation (4.8) in this case. Thus, $H_c(T)$ can not be directly measured in

type II superconductors, but must be inferred. It can of course always be calculated theoretically.

Along with the thermodynamic critical field, one can also define a deviation function :

$$D(t) = \frac{H_c(T)}{H_c(0)} - (1 - t^2) \,, \tag{4.9}$$

where $t = \frac{T}{T_c}$ is the reduced temperature. This particular function is an outgrowth of the two fluid model of Gorter and Casimer[5] mentioned briefly in the first chapter. In this model, the electron gas is considered to consist of two fractions. One fraction is made up of normal electrons and the other of the superconducting electrons. The superconducting electrons are treated as a superfluid, producing no friction and having zero entropy. The fraction of normal or superconducting "fluid" is temperature dependent with the normal component vanishing at $T = 0$ and the superconducting fraction disappearing at T_c. The observed properties are a function of the fraction of superconducting "fluid" and thus of temperature as well. For the critical field, $H_c(T)$, the two-fluid model predicts the relationship $\frac{H_c(T)}{H_c(0)} = (1 - t^2)$.

The thermodynamic critical field and the deviation function can be exploited in determining the behavior of $\Delta C(T)$ near the critical temperature. For example, if one assumes that the two fluid model holds and using the relationships of $\Delta C(T)$ and $H_c(T)$ with $\Delta F(T)$, one can derive[25]

$$\Delta C(T) = -\frac{H_c^2(0)}{2\pi T_c}(t - 3t^3) \,. \tag{4.10}$$

The term linear in t in this equation can be associated with $C_N(T)$, while the cubic term is related to $C_S(T)$. Since superconductors usually deviate from the two-fluid prediction, this t^3 behavior is generally not followed. This sort of analysis can be extended further if one knows the deviation function .

Marsiglio and Carbotte[50,38] have done work along these lines in deriving some strong coupling correction formulas to BCS ratios. More specifically, they derived the formula

$$\frac{\Delta C(T_c)}{\gamma_o T_c} = 1.43\left(1 + 53\left(\frac{T_c}{\omega_{\ln}}\right)^2 \ln\left(\frac{\omega_{\ln}}{3T_c}\right)\right) . \tag{4.11}$$

The general form of this equation was derived from the full Eliashberg equations on the imaginary axis but making the approximation that $\Delta(i\omega_n)$ and $Z(i\omega_n)$ take the form of step functions. Essential to this approximation was the requirement that $\frac{T_c}{\omega_{\ln}} \ll 1$. Another important aspect of the derivation of this formula was that the Coulomb repulsion, μ^*, was neglected. However, the final formula shown here required some fitting. In equation (4.11), the factors 53 and 3 that appear in the formula were obtained by using a fit to data obtained not by direct experiment but from numerical calculations for real materials. Beyond this, it was shown after "tedious" algebra that just below T_c

$$\frac{\Delta C(T)}{\gamma_o T_c} = \frac{\Delta C(T_c)}{\gamma_o T_c} + (1-t)g . \tag{4.12}$$

Differentiating equation (4.12) with respect to t (note: $\frac{d}{dt} = T_c\frac{d}{dT}$) yields

$$(d\Delta C(T)/dT)/\gamma_o = -g . \tag{4.13}$$

Marsiglio and Carbotte[38,50] have also derived a strong coupling correction formula for g. It is given by

$$g = -3.77\left(1 + 117\left(\frac{T_c}{\omega_{\ln}}\right)^2 \ln\left(\frac{\omega_{\ln}}{2.9T_c}\right)\right) . \tag{4.14}$$

In obtaining the fitted numbers 117 and 2.9 that appear in this formula, numerical calculations of the deviation function were used. This is possible since $D(t)$ can be expanded near T_c giving the form

$$D(t) = \alpha(1-t) + \beta(1-t)^2 . \tag{4.15}$$

From the sort of thermodynamic relations discussed here, one can determine g from α and β. In the next section of this chapter, the normalized slope, $(d\Delta C(T)/dT)/\gamma_o$, shall be discussed extensively. Unfortunately, it contains γ_o so it will not be used to compare with experiment. Instead, another normalized slope can be defined that will be used for this purpose. It is defined by

$$R = \frac{T_c}{\Delta C(T_c)} \frac{d\Delta C(T)}{dT}\Big|_{T_c} . \tag{4.16}$$

4.3 THEORETICAL RESULTS

As in the previous chapter, we shall examine various quantities as a function of the strong coupling parameter T_c/ω_{ln}. The LSCO spectrum derived by Weber[92] is used for $\alpha^2F(\omega)$ and different values of T_c/ω_{ln} were obtained by introducing scaling factors B and b such that $\alpha^2F(\omega) \rightarrow B\alpha^2F(b\omega)$, as discussed in the last chapter. A delta function spectrum is also considered:

$$\alpha_E^2F(\omega) = A\,\delta(\omega - \omega_E) . \tag{4.17}$$

Blezius and Carbotte[116,117] were able to show that various quantities associated with the specific heat were given by functional forms (which we shall label here as f_i, where $i \equiv$ integer) which can only be determined numerically. For example, for a delta function spectrum, they demonstrated that the free energy as given by the Bardeen-Stephen formula can be written in the form:

$$\Delta F(T) = N(0)A^2 f_1(\bar{\omega}_E, \mu^*, \bar{T}) \tag{4.18}$$

where $\bar{T} = T/A$, $\bar{\omega}_E = \omega_E/A$. For $\bar{T}_c$, the functional form can be written in this case as $\bar{T}_c = f_2(\bar{\omega}_E, \mu^*)$. This relationship can be inverted to give

$\omega_E = f_3(\omega_E/T_c, \mu^*)$. We can now write a final functional form for $\Delta F(T)$:

$$\Delta F(T) = N(0)A^2 f_4(\omega_E/T_c, \mu^*, t) , \tag{4.19}$$

with t of course being the reduced temperature . Given this, the specific heat difference can now be written as

$$\Delta C(T) = \frac{TN(0)A^2}{T_c^2} \frac{d^2}{dt^2} f_4(\omega_E/T_c, \mu^*, t) . \tag{4.20}$$

So $\Delta C(T)$ will depend on $N(0)$ and A. However, we can normalize $\Delta C(T)$ in such a way that these dependencies drop out. For example, we can write

$$\Delta C(T)/\Delta C(T_c) = f_5(\omega_E/T_c, \mu^*, t) , \tag{4.21}$$

which is independent of $N(0)$ and A. The ratio $\Delta C(T)/\gamma_o T_c$ also has the same sort of functional form. The fact that quantities such as these have functional forms that are independent of $N(0)$ and A will become extremely important later in this section. As we shall see, this property has been exploited in order to establish maxima in the slope of the specific heat jump as well as for the crossover temperature.

In Fig. 4.3, $\Delta C(T)/\Delta C(T_c)$ is plotted vs. $t = T/T_c$ for several different values of T_c/ω_{ln}. The spectrum in this case is LSCO. It is evident from this figure that the BCS curve shows a smaller slope near T_c than all the other curves. What appears to occur is that as the coupling strength increased from BCS to $T_c/\omega_{ln} = 0.05$ and then to $T_c/\omega_{ln} = 0.20$, the curves drop progressively more swiftly. However, for the two curves corresponding to the strongest coupling, $T_c/\omega_{ln} = 0.5$ and $T_c/\omega_{ln} = 1.0$, it is evident that this trend reverses itself somewhat but not back to the BCS behavior. Indeed, what occurs for $T_c/\omega_{ln} = 1.0$ for intermediate temperatures, $0.15 \lesssim T/T_c \lesssim 0.65$, is quite striking.

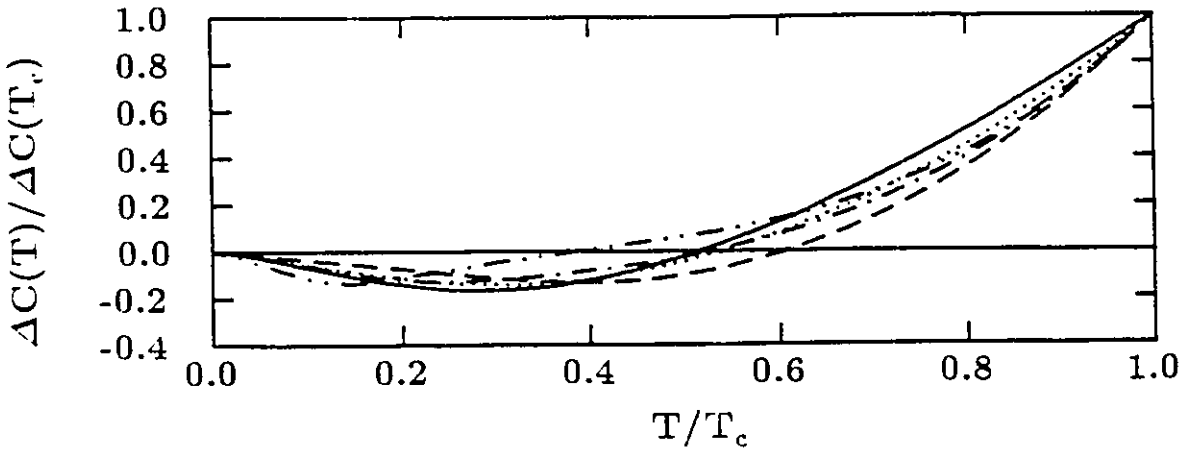

Figure 4.3 $\Delta C(T)/\Delta C(T_c)$ is plotted vs. $t = T/T_c$ for BCS (solid line), $T_c/\omega_{ln} = 0.05$ (dotted), $T_c/\omega_{ln} = 0.20$ (dashed), $T_c/\omega_{ln} = 0.5$ (dot-dashed) and $T_c/\omega_{ln} = 1.0$ (double dot-dashed). These curves were produced using the $\alpha^2F(\omega)$ of LSCO.

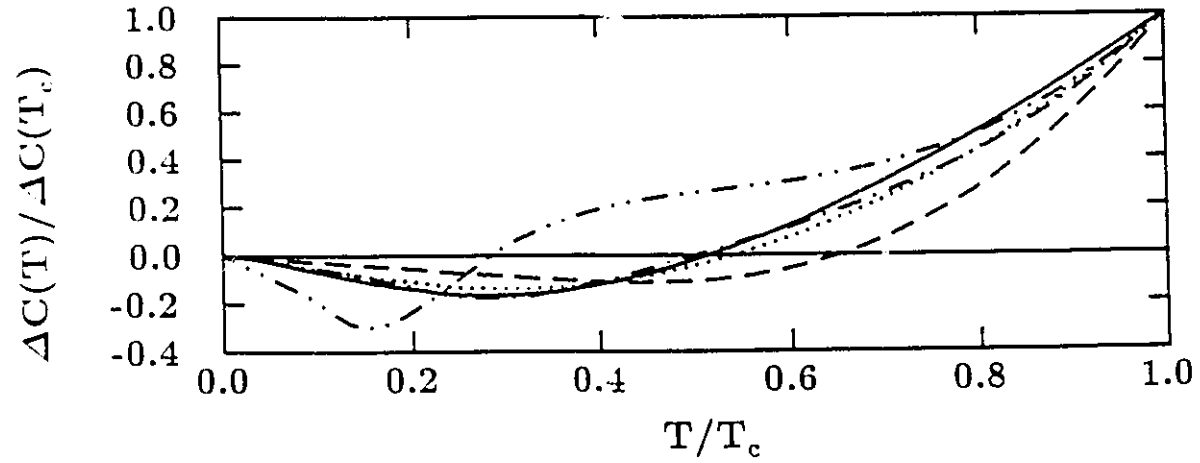

Figure 4.4 $\Delta C(T)/\Delta C(T_c)$ is plotted vs. $t = T/T_c$ for BCS (solid line), $T_c/\omega_{ln} = 0.05$ (dotted), $T_c/\omega_{ln} = 0.20$ (dashed), $T_c/\omega_{ln} = 0.5$ (dot-dashed) and $T_c/\omega_{ln} = 1.0$ (double dot-dashed). In this case, the $\alpha^2F(\omega)$ was delta function.

In this range, $\Delta C(T)/\Delta C(T_c)$ appears to be almost linear in t which is quite different to what occurs for the weaker coupling strengths. While the slope near T_c is greater than it is for BCS, the temperature where $\Delta C(T) = 0$ is quite significantly lower.

In Fig. 4.4, $\Delta C(T)/\Delta C(T_c)$, is again plotted vs. $t = T/T_c$ for several different values of T_c/ω_{ln}, but this time for a delta function spectrum. One can identify the same sorts of trends here as in the previous figure, but here the behavior appears to be even more radical. The $T_c/\omega_{ln} = 0.2$ curve drops more quickly than the corresponding curve in the previous figure. The $T_c/\omega_{ln} = 1.0$ curve is even more unusual than it was in the previous figure. The ratio $\Delta C(T)/\Delta C(T_c)$ stays considerably above zero until fairly low temperatures and appears to be fairly level for a large temperature range. Another interesting feature of this curve is that it has a minimum that falls well below the BCS minimum. None of the curves of the previous figure do this. As stated, one can identify similar trends occurring in both figures, but it is evident that there is considerable amount of $\alpha^2F(\omega)$ shape dependence. This is particularly true for large coupling strengths.

The normalized slope, $(d\Delta C(T)/dT)/\gamma_o$ evaluated at T_c, is plotted vs. T_c/ω_{ln} for the LSCO spectrum and a delta function in Fig. 4.5. for the purposes of these calculations, the coulomb pseudopotential has been set at $\mu^* = 0.09$. The cutoff frequency for all the results shown from this point onwards in this section is $\omega_c = 1000$ meV. As mentioned in the previous section, this slope is equal to in magnitude but opposite in sign to Marsiglio and Carbotte's parameter g. This being the case, it is no surprise that both curves start off at a value of 3.77 in the BCS limit. It should be noted however that for the calculations shown here, $(d\Delta C(T)/dT)/\gamma_o$ was obtained

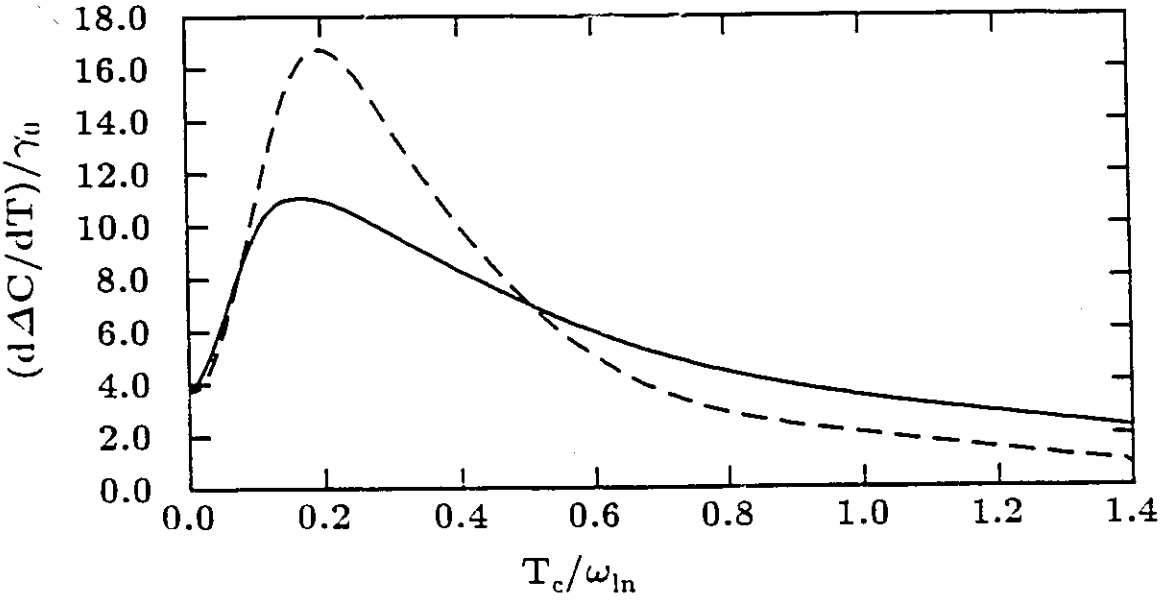

Figure 4.5 $(d\Delta C(T)/dT)/\gamma_0$ evaluated at T_c, is plotted vs. T_c/ω_{ln} for the LSCO spectrum (solid line) and a delta function spectrum (dashed line).

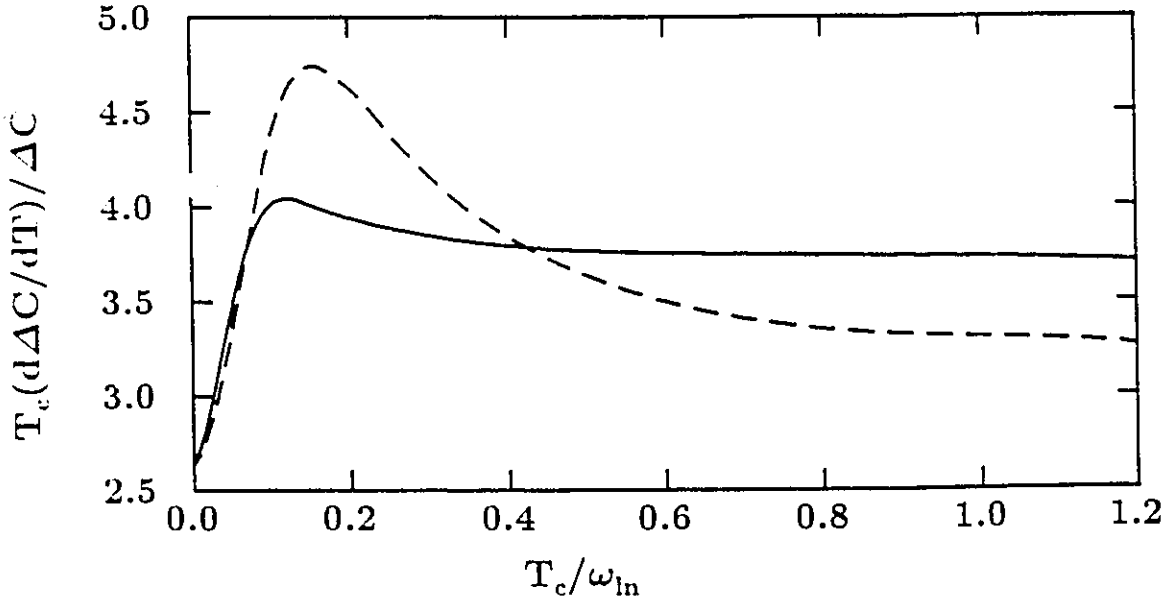

Figure 4.6 $R = T_c(d\Delta C(T)/dT)/\Delta C(T_c)$ is plotted vs. T_c/ω_{ln} for the LSCO spectrum (solid line) and a delta function spectrum (dashed line).

by numerically differentiating results for $\Delta C(T)$ and γ_n from the deviation function as Marsiglio and Carbotte had done. As T_c/ω_{ln} is increased, both curves rapidly increase and reach maxima at $T_c/\omega_{ln} \sim 0.2$. Beyond these maxima, the curves drop rapidly and eventually fall below the initial BCS value. Thus, a value for this quantity that is less than BCS can be taken as being characteristic of very strong coupling. This type of behavior as a function of coupling strength has been noted for other superconducting properties in previous work. In particular, the normalized specific heat jump, $\Delta C(T_c)/\gamma_o T_c$, behaves in a very similar manner as a function of T_c/ω_{ln} and returns to it's BCS value at approximately the same value of T_c/ω_{ln}. As was the case for $\Delta C(T)/\Delta C(T_c)$, it is apparent here that the delta function $\alpha^2 F(\omega)$ gives the more extreme behavior. It yields a maximum that is much larger than the LSCO case - 16.7 as compared with 11.1, and falls well below the LSCO curve for $T_c/\omega_{ln} \gtrsim 0.6$. From the scaling arguments presented earlier, $(d\Delta C(T)/dT)/\gamma_o$ is independent of A for a delta function. As shall be shown later, this implies that the maximum value 16.71 is in fact the largest value that this slope can attain for $\mu^* = 0.09$.

In Fig. 4.6, the other normalized slope defined in the previous section, $R = T_c(d\Delta C(T)/dT)/\Delta C(T_c)$ evaluated at T_c, is plotted vs. T_c/ω_{ln} for the LSCO spectrum and a delta function for $\mu^* = 0.09$. One should note that taking the slopes off the curves displayed for $\Delta C(T)/\Delta C(T_c)$ in Fig. 4.3 and Fig. 4.4 gives this normalized slope directly. In this case, the BCS value of this parameter is 2.634. As we increase T_c/ω_{ln} , both curves rapidly increase as they did for $(d\Delta C(T)/aT)/\gamma_o$, but reach far less impressive maxima compared with the initial BCS value. The LSCO curve barely peaks above $R = 4.0$ and the delta function curve reachs $R \sim 4.75$. As was the case for $(d\Delta C(T)/dT)/\gamma_o$,

this delta function maximum should represent an absolute maximum for this quantity for this value of μ^*. Interestingly, neither curve drops below the BCS value even for $T_c/\omega_{ln} = 1.2$. In fact, it looks almost as if this slope saturates for very strong coupling. The reason for this difference in behavior is probably due to how the slope has been normalized in this case. With $(d\Delta C(T)/dT)/\gamma_o$, the inclusion of γ_o tends to damp this quantity considerably for large T_c/ω_{ln}. The reason for this is apparent from equation (4.1) which shows that γ_o is directly proportional to λ and from the last chapter where it was shown that λ increases rapidly with T_c/ω_{ln}.

In the previous section, formulas for strong coupling corrections to $y = -(d\Delta C(T)/dT)/\gamma_o$ and $\Delta C(T_c)/\gamma_o T_c$ were discussed. Using the same form for the correction function, one can establish a formula for the strong coupling corrections to R. This is given by

$$R = 2.634\left(1 + 38\left(\frac{T_c}{\omega_{ln}}\right)^2 \ln\left(\frac{\omega_{ln}}{3.2T_c}\right)\right) . \qquad (4.22)$$

The factors 38 and 3.2 that appear in this formula were obtained by trying to get the best possible fit to calculations involving some of the same systems used by Marsiglio and Carbotte. The results of this fit are displayed in Fig. 4.7. In this figure, R is plotted vs. T_c/ω_{ln}. The curve is just a plot of the function given by equation (4.22). The dots represent calculations using full $\alpha^2F(\omega)$. The fitted curve and the data points both indicate that R reaches a maximum just below $T_c/\omega_{ln} = 0.2$. This is agreement with what was shown in the previous figure. The reader should be reminded that $T_c/\omega_{ln} \sim 0.25$ represents the upper edge of the conventional strong coupling region.

Another quantity that can be read directly off Fig. 4.3 and Fig. 4.4 is the crossover temperature, where $\Delta C(T) = 0.0$. In Fig. 4.8, the reduced

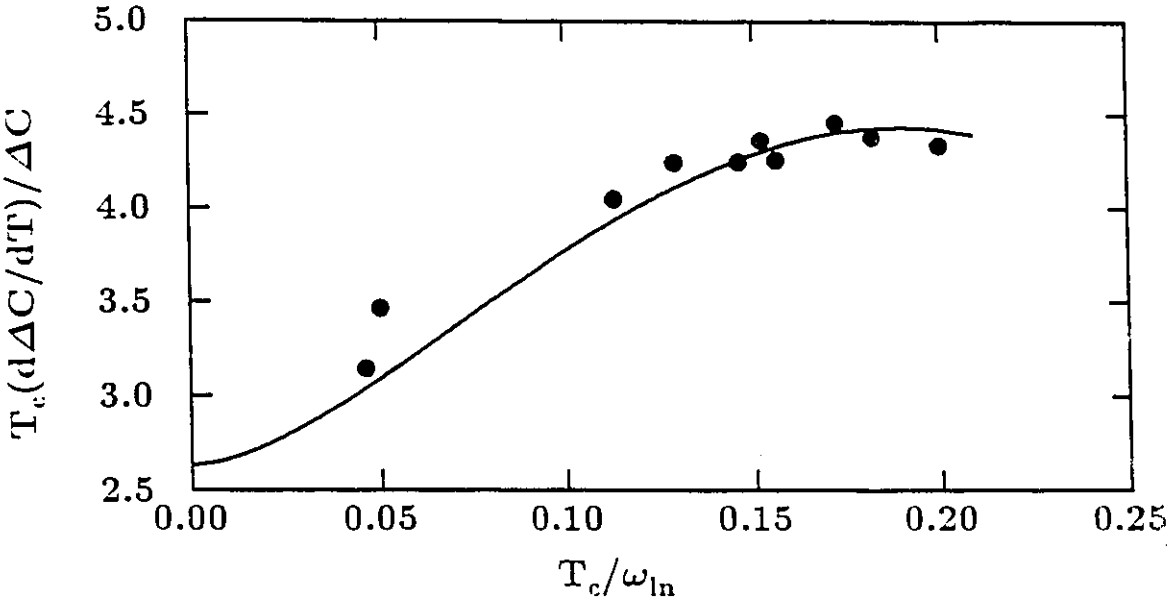

Figure 4.7 The approximate formula for R given in equation (4.22) is plotted vs. T_c/ω_{ln}. The dots represent full calculations for real materials. In order of increasing T_c/ω_{ln} these are Tl, In, $Nb_3Al(2)$, $Nb_3Al(3)$, Nb_3Sn, $Pb_{0.9}Bi_{0.1}$, $Nb_3Al(1)$, $Pb_{0.8}Bi_{0.2}$, $Pb_{0.7}Bi_{0.7}$ and $Pb_{0.65}Bi_{0.35}$.

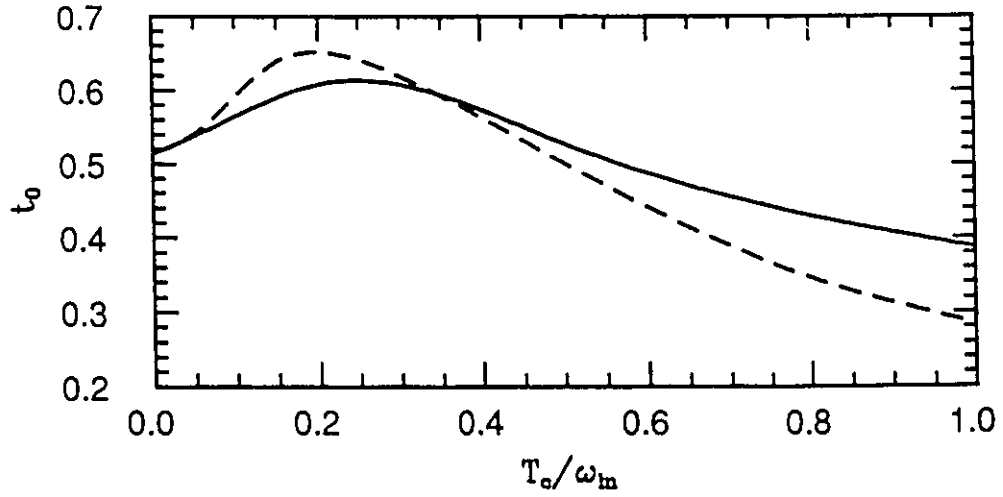

Figure 4.8 The reduced crossover temperature, t_0, is plotted vs. T_c/ω_{ln} for the LSCO spectrum (solid line) and a delta function spectrum (dashed line).

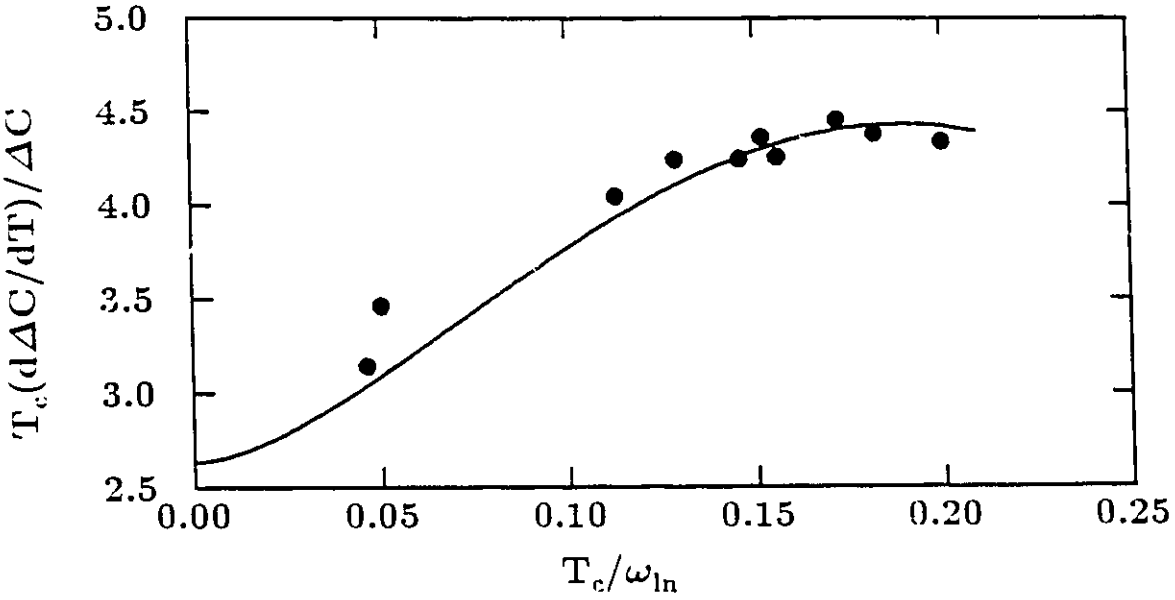

Figure 4.7 The approximate formula for R given in equation (4.22) is plotted vs. T_c/ω_{ln}. The dots represent full calculations for real materials. In order of increasing T_c/ω_{ln} these are Tl, In, $Nb_3Al(2)$, $Nb_3Al(3)$, Nb_3Sn, $Pb_{0.9}Bi_{0.1}$, $Nb_3Al(1)$, $Pb_{0.8}Bi_{0.2}$, $Pb_{0.7}Bi_{0.7}$ and $Pb_{0.65}Bi_{0.35}$.

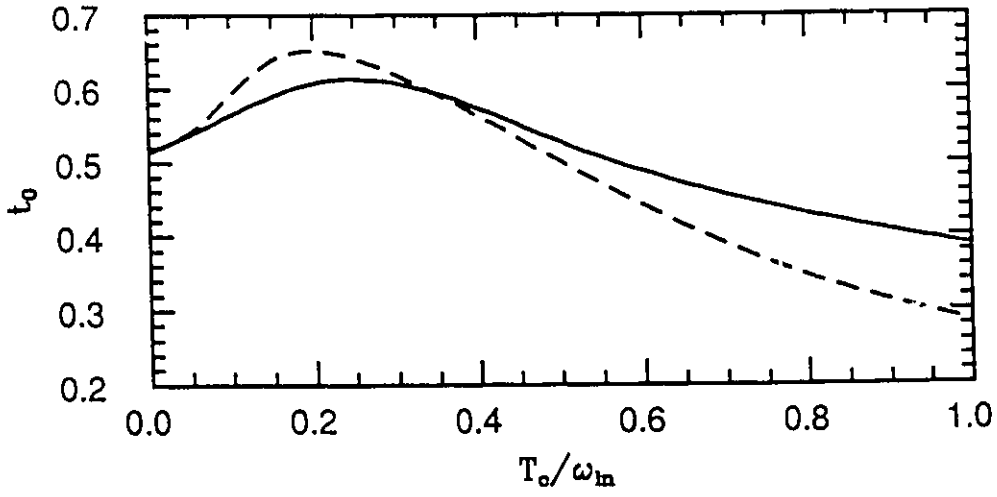

Figure 4.8 The reduced crossover temperature, t_0, is plotted vs. T_c/ω_{ln} for the LSCO spectrum (solid line) and a delta function spectrum (dashed line).

crossover temperature, t_0, is plotted vs. T_c/ω_{ln} for the two spectra considered previously. For BCS, $t_0 = 0.514$. As with the normalized slopes, this quantity achieves a maximum and then turns over as a function of T_c/ω_{ln} . The actual maximum in t_0 that is achieved does not seem that much larger than the BCS value. In the case of the delta function, $(t_0)^{max} \sim 0.65$ and for LSCO it is $(t_0)^{max} \sim 0.61$. That this is the case shall become important when experimental results are discussed. On the other hand, it is evident from this figure that t_0 can be much lower than BCS in the very strong coupling region, $T_c/\omega_{ln} \sim 1.0$. For both curves, the point where t_0 reattains it's BCS value is $T_c/\omega_{ln} \sim 0.5$. If one looks at the curves in Fig. 4.3 and Fig. 4.4 that correspond to this value of T_c/ω_{ln}, it is evident that, while they crossover at about the same temperature as the BCS curve, the overall behavior of these $\Delta C(T)/\Delta C(T_c)$ curves is somewhat different that for BCS.

A strong coupling correction formula to t_0 can also be established. From a fit to the same real spectra used to fit the formula for R it has been determined that the formula

$$t_0 = 0.514\left(1 + 11.5\left(\frac{T_c}{\omega_{\ln}}\right)^2 \ln\left(\frac{\omega_{\ln}}{3.2T_c}\right)\right) \tag{4.23}$$

provides a good representation of the data. This formula along with the results for the real spectra is plotted in Fig. 4.9. It should be pointed out that, unlike the strong coupling correction formulas (4.11), (4.14) and (4.22) which can all be justified by mathematical derivation, equation (4.23) is purely empirical in nature.

Now, in order to prove the previous assertions about the maxima of the various quantities that have been studied here, it is necessary to discuss functional derivatives. The functional derivative of T_c was introduced

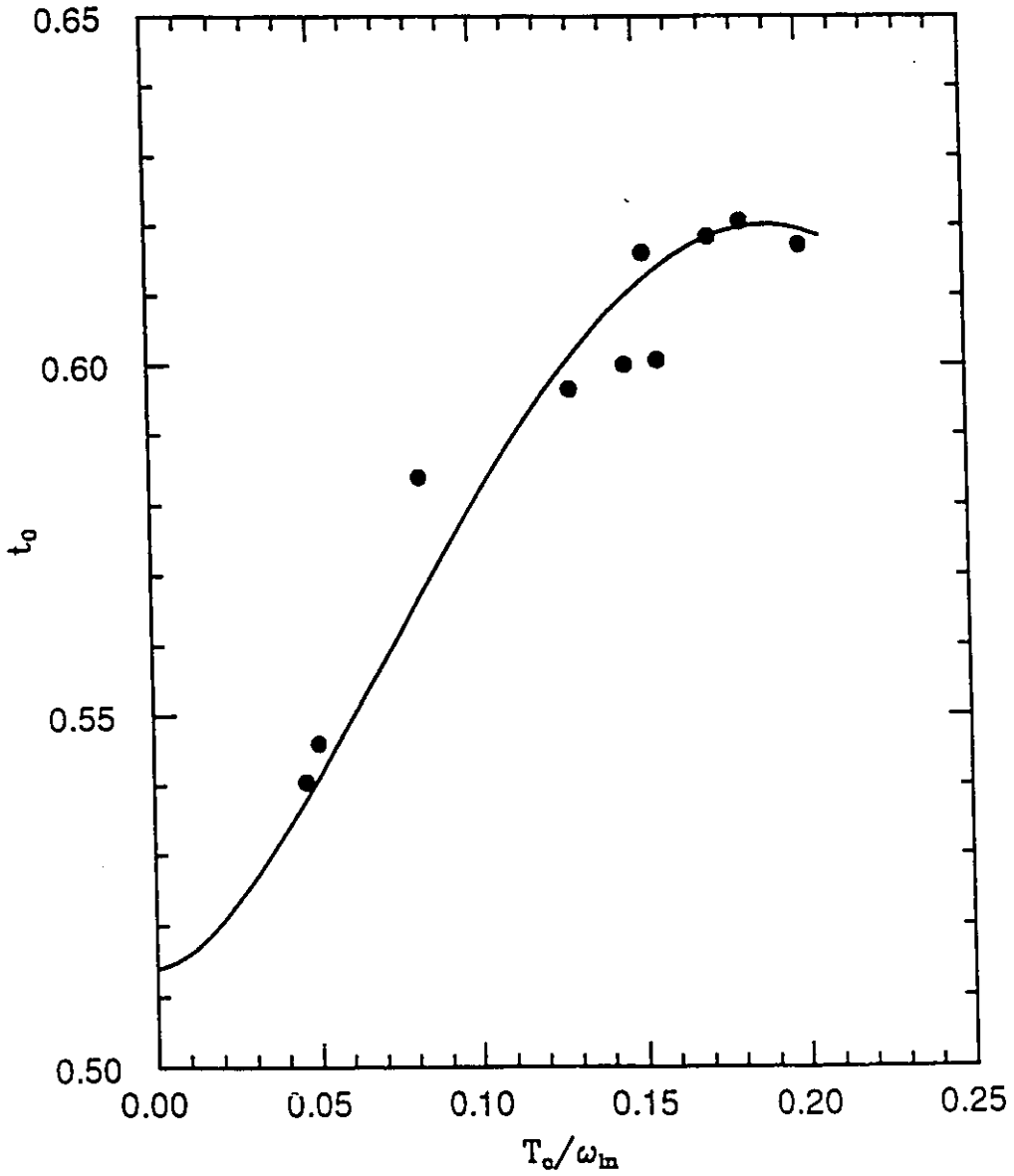

Figure 4.9 The approximate formula for t_0 given by equation (4.23) is plotted vs. T_c/ω_{ln}. Once again, the dots represent full calculations for real materials. In order of increasing T_c/ω_{ln} these are Tl, In, $Nb_3Al(2)$, $Nb_3Al(3)$, Nb_3Sn, $Pb_{0.9}Bi_{0.1}$, $Nb_3Al(1)$, $Pb_{0.8}Bi_{0.2}$, $Pb_{0.7}Bi_{0.7}$ and $Pb_{0.65}Bi_{0.35}$.

in the chapter on the critical temperature and the isotope effect. However, the functional derivative of practically every quantity related to superconductivity can be calculated. This can be done by brute force as was done for T_c in the last chapter. However, for some superconducting quantities, we are fortunate in that analytic formulas for the functional derivatives have been derived. This is the case for the specific heat jump. In particular, Marsiglio *et al.* [118] derived the following formula:

$$\frac{1}{\gamma_o}\frac{[\delta\Delta C(T)/T_c]}{\delta\alpha^2F(\omega)} = \frac{N(0)}{\gamma_o}\frac{T}{T_c}\frac{d^2}{dT^2}\left[(\pi T)^2\sum_{n,m}\left\{\frac{\tilde{\omega}_n}{\sqrt{\tilde{\omega}_n^2+\tilde{\Delta}_n^2}}\frac{\tilde{\omega}_m}{\sqrt{\tilde{\omega}_m^2+\tilde{\Delta}_m^2}} - sgn(\omega_n\omega_m)\right\}\right.$$

$$\left.\times\left\{\frac{2\omega}{\omega^2+(\omega_n-\omega_m)^2} - \frac{2}{T_c}(\omega_n-\omega_m)^2\frac{\delta T_c}{\delta\alpha^2F(\omega)}\int\frac{2\omega' d\omega'\alpha^2F(\omega')}{\omega'^2+(\omega_n-\omega_m)^2}\right\}\right] . \quad (4.24)$$

In order to use this formula, one must have knowledge of the renormalized gaps and frequencies as well as $\delta T_c/\delta\alpha^2F(\omega)$. For the calculations here, the functional derivative of T_c was obtained by using a formula[119,120] rather than by brute force. Note that formula (4.24) is independent of $N(0)$ as it is canceled out by γ_o. This formula can be easily related to other functional derivative formulas involving the specific heat. For example, the functional derivative $(\delta\Delta C(T)/\delta\alpha^2F(\omega))/\gamma_o$ would be given by

$$\frac{1}{\gamma_o}\frac{\delta\Delta C(T)}{\delta\alpha^2F(\omega)} = \frac{1}{\gamma_o}\frac{[\delta\Delta C(T)/T_c]}{\delta\alpha^2F(\omega)} + \frac{1}{\gamma_o}\frac{\delta T_c}{\delta\alpha^2F(\omega)} . \quad (4.25)$$

To obtain this equation, we have used the relation $\Delta C(T) = T_c(\Delta C(T)/T_c)$ and the fact that functional derivatives obey the same rules as regular derivatives when it comes to multiplication and division. Similarly, one can show that the functional derivative of the parameter R is given by:

$$\frac{\delta R}{\delta\alpha^2F(\omega)} = \frac{1}{\Delta C(T_c)}\frac{d\Delta C(T)}{dT}\Big|_{T_c}\frac{\delta T_c}{\delta\alpha^2F(\omega)} - \frac{T_c}{\Delta C^2(T_c)}\frac{d\Delta C(T)}{dT}\Big|_{T_c}\frac{\delta\Delta C(T_c)}{\delta\alpha^2F(\omega)}$$

$$+\frac{T_c}{\Delta C(T_c)}\frac{d}{dT}\left(\frac{\delta\Delta C(T)}{\delta\alpha^2F(\omega)}\right)\Big|_{T_c} . \tag{4.26}$$

The functional derivative of $(d\Delta C(T)/dT)/\gamma_0$ evaluated at T_c can be obtained in exactly the same manner. For this functional derivative, one must also know the functional derivative of γ_0. This is found using the relationship between γ_0 and λ and the definition of λ :

$$\frac{\delta\gamma_0}{\delta\alpha^2F(\omega)} = \frac{2}{3}\pi^2 N(0)\left(\frac{2}{\omega}\right) . \tag{4.27}$$

In Fig. 4.10, the functional derivative $\delta[(d\Delta C(T)/dT)/\gamma_0]/\delta\alpha^2F(\omega)$ is plotted for three different delta functions: $\omega_E = 15T_c$ (dashed), $\omega_E = 10T_c$ (dotted), and $\omega_E = 4T_c$ (solid). The μ^* has been set at 0.09 to correspond to the same case as displayed in Fig. 4.5. Note that $\omega_E/T_c = 10 \rightarrow T_c/\omega_E = 0.1$. The maximum for the delta function curve in Fig. 4.5 occurs at $T_c/\omega_{ln} \simeq 0.196$. This means that the first two curves in this figure correspond to delta functions that are placed below the maximum. The last curve on the other hand corresponds to a situation where the delta function is beyond the maximum in Fig. 4.5. All three functional derivative curves show the same basic behavior. Near zero frequency, they diverge toward $-\infty$ as a direct result of the inclusion of $\delta\gamma_0/\delta\alpha^2F(\omega)$. They also all have maxima for $\omega/T_c \sim 6$. The maximum for $\omega_E = 4T_c$ is below zero in contrast to the other two curves.

The fact that these functional derivative curves have maxima implies that the quantity $(d\Delta C(T)/dT)/\gamma_0$ evaluated at T_c can be optimized. This can be done by transferring the spectral weight of a given $\alpha^2F(\omega)$ away from frequencies where the functional derivative is smaller than it's value at maximum and concentrate it at the optimum frequency where it has the maximum effect. Given that such a process is required to increase the value

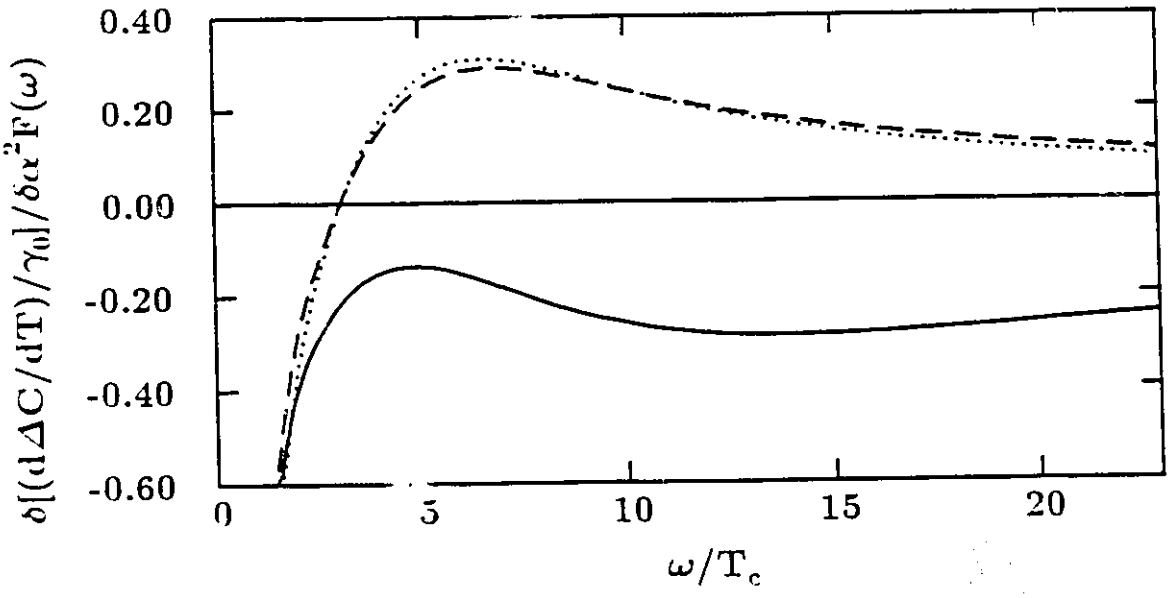

Figure 4.10 $\delta[(d\Delta C(T)/dT)/\gamma_0]/\delta\alpha^2F(\omega)$ is plotted vs. ω/T_c for the delta functions $\omega_E = 15T_c$ (dashed), $\omega_E = 10T_c$ (dotted), and $\omega_E = 4T_c$ (solid).

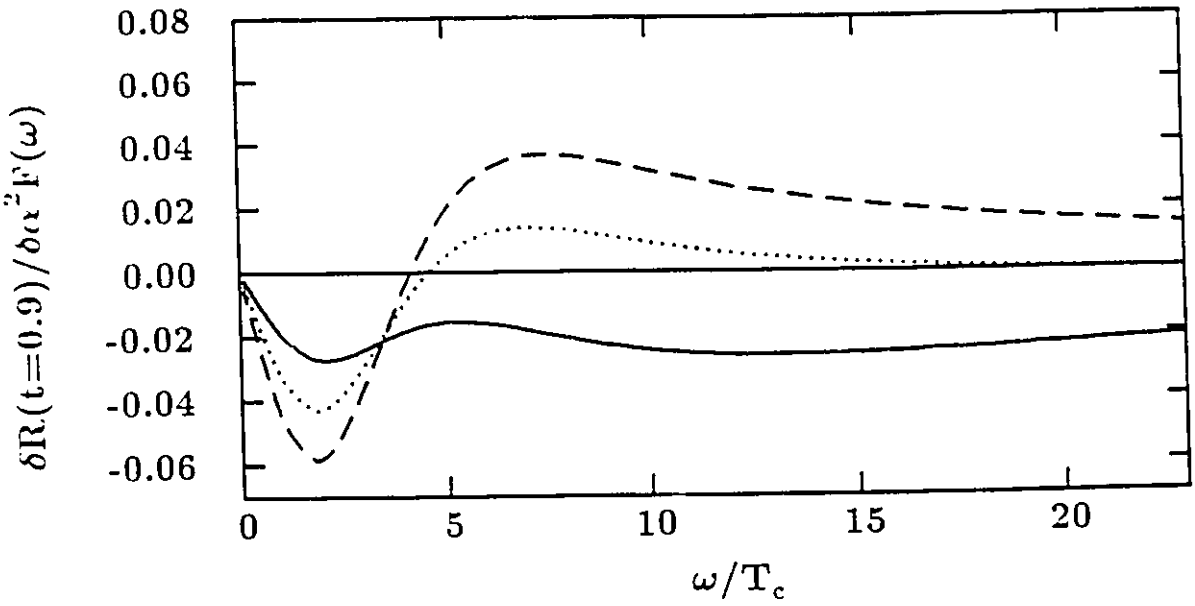

Figure 4.11 The functional derivative for the normalized slope evaluated at $t = 0.9$ is plotted vs ω/T_c for the delta functions $\omega_E = 12T_c$ (dashed), $\omega_E = 8T_c$ (dotted), and $\omega_E = 4T_c$ (solid).

of $(d\Delta C(T)/dT)/\gamma_0$ evaluated at T_c, leads one to believe that a delta function should be used with ω_E placed at the optimum frequency in order to obtain the maximum value for this quantity. For this reason, the maximum in the delta function curve in Fig. 4.5 should represent the absolute maximum value this quantity can take for $\mu^* = 0.09$.

Similar arguments applied to other superconducting properties have been applied in the past. In particular, the Leavens and Carbotte[55] T_c inequality given in equation (3.6) was a result of similar considerations. One important difference is that the inequality involved the spectral area A. As stated earlier, the area A cancels out of the quantities studied in this chapter and so the maxima should only depend on μ^*. These arguments have also been applied to the specific heat jump itself by Blezius and Carbotte[116,117] and to the upper critical magnetic field by Akis *et al.* [121]. Carbotte has also written reviews[122,43].

The maximum given in Fig. 4.5 occurs for $(\omega_E)_{opt} = 5.1T_c$. Ideally, what should occur if one calculates the functional derivative curve for a delta function placed at this frequency, is that the curve should be negative definite except for the maximum which should touch zero right at $(\omega_E)_{opt}/T_c$. Such a functional derivative curve is not displayed in Fig. 4.10 because of numerical problems associated with the extrapolation of the specific heat to T_c. The result is that the maximum in the functional derivative touchs zero at a frequency close to but not on $(\omega_E)_{opt}/T_c$. Such problems can be put in perspective when one notes that in order to obtain $(d\Delta C(T)/dT)/\gamma_0$ one is essentially taking the third derivative of the free energy and we are then in turn taking it's functional derivative.

We wish now to discuss the functional derivative of the parameter R. Returning to Fig. 4.6, the maximum in the delta function curve for this quantity occurs for $T_c/\omega_{ln} \simeq 0.16$ — $(\omega_E)_{opt} = 6.1T_c$. Again, ideally $\delta R/\delta\alpha^2F(\omega)$ should touch zero at this frequency, however this functional derivative is even more sensitive to the difficulties we have mentioned earlier. For this reason, we consider instead the functional derivative:

$$\frac{\delta R(t=0.9)}{\delta\alpha^2F(\omega)} = \frac{\delta}{\delta\alpha^2F(\omega)}\left[\left(\frac{d\Delta C(t)}{dt}\right)_{t=0.9}/\Delta C(T_c)\right] .$$

The quantity for which the functional derivative is being taken here is defined the same way as R, except that the slope is evaluated at $t = 0.9$ rather than right at T_c. In this way some of the extrapolation problems that occur at T_c are avoided but it is still difficult to obtain this functional derivative with as high accuracy as one would like. In Fig. 4.11, this functional derivative is plotted for three different choices of delta function: $\omega_E = 12T_c$ (dashed), $\omega_E = 8T_c$ (dotted), and $\omega_E = 4T_c$ (solid). The μ^* has again been set at 0.09 . Note that these functional derivatives do not diverge at zero frequency since γ_0 no longer enters into the calculation. As with the previous figure, all the curves show maxima and so the the same arguments discussed previously should apply here as well.

In Fig. 4.12, $(d\Delta C(t)/dt)_{t=0.9}$ is plotted vs. T_c/ω_E. As was the case with R, the curve has a well defined maximum at $(\omega_E)_{opt} = 6.1T_c$. From this one concludes that the functional derivative curves shown in the previous figure show the right progression: the maximum for $\omega_E = 4T_c$ is below zero while the maxima for $\omega_E = 8T_c$ and $\omega_E = 12T_c$ are above zero with the maximum in the functional derivative becoming larger the higher the frequency it is evaluated at. Before passing on, it is worth noting that the actual maximum

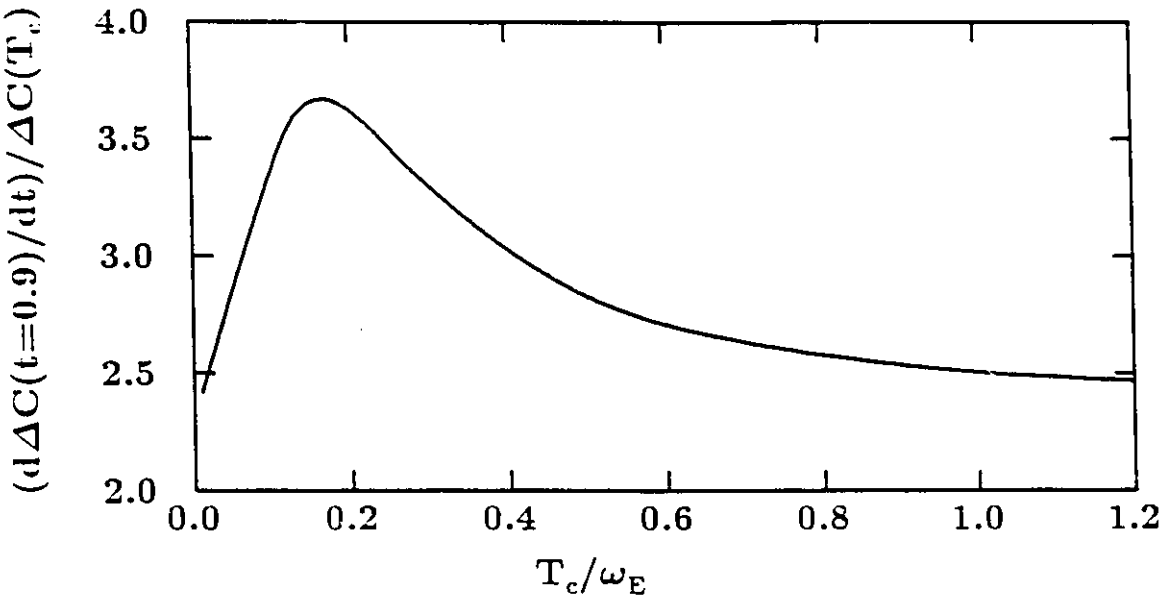

Figure 4.12 $(d\Delta C(t)/dt)_{t=0.9}$ is plotted vs. T_c/ω_E.

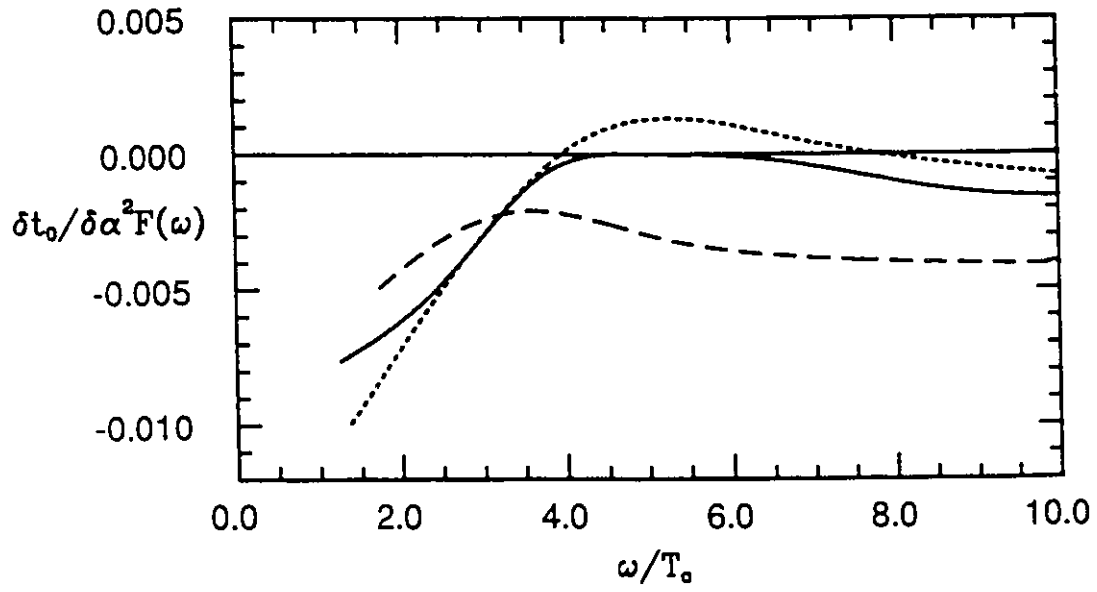

Figure 4.13 $\delta t_0/\delta\alpha^2F(\omega)$ vs. ω/T_c is plotted for the delta functions $\omega_E = 3.5T_c$ (dashed), $\omega_E = 5.1T_c$ (solid), and $\omega_E = 5.6T_c$ (dotted).

of $(d\Delta C(t)/dt)_{t=0.9}$ curve displayed in Fig. 4.12 as approximately 3.67. This is substantially less than the maximum for R given in Fig. 4.6 which was 4.76. Again it should be emphasized that the slope $(d\Delta C(t)/dt)_{t=0.9}$ is defined in the same way as R, except for the fact that it is taken at $t = 0.9$ rather than at T_c. This is important when it comes to interpreting experimental results since this slope appears to be quite sensitive to how it is taken.

For the crossover temperature t_0, there are no analytic formulas to turn to in order to calculate the functional derivative. This being the case, one must turn to the brute force technique described earlier in order to calculate $\delta t_0/\delta\alpha^2F(\omega)$. The results of these calculations are shown in Fig. 4.13. The curves correspond to the following three delta function spectra : $\omega_E = 3.5T_c$ (dashed), $\omega_E = 5.1T_c$ (solid), and $\omega_E = 5.6T_c$ (dotted). The μ^* has again been set at 0.09 . In this case, the maximum in the functional derivative touchs zero for $\omega_E = 5.1T_c$. This is the desired behavior. Examination of the data used to produce the delta function curve of t_0 vs. T_c/ω_{ln} in Fig. 4.8 indicates that the maximum in t_0 is at this frequency. The other two curves indicate that we have the right progression. The $\omega_E = 3.5T_c$ curve has a peak less than zero while the $\omega_E = 5.6T_c$ curve peaks above zero. This is all confirmation that the functional derivative technique does indeed work for t_0.

In figures 4.14, 4.15 and 4.16 the maxima of $(d\Delta C(T)/dT)/\gamma_0$ evaluated at T_c, R and t_0 respectively are plotted as a function of μ^*. Once again it should be mentioned that the cutoff frequency is $\omega_c = 1000$ meV. The solid dots again represent theoretical calculations using several real $\alpha^2F(\omega)$. In all cases, the real spectra results fall significantly below the maxima curves giving confidence that the calculated values for these quantities do indeed represent the maximum values. All three quantities appear to increase with

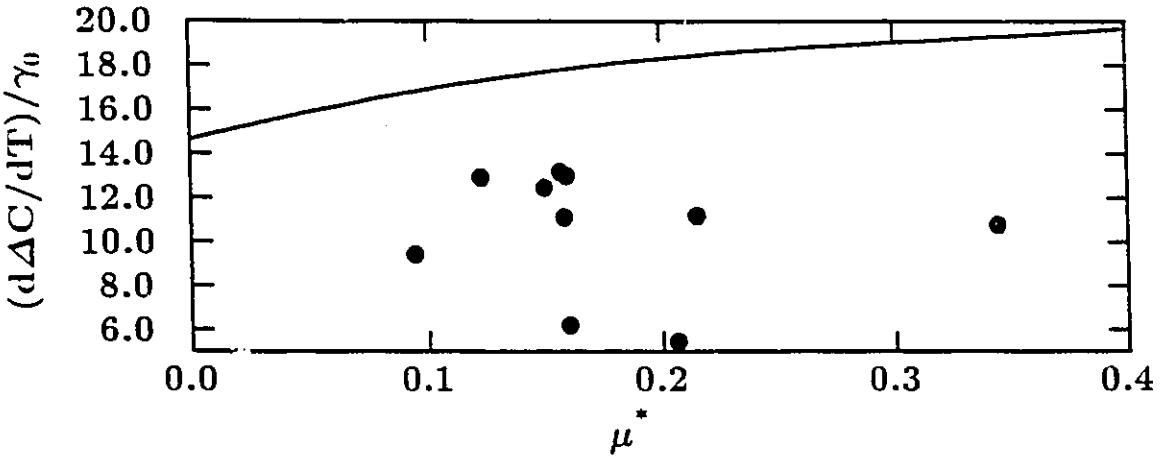

Figure 4.14 The maximum of $(d\Delta C(T)/dT)/\gamma_0$ evaluated at T_c is plotted as a function of μ^*. The dots represent results obtained for real materials.

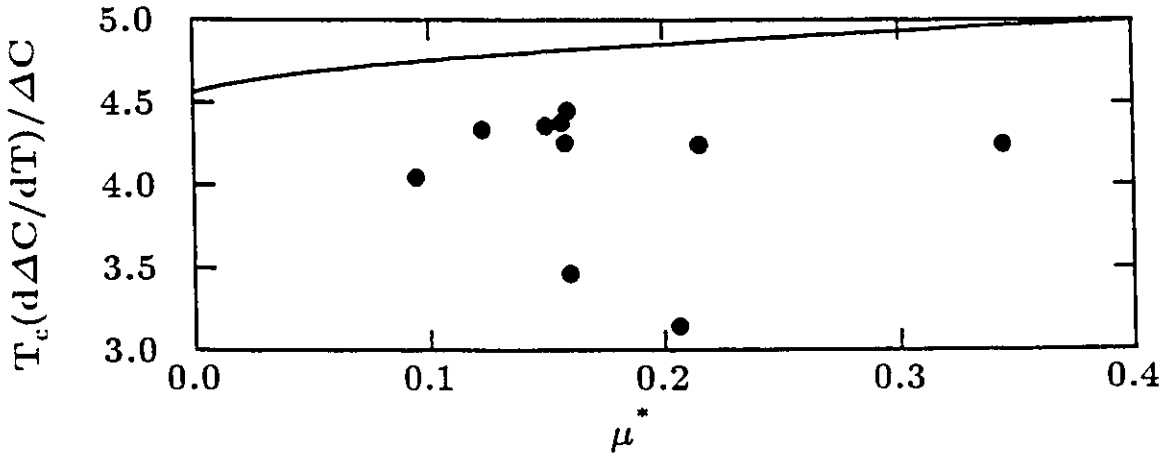

Figure 4.15 The maximum of R is plotted as a function of μ^*.

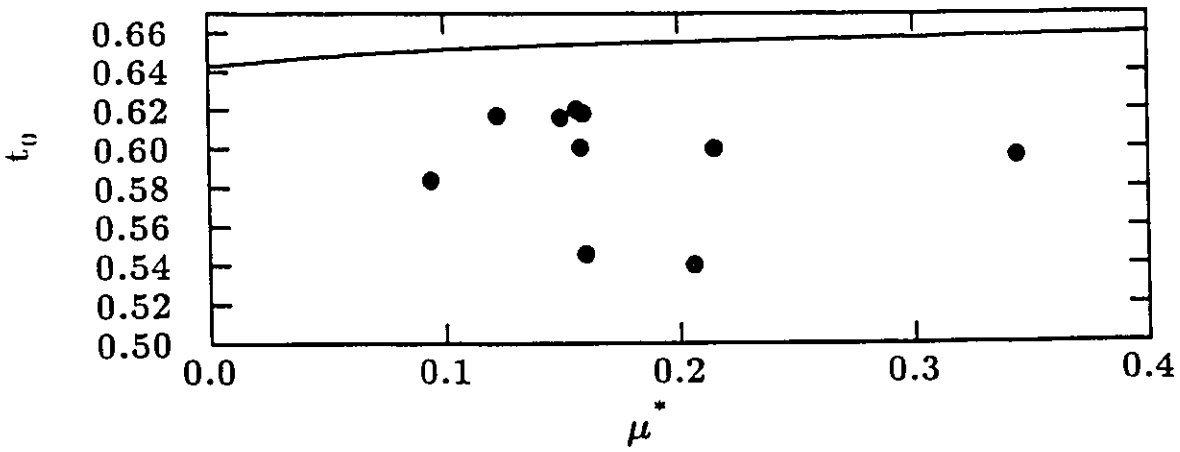

Figure 4.16 The maximum of t_0 is plotted as a function of μ^*.

μ^* but the rate of increase does not appear to be particularly large. The largest variation appears in $(d\Delta C(T)/dT)/\gamma_o$ evaluated at T_c, which has a maximum that ranges from 14.64 for $\mu^* = 0.0$ to 19.66 for $\mu^* = 0.4$, an increase of 34.3 percent. In contrast, the maximum in R ranges from 4.44 to 5.00, a variation of 12.7 percent, while the maximum in t_0 ranges only from 0.6424 to 0.6597, a difference of only 2.7 percent. Since the variations in R^{max} and t_0^{max} are fairly small, one can safely make the generalizations that $R^{max} \sim 5.0$ and $t_0^{max} \sim 0.65$. These values shall be used when experimental results in the next section.

4.4 EXPERIMENTAL COMPARISON

As stated earlier, quantities such a the normalized slope R and the crossover temperature t_0 can be extracted from several experiments that have been performed on high-T_c oxides. In t. :s section, a brief sampling of these experiments is given. Almost certainly one could find more experiments than are cited here to compare with, but the intention here is just to give a feel for what the experiments tell us rather than to be exhaustive.

The main problem with trying to obtain these quantities is, of course, is being able to determine the normal state electronic specific heat below the critical temperature. In a conventional superconductor, this can be done by applying a sufficiently high magnetic field in order to drive the sample into the normal state. In the oxide materials, the critical magnetic fields that are required are so large as to make this procedure impossible except for temperatures extremely close to T_c.

An alternative to using a magnetic field to make the sample normal below T_c is altering the composition of the material so that it no longer

superconducts but in the meantime is similar enough to the original material so that the normal state properties are not significantly changed.

Experiments along these lines have been performed by Junod *et al.* [107]. Doping YBCO with iron, the compound $YBa_2(Cu_{1-x}Fe_x)_3O_7$ was formed. In a sample with x=0.04, it was found that the specific heat jump was completely suppressed. While this sample had tetragonal structure, it appeared to have essentially the same specific heat above T_c as the undoped orthorhombic sample it was compared with. While the doped sample had no jump, apparently a significant fraction of it still was superconducting with a $T_c \sim 70K$. At any rate, Junod obtained $\Delta C(T)$ by taking the difference $C_{undoped}(T) - C_{doped}(T)$. From the curve that was generated one could extract the slope R. From looking at his data, one would find that $R \sim 8 - 14$, depending on which interval you took the slope. Thus even the lower bound for this parameter found from this experiment is much larger than the maximum of about 5 that is allowable in Eliashberg theory as was established in the previous section. The crossover temperature t_0 can also be extracted from Junod's data. It appears to be of the order of $t_0 \sim 0.85$, which is significantly higher than the Eliashberg upper bound of 0.65 established earlier. The actual temperature of the crossover is about $78K$, above the T_c of the doped sample. One major problem with Junod's results is that the entropy is not balanced - recall equation (4.7) in section 4.2 . There is far too much negative weight below the crossover temperature to be compensated for by the excess specific heat between it and T_c.

An experiment by Loram and Mirza[109] compared $YBa_2Cu_3O_7$ with the nonsuperconducting material $YBa_2Cu_3O_6$. From their results one extracts a value of R that is about 5.0 . The crossover temperature appeared

to be about $t_0 \sim 0.68$, which is larger than the maximum we have set but not by a particularly large amount. Indeed, from this experiment by itself one might be tempted to conclude that YBCO is a strong coupling superconductor with $T_c/\omega_{ln} \simeq 0.2$. Loram and Mirza maintain the entropy balance but this is is due to the fact that it was used as a constraint for some parameter fitting. As was the case with Junod, the samples being compared had different structures. In fact, the specific heat for the nonsuperconducting sample was *larger* than for the superconducting one. Loram and Mirza are seemingly able to overcome this difficulty by the introduction of corrections for various physical effects so that the specific heat difference could still be extracted.

Superconducting samples can also be made normal by neutron irradiation. Experiments along these lines have been performed by Aleksashin *et al.* [110,111]. They found that, if the radiation damage is sufficient, that the specific heat jump can be wiped out. In the meantime, the specific heat above T_c does not seem to change making the irradiated samples good nonsuperconducting references. Their data for $\Delta C(T)$ for YBCO appears to yield a value of $R \simeq 7.0$ and a crossover in the region of $t_0 \sim 0.8$. These values are again larger than the Eliashberg maxima that have been set for them. However, as was the case for Junod, the entropy is not balanced. Interestingly, Aleksashin has done similar experiments on $La_{1.83}Sr_{0.17}CuO_4$. For their sample, which had a $T_c \sim 35K$, the extracted $\Delta C(T)$ is more consistent with conventional Eliashberg superconductors. The value of R one obtains from the data is $R \sim 3.2$, which from examining Fig. 4.7 translates to a coupling strength of $T_c/\omega_{ln} \simeq 0.05$. This indicates that this material is a weak coupler. On the other hand, the crossover temperature is still rather high - $t_0 \sim 0.67$. Unlike the YBCO experiment, the entropy does balance in this case.

A normal reference sample is not necessarily required to obtain R or t_0 from experimental data. Junod has also used brute force fitting of the entire specific heat curve of YBCO to separate the electronic and lattice components of the specific heat[106]. Below T_c, the two-fluid model is used to aid in the fitting of the electronic part so that the crossing temperature he obtains, $t_0 = 0.58$, while being well within the conventional Eliashberg range must be taken with a grain of salt. The slope R that one obtains from the experimental data analyzed this way is about $R \simeq 7.4$.

Shilling *et al.* [112] have experimented on $Bi_{1.6}Pb_{0.4}Sr_2Ca_2Cu_3O_{10}$ and analyzed their data using multi-parameter fits to obtain the phonon and electronic contributions to the specific heat. This particular superconductor had $T_c = 106.7K$. To fit the electronic contribution, they assumed that $C_{el}(T)$ had the following form:

$$C_e(T) = \begin{cases} (C_{es}(\alpha, T)/\gamma_o T_c)\gamma_o T_c & \text{if } T < T_c; \\ \gamma_o T & \text{if } T > T_c \end{cases} . \qquad (4.27)$$

In this equation, $C_{es}(\alpha, T)/\gamma_o T_c$ is the normalized superconducting specific heat appropriate to the strong coupling parameter α. They used the gap ratio $2\Delta(0)/k_B T_c$ as their strong coupling parameter. The gap ratio makes a good strong coupling parameter as it increases monotonically as a function of λ and T_c/ω_{ln}. They obtained fits assuming values from $\alpha = 2\Delta(0)/k_B T_c = 3.53$ (BCS) all the way up to $\alpha = 6.8$. This final value of α corresponds to $T_c/\omega_{ln} \sim 0.5$ which is well above the conventional strong coupling range[38]. This approach distinguishes Shilling *et al.* from many other experimenters who have done similar fits but by assuming that the BCS case holds and not taking into account any strong coupling effects. Through this sort of analysis, they were able to make an estimate of R for this material. The

value they obtain is $R = 25 \pm 4$, which is radically higher than the Eliashberg maximum. The authors also mention that they have also obtained results for $Tl_2Ba_2CaCu_2O_{10}$. They estimate $R \sim 10$ for this material.

From this brief survey of experiments on the high-Tc oxides, it appears that there is the strong possibility that several of these materials give values for R and t_0 that are beyond the range that has been established for them in Eliashberg theory in the previous section. If one does believe these experiments, then there are two possible conclusions. The first possibility is that Eliashberg theory is not applicable to these particular materials at all and a totally new theory of superconductivity must be developed. This is the approach that theorists too numerous to mention have taken. The second possibility is that Eliashberg theory may still apply but that important modifications must be incorporated.

What possible modifications might be considered? Extensive calculations have been done by Williams and Carbotte[123,124] including spin fluctuations in the Eliashberg formalism. Spin fluctuations are logical to study in the context of the oxide superconductors because the parent compounds of most of the oxides are antiferromagnetic insulators. If the superconductivity is s-wave in nature as it is in standard BCS-Eliashberg theory, then these spin fluctuations tend to suppress superconductivity. Under these sorts of circumstances, Williams and Carbotte were able to achieve values of R as high as 7.6. On the other hand, if the paired superconducting electrons participate in d-wave states, spin fluctuations can actually enhance superconductivity. Williams and Carbotte have also studied this possibility. In this case, the largest value for R that was achieved was 9.75, about twice the conventional Eliashberg maximum. The highest value of t_0 that was achieved

was 0.72. The values for R attained by including spin fluctuations appear to be more consistent with the experiments that have been discussed. However, the result for $Bi_{1.6}Pb_{0.4}Sr_2Ca_2Cu_3O_{10}$ is still highly problematic.

Another effect that has not been considered here are fluctuations. In the presence of fluctuations, one expects that the specific heat rather than simply jumping at T_c becomes divergent[24,106,125,126]. Obviously, this would have a dramatic effect on the normalized slope R. Fluctuations would also tend to increase t_0 because of the entropy conservation restriction. There is something called the Ginzberg criterion which basically states that below a reduced temperature $t_G \propto \xi^{-3}$, where ξ is the coherence distance, fluctuations are unimportant. In conventional superconductors where ξ is of the order of thousands of angstroms, fluctuations are expects in a region near T_c so tiny as to render them impossible to observe and thus unimportant. In the oxides, ξ is more of the order of tens of angstroms so for these materials fluctuations may indeed play an important role. Whether or not they have been observed is still a cause for debate. Some work has been done combining fluctuation effects with Eliashberg theory[127,128].

4.5 CONCLUSIONS

The electronic specific heat of Eliashberg superconductors has been studied as a function of the strong coupling parameter T_c/ω_{ln} and the coulomb repulsion μ^*. The quantities that have been concentrated on are the normalized specific heat difference, $\Delta C(T)/\Delta C(T_c)$, what we have called the crossover temperature , t_0, the slope evaluated at T_c normalized by the Sommerfeld constant, $(d\Delta C(T)/dT)/\gamma_o$, and the slope normalized by the jump,

$R = T_c(d\Delta C(T)/dT)/\Delta C(T_c)$, again evaluated at T_c. The studies were performed primarily with the scaled $\alpha^2F(\omega)$ of LSCO as well as with delta functions. From using these two different types of $\alpha^2F(\omega)$, it was discovered that spectral shape does indeed play a role in the values that these quantities take but that the qualitative trends that were observed remained unchanged. Starting from the BCS limit, the normalized slopes and the crossover temperature all increased as T_c/ω_{ln} was increased. Eventually, all three quantities peak at approximately $T_c/\omega_{ln} \sim 0.2$ and turn over. At a sufficiently large coupling strength, t_0 and $(d\Delta C(T)/dT)/\gamma_o$ actually fall below their BCS values. This behavior is consistent with the behavior found for many other superconducting properties. The parameter R on the other hand appears to saturate at large T_c/ω_{ln}.

Using functional derivative arguments, maxima for the parameters $(d\Delta C(T)/dT)/\gamma_o$, R and t_0 were established. The maxima for R and t_0 were found to be particularly insensitive to the value of μ^* and being of the order of 5.0 and 0.65 respectively. These maxima should not be violated by any conventional Eliashberg superconductor. Superconductors that rely on the electronic boson exchange mechanisms such as those discussed in the previous chapter should not exceed these maxima as well.

Experiments seem to indicate that R and t_0 may indeed exceed the theoretical maxima set here at least in some of the oxide superconductors. If this is true, this indicates that traditional strong coupling Eliashberg theory may not be applicable to these materials or, at the very least, additional factors need to be taken into account.

Chapter 5

Nuclear Spin Relaxation

5.1 INTRODUCTION

Generally, the nuclei of atoms are objects that have an intrinsic spin angular momentum, $\hbar\vec{I}$. This angular momentum gives rise to a magnetic moment $\vec{\mu}$:

$$\vec{\mu} = \gamma_n \hbar \vec{I} \ . \tag{5.1}$$

Here, γ_n is the gyromagnetic ratio of the nucleus. The magnetic moments of the nuclei in a solid will interact with an applied magnetic field $\vec{B}_a$. If $\vec{B}_a = (0, 0, B_o)$ the energy of this interaction will be given by

$$V = -\mu_z B_o = -\gamma_n \hbar B_o I_z \ . \tag{5.2}$$

The allowed values of I_z are $m_I = I, I-1, ..., -I$. So for the simple case where $I = \frac{1}{2}$, then $I_z = \pm\frac{1}{2}$. Since there are two allowed values of I_z, the energy

level of the nucleus is split into two levels by the applied field. Denoting the difference in energy between these levels as $\hbar\omega_{nuc}$, then we find that[129]

$$\omega_{nuc} = \gamma_n B_o \tag{5.3}$$

is the fundamental condition for magnetic resonance and ω_{nuc} is the resonance frequency. Of course, for nuclei of higher spin this situation becomes more complicated for obvious reasons.

The magnetic resonance of nuclei in solids is influenced by the presence of conduction electrons as the magnetic moments of electrons and nuclei interact. One such interaction between nucleus and electron is the contact hyperfine interaction. In this interaction, the electron can be viewed as applying an effective magnetic field on the nucleus. It can be written as[129]

$$V_{HF} = \frac{8\hbar}{3}|\psi_{k_F}(0)|^2 \vec{I} \cdot \vec{S} \tag{5.4}$$

where $\vec{S}$ is the spin operator of the electron and $\psi_{k_F}(0)$ denotes the Bloch function amplitude at the nuclear site. The subscript k_F is included on this amplitude because only electrons near the top of the Fermi sea are important for this interaction. Due to the Pauli principle, only these electrons which are near vacant energy states are able to absorb or transfer the energy of a nuclear transitions. Not surprisingly, going from the normal state to the superconducting state has a strong effect on this interaction as the same electrons are directly involved.

There are two effects of this interaction that are important. The first is the Knight shift. This effect comes about since the electrons alter the static magnetic field seen by the nuclei and as a result shift the value of the external magnetic field required for resonance. How it comes about can be

seen by combining equation 5.4 with 5.2 and replacing $\bar{S}$ with the average $\langle S_z \rangle$. This spin average is proportional to the Pauli spin susceptibility χ_P. After the appropriate substitutions, one finds that the combined interaction will have the form:

$$V = -\gamma_n \hbar B_o (1 + \frac{\Delta B}{B_o}) I_z \tag{5.5}$$

with the Knight shift given by:

$$K = (\frac{\Delta B}{B_o}) = \frac{8\pi}{3} |\psi_{k_F}(0)|^2 \chi_P \ . \tag{5.6}$$

So, it is apparent that, by measuring the Knight shift, one is essentially measuring the susceptibility of the conduction electrons.

The second important effect has to do with the transfer of energy from the nuclei to the electrons. In thermodynamic equilibrium, the nuclear spin states in a magnetic field will be populated according to Boltzmann statistics. So in the case where $I_z = \pm \frac{1}{2}$, the equilibrium nuclear magnetization is given by

$$M_{zo} = \mu_B (n_\uparrow - n_\downarrow) \tag{5.7}$$

where μ_B is the Bohr magneton and the populations $n_\uparrow$ and $n_\downarrow$ are related by

$$n_\uparrow / n_\downarrow = exp(2\mu_B B_o / k_B T) \ . \tag{5.8}$$

Away from equilibrium, this relation for the populations does not hold. A nuclear system not in equilibrium will eventually relax towards it equilibrium magnetization. This process can be described by a simple differential equation:

$$dM_z/dt = (M_{zo} - M_z)/T_1 \tag{5.9}$$

where T_1 is the relaxation time. In a metal, the hyperfine interaction will be the dominant means by which the nuclei relax. Thus, in order to calculate T_1, one is required to calculate a transition probability with a matrix element for V_{HF} that includes electronic Bloch states as well as the nuclear states. In the superconducting state, the Bloch electronic states are replaced by BCS wave functions.

In this chapter, we will therefore be mainly concerned with calculating the Knight shift and the nuclear spin relaxation rate, $R = 1/T_1$, for the superconducting state. The theory and relevant equations for these quantities for Eliashberg superconductors will be summarized in the next section. In the section following, results for varying coupling strengths are presented. In the next section we include in an approximate way the effects of the type of anisotropy one might expect in the oxides. After that, we compare results with some recent experiments. As part of this comparison, we include the effects of the Fermi liquid corrections of Monien and Pines[130] as well as strong coupling[131,132] and anisotropy[132]. Conclusions are drawn in the final section of this chapter.

5.2 THE SUPERCONDUCTING STATE

As outlined in the introduction, the Knight shift is proportional to the Pauli susceptibility of the electrons. This susceptibility is just given by

$$\chi_P = M_z/B_o \ . \tag{5.10}$$

Thus, one must evaluate equation (5.7) for M_z but in this case we are speaking about the spin populations of the electrons not the nuclei. These populations

will be given by a sum over Fermi factors such that for a weak applied field

$$M_z = \mu_B \sum_{\vec{k}} [f(\epsilon_k - \mu_B B_o) - f(\epsilon_k + \mu_B B_o)] \simeq -2\mu_B^2 B_o \sum_k \frac{df}{d\epsilon_k} . \qquad (5.11)$$

The sum over k in this equation can be replaced by an integration over energy, using the electronic density of states. For the normal state, this leads to the result that $\chi_n = 2\mu_B^2 N(0)$, which is generally valid for temperatures from absolute zero to ones much higher than any superconducting T_c. In the superconducting case, the superconducting density of states enters into this equation. Taking the ratio between normal and superconducting states, we can obtain what is called the Yosida function[133] :

$$Y(T) = 2 \int_0^\infty d\omega [\frac{-df}{d\omega}] \mathrm{Re}[\frac{\omega}{\sqrt{\omega^2 - \Delta^2(\omega, T)}}] . \qquad (5.12)$$

Note that this function is equal to both χ_s/χ_n and K_s/K_n. From an analysis with BCS theory, it can be shown that $Y(T) \sim \exp(-\Delta_o/k_B T)$ at low temperatures . That $Y(T)$ becomes vanishingly small at low temperatures is a reflection of the fact that in the superconducting state electrons are in Cooper pairs with zero net spin and so, to obtain a finite magnetic moment, pairs must be broken requiring energy 2Δ. This is an energy the weak applied field is unable to provide. As the temperature is increased, Cooper pairs are broken thermally at an increasing rate so that the value of the Yosida function rises eventually reaching one at T_c.

The nuclear spin relaxation rate $R = 1/T_1$ requires the calculation of transition rates of the form

$$P_{m\vec{k}'s';n\vec{k}s} = (2\pi/\hbar)| < n\vec{k}s|V_{HF}|m\vec{k}'s' > |^2 \delta(E_f - E_i - \hbar\omega_{nuc}) \qquad (5.13)$$

where m and n are the initial and final states of the nucleus, E_i, $\vec{k}$ and s and E_f, $\vec{k}'$ and s' are the initial and final energy, momentum and spin states of

the electron. To obtain the actual relaxation rate involves summing over all these states. It should be noted that $\hbar\omega_{nuc}$ is relatively small in comparison to the electronic energies so that $E_i \simeq E_f \simeq E$. In the end, for the normal state one finds for $E_f - E_i \ll k_B T \ll E_F$ that

$$R_n \propto \int N^2(E) f(E)[1 - f(E)] dE \propto N^2(0) k_B T \ . \tag{5.14}$$

This occurs in this case because the function $f(E)[1 - f(E)]$ is highly peaked in a region of $k_B T$ about the Fermi energy. So we see that the standard theory predicts that R_n is proportional to temperature. This is an important point as we shall see later .

In the superconducting state and using BCS theory[7,134,135], one ends up evaluating the same sort of matrix elements but of course BCS wave functions take the place of the standard electronic wave functions. In this case, one finds

$$R_s \propto \int N_{BCS}(E_i) N_{BCS}(E_f) C(E_i, E_f) f(E_i)[1 - f(E_f)] dE_i \ . \tag{5.15}$$

This is quite similar to equation (5.14). For reasons that shall become apparent later, E_i and E_f have not been set to E . There are two major differences between this equation and the earlier one. The first is that the normal state density of states is replaced by the BCS expression. Note that the BCS expression is given by

$$\frac{N_{BCS}(\omega)}{N(0)} = \begin{cases} 0, & \text{if } \omega < \Delta(T); \\ \frac{\omega}{\sqrt{\omega^2 - \Delta^2(T)}}, & \text{if } \omega > \Delta(T); \end{cases} \ . \tag{5.16}$$

The most significant feature of the BCS density of states is the square root singularity about the BCS gap. The other difference is the appearance of an extra factor $C(E_i, E_f)$ which is given by

$$C(E_i, E_f) = 1 + \Delta^2(T)/E_i E_f \ . \tag{5.17}$$

This is a coherence factor that represents the correlations between electrons in the superconducting state. Combining the normal and superconducting expressions, one finds

$$(R_s/R_n)_{BCS} = \frac{2}{k_B T}\int_{\Delta(T)}^{\infty} \frac{[E_i E_f + \Delta^2(T)]f(E_i)[1-f(E_f)]}{\sqrt{(E_i^2-\Delta^2(T))(E_f^2-\Delta^2(T))}}dE_i \ . \qquad (5.18)$$

As in the case for the Yosido function, one finds that $(R_s/R_n)_{BCS}$ goes as $\exp(-\Delta_o/k_B T)$ for $T \sim 0$. Near T_c, if we assume $\hbar\omega_{nuc}$ is small so that we can set $E_i = E_f$ in the above integral, one obtains the disturbing result that $(R_s/R_n)_{BCS}$ diverges logarithmically. This is due to square root singularity in the BCS density of states. However, if we retain the energy difference, one finds that the normalized relaxation rate has a large peak just below T_c before falling off. This is the so called Hebel-Slichter peak. This sort of peak has been observed in conventional materials such as Aluminum[134,136]. However, it was realized right from the beginning that the peaks that were observed were too small to be explained by the difference in nuclear levels alone. What was required was some sort of mechanism that broadens the electron energy levels and smears out the density of states. This can be accomplished several ways[135]. It will occur if the gap is spatially inhomogeneous or in other words a function of $\mathbf{r}$. It will also occur if the gap function is anisotropic: $\Delta \rightarrow \Delta_{\vec{k}}$. Another solution is to make the gap complex. This final scenario of course is exactly the situation we have in Eliashberg theory where, as explained earlier, introducing lifetime electron effects due to the electron-phonon interaction means we must replace the BCS gap $\Delta(T)$ with a complex gap function $\Delta(\omega, T)$.

The equivalent expression to equation (5.18) in Eliashberg theory is

$$R_s/R_n = 2\int_0^{\infty}[\frac{-df}{d\omega}][N_s^2(\omega)+M_s^2(\omega)]d\omega \ . \qquad (5.19)$$

For this equation, we have neglected the energy difference due to $\hbar\omega_{nuc}$ and this results in the derivative of the Fermi function appearing. Here, the BCS density of states is replaced by

$$N_s(\omega) = \mathrm{Re}[\frac{\omega}{\sqrt{\omega^2 - \Delta^2(\omega,T)}}] \,, \tag{5.20}$$

which was previously encountered back in chapter 2. Recall, we used this earlier in the Yosida function, equation (5.12). The additional factor $M_s(\omega)$ is the so called "anomalous" density of states and arises from the coherence factor:

$$M_s(\omega) = \mathrm{Re}[\frac{\Delta(\omega,T)}{\sqrt{\omega^2 - \Delta^2(\omega,T)}}] \,. \tag{5.21}$$

This Eliashberg equation can be obtained by essentially just replacing the BCS terms of equation (5.18) with their Eliashberg counterparts. To derive this equation formally, one has to evaluate a spin-spin correlation function using Green's function techniques but in the end of course the result is just the same.

So in order to calculate R_s/R_n, one requires the calculation of complex gap function $\Delta(\omega,T)$, which as explained earlier was up until recently a rather formidable task. Fibich[137] tried to get around this by deriving an approximate formula which replaced the full gap function by its value at the "branch point":

$$\Delta_1(T) = \mathrm{Re}\{\Delta(\omega = \Delta_1(T),T)\} \,, \tag{5.22}$$

$$\Delta_2(T) = \mathrm{Im}\{\Delta(\omega = \Delta_1(T),T)\} \,. \tag{5.23}$$

It should be noted that equation (5.22) is simply a restatement of how the gap edge is defined in Eliashberg theory. Substituting these in for the real

and imaginary parts of the gap function, Fibich was able to obtain the result:

$$R_s/R_n = 2f(\Delta_1)[1 + \frac{\Delta_1(T)}{2k_BT}[1 - f(\Delta_1)]\ln(\frac{4\Delta_1(T)}{|\Delta_2(T)|}) \ . \qquad (5.24)$$

5.3 STRONG COUPLING RESULTS

In this section, we study the normalized nuclear spin relaxation rate R_s/R_n and the Yosida Function $Y(T)$ as calculated using the formulas given by equations (5.19) and (5.12). for different values of the strong coupling parameter T_c/ω_{ln}. Noting that choice of $\alpha^2F(\omega)$ should have little qualitative effect on our results, we chose to do the bulk of our calculations with one spectrum, the $\alpha^2F(\omega)$ of Pb. The scaling techniques used in the previous two chapters to obtain different values of T_c/ω_{ln} were also employed here. Since the effects of strong coupling was what we were primarily interested in at this point, we have for simplicity set the coulomb pseudopotential μ^* equal to zero. It should be noted that results along the same lines as those shown in this section for the nuclear spin relaxation have also been obtained by Allen and Rainer[138].

In Fig. 5.1, we show results for R_s/R_n as a function of reduced temperature T/T_c for several different values of T_c/ω_{ln}, namely 0.05, 0.1, 0.15, 0.2 and 0.3. For the first curve, which applies for $T_c/\omega_{ln} = 0.05$, we see a well developed Hebel-Slichter peak at about $T/T_c \sim 0.8$ with a value of about ~ 3.0. Now this value of T_c/ω_{ln} is fairly close to the BCS weak coupling limit. If one were to use the BCS formula including the nuclear resonance frequency, $\hbar\omega_{nuc}$, one would obtain a peak that would be about an order of magnitude larger. As the coupling strength is increased, we see, from the progression of curves, that the size of the peak is reduced. When we reach the final curve

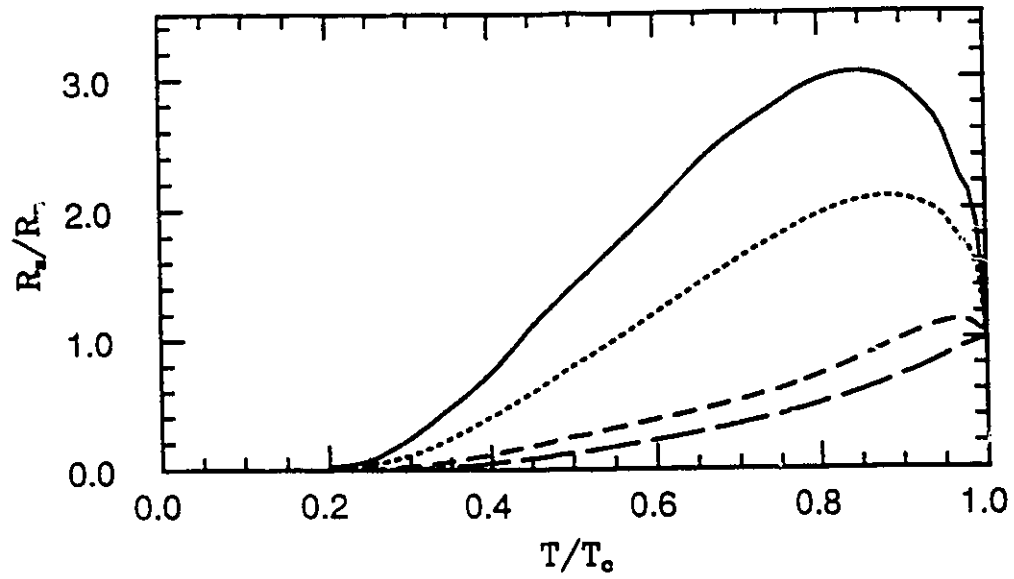

Figure 5.1 R_s/R_n is plotted as a function of reduced T/T_c for the following values of T_c/ω_{ln}: 0.05 (solid line) , 0.1 (dotted) , 0.15 (short dashed) , 0.2 (long dashed) and 0.3 (dash-dotted).

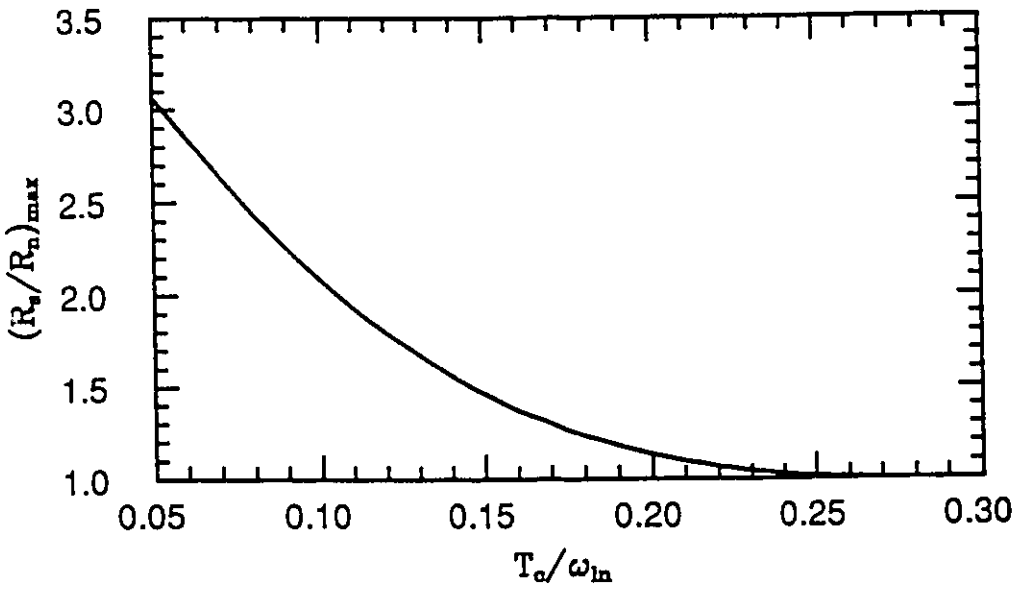

Figure 5.2 $(R_s/R_n)_{max}$ is plotted as a function of T_c/ω_{ln}.

for $T_c/\omega_{ln} = 0.3$ the peak vanishes. Another feature to notice is the position of the peaks. The position of the peaks appears closer and closer to T_c as we go from the $T_c/\omega_{ln} = 0.05$ curve to the $T_c/\omega_{ln} = 0.20$ curve, the final curve that shows a peak. Also noteworthy is the low temperature behavior. The $T_c/\omega_{ln} = 0.05$ curve rises rapidly beyond $T/T_c = 0.2$. When we reach the $T_c/\omega_{ln} = 0.3$ curve, the rise is much less dramatic. In this case, $R_s/R_n < 0.1$ even up to $T/T_c \simeq 0.75$.

In Fig. 5.2, we show results for the peak in R_s/R_n, namely $(R_s/R_n)_{max}$, as a function of T_c/ω_{ln}. It is quite apparent that the value of $(R_s/R_n)_{max}$ drops off quite rapidly with coupling strength. Note that the curve is started at $T_c/\omega_{ln} = 0.05$. Numerically, it was difficult to get results much lower in coupling strength than this. This is not surprising since the curve should diverge logarithmically as $T_c/\omega_{ln} \to 0$, the BCS limit. It is noteworthy that $(R_n/R_s)_{max}$ has already almost reached a value of one at $T_c/\omega_{ln} \sim 0.25$. There are conventional superconductors for which Eliashberg theory is known to apply that are in this range of T_c/ω_{ln}.

In Fig. 5.3, we show R_s/R_n results for two systems. The solid curve is for a system with $T_c/\omega_{ln} = 0.24$, amorphous Ga. For the purposes of this calculation we have used the $\alpha^2F(\omega)$ of Ga calculated by Chen *et al.* [139]. This material has a $T_c = 8.56K$ and a coulomb pseudopotential of $\mu^* = 0.174$ for a cutoff of 162 meV. As expected from the results of the previous figure, the Hebel-Slichter peak has almost been completely eliminated. This is an interesting result since it has been generally thought that electron-phonon superconductors should have this peak in their nuclear spin relaxation rates and that its absence might represent the possibility that some other more exotic mechanism may be responsible for the superconductivity. Clearly, this

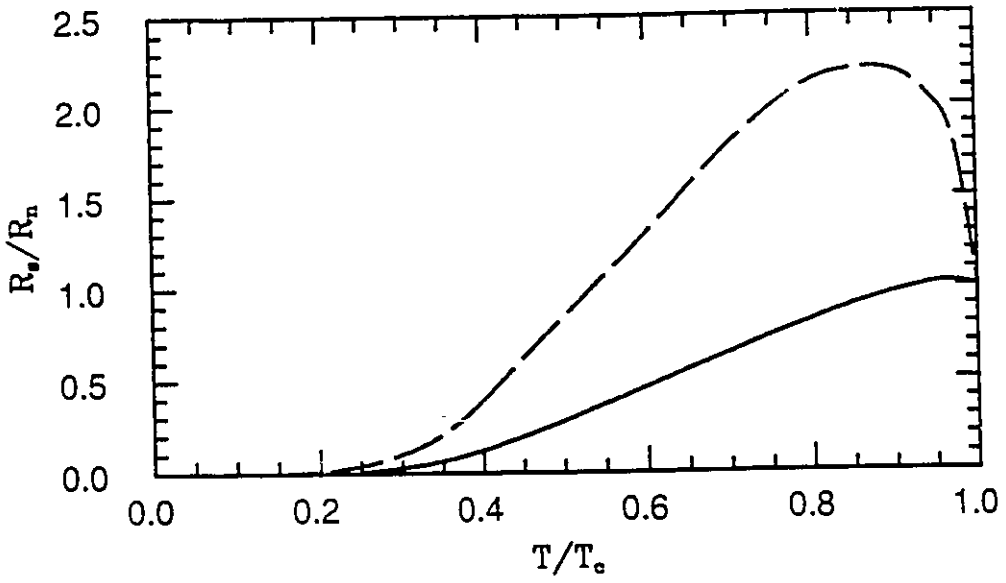

Figure 5.3 R_s/R_n is plotted as a function of reduced T/T_c for the materials amorphous Ga (solid line) and V_3Si (dashed).

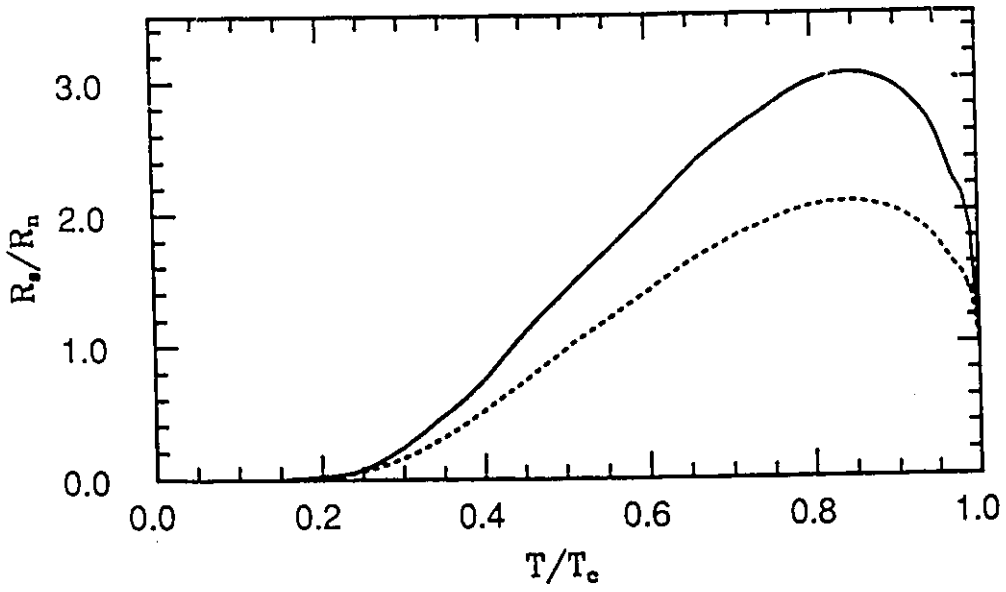

Figure 5.4 R_s/R_n is again plotted as a function of reduced T/T_c . The solid line represents the results from the full calculation using a Pb spectrum with $T_c/\omega_{ln} = 0.05$. The dotted line corresponds to results obtained by using the Fibich formula given in equation (3.24).

is not neccessarily the case. This result could be tested experimentally. The dashed curve is for V_3Si. This material is relatively weak coupling having $T_c/\omega_{ln} = 0.07$. For the $\alpha^2F(\omega)$ calculated by Killstrom[140] for this material, $T_c = 16.36K$ and $\mu^*(267\text{meV}) = 0.139$. The fact that this curve shows a significant peak is no surprise considering the weak coupling nature of this material. What is mildly surprising is that the peak is not higher. Reading off of Fig. 5.2, one finds for $T_c/\omega_{ln} = 0.07$ that $(R_s/R_n)_{max} \sim 2.7$ which is about 20 percent higher than what we see for the actual peak in V_3Si. Again, it should be emphasised that all the calculations in the first two figures were done with a Pb spectral shape. What this indicates is that the actual spectral shape $\alpha^2F(\omega)$ is probably important in determining the quantitative results. However, the qualitative trend, $(R_s/R_n)_{max}$ with T_c/ω_{ln}, which what we are most interested in, still holds. Another detail worth noting is that the calculations for V_3Si and Ga were both done with finite μ^*, whereas the results of the first two figures have $\mu^* = 0.0$.

In Fig. 5.4, we compare the results of the Fibich formula of equation (3.24) with the results of the full calculation. The solid curve applies for $T_c/\omega_{ln} = 0.05$ and is the same curve shown in Fig. 5.1 for that case. The dashed curve is the Fibich result for the same case. It is clear that the Fibich formula over estimates the effect of electron-phonon damping and cannot be used to get quantitative results as it predicts for this case a peak of just above two rather than the true value for this case which is about three. The truth of this dicovery seems to have been noticed previously by Scalipino[32]. This is somewhat unfortunate as the results of the full calculations shown here were quite time consuming to obtain numerically.

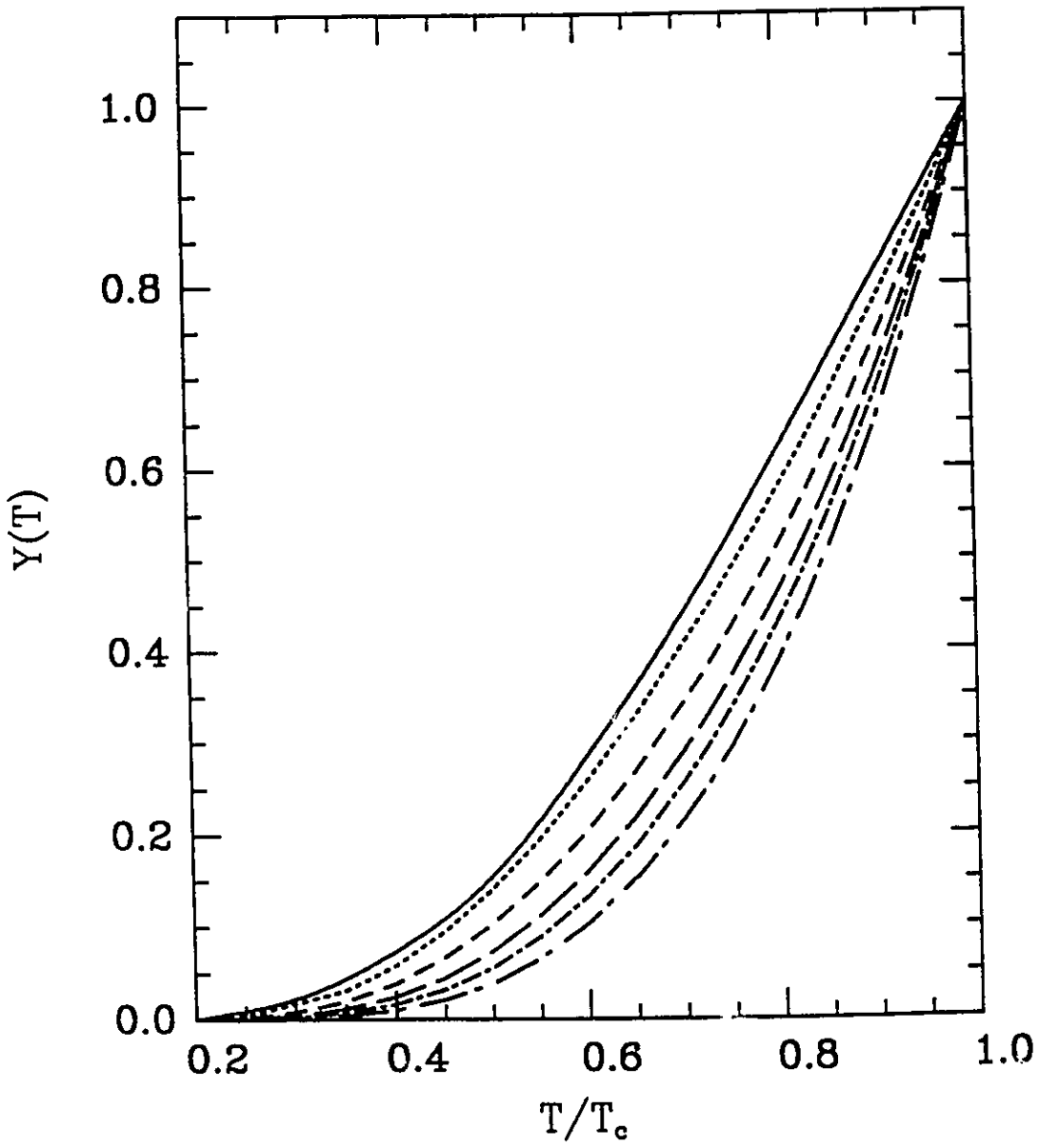

Figure 5.5 $Y(T)$ is plotted as a function of reduced T/T_c for the following values of T_c/ω_{ln}: BCS (solid line) , 0.05 (dotted) , 0.10 (short dashed) , 0.15 (long dashed) , 0.2 (short-dash-dotted) and 0.3 (long dash-dotted).

In Fig. 5.5, we show the Yosida function $Y(T)$ as a function of T/T_c for T_c/ω_{ln}=0.05, 0.1, 0.15, 0.2 and 0.3 as well as the BCS result. All the curves show the same basic behavior starting at one at T_c and the decreasing monotonically to zero as the temperature is reduced. The noticable trend here is that as the coupling strength is increased, the curves fall lower and lower below the BCS curve and approach zero more quickly.

5.4 APPROXIMATE INCLUSION OF ANISOTROPY

As mentioned earlier, anisotropy in the gap function is another mechanism for reducing the Hebel-Slichter peak. It's potential importance in conventional superconductors has long been recognized. Indeed, the sort of calculations outlined in the previous section only apply exactly to conventional superconductors in the dirty limit where any anisotropy is washed out by impurity scattering[141,142]. However, the level of anisotropy one usually sees in a conventional material is probably not large enough to cause any profound change in the nuclear relaxation rate. One can define a parameter a_k which represents the deviation of the gap function from it's Fermi surface average. Experiments on Al have yielded a variation of ± 0.1 in a_k over the Fermi surface[143] and a corresponding mean square anisotropy of $< a_k^2 >= 0.011$[144]. Daams[142] worked on theoretical models where the typical mean square anisotropy used was of the order of $< a_k^2 >= 0.04$.

The influence of anisotropy in the high-T_c oxides is another story entirely. These materials for the most part are highly anisotropic. As discussed

in the introduction, the superconductivity in a material such as YBCO appears to be strongly tied to the Cu-O sheets that occur within it. Not surprisingly, there has been much effort trying to incorporate the planar nature of the oxides into various theoretical models.

Thus, in order to make a better connection with the oxides, an examination of the influence of anisotropy on NMR would seem to be required. In order to do this, we follow a prescription along the lines of that proposed by Schneider *et al.* [145] and by Statt[146,147]. That is, we consider a gap function that has the form:

$$\Delta(k_z, \omega, T) = \Delta_i(\omega, T)[1 + \alpha \cos(k_z a)] \tag{5.25}$$

where k_z is the momentum perpendicular to the plane and a is the lattice parameter in this same direction, Δ_i refers to the gap function as determined by the isotropic Eliashberg equations and α is the parameter that characterizes the anisotropy. So the basic form of the gap function in this case is to have two components: one isotropic and the other anisotropic with a cosine dependence. Note that with this form, the gap function has the desired property that it is a maximum in the plane and decreases as we rotate out of the plane. However,this is at best an approximation. While the gap function may indeed have this type of form, in order to do this problem exactly it has to be incorporated into the the Eliashberg equations right from the beginning and not as an afterthought as we have done here. Extensive work has been done on a set anisotropic Eliashberg equations that been derived with this form[132,148]. More comments shall be made about this later.

It turns out to be a simple task to modify the formulas for the Yosida function and the nuclear spin relaxation in order to accommodate

the anisotropy. Following the example of Clem[141], one simply takes the momentum average of the density of states and the anomalous density of states. In other words, all that is required is to use

$$N_s(\omega) = \frac{a}{\pi}\int_0^{\pi/a} dk_z \mathrm{Re}[\frac{\omega}{\sqrt{\omega^2 - \Delta^2(k_z,\omega,T)}}] \tag{5.26}$$

and

$$M_s(\omega) = \frac{a}{\pi}\int_0^{\pi/a} dk_z \mathrm{Re}[\frac{\Delta(k_z,\omega,T)}{\sqrt{\omega^2 - \Delta^2(k_z,\omega,T)}}] \tag{5.27}$$

instead of the isotropic expressions given by equations (3.20) and (3.21) in the formulas for $Y(T)$ and R_s/R_n.

In Fig. 5.6. having fixed ourselves at a relatively weak coupling $T_c/\omega_{ln} = 0.1$, we plot R_s/R_n as a function of T/T_c for four different values of α: 0.0,0.2,0.5 and 0.8. The case where $\alpha = 0.8$ is highly anisotropic. Indeed, $\alpha = 1.0$ would represent a case where the gap would actually hit zero at certain points on the Fermi surface. At the higher end of the temperature scale,there are two effects to notice. These are that the Hebel-Slichter peak is diminished as we increase α and that it also shifts closer to T_c. We observed both these effects previously when we were considering the influence of coupling strength by itself in the previous section. So it appears that in this temperature range at least that it might be difficult to distinguish between damping effects and the effect of anisotropy. The lower temperature range is a different story. Here, the curves actually cross and the one with the highest anisotropy is well above the others at $T/T_c \sim 0.2$. Now it was mentioned earlier that for this quantity one expects an exponential decay at lower temperatures. This type of behaviour seems to be postponed to temperatures lower than are depicted here, particularly for $\alpha = 0.8$. It should be

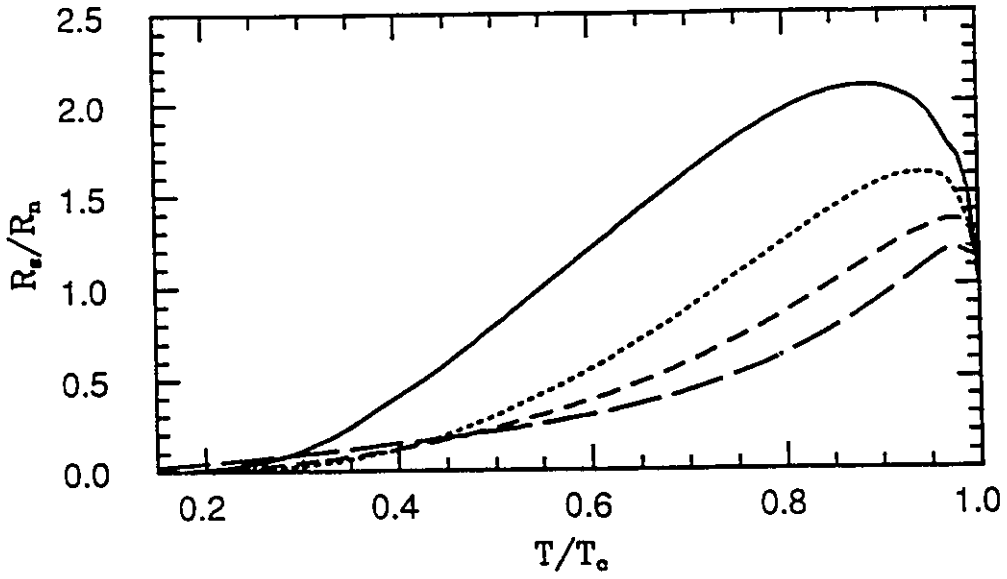

Figure 5.6 R_s/R_n is plotted as a function of reduced T/T_c for the following values of α: 0.0 (solid line) , 0.2 (dotted) , 0.5 (short dashed) and 0.8 (long dashed). T_c/ω_{ln} has been fixed at 0.1.

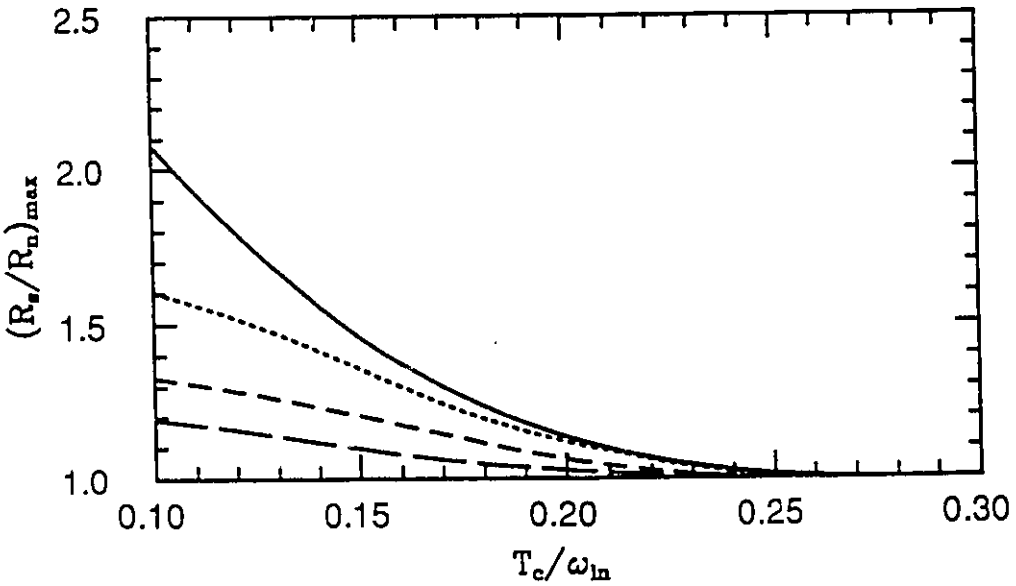

Figure 5.7 $(R_s/R_n)_{max}$ is plotted as a function of T_c/ω_{ln} for the following values of α: 0.0 (solid line) , 0.2 (dotted) , 0.5 (short dashed) and 0.8 (long dashed).

noted that when $\alpha = 1.0$, so that the gap has zeroes on the Fermi surface, one expects the exponential law to be replaced by a power law of some sort[126].

In Fig. 5.7, we show the important effect that introducing anisotropy has on the Hebel-Slichter peak by plotting $(R_s/R_n)_{max}$, as a function of T_c/ω_{ln} for several different values of the anisotropy parameter α. Note that the curves begin at $T_c/\omega_{ln} = 0.1$. Again, this represents a relatively weak coupling regime. It is evident that in this regime that anisotropy has a strong effect on the value of the peak. This can be illustrated by simply noticing that the curve for $\alpha = 0.2$ begins about 25 percent lower than the curve with no anisotropy at all. The conclusion one can draw from this that in this regime that the inclusion of anisotropy is probably very important if one wants accurate quantitative results. However, while the peaks are significantly reduced as we increase α in this region, the value of $(R_s/R_n)_{max}$ is still significantly above one even for $\alpha = 0.8$. This seems to imply that anisotropy by itself will reduce the Hebel-Slichter peak but not eliminate completely. This is a very important point. In the stronger coupling range the difference between the isotropic and anisotropic is much less significant as the peak is already being eliminated by damping effects. It is also evident from this figure that the value of T_c/ω_{ln} for which the peak is eliminated does not really change that much even when the anisotropy is included.

In Fig. 5.8, we again fix ourselves at $T_c/\omega_{ln} = 0.1$, but in this case we plot the Yosida function vs. T/T_c for four different values of α: 0.0, 0.2, 0.5 and 0.8. Near T_c, anisotropy has very little effect on $Y(T)$ except to reduce it slightly. However, the curves start crossing over at $T/T_c \simeq 0.8$ and we see at lower temperatures that anisotropy can lead to much larger values of $Y(T)$. This reminiscent to the effect we saw on R_s/R_n in Fig. 5.6, but it is even more

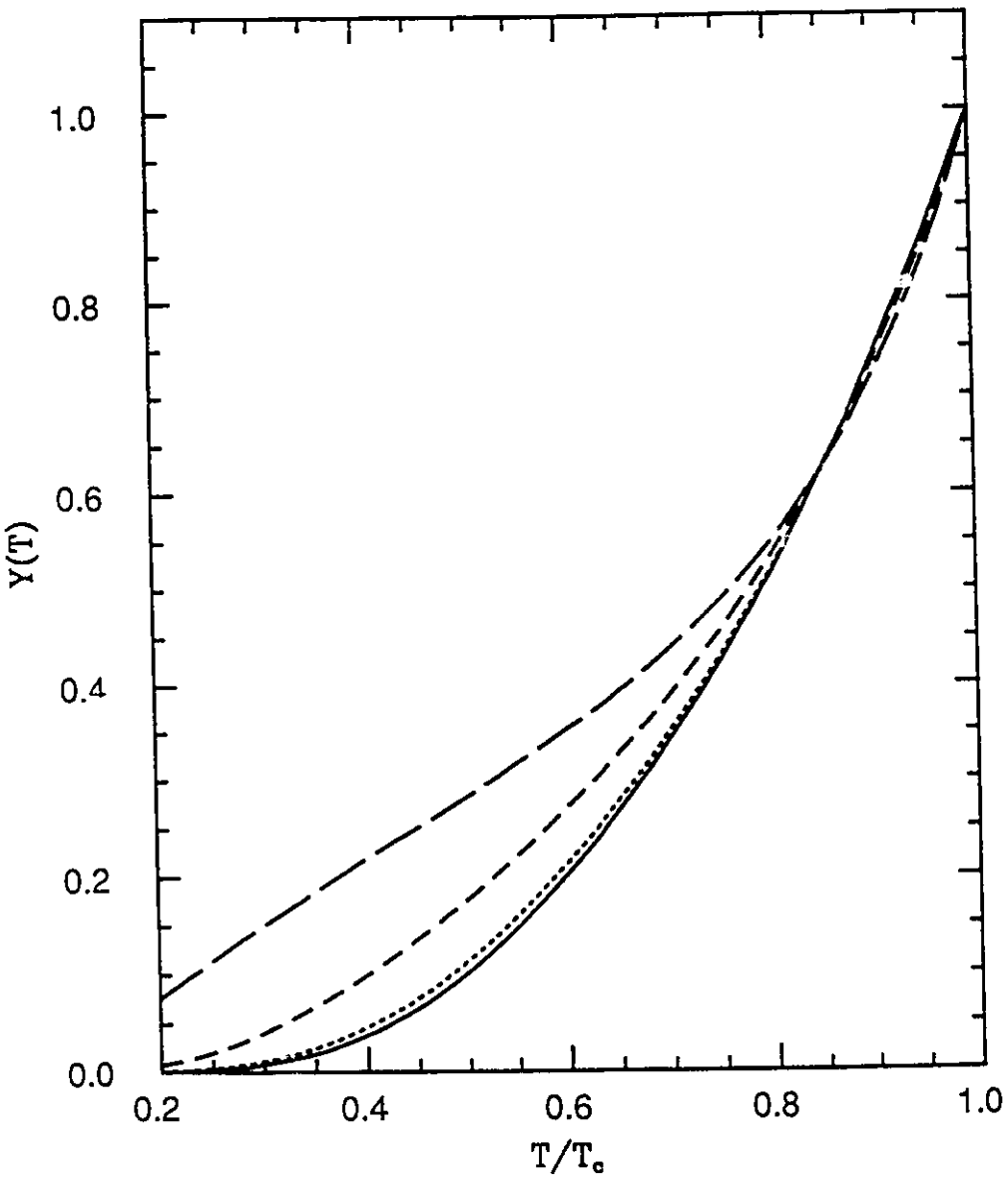

Figure 5.8 $Y(T)$ is plotted as a function of reduced T/T_c for the following values of α: 0.0 (solid line) , 0.2 (dotted) , 0.5 (short dashed) and 0.8 (long dashed). T_c/ω_{ln} has been fixed at 0.1.

dramatic here. As will be outlined in the next section, this effect will play an important role in interpreting experimental results when we consider the addition of Fermi liquid corrections on top of strong coupling and anisotropy.

We close this section by commenting on the validity of the anisotropy ansatz we have used here. As mentioned earlier, a set of anisotropic Eliashberg equations that correspond to the type of anisotropy we have here have been derived. These equations were used to obtain what are essentially exact results for R_s/R_n. In comparing the exact results with the results obtained with the ansatz used here, it was discovered that the agreement was good but not perfect in the temperature range considered[132]. More results have been produced using the full anisotropic Eliashberg equations as time has gone on[148].

5.5 FERMI LIQUID CORRECTIONS AND EXPERIMENTAL COMPARISON

Experiments on the high T_c oxides have shown evidence that the Hebel-Slichter peak may be absent in these materials[149,150]. An exception to this *may* be LSCO. An early experiment on this material by Seidal *et al.* [151,152] did show a peak and exponential behavior at low temperatures. Unfortunately, the experimenters found that, to fit the low temperature data, a gap corresponding to $2\Delta_o/k_BT_c = 7.1$ was required. This would indicate a coupling strength of $T_c/\omega_{ln} \sim 0.6$[38,43], well beyond the point where one would still expect to see a peak. The possible absence of the coherence peak in the oxides was the main encouragement for the work that has been presented here. As we have seen previously, the peak in R_s/R_n can be reduced by strong coupling effects and anisotropy. However, in order to do a true comparison

with experiment, one must also take into account the fact that not only does the nuclear spin relaxation rate in the superconducting state deviate from what one usually sees in conventional materials, the normal state apparently does as well. In the case of YBCO it has been found that the spin relaxation of the Cu nuclei that lie in the planes is anomalously large when compared to what one expects from the band structure in the temperature region just above T_c[150,130]. It has also been determined that the relaxation rate is only weakly temperature dependent and only rises by about 50 percent in the region between 100 K and 300 K.

In order to take these differences into account, we have followed the proposal put forth by Monien and Pines[130]. They suggest that antiferromagnetic coupling between quasiparticles accounts for this anomalous behavior. When there are spin-spin correlations between electrons, one finds that the magnetic susceptibility of the electrons becomes modified. By using mean field theory, one finds that this modification takes the form :

$$\chi = \frac{\chi_o}{1 - \beta\chi_o} \tag{5.28}$$

where χ_o is the susceptibility in the absence of correlations and the factor $\beta = N(0)J_{eff}$ involves the quasiparticle density of states at the Fermi energy and the effective antiferromagnetic coupling. Monien and Pines have determined that this modification in the susceptibility of the electrons leads in turn to a modification of the nuclear spin relaxation rate $R = 1/T_1$:

$$R = \frac{1}{T_1} = \frac{1}{(T_1)_o}\frac{1}{[1 - \lambda(T)]^2} \tag{5.29}$$

where $\lambda(T) =< N(0)J_{eff}Re\{\chi_o\} >$ is an average temperature dependent enhancement factor. Taking this modification into the superconducting state,

one finds that the corrected normalized superconducting relaxation rate now involves the Yosida function :

$$R_s/R_n = (R_s/R_n)_o[1 - \lambda(T_c)]^2/[1 - \lambda(T_c)Y(T)]^2 \tag{5.30}$$

where $(R_s/R_n)_o$ takes into account the strong coupling and anisotropic effects discussed previously and note here that, for simplicity, $\lambda(T)$ at T_c is used.

Before comparing with experiment, it is prudent to see just what sort of effects that incorporating these antiferromagnetic corrections generally have. In Fig. 5.9, we display we plot R_s/R_n against T/T_c for several different values of $\lambda(T_c)$, namely 0.0, 0.3, 0.5, 0.7 and 0.9. In this case, we have set $T_c/\omega_{ln} = 0.1$ and neglected anisotropy. It is apparent that these corrections tend to damp out the Hebel-Slichter peak. So we have yet another mechanism for doing this. However, there are some significant differences from what we have previously encountered. As we increase $\lambda(T_c)$, one notes that the peaks sharpen quite noticeably and tend to fall off rapidly. Indeed, the curve for $\lambda(T_c) = 0.9$ is already below $R_s/R_n = 0.1$ for $T/T_c = 0.8$.

In Fig. 5.10, we plot $(R_s/R_n)_{max}$ vs. T_c/ω_{ln} for $\lambda(T_c) = 0.0, 0.15, 0.3$ and 0.5. As from the previous figure, it is evident that these corrections reduce the peak height. Unlike the anisotropic case, however, the effect of these corrections has an important influence on how much strong coupling is required to remove the Hebel-Slichter peak completely. In the case with no corrections, the peak dissappears for $T_c/\omega_{ln} \sim 0.27$. For $\lambda(T_c) = 0.5$, this is reduced to $T_c/\omega_{ln} \sim 0.20$.

In Fig. 5.11, we see how having both antiferromagnetic corrections and anisotropy affects R_s/R_n. Here we plot R_s/R_n vs. T/T_c for $T_c/\omega_{ln} = 0.1$

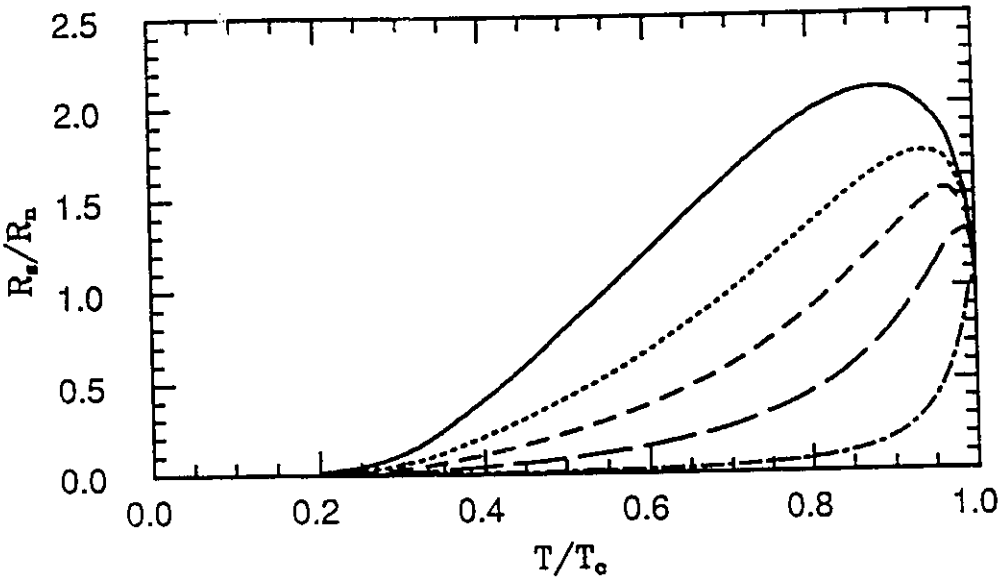

Figure 5.9 R_s/R_n is plotted as a function of reduced T/T_c for the following values of $\lambda(T_c)$: 0.0 (solid line) , 0.3 (dotted) , 0.5 (short dashed) , 0.7 (long dashed) and 0.9 (dash-dotted). T_c/ω_{ln} has been fixed at 0.1 and there is no anisotropy.

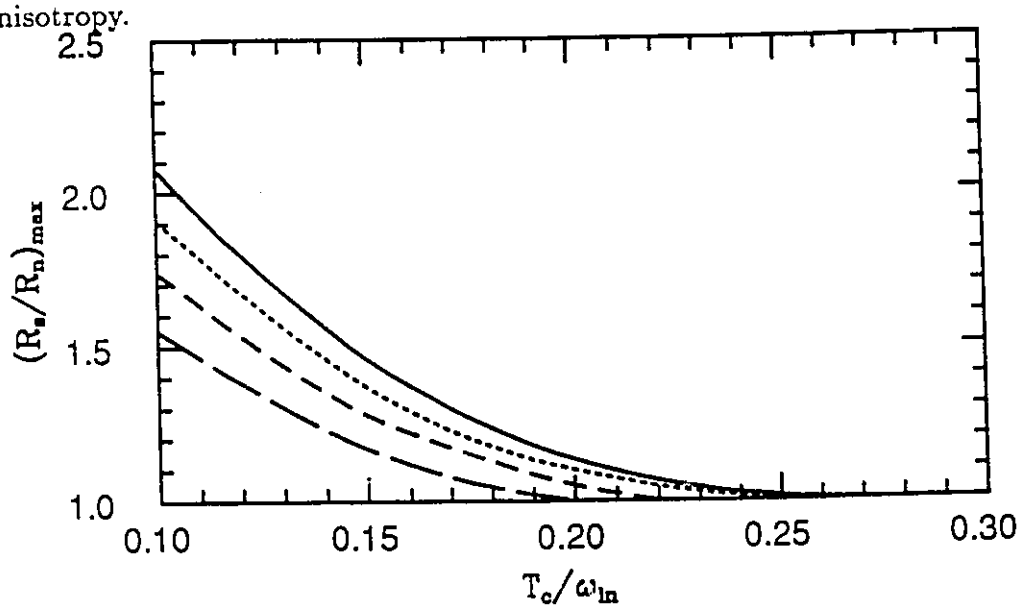

Figure 5.10 $(R_s/R_n)_{max}$ is plotted as a function of T_c/ω_{ln} for the following values of $\lambda(T_c)$: 0.0 (solid line) , 0.15 (dotted) , 0.3 (short dashed) and 0.5 (long dashed).

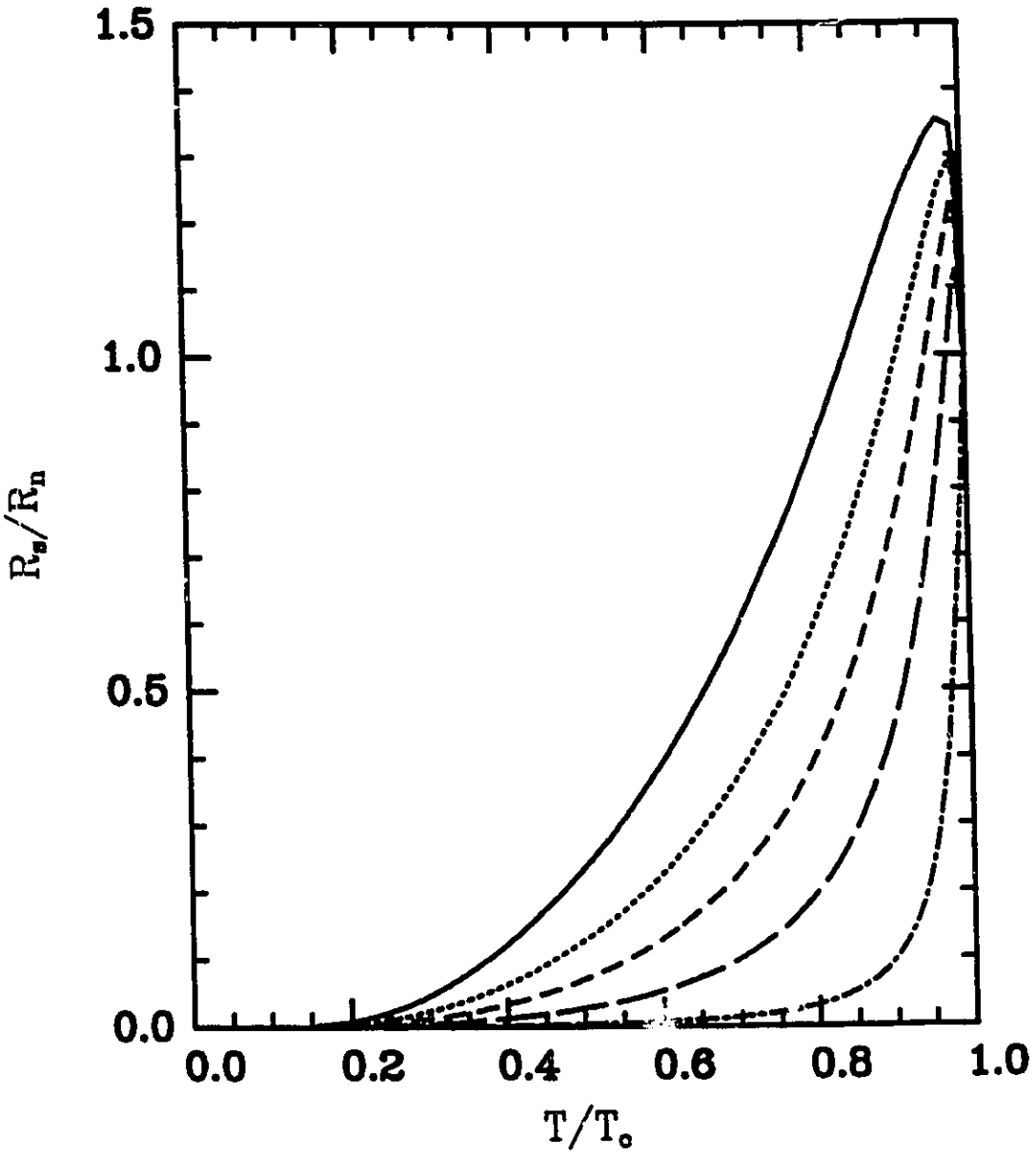

Figure 5.11 R_s/R_n is plotted as a function of reduced T/T_c for the following values of $\lambda(T_c)$: 0.0 (solid line) , 0.3 (dotted) , 0.5 (short dashed) , 0.7 (long dashed) and 0.9 (dash-dotted). T_c/ω_{ln} has again been fixed at 0.1 but this time the anisotropy factor is $\alpha = 0.5$.

and the anisotropy factor $\alpha = 0.5$. We use the same $\lambda(T_c)$'s as in Fig. 5.9. We notice in this case that the combination of anisotropy and antiferromagnetic corrections causes the curves to sharpen even more than they were in Fig. 5.9 and reduces their height. This suggests the possibility that even if there was a Hebel-Slichter peak, it might be somewhat difficult to observe experimentally. Not surprisingly, the curves drop even more rapidly than they do in Fig. 5.9 and, particularly for the case where $\lambda(T_c) = 0.9$, appear to behave almost as if they were hyperbolic.

So, now in fitting experimental data, we have three things we can vary: electron-boson coupling strength, anisotropy and antiferromagnetic corrections. If one were just interested in reducing the Hebel-Slichter peak, one of these factors would be sufficient. However, here we are concerned with the entire temperature range and fortunately these three factors cause somewhat different behavior at the lower temperature range. Another important detail is that whatever parameters we use to fit the nuclear spin relaxation rate should also be able to fit the Yosida function.

In what follows, it should be emphasized that no exhaustive search in parameter space was undertaken. The most appropriate data from that amassed for the previous sections was selected. Almost certainly one could get better fits than what we obtain here but this would be an extremely time consuming task. It should also be mentioned that Monien and Pines have also tried fitting to experimental data, but with anisotropic models that are somewhat different than that depicted here. Statt also did some experimental comparison but did not include any antiferromagnetic corrections and included strong coupling effects only in an approximate way.

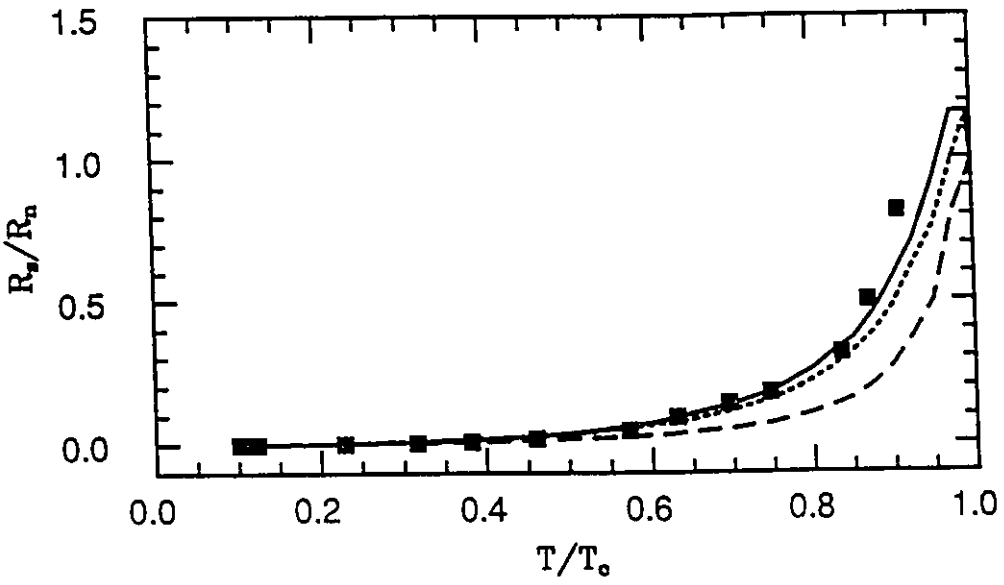

Figure 5.12 R_s/R_n is plotted as a function of reduced T/T_c. The curves correspond to $\alpha = 0.7$ and $\lambda(T_c) = 0.7$ (solid line), $\alpha = 0.65$ and $\lambda(T_c) = 0.7$ (dotted) and $\alpha = 0.8$ and $\lambda(T_c) = 0.8$ (dashed). T_c/ω_{ln} has been fixed at 0.05 for all three cases. The squares represent the data of Barrett *et al.* .

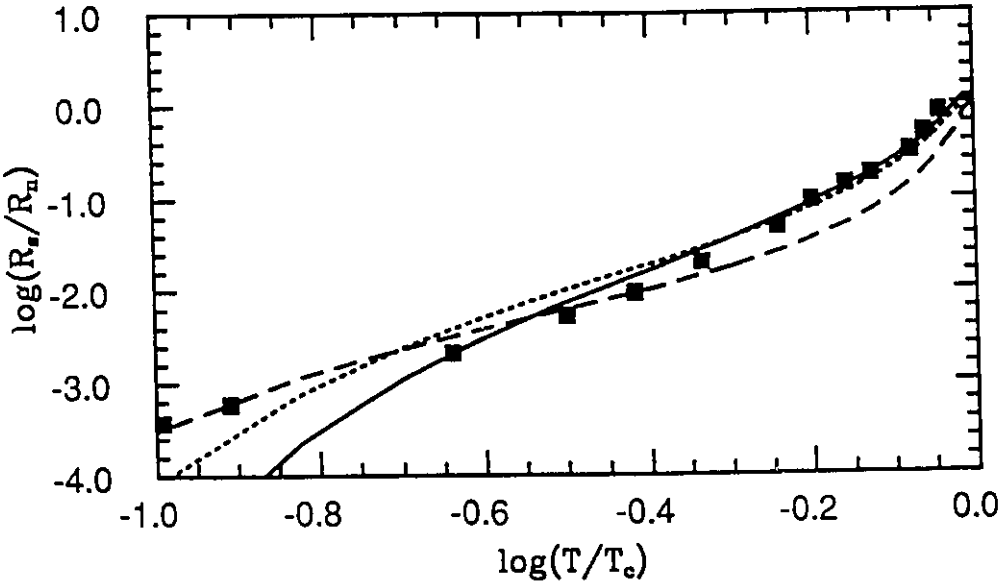

Figure 5.13 As in Fig. 12 but now a log-log plot of R_s/R_n is displayed.

In Fig. 5.12, we show our best results for the nuclear spin relaxation rate R_s/R_n. The solid squares depict the experimental data of Barrett *et al.* . For our fits, we have included strong coupling, anisotropy and antiferromagnetic corrections. For all three curves displayed, $T_c/\omega_{ln} = 0.05$ which is rather weak coupling. It was discovered that increasing the coupling decreased the quality of the fit over the entire temperature range. This is contrary to a conclusion drawn by Monien and Pines. The three curves shown correspond to $\alpha = 0.7$ and $\lambda(T_c) = 0.7$ (solid line), $\alpha = 0.65$ and $\lambda(T_c) = 0.7$ (dotted line) and $\alpha = 0.8$ and $\lambda(T_c) = 0.8$ (dashed line). From this figure, at higher temperatures it appears that the case where $\alpha = 0.7$ and $\lambda(T_c) = 0.7$ fits the data fairly well. The other two cases fall further off, particularly where $\alpha = 0.8$ and $\lambda(T_c) = 0.8$

In Fig. 5.13, we show the same data but now we display things on a logarithmic scale which tends to show the lower temperature range much better. From this plot, it is evident that the fit that seemed to work well in the previous figure does a poor job of accounting for the low temperature data . However, the curve for $\alpha = 0.8$ and $\lambda(T_c) = 0.8$ which did not seem to fit the data very well in the last figure, appears to fit the low temperature data extremely well. The case with $\alpha = 0.65$ and $\lambda = 0.7$ represents a compromise between these two extremes. At any rate, none of the three curves appear to fit the entire temperature range completely.

In Fig. 5.14, we plot the Yosida function against T/T_c. The solid circles are the experimental data for Takigawa *et al.* [153] and the open circles with error bars are from Barrett *et al.* . The curves are $T_c/\omega_{ln} = 0.05$ and α's of 0.5, 0.65 and 0.8. Here it is apparent that the data of Takigawa *et al.* can be fit fairly well by the case with $\alpha = 0.8$ for $T/T_c \leq 0.7$. In this range,

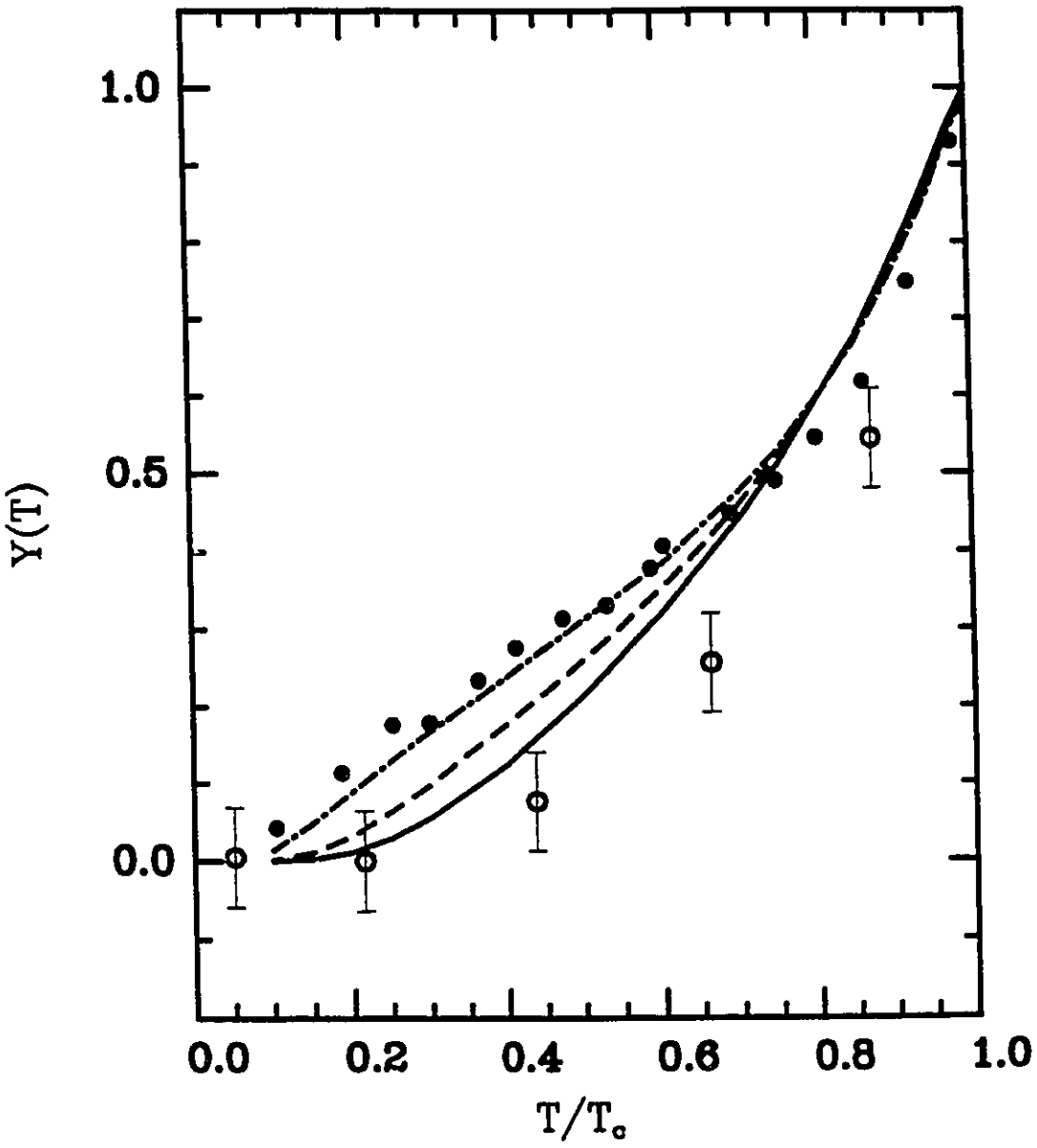

Figure 5.14 $Y(T)$ is plotted as a function of reduced T/T_c. The curves correspond to α = 0.5 (solid line), α = 0.65 (dotted), and α = 0.8 (dash-dotted). T_c/ω_{ln} has been fixed at 0.1 here. The open circles represent the data of Barrett *et al.* and the solid circles represent the data of Takigawa *et al.* .

this experimental data appears to have the same characteristic anisotropic behavior that we saw in the previous section. The behavior near T_c is problematic for all cases considered. As for the data of Barrett *et al.* , it appears that none of the choices we have considered here even come close to fitting it. If one refers back to Fig. 5.5, it appears that what is probably required for this data is to use a much stronger coupling model. However, as commented earlier, this would lead to poorer fits to R_s/R_n. It should be said that Monien and Pines fitted to the Yosida function and used this fit to then calculate R_s/R_n. We have essentially done the opposite : fit to R_s/R_n and worry about the Yosida function as an afterthought.

5.6 CONCLUSIONS

Perhaps the strongest conclusion that can be drawn from the results that have been displayed in this chapter is that the experimentally observed absence of a Hebel-Slichter peak in the normalized nuclear spin relaxation rate can not by itself be taken as evidence that one must appeal to a new theory of superconductivity and abandon strong-coupling Eliashberg theory. In fact, there should be some known Eliashberg superconductors that do not have such a peak. As we have outlined, there are a number of ways to dampen the Hebel-Slichter peak. However,these different mechanisms for damping out the peak, strong coupling, anisotropy and antiferromagnetic corrections, cause different effects on R_s/R_n at low temperature. Similarly for the Yosida function, it was found that strong coupling and anisotropy have essentially the opposite effect at low temperature with anisotropy increasing $Y(T)$ and strong coupling decreasing it.

We have attempted crude fits to the experimental data and discovered that it is somewhat difficult to fit the entire temperature range. However, the most significant qualitative feature in the data, a rapid drop in R_s/R_n below T_c, can easily be reproduced. The best fits to the data are consistent with a model that combines phonons with higher energy bosons such that the average boson frequency is such that $T_c/\omega_{ln} \simeq 0.05$ along with high anisotropy and antiferromagnetic corrections.

In closing this chapter, it should be mentioned that the nuclear spin relaxation rate has also been calculated in the context of the marginal Fermi-liquid model[154]. Interestingly, the lack of a coherence peak in this quantity is an immediate biproduct of this model with none of the additional factors such as anisotropy being necessary to produce this effect.

Chapter 6

The Conductivity

6.1 INTRODUCTION

In this chapter, strong coupling results are presented for the conductivity. The primary focus is on studying how the frequency dependent conductivity changes as a function of temperature. The real axis Eliashberg equations of Marsiglio, Schossmann and Carbotte[37,38] are utilized to aid in achieving this purpose.

After some background material is provided in the next section, the concern will be on a theoretical study of how well the superconducting gap can be tracked as a function of temperature by utilizing optical data. As will be shown, how easily the gap can be extracted depends strongly on the impurity concentration and on the coupling strength of the superconductor. It is important to note that, in this chapter and for the rest of this thesis, we consider only impurities that do not have a finite magnetic moment. These

theoretical results will be compared with some experimental papers on the oxides, where the authors have attempted to extract the superconducting gap from their data.

The next section of this chapter will deal with the conductivity in the very low frequency range. As was the case with the nuclear spin relaxation discussed in the previous chapter, one expects to see a coherence peak in the the real part of the conductivity in a weak to moderately coupling superconductor. This peak is studied as a function of coupling strength, frequency and impurity concentration. The results of some recent microwave experiments are also discussed.

The chapter closes with a brief conclusion.

6.2 BACKGROUND MATERIAL

Drude has provided a simple model by which the A.C. conductivity of a metal can be obtained. In this model all quantum effects are neglected and the electrons are treated as a classical gas. The electrons in the metal are then subject to two forces: 1) the force due to the applied electric field, $-eE$, where e is the electric charge, and 2) a viscous damping force which results from the relaxation of electrons towards equilibrium due to various elastic scattering processes. Solving the equation of motion for electrons subject to these forces eventially yields the following expression for the A.C. conductivity[155,156]:

$$\sigma(\omega) = \frac{\sigma_{D.C.}}{1 - i\omega\tau} . \tag{6.1}$$

In this formula, τ is the relaxation time. The reciprocal of this is the relaxation rate which is determined by the probability of collisions with such

things as impurities, τ_{imp}, and phonons, τ_{ph}, as well as numerous other scattering processes which shall be ignored here for the sake of simplicity. The net scattering rate is given by Matthiessen's rule :

$$1/\tau = 1/\tau_{imp} + 1/\tau_{ph} + \cdots . \tag{6.2}$$

The scattering rate due to impurities is generally independent of temperature. However, the phonons that contribute to the phonon scattering rate are created thermally so that $1/\tau_{ph}$ is directly tied to the temperature and vanishes for $T = 0$. The D.C. conductivity, $\sigma_{D.C}$ which appears in equation (6.1) is in turn given by

$$\sigma_{D.C.} = \frac{ne^2\tau}{m^*} , \tag{6.3}$$

where m^* is the effective mass of the electron, which includes band effects and electron-phonon renormalization, and n is the density of the electrons in the metal. A closely related quantity is the plasma frequency, ω_p, which is given by

$$\omega_p^2 = \frac{4\pi ne^2\tau}{m^*} . \tag{6.4}$$

For $\omega < \omega_p$, The applied electric field decays exponentially inside the metal while for $\omega > \omega_p$ the applied electric field can propagate through as the metal becomes transparent.

The A.C. conductivity given in equation (6.1) can be broken up into real and imaginary parts:

$$\sigma(\omega) = \sigma_1 + i\sigma_2 = \frac{\omega_p^2\tau/4\pi}{1+\omega^2\tau^2} + i\left(\frac{\omega\omega_p^2\tau^2/4\pi}{1+\omega^2\tau^2}\right) . \tag{6.5}$$

Note that the real part of the conductivity takes on a lorentzian form. This is the signature of Drude conductivity. It can be easily shown that $\sigma_1(\omega)$

satisfies the sum rule

$$\int_0^\infty d\omega \sigma_1(\omega) = \frac{\omega_p^2}{8} . \tag{6.6}$$

This sum rule is extremely important as it not only applies for the simple Drude model discussed here but generally as well.

The Drude model, crude as it is, is only strictly applicable in the low frequency and low temperature limits where elastic and quasielastic scattering processes dominate. At higher frequencies, additional inelastic processes play an important role as various types of excitations can be created. To deal with these, the Drude model can be modified by introducing frequency dependent scattering rates[156,28].

The most elementary theory for the conductivity of a superconductor was derived by London[157]. London's theory was an outgrowth of the two fluid model discussed in the context of the thermodynamic critical field in Chapter 4. In this model, a fraction $n_s(T)/n$ of the conduction electrons participate in the supercurrent below T_c. This supercurrent is given by the equation :

$$\mathrm{j}_s = -\frac{n_s e^2}{m^* c}\mathrm{A} , \tag{6.7}$$

where c is the speed of light and A is the vector potential which is related to the magnetic field B through $\mathrm{B} = \nabla \times \mathrm{A}$. A consequence of London's equation is the result that an applied B field will decay exponentially as it penetrates into the superconductor. The length scale for this decay is the London penetration depth,

$$\lambda_L = \left(\frac{m^* c^2}{4\pi n_s e^2}\right)^{\frac{1}{2}} = \frac{c}{\omega_{ps}} . \tag{6.8}$$

For $T = 0$ K, $n_s = n$ and so $\omega_{ps} = \omega_p$. The conductivity of a London model superconductor is given by

$$\sigma_1(\omega) = \frac{1}{8}\omega_{ps}^2\delta(\omega) \ , \tag{6.9}$$

which is essentially just equation (6.5) in the limit that $1/\tau \rightarrow 0$, which corresponds to there being no scattering events at all.

In the case of BCS theory, the situation becomes more complicated. This is particularly due to the presence the superconducting gap, Δ. Mattis and Bardeen calculated the frequency dependent conductivity in the BCS limit. Importantly, their theory applies for the dirty limit which can be defined through the expressions :

$$\frac{1}{\tau_{imp}} \gg 2\Delta \equiv l \ll \xi \ . \tag{6.10}$$

In the second expression above, l is the mean free path and ξ is the superconducting coherence distance. The equivalence between these two expressions holds because $1/\tau_{imp} = v_F/l$ and in BCS $\xi = v_F/\pi\Delta$, where v_F is the Fermi velocity. In Mattis-Bardeen theory, the delta function in the conductivity at the origin is retained. However, for frequencies above 2Δ, Cooper pairs can be broken and these excited electrons can then subsequently scatter off impurities. The result is that an absorption feature is observed rising rapidly beginning right at 2Δ. To illustrate this, the Mattis-Bardeen result for $T = 0$ is plotted in Fig. 6.1. Note what is actually plotted is $\sigma_1(\omega)/\sigma_N$ vs. $\omega/2\Delta_o$. In the dirty limit, the normal state conductivity σ_N is virtually constant. Since we are at zero temperature, $\int d\omega\sigma_1(\omega) = \int d\omega\sigma_N(\omega) = \omega_p^2/8$. Given this conservation of area, it follows that the area between the Mattis-Bardeen curve illustrated and the line for $\sigma_1(\omega)/\sigma_N = 1$, which is also illustrated, must go

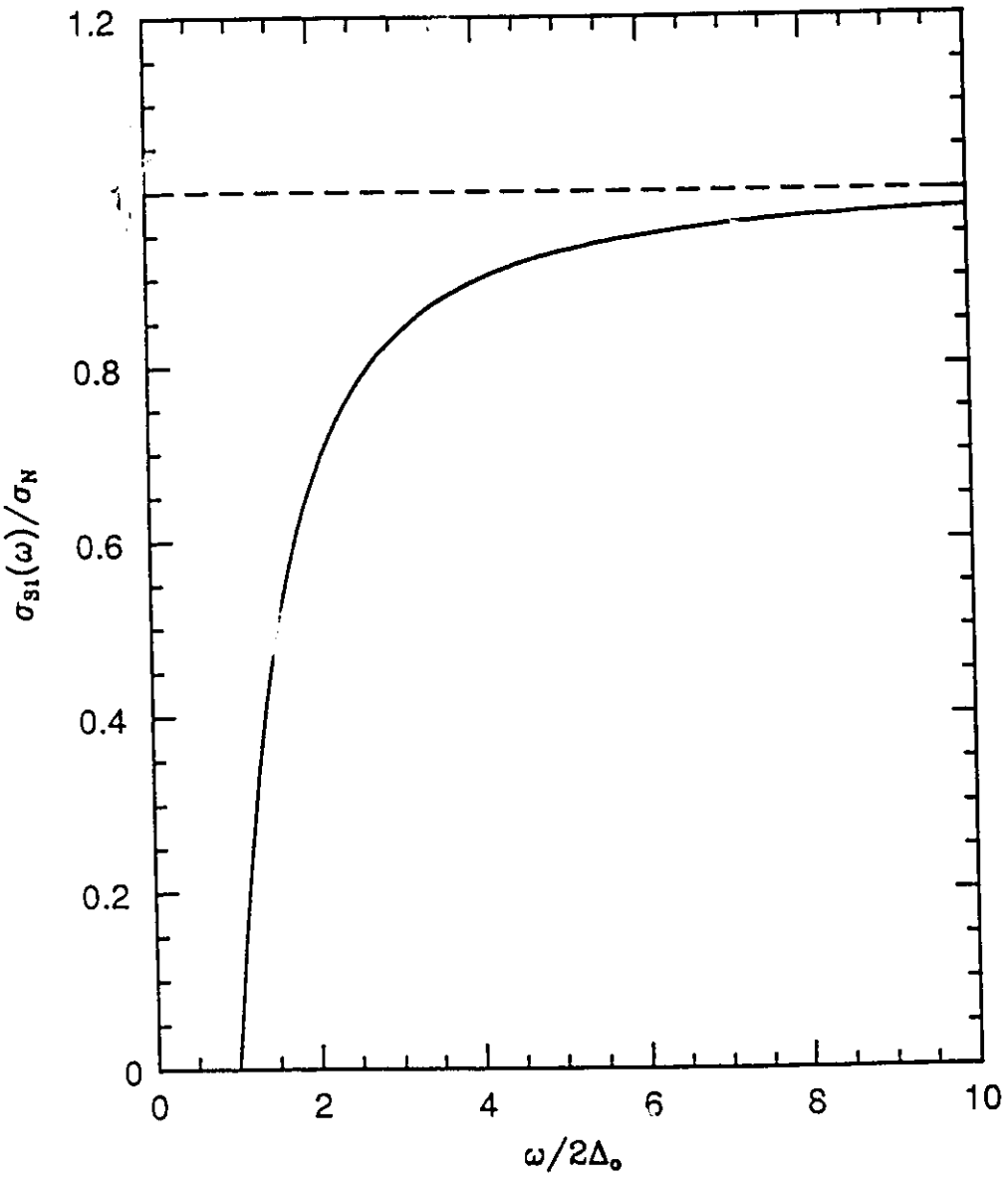

Figure 6.1 $\sigma_1(\omega)/\sigma_N$ is plotted vs. $\omega/2\Delta_o$ according to the prescription of Mattis and Bardeen[158], which applies for the BCS dirty limit. The dashed line represents $\sigma_1(\omega)/\sigma_N = 1$.

into the delta function at the origin. One conclusion that can be drawn from this is that the London model and the Mattis-Bardeen result would become equivalent in the limit $2\Delta \rightarrow \infty$. It should also be mentioned that BCS theory in the clean limit would again reduce back to the London theory result because in the absence of any scattering from impurities there can be no absorption above 2Δ. The reason for this is because of momentum conservation. Energy conservation can be easily satisfied by having the excited electrons absorb the photon energy. However, the magnitude of the momentum of a photon is generally quite small in comparison with the excited electrons. This requires additional elastic scattering events with impurities for the electronic momentum to be conserved.

In order to obtain the Mattis-Bardeen result as well as generalizing to the Eliashberg case requires perturbation theory. The perturbing Hamiltonian has the form[27]

$$H_{ext} = \int d^3x j_\mu(x) A^\mu(x) \ , \tag{6.11}$$

where $j_\mu(x) = (\rho(x), \mathbf{j}(x))$ and $A^\mu = (-\phi(x), \mathbf{A}(x))$. Note that the factors $\rho(x)$ and $\phi(x)$ are the electronic density and the electromagnetic scalar potential respectively . Ultimately, one finds from the perturbation theory that calculating the conductivity leads one to evaluate a current-current correlation function:

$$K_{\mu\nu}(x, x') = -i < T\{j_\mu(x) j_\nu(x')\} > \ , \tag{6.12}$$

where the T implies that this is a time ordered product. To obtain the actual conductivity in Eliashberg theory requires that this correlation function be Fourier transformed into momentum and energy space and then be expressed

in terms of Eliashberg Green's functions. Nam did this calculation and obtained an expression for the conductivity on the real frequency axis. As with the Mattis-Bardeen result, this formula only applied for the dirty limit.

More recently, Bicker's *et al.* [159] obtained an expression for the Eliashberg conductivity based on an imaginary axis formulation that could be applied for all impurity concentrations. Their starting point is a correlation function which, to lowest order, is given by

$$\Pi(i\nu_m) = 2T \sum_{n,\vec{k}} Tr\{ev_x G(\vec{k}, i\omega_n + i\nu_m) G(\vec{k}, i\omega_n) ev_x\} \ . \tag{6.13}$$

where v_x is the component of the Fermi velocity in the x direction. Putting in the Eliashberg Green's functions discussed in Chapter 2 and using the fact that $2e^2 N(0) < v_x^2 > \simeq ne^2/m = \omega_p^2/4\pi$, Bicker's *et al.* obtained the formula :

$$\Pi(i\nu_m) = \frac{\omega_p^2}{4\pi} \pi T \sum_n S_{n,m} \ , \tag{6.14}$$

where

$$S_{n,m} = \begin{cases} \frac{\tilde{\omega}_n(\tilde{\omega}_n + \tilde{\omega}_{n+m}) + \tilde{\Delta}_n(\tilde{\Delta}_n - \tilde{\Delta}_{n+m})}{R_n P_{n,m}} \\ -\frac{\tilde{\omega}_{n+m}(\tilde{\omega}_n + \tilde{\omega}_{n+m}) + \tilde{\Delta}_{n+m}(\tilde{\Delta}_n + \tilde{\Delta}_{n+m})}{R_{n+m} P_{n,m}} & \text{if } m \neq 0, -2n-1; \\ \tilde{\Delta}_n^2 / R_n^3 & \text{if } m = 0; \\ 1/R_n & \text{if } m = -2n-1; \end{cases} \tag{6.15}$$

$$P_{n,m} = \tilde{\omega}_n^2 - \tilde{\omega}_{n+m}^2 + \tilde{\Delta}_n^2 - \tilde{\Delta}_{n+m}^2 \tag{6.16}$$

and

$$R_n = \sqrt{\tilde{\omega}_n^2 + \tilde{\Delta}_n^2} \ . \tag{6.17}$$

The dependence that $\Pi(i\nu_m)$ has on impurities comes from $\tilde{\omega}_n$ and $\tilde{\Delta}_n$. To go from these quantities in the pure case to the impure case one adds the factors $\frac{\pi t^+ \omega_n}{\sqrt{\omega_n^2 + \Delta_n^2}}$ and $\frac{\pi t^+ \Delta_n}{\sqrt{\omega_n^2 + \Delta_n^2}}$ to them respectively. The parameter t^+ can be

thought of as the impurity concentration. It is related to the scattering rate by

$$t^+ = \frac{1}{2\pi\tau_{imp}} . \tag{6.18}$$

After $\Pi(i\nu_m)$ is evaluated, it can be used to obtain the conductivity after it is analytically continued to the real frequency axis via Padé approximants :

$$\sigma(\omega,T) = \frac{i\Pi(i\nu_m \rightarrow \omega + i0^+)}{\omega} . \tag{6.19}$$

Lee, Rainer and Zimmermann[160] have also derived a formula for the conductivity of Eliashberg superconductors that is applicable to all impurity concentrations. This formula however is written directly on the real frequency axis :

$$\sigma(\omega,T) = \frac{N(0)e^2v_F^2}{4\pi^2\omega}\int_{-\infty}^{+\infty} d\epsilon \Bigg[\tanh\left(\frac{\epsilon}{2k_BT}\right) M(\epsilon,\omega)\Big\{g(\epsilon)g(\epsilon+\omega)+h(\epsilon)h(\epsilon+\omega)+\pi^2\Big\}$$

$$- \tanh\left(\frac{\epsilon+\omega}{2k_BT}\right) M^*(\epsilon,\omega)\Big\{g^*(\epsilon)g^*(\epsilon+\omega)+h^*(\epsilon)h^*(\epsilon+\omega)+\pi^2\Big\}$$

$$+\Big\{\tanh\left(\frac{\epsilon+\omega}{2k_BT}\right) - \tanh\left(\frac{\epsilon}{2k_BT}\right)\Big\} L(\epsilon,\omega)\Big\{g^*(\epsilon)g(\epsilon+\omega)+h^*(\epsilon)h(\epsilon+\omega)+\pi^2\Big\}\Bigg] , \tag{6.20}$$

where

$$g(\epsilon) = \frac{-\pi\tilde{\epsilon}(\epsilon)}{\sqrt{\tilde{\Delta}^2(\epsilon)-\tilde{\epsilon}^2(\epsilon)}} , \tag{6.21}$$

$$h(\epsilon) = \frac{-\pi\tilde{\Delta}(\epsilon)}{\sqrt{\tilde{\Delta}^2(\epsilon)-\tilde{\epsilon}^2(\epsilon)}} , \tag{6.22}$$

$$M(\epsilon,\omega) = \left\{\sqrt{\tilde{\Delta}^2(\epsilon+\omega)-\tilde{\epsilon}^2(\epsilon+\omega)}+\sqrt{\tilde{\Delta}^2(\epsilon)-\tilde{\epsilon}^2(\epsilon)}+\frac{1}{\tau_{imp}}\right\}^{-1} \tag{6.23}$$

and

$$L(\epsilon,\omega) = \left\{\sqrt{\tilde{\Delta}^2(\epsilon+\omega)-\tilde{\epsilon}^2(\epsilon+\omega)}+\sqrt{\tilde{\Delta}^{*2}(\epsilon)-\tilde{\epsilon}^{*2}(\epsilon)}+\frac{1}{\tau_{imp}}\right\}^{-1} \tag{6.24}$$

Note here that the dependence due to impurity scattering has been made explicit in equations (6.23) and (6.24) . Marsiglio[161] has also derived a real axis formula for the conductivity. In his derivation, he analytically continued the correlation function given in equation (6.13) by performing the sum over Matsubara frequencies. As it turns out, Marsiglio's formula is equivalent to the formula of Lee *et al.* 's, which was derived in a more general and complicated manner.

Unlike the BCS case, all these Eliashberg formulas have incorporated within them Holstein processes. In a Holstein process, part of the energy transfered from absorbing electromagnetic radiation to the electrons goes to creating a phonon or perhaps some other bosonic excitation. In this way, a phonon which is not optically active by itself can still be observed in the conductivity. In the superconducting state in the absence of impurities, this would lead to there being an onset of absorption in $\sigma_1(\omega)$ at $2\Delta + \omega_0$, where ω_0 is the minimum phonon energy, since 2Δ is still required to break the Cooper pair and the further ω_0 is required to conserve energy in the inelastic scattering process with the phonon. Note here that impurities are not necessary here for momentum conservation as this is taken care of by the phonons. With the presence of these Holstein processes, one would expect to see structure in $\sigma_1(\omega)$ that would correspond to peaks in the $\alpha^2F(\omega)$. In the superconducting state, this structure is all shifted by 2Δ .

In addition to these Holstein processes, at finite temperature a certain amount of Cooper pairs are broken thermally. These thermally excited electrons give rise to a Drude feature in the conductivity - the Lorentzian form centered about $\omega = 0$ discussed earlier. In the absence of impurities, these Eliashberg formulas should still yield this Lorentzian form. The reason

for this is because $1/\tau_{ph}$ is still present but buried within the formulas. In the BCS limit, where the phonons are not treated explicitly, a Drude feature would not occur even for finite temperatures in the pure case.

6.3 THE TEMPERATURE DEPENDENCE OF THE ABSORPTION EDGE

To illustrate how the optical conductivity behaves as a function of temperature the $\alpha^2F(\omega)$ used by Bickers *et al.* for their imaginary frequency axis calculations was chosen. They use a truncated Lorentzian with peak position ω_o, width Γ_o and cut off Γ_o

$$\alpha^2F(\omega) \propto \left\{ \frac{1}{(\omega-\omega_o)^2+\Gamma_o^2} - \frac{1}{\Gamma_c^2-\Gamma_o^2} \right\} \quad |\omega-\omega_o| < \Gamma_c$$

$$= 0 \qquad\qquad |\omega-\omega_o| > \Gamma_c \qquad (14)$$

with ω_o=50 meV, Γ_o=5 meV and Γ_c=15 meV. For the real axis calculations to be shown here, the critical temperature was set at $T_c = 50K$. In order to get a 50K superconductor with $\mu^* = 0.0$ the mass renormalization factor that was required $\lambda = 0.8$. The zero temperature gap comes out to be Δ_o=8.55 meV so that $2\Delta_o/k_BT_c$=3.97 which indicates relatively weak coupling. The Allen and Dynes average for this spectrum was $\omega_{ln} = 49.3$ meV. This is fairly high compared to the values that this parameter takes for conventional superconductors, which is usually of the order of 10 meV. The strong coupling index in this case is $T_c/\omega_{ln} = 0.09$ which is in the intermediate range.

In Fig. 6.2, we plot the real part of the optical conductivity vs. frequency for several different temperatures. In order to generate these curves, the conductivity equations of Lee *et al.* shown in the previous section were used. In this case, no impurities have been added so that $t^+ = 0.0$ meV. The

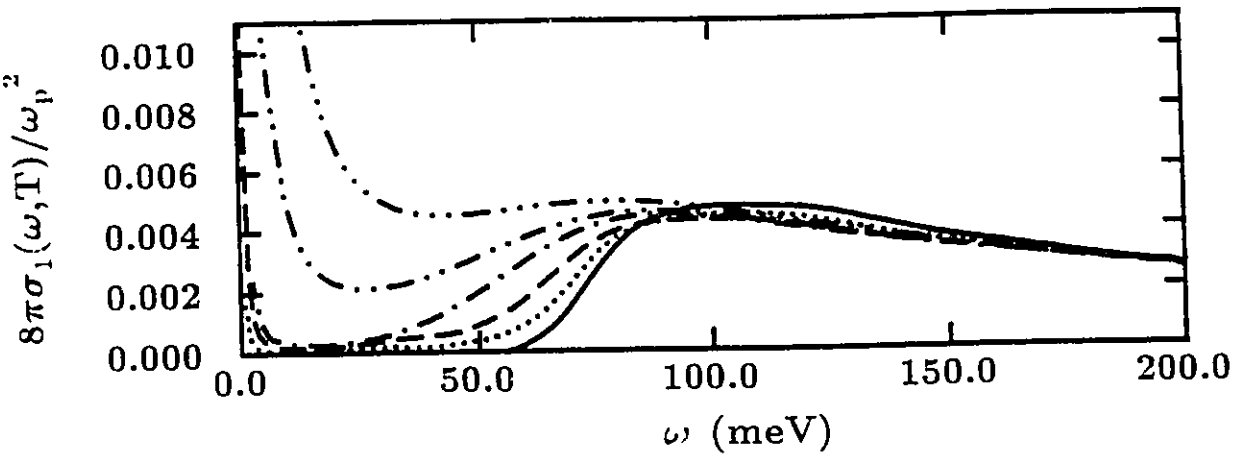

Figure 6.2 $8\pi\sigma_1(\omega,T)/\omega_p^2$ is plotted vs. ω for the lorentzian $\alpha^2F(\omega)$ with ω_{ln} = 49.3 meV and $2\Delta_o/k_BT_c$=3.97. The different curves correspond to the temperatures T = 12.5K (solid line), T = 40.0K (dotted), T = 46.25K (dashed) , T = 50.0K (dot-dashed), T = 75.0K (dot-dot-dashed) and T = 100.0K (dot-dot-dot-dashed).

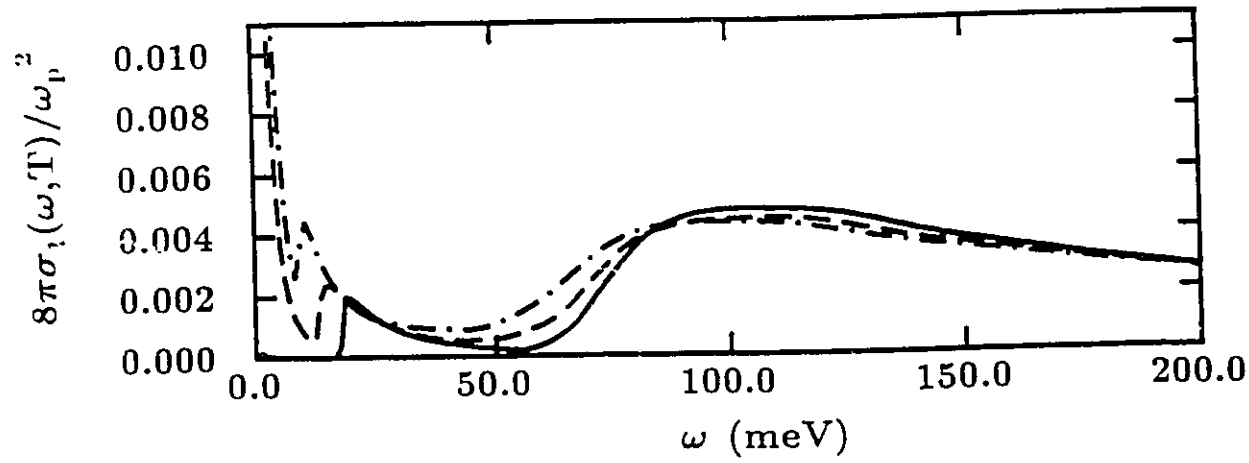

Figure 6.3 $8\pi\sigma_1(\omega,T)/\omega_p^2$ is again plotted vs. ω for the same case except now impurities are included, t^+ = 0.17 meV. The curves correspond to the temperatures T = 12.5K (solid line), T = 40.0K (dotted), T = 46.25K (dashed) and T = 50.0K (dot-dashed).

conductivity has been expressed in the dimensionless form $8\pi\sigma_1(\omega,T)/\omega_p^2$. The temperatures that have been used are : $T = 12.5K$ (solid line), $T = 40.0K$ (dotted), $T = 46.25K$ (dashed) , $T = 50.0K$ (dot-dashed), $T = 75.0K$ (dot-dot-dashed) and $T = 100.0K$ (dot-dot-dot-dashed). Note that the three higher temperatures correspond to the normal state. For the solid curve which corresponds to the lowest temperature, there is no absorption visible on this scale until twice the gap value (17.1 meV) plus the lowest phonon frequency (35.0 meV) - 52.1 meV. This curve is low enough in temperature to effectively represent what occurs at zero temperature. Since the onset in this case does occur at 52.1 meV and not at $2\Delta(T)$, it is obvious that one would have difficulty in extracting the gap in this sort of situation unless one had independent knowledge on the phonon spectrum. As the temperature is increased, a Drude structure in the region of $\omega = 0.0$ meV appears and then grows more prominent. Absorption becomes apparent at all frequencies, even for the remaining two curves that fall below the critical temperature. As one would expect, the rises in absorption that these two curves display are shifted downward in frequency in comparison to the low temperature curve as the magnitude of the gap is being reduced. The rise in absorption in the curve right at the critical temperature is of course lower still. However, trying to extract the temperature dependence of the gap from curves such as these is problematic. This is due in part to thermal smearing. Note that the $T = 75K$ curve, which is well above T_c, has the same features as the lower temperature curves: a Drude feature at low frequency followed by a depression and finally a rise corresponding to the Holstein region. Note that the rise in the 75 K curve occurs at a lower frequency than the 50 K curve. If one did not know any better, one might think that one is still observing the closing of

the gap. For the 100 K curve, the thermal smearing is such that the increase in absorption is almost completely wiped out.

In Fig. 6.3, $8\pi\sigma_1(\omega,T)/\omega_p^2$ is again plotted vs. ω but in this case the impurity concentration is $t^+ = 0.17$ meV . The temperatures that have been used are: $T = 12.5K$ (solid line), $T = 40.0K$ (dotted), $T = 46.25K$ (dashed) and $T = 50.0K$ (dot-dashed). With this impurity concentration, the solid curve is nearly identical to the model C used in the paper of Lee *et al.* . For their calculations they set $T = 0K$ but, as was discussed earlier, $T = 12.5K$ is close enough to zero temperature to be representative of it. With impurities included, a sharp peak in the absorption is observed at exactly $2\Delta(T = 12.5K) = 17.1$ meV. In the $T = 40.0K$ and $T = 46.25K$ curves this impurity absorption peak continues to be well defined but occurs at lower frequencies as the gap reduces as T_c is approached . For the curve right at T_c, the absorption peak has completely disappeared. In this case, it is evident that the temperature dependence of the gap can be tracked. Beyond the impurity peak, the curves in this figure also show an increase in absorption in the Holstein region as was seen in the pure case. In fact, the presence of impurities seems to have had little effect on this feature.

Results along the same lines as those shown in this figure have been obtained previously by Brandt *et al.* [162]. In that paper, Lee *et al.* 's general formula for the conductivity was used to derive a formula for the conductivity in the BCS limit. In the BCS case, one obtains impurity peaks at twice the gap as we have seen here. However, as one would expect, the large structure due to Holstein processes is completely absent.

Besides a Lorentzian centred at 50 meV, a second model $\alpha^2F(\omega)$ was studied. Again a truncated Lorentzian with Γ_o=5 meV and Γ_c=15 meV was

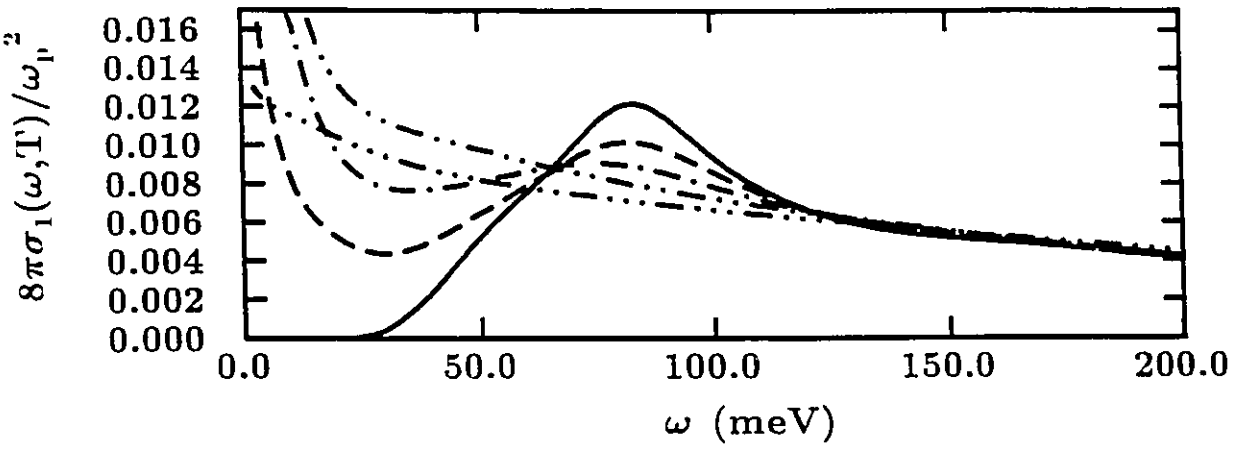

Figure 6.4 $8\pi\sigma_1(\omega,T)/\omega_p^2$ is plotted vs. ω for the lorentzian $\alpha^2F(\omega)$ with ω_{ln} = 11.6 meV and $2\Delta_o/k_BT_c$=6.14. The different curves correspond to the temperatures $T = 12.5K$ (solid line), $T = 40.0K$ (dashed), $T = 46.25K$ (dot-dashed) , $T = 50.0K$ (dot-dot-dashed) and $T = 100.0K$ (dot-dot-dot-dashed).

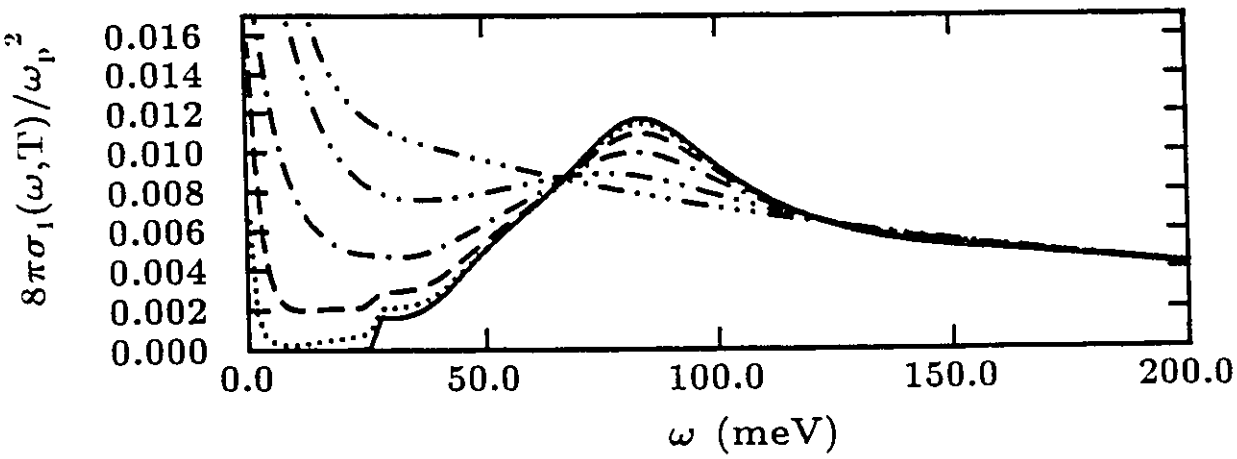

Figure 6.5 $8\pi\sigma_1(\omega,T)/\omega_p^2$ is again plotted vs. ω for the same model as the previous figure, but with a finite impurity concentration of t^+ = 1.0 meV. The curves correspond to the temperatures $T = 12.5K$ (solid line), $T = 25.0K$ (dotted), $T = 32.25K$ (dashed), $T = 40.0K$ (dot-dashed), $T = 46.25K$ (dot-dot-dashed) and $T = 50.0K$ (dot-dot-dot-dashed).

used but in this case ω_o=15 meV so that phonons would extend all the way down to ω = 0.0 meV. For a T_c = 50K, the mass enhancement had to be set at λ = 3.8, which is large in comparison to what is observed for conventional superconductors. The Allen and Dynes parameter is ω_{ln} = 11.6 meV so that T_c/ω_{ln} = 0.37 which puts us beyond the conventional strong coupling regime discussed in earlier chapters. The gap at zero temperature in this case is Δ_o = 13.23 meV and the gap ratio is $2\Delta_o/k_BT_c$ = 6.14 which is again very large. Results for this model in the pure limit are displayed in Fig. 6.4. The same temperature set as in Fig. 6.2 is used with the exception of 75 K . Considering the solid curve which represents the lowest temperature run we see that the onset of absorption now occurs at twice the gap edge. However, unlike the previous figure where the onset was well indicated by an impurity peak, the rise in absorption here is quite gradual and makes determination of the gap difficult. Note how the shape of the Lorentzian $\alpha^2F(\omega)$ is reflected strongly in the absorption in the Holstein region. At the temperatures T = 40.0K and T = 46.25K the Drude features near ω = 0.0 are much more pronounced than they were for the weaker coupling case studied in Fig. 6.2. Despite the difficulties discussed in that case, the gap in even more difficult to track here because of these enhanced Drude features. For the two highest temperatures, the Lorentzian shape of the absorption observed for the lowest temperature is completely lost.

In Fig. 6.5, impurities are now included with this strong coupling model. The impurity concentration here has been set at t^+ = 1.0 meV. The temperature set used here is: T = 12.5K (solid line), T = 25.0K (dotted), T = 32.5K (dashed) , T = 40.0K (dot-dashed), T = 46.25K (dot-dot-dashed)

and $T = 50.0K$ (dot-dot-dot-dashed). Unlike Fig. 6.2 where the onset of absorption was indicated by a sharp impurity peak, the lower temperature curves have an impurity edge at twice the value of the gap. As T_c is approached even this edge is wiped out making it impossible to track the temperature dependence of the gap all the way to T_c. It is worth mentioning at this point that as the coupling strength is increased, impurities tend to have less of an effect. It can be shown[34] that the way that the impurities enter into the Eliashberg equations is approximately like $t^+/(1+\lambda)$. Since there is a $1+\lambda$ scaling, more impurities are required to have the same effect.

In Fig. 6.6, $\Delta(T)/\Delta_o$ is plotted as a function of T/T_c. The curve represents the BCS limit. The circles represent values of the gap corresponding to the first Lorentzian model used here. They were determined by the requirement $\Delta(T) = Re\{\Delta(\omega = \Delta(T), T)\}$, where $\Delta(\omega, T)$ is the Eliashberg gap function. Using values obtained from the impurity peaks in Fig. 6.2 one obtains essentially the same results. The diamonds correspond to the stronger coupling case. Once again $\Delta(T) = Re\{\Delta(\omega = \Delta(T), T)\}$ was used to obtain these points. As is expected for a strong coupling superconductor, the points fall well above the BCS curve.

In Fig. 6.7, $8\pi\sigma_1(\omega, T)/\omega_p^2$ is again plotted vs. ω . Here results using Padé approximants are compared with some of the real frequency axis results displayed earlier. In the upper frame, the solid curve corresponds to the conductivity for the strong coupling Lorentzian with $t^+ = 1.0$ meV and $T = 12.5$ K as evaluated using Lee *et al.* 's real axis conductivity formula. This curve also appears in Fig. 6.4. The dashed curve shows results using Bickers *et al.* 's imaginary axis formula for the conductivity, which gives results that must be analytically continued to the real axis using the Padé technique. The

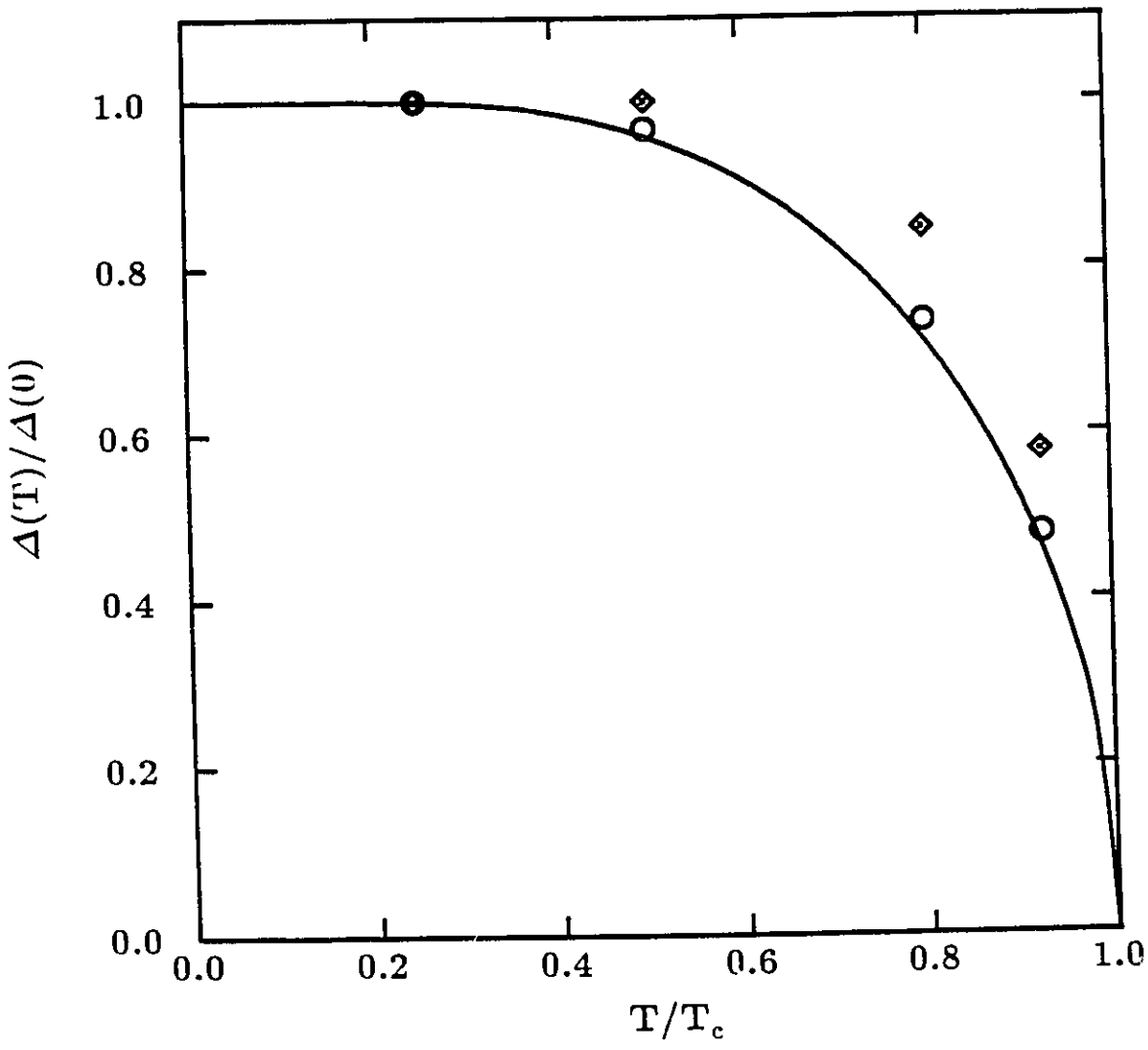

Figure 6.6 In Fig. 6, $\Delta(T)/\Delta_o$ is plotted vs. T/T_c for the BCS limit. The circles represent values of the gap obtained for the weak coupling model. The diamonds correspond to gap values obtained from the strong coupling model.

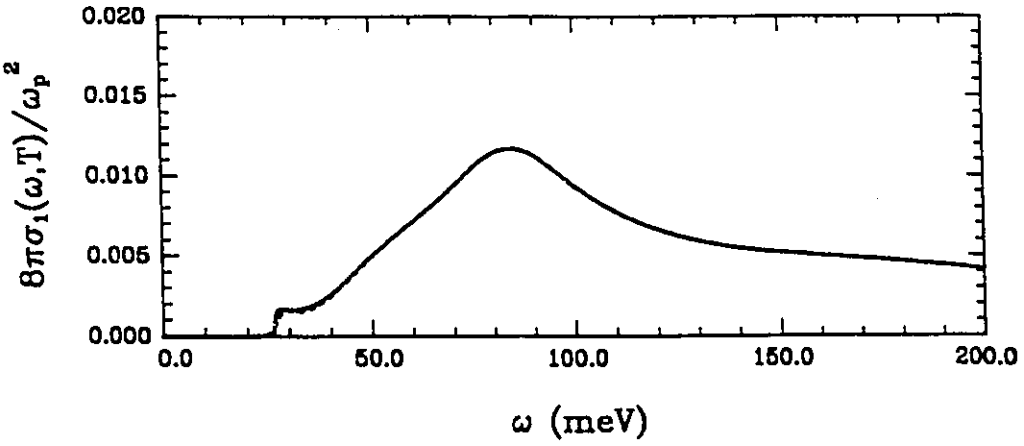

Figure 6.7 $8\pi\sigma_1(\omega,T)/\omega_p^2$ is again plotted vs. ω . The solid line corresponds to the strong coupling Lorentzian model with t^+ = 1.0 meV and T = 12.5 K. The dashed curve corresponds to the same parameters but was obtained using the Bickers *et al.* formula.

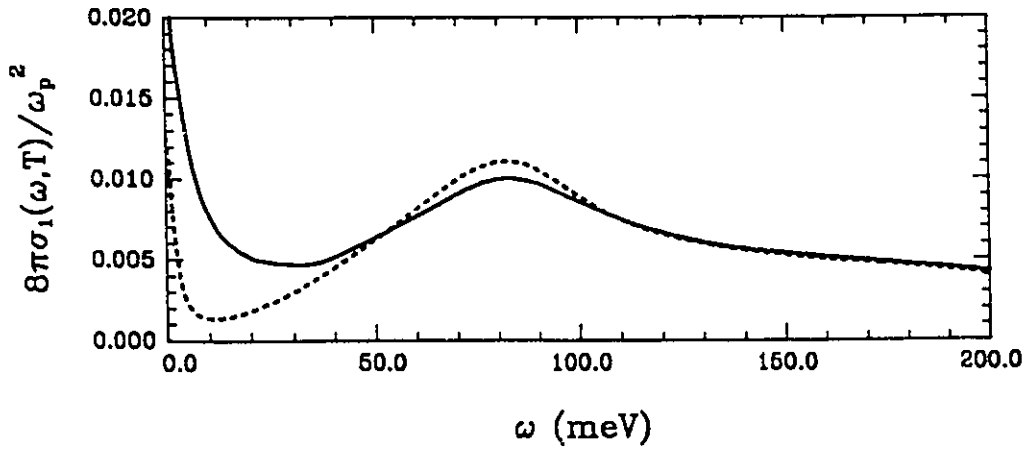

Figure 6.8 $8\pi\sigma_1(\omega,T)/\omega_p^2$ is again plotted vs. ω for the same case as above except the temperature has been raised to T = 40 K. The solid line corresponds results obtained from Lee *et al.* 's formula. The results used to obtain the dashed curve were obtained using Bickers *et al.* formulation.

agreement between the two different techniques is quite good in this case. In Fig. 6.8, the conductivity is again evaluated for the same case except now the temperature has been raised much closer to T_c, T= 40 K. Here, the differences between the real axis results given by the solid curve and the imaginary axis results given by the dashed curve are quite significant. The differences are particularly prominent at low frequency where it is obvious that the Padé approximants do not reproduce the real axis results very well. The lesson here is that the imaginary axis formulation when analytically continued to the real axis using Padé approximants can not be trusted to give accurate results except at low temperature. These results are consistent with what occurs for $\Delta(\omega)$ and $Z(\omega)$ when obtained using the Padé technique, as discussed in Chapter 2.

In Fig. 6.9, the normalized conductivity $\sigma_1(\omega,T)/\sigma_N(\omega,T)$ is plotted vs. ω. The temperature is fixed at T = 12.50 K and the three curves correspond to the weak coupling case with t^+ = 0.17 meV (solid), the weak coupling case with t^+ = 0.0 meV (dotted) and the strong coupling case with t^+ = 1.0 meV (dashed). The normal state conductivity $\sigma_N(\omega,T)$ can be obtained using the formula

$$\sigma_N(\omega,T) = \frac{N(0)e^2v_F^2}{2\omega}\int_{-\infty}^{\infty} d\epsilon\left(\tanh\left(\frac{\epsilon+\omega}{2T}\right) - \tanh\left(\frac{\epsilon}{2T}\right)\right) \left\{\frac{1}{-i\tilde{\epsilon}_N(\epsilon)+\tilde{\epsilon}_N^*(\epsilon)+1/\tau_{imp}}\right\}, \tag{6.25}$$

where the $\tilde{\epsilon}_N(\epsilon)$ are the normal state renormalized frequencies which can be in turn be calculated using the formula

$$\tilde{\epsilon}_N(\epsilon) = \epsilon + \int_0^{\infty} d\Omega\alpha^2F(\Omega)\left(\ldots\psi\left(\frac{\Omega}{2T}\right) - \psi\left(\frac{1}{2}+i\frac{\Omega-\epsilon}{2T}\right) + \psi\left(\frac{1}{2}-i\frac{\Omega+\epsilon}{2T}\right)\right), \tag{6.26}$$

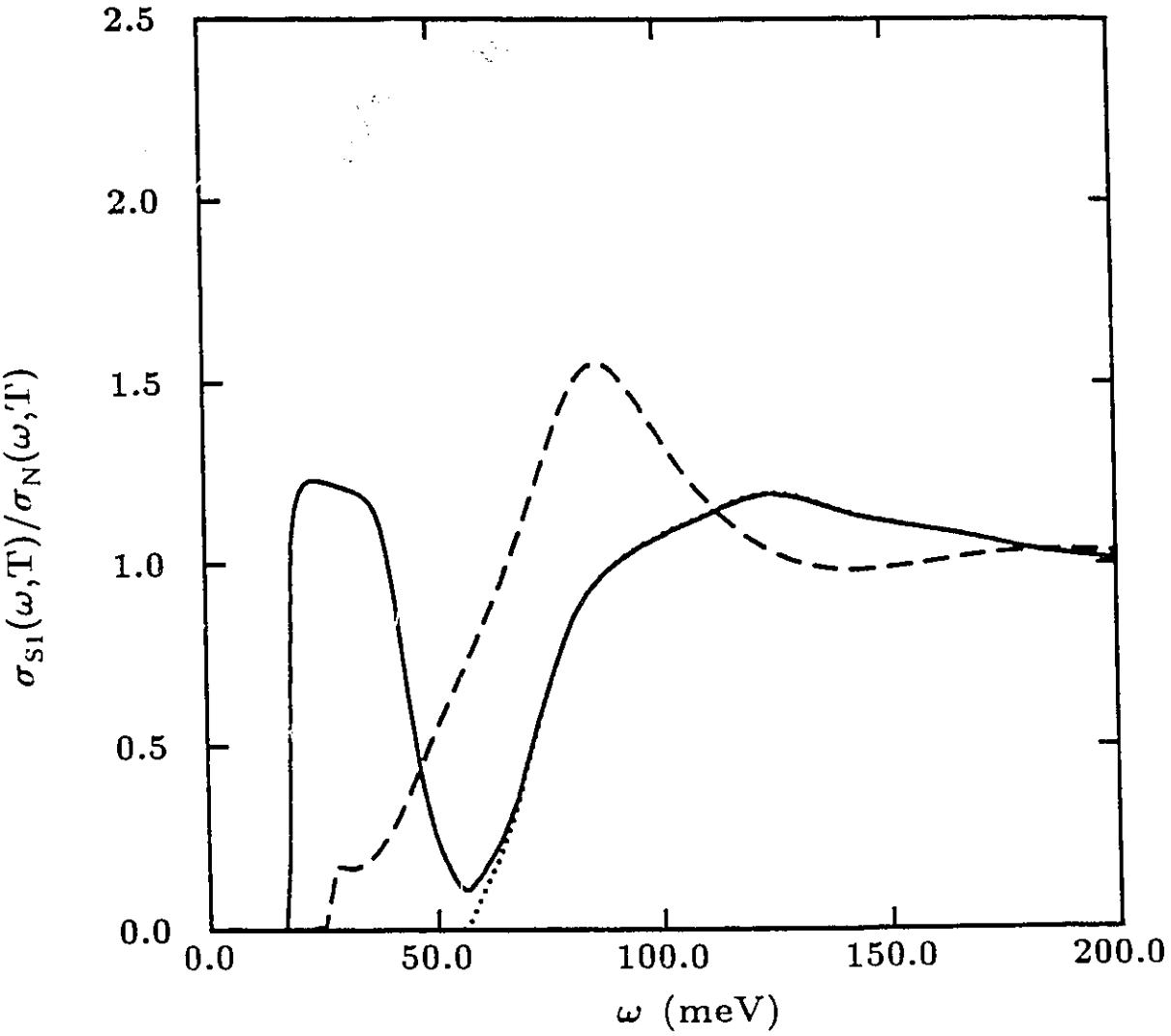

Figure 6.9 $\sigma_1(\omega,T)/\sigma_N(\omega,T)$ is plotted vs. ω. the curves correspond to the weak coupling case with $t^+ = 0.17$ meV (solid), the weak coupling case with $t^+ = 0.0$ meV (dotted) and the strong coupling case with $t^+ = 1.0$ meV (dashed). The temperature is $T = 12.50$ K.

where ψ is the digamma function. Equation (6.25) is just the Lee formula (6.20) taken in the normal state limit. The formula (6.26) for the normal state renormalized frequencies can similarly be obtained from taking the superconducting equation for the renormalization function shown in Chapter 2 in the normal state limit. From the solid curve in this figure, it is evident that the impurity peak originally observed in Fig. 6.2 appears here as well but becomes even more pronounced when we normalize $\sigma_1(\omega,T)$ with $\sigma_N(\omega,T)$. Interestingly, this ratio for the region just above $\omega = 2\Delta(T)$ is greater than unity. On the other hand, normalizing by σ_N seems to have little effect on the strong coupling case, represented by the dashed curve. This curve is quite similar to the plot $8\pi\sigma_1(\omega,T)/\omega_p^2$ shown in Fig 6.5 for the same set of parameters. Just as in Fig. 6.5, the onset of absorption at 2Δ takes the form of an edge rather than a well developed peak. The ratio does appear to have a small peak in this region but it is of the order of $\sigma_1/\sigma_N \sim 0.2$ which is much less than unity. These results are closely related to the subject of next section of this chapter, which deals with coherence effects that appear in the ratio σ_1/σ_N. Not surprisingly, the dashed curve which corresponds to a case with no impurities shows no peak at all in the region $\omega \sim 2\Delta$. As one moves up in frequency, the Holstein region is entered. At this point, it is interesting to compare this figure with Fig. 6.1. In that figure, the Mattis-Bardeen result for σ_1/σ_N was plotted and was basically featureless beyond the immediate region of $\omega \sim 2\Delta$. Here, the features of the $\alpha^2F(\omega)$ are reflected in this ratio. The strong coupling curve shows it quite strongly as one would expect, but even the two weak coupling curves show quite significant effects. In both weak coupling and strong coupling cases the ratio σ_1/σ_N appears to become significantly larger than unity in the Holstein region.

These theoretical results can be contrasted with what is actually observed experimentally in the oxides. In several of these materials, an onset in the absorption reminiscent to what we have observed here theoretically has been seen in experiments done in the infrared frequency range[156,23,163–167]. This resemblance to the predictions of BCS-Eliashberg theory has lead some authors[164,165] to associate this feature with 2Δ. In the case of YBCO, this interpretation has lead to predictions of the gap ratio as high as $2\Delta_o/k_BT_c \sim 8$. In the standard electron-phonon Eliashberg formalism, this would indicate very strong coupling. However, when the ratio σ_1/σ_N is taken with the experimental data, this quantity is quite flat and ~ 1 in the region above the onset[165]. From the previous figure, it is obvious that one should see some structure in this frequency region. This was a point noted by the authors of that paper[165]. Since the oxides have such small coherence distances, it is expected that these materials tend toward the clean limit. From our previous discussion, this would point toward the observed onset of absorption being indicative of $2\Delta + \omega_o$ and not 2Δ and so the the gap ratio could potentially be much smaller. However, even if this is the case, phonon structure should probably still be observed in σ_1/σ_N. In the case of the marginal Fermi liquid model[168,169], the $\alpha^2F(\omega)$ is gapped and so the onset in the clean limit should occur at 4Δ instead of 2Δ. The $\alpha^2F(\omega)$ that one uses in this model is flat and small in magnitude and so the Holstein features that arise can be such that the deviations from $\sigma_1/\sigma_N \sim 1$ are small, if the parameters of the model are chosen correctly.

There is also the problem of the temperature dependence of this onset. The theoretical results shown here indicate that this onset should shift

downward reflecting the closing of the superconducting gap as the temperature is increased. Analogous results have been obtained in the context of the marginal Fermi liquid model. Experimentally, one finds that the position of the onset of absorption in YBCO does not vary much with temperature. Indeed, Schlesinger *et al.* [164] have extracted $2\Delta(T)$ from this onset and find it to be virtually flat, dropping only slightly near T_c. In fact, there are indications that this "gap" persists even above T_c[156,167,170].

6.4 COHERENCE EFFECTS IN THE LOW FREQUENCY CONDUCTIVITY

In the previous chapter, the effects of coherence in the superconducting state on the nuclear spin relaxation were studied extensively. A subject that is discussed less in the literature is the fact that analogous coherence peaks should be seen in the low frequency conductivity. The Mattis-Bardeen[158] formula for the real part of the conductivity of a BCS superconductor normalized by the normal state conductivity consists of 2 pieces. One piece is zero for $\omega < 2\Delta$. The remaining term on the other hand is identical to the BCS formula for the nuclear spin relaxation. This fact was noticed in the original BCS paper[7].

As was mentioned earlier, while the BCS theory is successful in predicting the occurance of a peak in the nuclear spin relaxation rate, the actual magnitude of the peak is problematic. If one leaves the hyperfine energy splitting in the BCS formula, one obtains a peak which is much larger than one would see in the experimental data of material such as Al. Since the hyperfine splitting is small, one is tempted to just set it equal to zero. In this case, instead of getting a peak, one obtains a logarithmic divergence near T_c because

of the square root singularity in the BCS density of states. Again, since the Mattis-Bardeen formula has basically the same features, it is expected that for finite frequencies it will generally overestimate the size of the peak in the conductivity, as well as give a divergence near T_c in the limit $\omega \to 0$.

As was the case for the nuclear spin relaxation, a mechanism is required for smearing out the superconducting density of states. The one such mechanism that shall be discussed in this chapter is in the inclusion of strong-coupling effects. On top of this,the frequency dependence of the coherence peak shall be investigated as well as the effect of altering the impurity concentration.

In order to investigate coherence in the low frequency conductivity, the $\alpha^2F(\omega)$ of Pb has again been used. This makes a direct comparison with the results of the previous chapter possible. As in previous chapters, the $\alpha^2F(\omega)$ has been scaled so that different values of T_c/ω_{ln} could be obtained. Since this sort of scaling applies, the actual frequencies for which the conductivity has been calculated are quoted normalized by either $2\Delta_o$ or T_c. For simplicity, μ^* has been set to zero in all cases.

In Fig. 6.10, we show results for the real part of the conductivity normalized by the normal state conductivity, $\sigma_1(T)/\sigma_N(T)$, vs. T/T_c for several values of T_c/ω_{ln}: 0.05 (solid line), 0.1 (dotted), 0.2 (short-dashed) and 0.3 (long-dashed). For all cases shown in this figure, the calculations have been done very close to zero frequency and we have set $t^+ = 500.0$ meV so that we are in effect in the dirty limit. We see as the coupling strength is increased, the peak in the conductivity, which has a value approximately 3.0 for $T_c/\omega_{ln} = 0.05$, is reduced to about 1.15 for $T_c/\omega_{ln} = 0.2$ and is eliminated for $T_c/\omega_{ln} = 0.3$. These results are nearly identical to those we obtained for

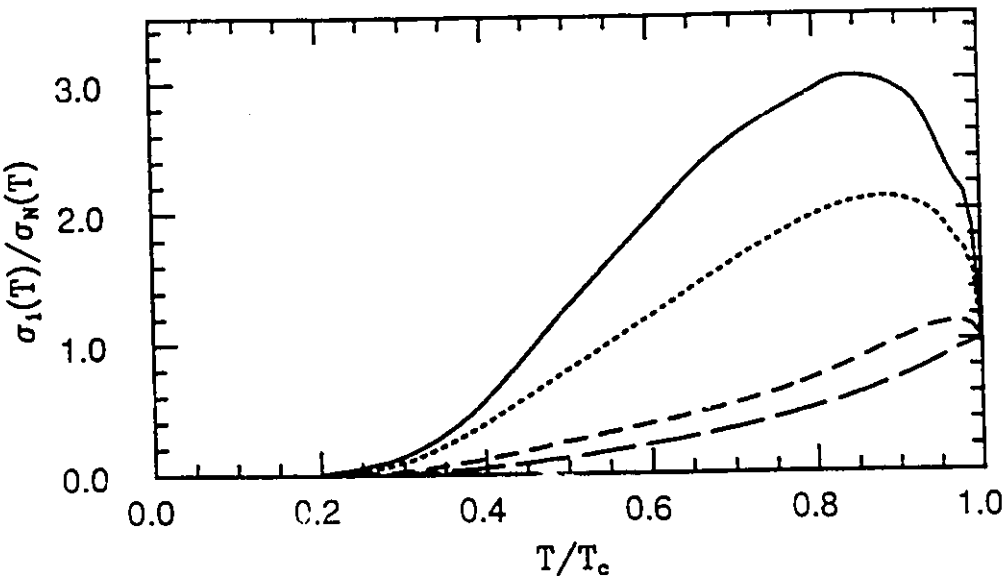

Figure 6.10 $\sigma_1(T)/\sigma_N(T)$ is plotted vs. T/T_c for several values of T_c/ω_{ln}: 0.05 (solid line), 0.1 (dotted), 0.2 (short-dashed) and 0.3 (long-dashed). The frequency in this case was very close to zero and the impurity concentration was $t^+ = 500.0$ meV.

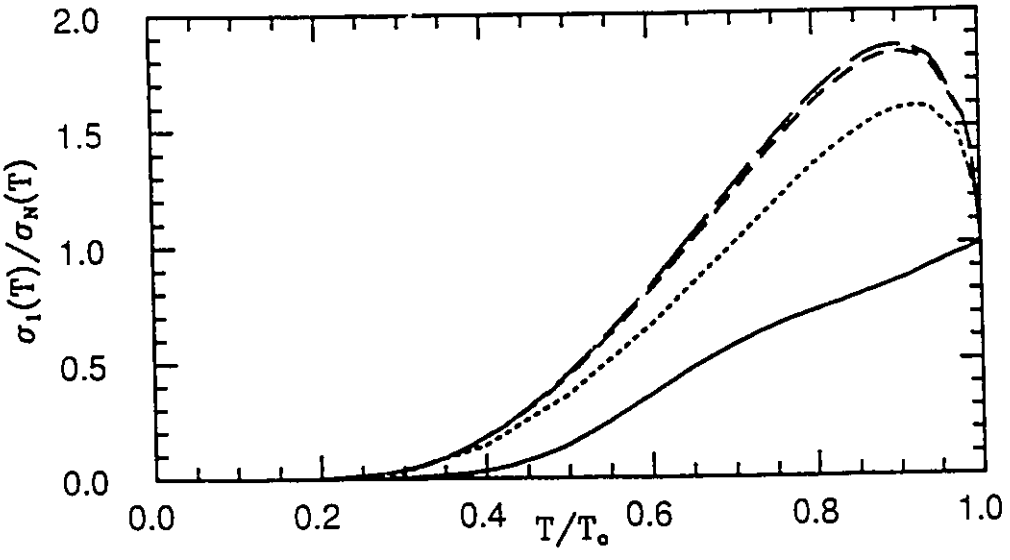

Figure 6.11 $\sigma_1(T)/\sigma_N(T)$ is again plotted vs. T/T_c for the impurity concentrations 0.0 (solid line), 0.2 (dotted), 1.0 (short-dashed) and 500.0 (long-dashed). The units are meV. In this case, $T_c/\omega_{ln} = 0.1$ and $\omega/2\Delta_o = 0.0156$.

the nuclear spin relaxation. That this should be the case is not obvious by looking at the conductivity formula of equation (6.2). Nonetheless, this is not a surprising result. As mentioned earlier, for low frequencies the Mattis-Bardeen result is equivalent to the NMR formula. In the strong coupling case, the correlation between the NMR and the conductivity is much easier to see by examining the Nam[171] formula for the conductivity:

$$\frac{\sigma_1(\nu,T)}{\sigma_N} = \frac{1}{\nu}\int_{\Delta}^{\nu+\Delta} d\omega \tanh\left(\frac{\beta(\nu-\omega)}{2}\right)\left\{N(\omega)N(\nu-\omega) - M(\omega)M(\nu-\omega)\right\}$$
$$+\frac{1}{\nu}\int_{\Delta}^{\infty} d\omega\left[\tanh\left(\frac{\beta(\nu+\omega)}{2}\right)-\tanh\left(\frac{\beta\omega}{2}\right)\right]\left\{N(\omega)N(\nu+\omega)+M(\omega)M(\nu+\omega)\right\} \tag{6.27}$$

In this formula, $N(\omega)$ and $M(\omega)$ are the superconducting density of states and the anomolous density of states used so extensively in the previous chapter. In the limit $\nu \to 0$, the first term in this formula vanishes while the second term becomes equivalent to equation (5.19) for the nuclear spin relaxation. It should be emphasized that this formula, unlike Lee *et al.* 's, applies only to the dirty limit.

In Fig. 6.11, we examine the effect of varying impurity concentration. Again we plot $\sigma_1(T)/\sigma_N(T)$ vs. T/T_c , but in this case we fix ourselves at $T_c/\omega_{ln} = 0.1$ and have used a finite frequency $\omega/2\Delta_o = 0.0156$. The curves apply for the following impurity concentrations. t^+: 0.0 (solid line), 0.2 (dotted), 1.0 (short-dashed) and 500.0 (long-dashed). The units are meV. As stated earlier, $t^+ = 500.0$ meV represents more or less the dirty limit. When we drop from $t^+ = 500.0$ meV to $t^+ = 1.0$ meV , there is almost no change in the peak. Even for the case where $t^+ = 0.2$ meV , there is still a substantial peak with $(\sigma_1(T)/\sigma_N(T))_{max} \sim 1.6$. The lesson here is, as long as the coupling strength is not particularly strong, even a relatively clean Eliashberg superconductor

should show a fairly well developed peak. In the pure case, $t^+ = 0.0$ meV , the peak is absent. However, it's ghost appears at $T/T_c \sim 0.7$.

In Fig. 6.12, we examine the effects of frequency dependence. Once again, we fix ourselves at $t^+ = 500.0$ meV and consider a coupling strength of $T_c/\omega_{ln} = 0.05$. We use the following frequencies: $\omega/2\Delta_o \sim 0.0$ (solid line), $\omega/2\Delta_o = 0.0022$ (long dashed), $\omega/2\Delta_o = 0.0087$ (short dashed), $\omega/2\Delta_o = 0.0347$ (dotted), $\omega/2\Delta_o = 0.1042$ (short dashed-dotted) and $\omega/2\Delta_o = 0.3126$ (long dashed-dotted). It is evident that increasing the frequency reduces the size of the peak. This result was to be expected. In the BCS case, it was noted[3] that the peak should disappear for $\omega/T_c \sim \frac{1}{2}$. In this relatively weak coupling case, the peak drops from about 3.0 for $\omega/2\Delta_o \sim 0.0$ to about 1.2 for $\omega/2\Delta_o = 0.1042$. By $\omega/2\Delta_o = 0.3126$.the peak has been completely eliminated. Translating this into ω/T_c, these largest two frequencies correspond to about $\omega/T_c = 0.388$ and $\omega/T_c = 1.16$, respectively.

In Fig. 6.13, we again examine the effects of frequency dependence, except here we fix ourselves at $T_c/\omega_{ln} = 0.1$ while keeping $t^+ = 500.0$ meV . The curves correspond to: $\omega/2\Delta_o \sim 0.0$ (solid line), $\omega/2\Delta_o = 0.0010$ (long dashed), $\omega/2\Delta_o = 0.0040$ (short dashed), $\omega/2\Delta_o = 0.0158$ (dotted), $\omega/2\Delta_o = 0.0474$ (short dashed-dotted) and $\omega/2\Delta_o = 0.1420$ (long dashed-dotted). The actual magnitude of the frequencies used here are the same as those used to obtain the results in the previous figure. Once again, the peak drops as a function of frequency . However, it is evident that in this more strong-coupling case the magnitude of the peak is less sensitive to the effect of increasing frequency. The peak only drops from about 2.1 near zero frequency to only about 1.8 for $\omega/2\Delta_o = 0.0158$. For $\omega/2\Delta_o = 0.0474$, the maximum is still near 1.5 . In fact, this particular curve has a larger maximum than the corresponding curve in

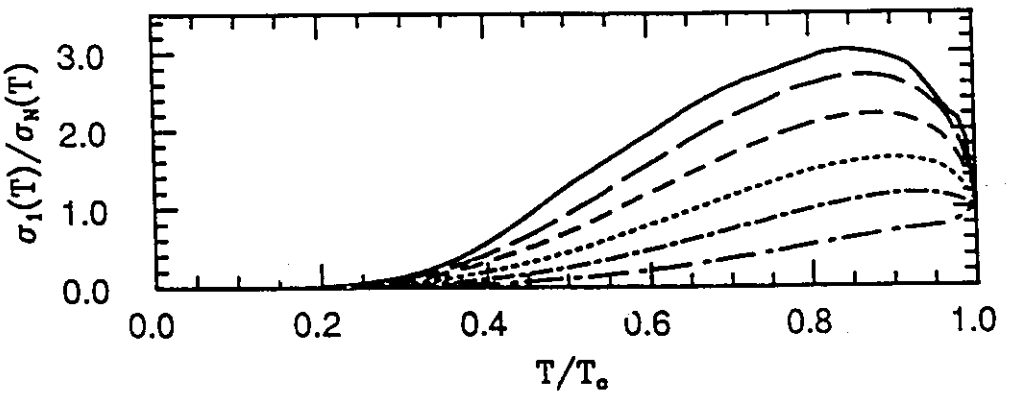

Figure 6.12 $\sigma_1(T)/\sigma_N(T)$ is plotted vs. T/T_c for the frequencies $\omega/2\Delta_o \sim 0.0$ (solid line), $\omega/2\Delta_o = 0.0022$ (long dashed), $\omega/2\Delta_o = 0.0087$ (short dashed), $\omega/2\Delta_o = 0.0347$ (dotted), $\omega/2\Delta_o = 0.1042$ (short dashed-dotted) and $\omega/2\Delta_o = 0.3126$ (long dashed-dotted). For these curves, the coupling strength was set at $T_c/\omega_{ln} = 0.05$ and the impurity concentration was $t^+ = 500.0$ meV.

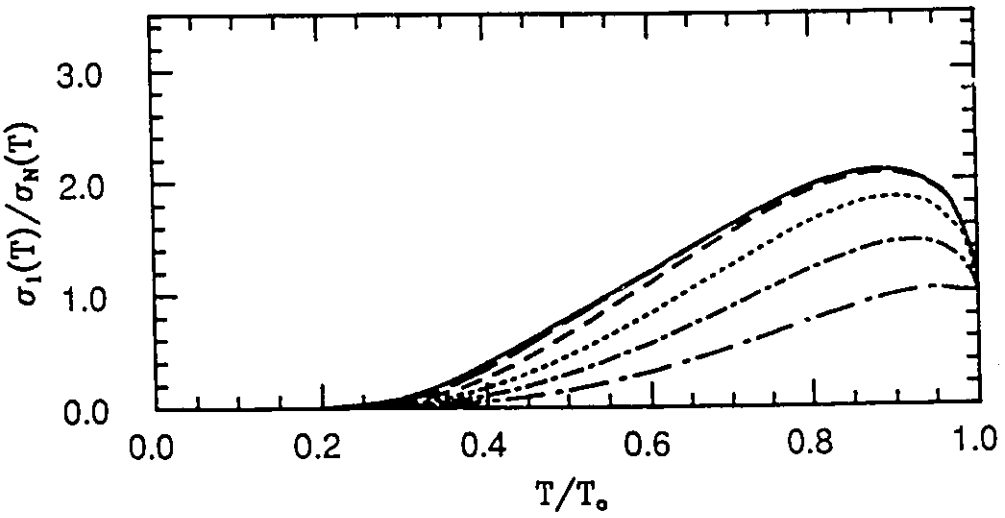

Figure 6.13 $\sigma_1(T)/\sigma_N(T)$ is again plotted vs. T/T_c, but this time the coupling strength has been increased to $T_c/\omega_{ln} = 0.1$. The curves correspond to the frequencies $\omega/2\Delta_o \sim 0.0$ (solid line), $\omega/2\Delta_o = 0.0010$ (long dashed), $\omega/2\Delta_o = 0.0040$ (short dashed), $\omega/2\Delta_o = 0.0158$ (dotted), $\omega/2\Delta_o = 0.0474$ (short dashed-dotted) and $\omega/2\Delta_o = 0.1420$ (long dashed-dotted).

the previous figure. $\omega/2\Delta_o = 0.1042$ (again the actual ω is the same), despite the fact that we have used a larger coupling strength. From this result, it becomes evident that one could not easily estimate coupling strength from experiment by using the low frequency conductivity by itself. In the final curve which is for $\omega/2\Delta_o = 0.1420$, the peak has been nearly eliminated. This frequency is equivalent to $\omega/T_c = 0.58$. This is similar to what was observed for BCS[3].

As far as the oxides are concerned, some experiments have been performed in the microwave region. This is the frequency range where one might expect the effects discussed in this section to be observed. In a paper by Cheah *et al.* [172], results are given for $\sigma_1(T)/\sigma_N(T)$ for YBCO. The experiment was performed at a frequency of 5 GHz, which translates to an energy of ~ 0.02 meV. This means that $\omega/T_c \sim 0.002$, so any coherence peak should not be damped out just because of the magnitude of the frequency. However, this experiment did not give much indication of there being a peak in the conductivity below T_c. On the basis of just the theoretical results shown here, this could be an indication of either very strong coupling or that the superconductor is in the extreme clean limit. The first of these two possibilities of course contradicts the infrared results discussed earlier. That their sample might have been in the clean limit is a possibility. However, it should be stressed that the results shown in Fig. 6.11 indicate that the restrictions on the impurity concentration for the coherence peak to be lost require the superconductor to be extremely clean indeed. Another effect which bears consideration but was not investigated in this section is that of anisotropy. In the last chapter, anisotropy was shown to to be a potentially important factor in damping out the peak the nuclear spin relaxation rate and thus

should play a nearly identical role here. It should be noted however that the conductivity in the anisotropic case makes for a somewhat more complicated situation than the nuclear spin relaxation rate as it becomes a tensor. A possible scenario that might explain Cheah's data and be consistent with the results of the previous chapter is a case where the superconductor is a weak coupler, but that the peak is damped by a combination of anisotropy and a low impurity concentration.

The story does not end here. An added twist has been provided by some more recent microwave experiments. The work of Nuss *et al.* [173] on YBCO indicate that peaks below T_c in $\sigma_1(T)/\sigma_N(T)$ may indeed exist after all. In their paper, they show curves for $\sigma_1(T)$ as a function of temperature for the frequencies 0.5 THz, 1.0 THz and 2.0 THz, all of which show quite significant peaks. Normalizing these frequencies by T_c yields approximate ω/T_c's of 0.25, 0.5 and 1.0. These are quite high in comparison with most of the frequencies used to obtain the results displayed earlier. In fact, $\omega/T_c = 1.0$ is well beyond the frequency where one would still expect to see a coherence peak in BCS theory. On the basis of this one point alone one can argue that the observed peaks could not be due to the usual BCS-Eliashberg coherence effects. As it turns out, a natural explanation comes from marginal Fermi liquid theory[173,101], where this sort of behaviour comes as a biproduct of a scattering rate that is predicted to drop dramatically below T_c due to the fact that the $\alpha^2 F(\omega)$ becomes gapped. There is compelling evidence that this is indeed the explanation as some experiments have shown that the scattering rate does indeed follow the marginal Fermi liquid prediction[174,175].

In addition to the experiments on YBCO, there has been at least one paper on $Bi_2Sr_2CaCu_2O_8$ that also shows peaks in $\sigma_1(T)/\sigma_N(T)$. The

work of Holczer *et al.* [176] shows fairly sharp peaks near T_c in this material. Experiments yielding similar results were performed on two different samples with different T_c's. The experiments were done at much lower frequency than those quoted for Nuss *et al.* on YBCO.

6.5 CONCLUSIONS

The conductivity for an Eliashberg superconductor has been calculated for arbitrary temperature T and impurity concentration t^+. For $t^+ = 0.0$ meV, it is found that $\sigma_1(\omega, T)$ shows no sharp structure by which the temperature depend gap $\Delta(T)$ can be easily identified. In this case, one needs to know the minimum frequency for the $\alpha^2 F(\omega)$ in order to be able to extract the gap. Even if this frequency is known, the onset is not always sharp and may not permit an accurate determination of Δ. When impurities are introduced, the onset of absorption begins at exactly 2Δ. In the weak coupling case, this took the form of an impurity peak which could be used to determine the temperature dependent gap. In the strong coupling case, there appears an impurity edge rather than a peak making it more difficult to obtain $\Delta(T)$ at finite T.

From the results for the low frequency conductivity, it appears that $\sigma_1(T)/\sigma_N(T)$ as a function of T/T_c behaves in a quite similar manner to the nuclear spin relaxation. Indeed, it seems unlikely that a superconductor would exhibit a peak due to coherence factors in the conductivity and not in the NMR if the strong-coupling Eliashberg formalism applies unless additional damping mechanisms can be invoked. In the high-T_c oxides, one such mechanism that has been proposed that would damp the peak in the NMR but not effect the conductivity are the antiferromagnetic Fermi-liquid corrections of

Monien and Pines discussed in previous chapter. The results also indicate that the impurity concentration need not be very large in order for a peak in the low frequency conductivity to appear. Finally, sensitivity of the peak to frequency seems to diminish with coupling strength.

Comparison with some experiments on the oxides appear to indicate that a strongly coupled Eliashberg model runs into some difficulty when it comes to accounting for the behavior in these materials, at least as far as the conductivity is concerned.

Chapter 7

Phonon Self-Energy Effects

7.1 INTRODUCTION

In Chapter 2, the derivation of the Eliashberg equations was discussed. One simplification that was used to derive these equations was to neglect phonon self-energy effects by using the bare phonon Green's functions. This can be justified in part by noting that the information about the phonons contained in $\alpha^2 F(\omega)$ is generally obtained experimentally. What one observes in any experiment are the phonons already renormalized by their various interactions. In this way, while they have not been taken into account formally, phonon self-energy effects are still included. However, a potential point for concern is what occurs at the critical temperature. As we have seen from previous chapters, many physical properties are affected profoundly when the electrons enter the superconducting state. Since phonons are renormalized by their interactions with electrons, it is logical that this

change of state would affect the phonons as well. The question is how large are these effects.

In appears that the answer to this question is that the effects are small, at least in conventional superconductors. Bardeen and Stephan[115] in deriving their formula for the free energy difference used the normal state phonon self-energy but discuss corrections introduced by the change in the phonon self-energy in the superconducting state. The conclusion was that the corrections required were not very significant, but did increase with coupling strength. A microscopic argument[177] for small effects has to do with the fact the electron-hole excitations that enter the phonon self-energy occur over an energy range of many eV's. If one thinks in terms of BCS theory, we know that superconductivity only effects electronic states in a region $\sim \hbar\omega_D$ about the Fermi surface, where $\hbar\omega_D$ is of the order of meV's. Since superconductivity influences only a tiny part of the energy range, the effects on the phonons should be small as well.

Despite this, it still has been possible to observe changes in the phonon spectrum in the superconducting state experimentally in some conventional materials. As an example, Shapiro, Shirane and Axe[178] performed inelastic neutron scattering experiments on Nb (T_c = 9.2 K). In these experiments, they were able to obtain precise linewidth and frequency measurements of some transverse acoustic modes. Generally what they found was that for phonons with frequencies less than 2Δ, a decrease in linewidth was observed below T_c On the other hand, dropping below the critical temperature had the effect of increasing the linewidth as zero temperature was approached for a phonon that had a frequency larger than 2Δ. This change in behavior at 2Δ provides a means by which the gap can be determined.

From Shapiro *et al.* 's data, it appears that $2\Delta/k_BT_c \sim 4.0$, which is fairly consistent with the types of values obtained for this ratio from other means. It should be noted that the observed changes in linewidth in either case were of the order of 10 to 20 percent. As for frequency shifts, they were able to detect a lowering of frequency or softening for several phonons. The softening was typically of the order of 1 percent but was as high as 3 percent in at least one case. While these shifts were small, they were definitely above instrument resolution. Interestingly, the softenings were observed in phonons that were both above and below 2Δ.

More recently, changes in linewidths and shifts in phonon frequency have been observed in YBCO. As was the case for Nb, these results are being used to try and determine a value for Δ as well as the electron-phonon coupling strength. Of course, it is desirable to use a theoretical formula for the phonon self-energy in order to compare with these experimental results. As it turns out, several such formulas have been derived and these shall be discussed in the next section. Besides these earlier formulas, the derivation of a new formula for the phonon self-energy, written directly on the real frequency axis and applicable for all coupling strengths, is discussed. In the third section of this chapter, the effects of coupling strength, temperature dependence and impurity concentration are all explored using this new formula. The results obtained using the new formula are also compared with results from an earlier formulation written on the imaginary frequency axis. This earlier formula requires the use of Padé approximants. Some experimental results will also be commented upon. A conclusion is to be found in the fourth section of this chapter.

7.2 FORMULAS FOR THE PHONON SELF-ENERGY

Zeyher and Zwicknagl[177,179,180] have performed and extensive analysis of the phonon self-energy using an imaginary frequency axis formulation. Along with considering the strong coupling Eliashberg case, they also derive a formula for the BCS limit. It should be noted that BCS formulas have been derived in the past[181,182]. In particular, Schuster[181] obtained a formula that could be applied for finite phonon momentum vector, $\vec{q}$. This formula was used to compare with the neutron scattering results for Nb discussed in the introduction. Despite being in the BCS limit, the theoretical results compared favourably with experiment.

Zeyher and Zwicknagl on the other hand concentrate exclusively on the $\vec{q} \rightarrow 0$ limit. There are two reasons for this. First of all, information about changes in phonon frequency and phonon linewidths for YBCO has been extracted from Raman experiments. In these experiments, laser light is used. In a Raman process, photons that enter the sample are scattered by optical phonons. Since generally $\vec{q}_{photon} << \vec{q}_{BZD}$, where $BZD \equiv$ Brillioun zone boundary, one obtains information about phonons in the region of the zone center, $\vec{q} \sim 0$. The second reason has to do with the mathematics. While a finite $\vec{q}$ derivation can be performed fairly straight forwardly in the BCS limit, the added complications involved in Eliashberg theory make such an analytical derivation extremely difficult. As we shall see, even in their $\vec{q} \rightarrow 0$ calculation some simplifying assumptions are introduced.

The starting point for Zeyher and Zwicknagl is a general formula for the phonon self-energy. This is illustrated by the set of Feynman diagrams in Fig. 7.1. The first diagram represents the phonon self-energy itself. The black

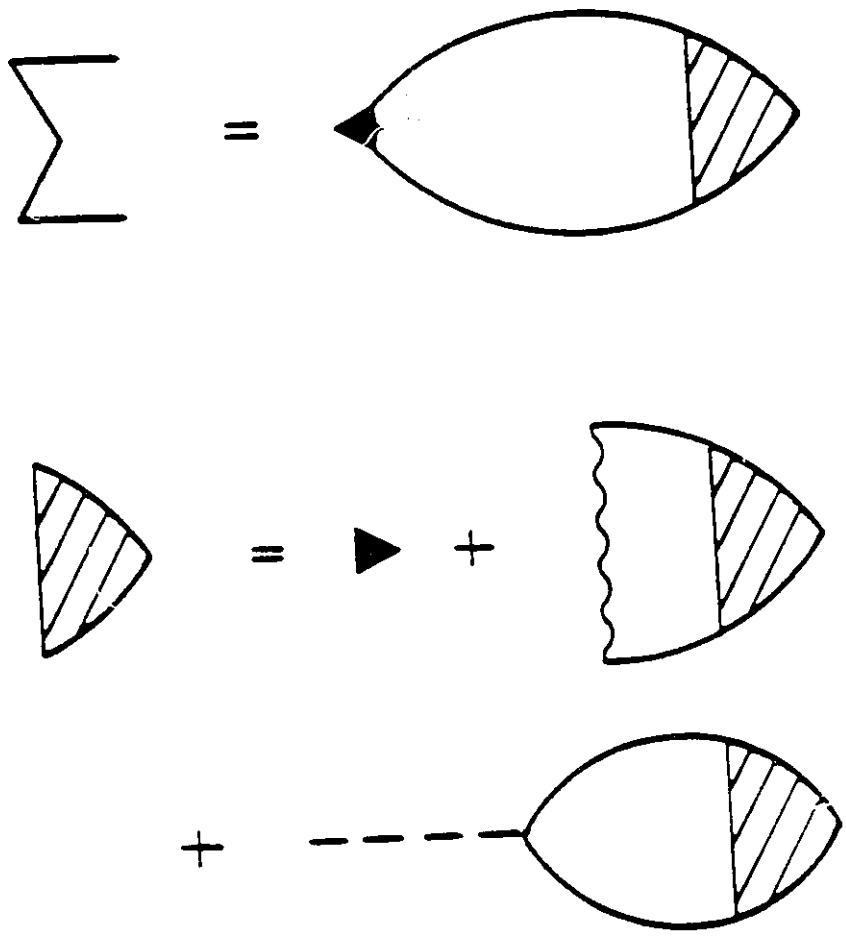

Figure 7.1 The Feynman diagrams that contribute to the phonon self-energy.

triangle represents a bare electron-phonon vertex. the shaded triangle represents the renormalized vertex. The solid lines represent electron propagators. Below this are the diagrams which enter the renormalized electron-phonon vertex. The wavy lines represent primarily phonon propagators, while the dashed line represents the Coulomb interaction. The actual analytic expressions corresponding to Fig. 7.1 are given by

$$\Sigma_\sigma(q) = T\sum_{\vec{k}} g^*_{\vec{k}\vec{k}+\vec{q}\sigma} Tr\{\tau_3 G(k+q)\Gamma_\sigma(k,k+q)\, G(k)\} \tag{7.1}$$

and

$$\Gamma_\sigma(k,k+q) = g_{\vec{k}\vec{k}+\vec{q}\sigma}\tau_3 - \frac{T}{N(0)}\sum_{\vec{k}'} \tau_3 G(k')\Gamma_\sigma(k'+q,k)\, G(k'+q)\tau_3 W(k,k')$$

$$+V_c(\vec{q})\tau_3 T\sum_{\vec{k}'} Tr\{\tau_3 G(k')\Gamma_\sigma(k',k'+q)\, G(k'+q)\}\ . \tag{7.2}$$

Note in these formulas that $k \equiv \vec{k}, i\omega_n$. In second term of the expression for the renormalized electron-phonon vertex, $\Gamma_\sigma(k,k+q)$, there appears the factor $W(k,k')$. This factor contains information about the virtual phonon exchange responsible for the superconductor as well as scaled Coulomb repulsion between the Cooper pairs. μ^*, and impurity effects:

$$W(k,k') = \lambda(k,k') - \mu^*\theta(\omega_c - |\omega_n - \omega_{n'}|) + \delta_{nn'}\frac{t^+}{T}\ , \tag{7.3}$$

where $\lambda(k,k')$ is the momentum dependent generalization of $\lambda(z)$ given by equation (2.27) in chapter 2. In this second term, the momentum transfer is determined by points on the Fermi surface. In the third term the momentum transfer is instead given by the external momentum $\vec{q}$. In this term, $V_c(\vec{q})$ is just the Fourier transform of the Coulomb potential:

$$V_c(\vec{q}) = \frac{4\pi e^2}{\Omega_c q^2}\ , \tag{7.4}$$

where Ω_c is the primitive cell volume.

This general formula for the phonon self-energy is quite complicated and unwieldy. Fortunately, Zeyher and Zwicknagl were able to show that under certain circumstances the situation could be greatly simplified. This required an appeal to group theory in order to do this. They argue that $G(k)$ which contains the order parameter must transform according to the trivial representation and further that the $V_c(\vec{q})$ term in the expression for $\Gamma_\sigma(q)$ must also transform according to the trivial representation because of the sum over k'. In a similar manner, they explain that the second term transforms like the trivial representation as well. For phonons that do not transform like the trivial representation these vertex corrections should thus be zero. This leads to the conclusion that for these phonons all that is required is to calculate the lowest order diagram. This is an important simplification. Even for phonons that do transform according to the trivial representation the situation becomes simplified in the $\vec{q} \to 0$ limit. In this limit, the Coulomb term dominates the equation for the vertex. Taking this into account and performing an average over momentum yields the result

$$\Gamma_\sigma(q) = \frac{g_{\vec{q}\sigma}}{1 - V_c(\vec{q})\Pi(q)} \,. \tag{7.5}$$

Since $V_c(\vec{q}) \to \infty$ as $\vec{q} \to 0$, the electron-phonon vertex becomes completely suppressed and this leads to the conclusion that totally symmetric phonons should not be observable by optical means.

In equation (7.5) there appears the susceptibility $\Pi(q)$, where $q \equiv \vec{q}, i\nu_n$. Since phonons are bosons, $\nu_n = 2\pi T n$ where $n = 0, \pm 1, \pm 2 \cdots$. In the

limit $\vec{q} \to 0$ and converting the momentum sum to an integral this is given by

$$\Pi(i\nu_n) = T\sum_m \Omega_c \int \frac{d^3k}{(2\pi)^3} Tr\{\tau_3 G(\vec{k}, i\omega_m + i\nu_n)\tau_3 G(\vec{k}, i\omega_m)\} \ . \qquad (7.6)$$

In the not fully symmetric case, where the vertex corrections drop out, calculating the self-energy really comes down to calculating this susceptibility. In particular, if one makes the assumption that $g_{\vec{k}\vec{k}\sigma}$ is independent of $\vec{k}$, then the relationship between the phonon self-energy and $\Pi(i\nu_n)$ becomes

$$\Sigma_\sigma(i\nu_n) = |g_\sigma|^2 \Pi(i\nu_n) \ . \qquad (7.7)$$

The first thing that must be done in order to evaluate $\Pi(i\nu_n)$ is switch from an integral over momentum to an integral over energy in the standard way[34]:

$$\Omega_c \int \frac{d^3k}{(2\pi)^3} \to \int_{-\infty}^{\infty} N(0) d\epsilon \ . \qquad (7.8)$$

Note for the energy ϵ that the $\vec{k}$ subscript has been dropped. For $G(\vec{k}, i\omega_m)$ one simply uses the expression (2.12) given in Chapter 2, with $\omega \to i\omega_n$. In order to take the trace one makes use of the matrix identities $\tau_3^2 = \tau_3^4 = I$ and $\tau_3\tau_1\tau_3\tau_1 = -I$. The traces of all the remaining matrix products are zero. After taking the trace, one ends up with the expression

$$\Pi(i\nu_n) = 2T\sum_m \int_{-\infty}^{\infty} N(0) d\epsilon \frac{-\tilde{\omega}_{n+m}\tilde{\omega}_m + \epsilon - \tilde{\Delta}_{n+m}\tilde{\Delta}_m}{(\tilde{\omega}_{n+m}^2 + (\epsilon^2 + \tilde{\Delta}_{m+n}))(\tilde{\omega}_m^2 + (\epsilon^2 + \tilde{\Delta}_n))} \ . \qquad (7.9)$$

To do the integral over ϵ one can use the following integral identity:

$$\int_{-\infty}^{\infty} d\epsilon \frac{\epsilon^2 - a}{(\epsilon^2 + b^2)(\epsilon^2 + c^2)} = \frac{\pi}{b + c}\left[1 - \frac{a}{bc}\right] \ . \qquad (7.10)$$

The final result is given by

$$\frac{\Pi(i\nu_n)}{N(0)} = 2\pi T\sum_m \frac{1}{\sqrt{\tilde{\omega}_n^2 + \tilde{\Delta}_n^2} + \sqrt{\tilde{\omega}_{n+m}^2 + \tilde{\Delta}_{n+m}^2}}\left\{1 - \frac{\tilde{\omega}_n\tilde{\omega}_{n+m} + \tilde{\Delta}_n\tilde{\Delta}_{n+m}}{\sqrt{\tilde{\omega}_n^2 + \tilde{\Delta}_n^2}\sqrt{\tilde{\omega}_{n+m}^2 + \tilde{\Delta}_{n+m}^2}}\right\} . \qquad (7.11)$$

What we are generally interested in is the superconducting state relative to the normal state, so that the quantity that is usually calculated is

$$\frac{\Delta\Pi(i\nu_n)}{N(0)} = \frac{\Pi(i\nu_n) - \Pi_N(i\nu_n)}{N(0)} , \tag{7.12}$$

where $\Pi_N(i\nu_n)$ is the normal state susceptibility given by

$$\Pi_N(i\nu_n) = 2\pi T \sum_m \frac{1}{|\tilde{\omega}_n^0| + |\tilde{\omega}_{n+m}^0|}\{1 - sgn(\tilde{\omega}_n^0\tilde{\omega}_{n+m}^0)\} . \tag{7.13}$$

The $\tilde{\omega}_n^0$'s are the normal state renormalized frequencies. Once $\frac{\Delta\Pi(i\nu_n)}{N(0)}$ is known for several $i\nu_n$'s, the Padé technique discussed in Chapter 2 can be used to analytically continue to the real axis so that $\frac{\Delta\Pi(\nu)}{N(0)}$ can be obtained. At this stage one is then able to calculate relative phonon shifts and linewidths from the real and imaginary parts of $\Delta\Sigma_\sigma(\nu)$. The actual relationship between the change in self-energy and the phonon shifts and linewidth changes at a particular frequency is given by[183]:

$$\Delta\Sigma_\sigma(\nu) = \Delta\nu - i\Delta\gamma , \tag{7.14}$$

where $\Delta\nu$ is the frequency shift and $\Delta\gamma$ is the change in linewidth.

While the phonon self-energy can be obtained using this imaginary axis technique developed by Zeyher and Zwicknagl, it is also of interest to write the self-energy formula directly on the real frequency axis. As stated in Chapter 2, two important problems with the Padé technique are a loss of very sharp structure and difficulties at higher temperature. These problems lead one to question any results obtained from imaginary axis formulation. As a check of their validity, they should be compared with results from a real axis

formulation. Indeed, the real axis results should be considered exact while the imaginary axis results are, at best, good approximations.

For the BCS case, the starting point for the exact analytic continuation to the real axis would be equation (7.9). In the BCS limit, one has $\tilde{\omega}_n \to \omega_n$ and $\tilde{\Delta}_n \to \Delta$. Using these substitutions, one can perform the sum over the Matsubara frequencies and then the integral over ϵ. At zero temperature, the final result for $\nu > 0$ is[179] :

$$\frac{\Pi(\nu)}{N(0)} = \begin{cases} -\frac{2}{\sqrt{(1-\bar{\nu}^2)\bar{\nu}^2}} \tan^{-1}\sqrt{\frac{\bar{\nu}^2}{(1-\bar{\nu}^2)}} & \text{if } \bar{\nu} < 1; \\ \frac{1}{\sqrt{(\bar{\nu}^2-1)\bar{\nu}^2}} \left\{ \ln\left(2\bar{\nu}^2 - 1 + \sqrt{\bar{\nu}^2(\bar{\nu}^2-1)}\right) - i\pi \right\} & \text{if } \bar{\nu} > 1 . \end{cases} \quad (7.15)$$

where $\bar{\nu} = \nu/2\Delta$. It should be noted that, in the specific case $\nu = 0$, $\Pi(\nu) = 0$. In this case, since there is no electron-phonon renormalization included, *i.e.*, $Z(\omega) = 1$, one finds that $\Pi_N = 0$ so that $\Delta\Pi = \Pi$ for BCS. Equation (7.15) is plotted as a function of $\nu/2\Delta$ in Fig. 7.2. The real part of $\frac{\Pi(\nu)}{N(0)}$ is represented by the solid line and the imaginary part by the dashed. Starting with the real part, we notice that it begins at -2 for $\nu \sim 0$ and then starts to drop, eventually reaching a singularity right at $\nu = 2\Delta$. This implies that phonons that are below 2Δ in frequency will shift downward in frequency or soften, with the shifts becoming larger as 2Δ is approached. Above $\nu = 2\Delta$, $\mathrm{Re}\{\Pi\}$ is positive definite, starting at a value of 2 and then gradually decaying with a $\bar{\nu}^{-2}$ law. This implies that phonons that occur above 2Δ will shift upward in frequency or harden. As for $\mathrm{Im}\{\Pi\}$, it is exactly zero below $\nu = 2\Delta$ which implies that the linewidths of the phonons in this range should be zero in the superconducting state. Above $\nu = 2\Delta$, $\mathrm{Im}\{\Pi\}$ begins at a negative singularity, then gradually increases and appears to approach zero asymptotically. Phonons in this region should broaden with the linewidths approaching infinity for $\nu \sim 2\Delta$.

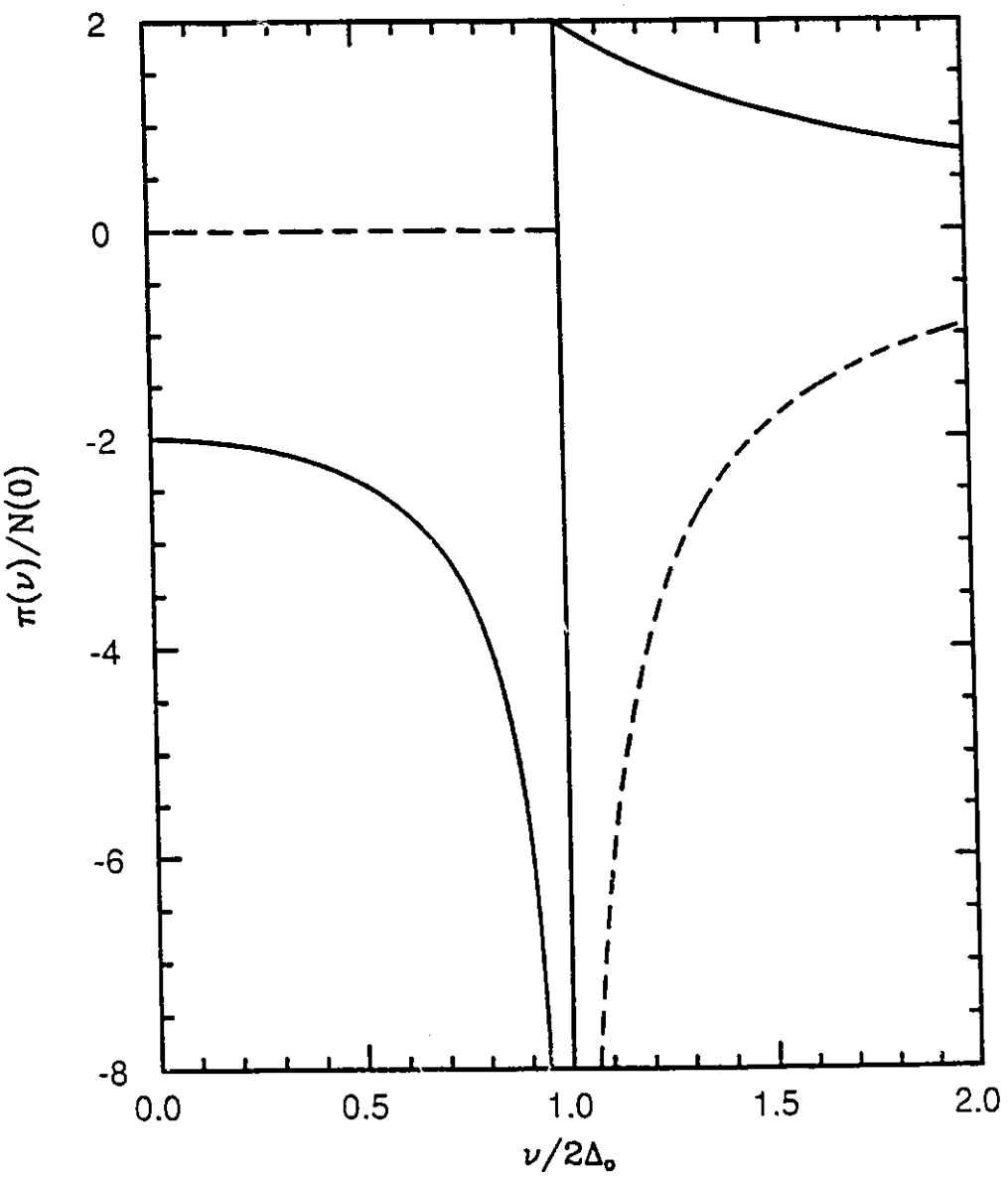

Figure 7.2 $\frac{\Pi(\nu)}{N(0)}$ in the BCS limit is plotted as a function of $\nu/2\Delta_o$. The solid line gives the real part and the dashed curve represents the imaginary part.

For the general Eliashberg case, the starting point for the analytic continuation is the stage just before equation (7.9). Instead of taking the trace, one introduces the spectral representation of the Green's functions

$$G(\vec{k}, i\omega_m + i\nu_n) = \int_{-\infty}^{\infty} \frac{d\omega'}{\pi} \frac{Im\{G(\vec{k},\omega')\}}{i\omega_m + i\nu_n - \omega'} \tag{7.16}$$

and

$$G(\vec{k}, i\omega_m) = \int_{-\infty}^{\infty} \frac{d\omega}{\pi} \frac{Im\{G(\vec{k},\omega)\}}{i\omega_m - \omega} \tag{7.17}$$

so that

$$\Pi(i\nu_n) = T\frac{N(0)}{\pi^2} \sum_m \int_{-\infty}^{\infty} d\epsilon \int_{-\infty}^{\infty} d\omega \int_{-\infty}^{\infty} d\omega' \frac{Tr\{\tau_3 Im\{G(\vec{k},\omega')\}\tau_3 Im\{G(\vec{k},\omega)\}\}}{(i\omega_m - \omega)(i\omega_m + i\nu_n - \omega')} . \tag{7.18}$$

At this point, the sum over the Matsubara frequencies can be performed using residues. After the sum is performed, we can reset $i\nu_n \rightarrow \nu + i\delta$, where δ is a positive infinitesimal. The result is the real axis formula

$$\Pi(\nu + i\delta) = T\frac{N(0)}{\pi^2} \sum_m \int_{-\infty}^{\infty} d\epsilon \int_{-\infty}^{\infty} d\omega \int_{-\infty}^{\infty} d\omega' [f(\omega') - f(\omega)]$$

$$\frac{Tr\{\tau_3 Im\{G(\vec{k},\omega')\}\tau_3 Im\{G(\vec{k},\omega)\}\}}{(\omega' + \nu - \omega + i\delta)} . \tag{7.19}$$

where $f(\omega)$ is the Fermi function. One of the integrals and the denominator can be eliminated by again exploiting the spectral representation. Also at this point it is useful to make the substitution

$$Im\{G(\vec{k},\omega)\} = \frac{1}{2i}[G(\vec{k},\omega + i\delta) - G(\vec{k},\omega - i\delta)] . \tag{7.20}$$

The formula now becomes

$$\frac{\Pi(\nu + i\delta)}{N(0)} = \frac{i}{2\pi} \int_{-\infty}^{\infty} d\epsilon \int_{-\infty}^{\infty} d\omega\, f(\omega) Tr\{\tau_3(G(\vec{k},\omega + \nu + i\delta) + G(\vec{k},\omega - \nu - i\delta))$$

$$\tau_3(G(\vec{k},\omega + i\delta) - G(\vec{k},\omega - i\delta))\} . \tag{7.21}$$

At this stage, the the Eliashberg form of the superconducting Green's function is substituted in and the traces are performed. We are left with an integral with four pieces. However, each piece is similar in form to the imaginary axis expression given in equation (7.9) and so we can exploit the integral given in equation (7.10) to help perform the integration over ϵ. Another important point is that it is desirable to keep everything in terms of frequencies that occur in the upper half of the complex plane, *i.e.*, $\omega + i\delta$ as opposed to $\omega - i\delta$. In order to do this, one can use the symmetries

$$\tilde{\omega}(-z) = -\tilde{\omega}(z)$$

$$\tilde{\omega}^*(z) = \tilde{\omega}(z^*)$$

$$\tilde{\Delta}(-z) = \tilde{\Delta}(z)$$

and

$$\tilde{\Delta}^*(z) = \tilde{\Delta}^*(z) \; . \tag{7.22}$$

The final result after taking the difference with the normal state is given by

$$\frac{\Delta\Pi(\nu)}{N(0)} = \int_{-\infty}^{\infty} d\omega \, \tanh(\frac{\omega}{2T}) \Bigg[\frac{1}{\Lambda(\omega) + \Lambda(\omega+\nu)} \Bigg\{ 1 - \frac{\tilde{\omega}(\omega)\tilde{\omega}(\omega+\nu) - \tilde{\Delta}(\omega)\tilde{\Delta}(\omega+\nu)}{\Lambda(\omega)\Lambda(\omega+\nu)} \Bigg\}$$
$$+ \frac{1}{\Lambda^*(\omega) - \Lambda(\omega+\nu)} \Bigg\{ 1 + \frac{\tilde{\omega}^*(\omega)\tilde{\omega}(\omega+\nu) - \tilde{\Delta}^*(\omega)\tilde{\Delta}(\omega+\nu)}{\Lambda^*(\omega)\Lambda(\omega+\nu)} \Bigg\} - \frac{2}{\tilde{\omega}_N^*(\omega) - \tilde{\omega}_N(\omega+\nu)} \Bigg] \tag{7.23}$$

where

$$\Lambda(\omega) = \sqrt{\tilde{\omega}^2(\omega) - \tilde{\Delta}^2(\omega)} \; . \tag{7.24}$$

Note that for all the frequencies in these two equations that an $i\delta$ should be added, but this notation has been dropped for convenience. The normal state renormalized frequencies, $\tilde{\omega}_N(\omega)$, can be evaluated using equation 6.26, from the last chapter. Using this formula, one can then evaluated the phonon self-energy difference purely on the real axis.

At this stage, the the Eliashberg form of the superconducting Green's function is substituted in and the traces are performed. We are left with an integral with four pieces. However, each piece is similar in form to the imaginary axis expression given in equation (7.9) and so we can exploit the integral given in equation (7.10) to help perform the integration over ϵ. Another important point is that it is desirable to keep everything in terms of frequencies that occur in the upper half of the complex plane, *i.e.*, $\omega + i\delta$ as opposed to $\omega - i\delta$. In order to do this, one can use the symmetries

$$\tilde{\omega}(-z) = -\tilde{\omega}(z)$$

$$\tilde{\omega}^*(z) = \tilde{\omega}(z^*)$$

$$\tilde{\Delta}(-z) = \tilde{\Delta}(z)$$

and

$$\tilde{\Delta}^*(z) = \tilde{\Delta}^*(z) \; . \tag{7.22}$$

The final result after taking the difference with the normal state is given by

$$\frac{\Delta\Pi(\nu)}{N(0)} = \int_{-\infty}^{\infty} d\omega \, \tanh(\frac{\omega}{2T}) \Bigg[\frac{1}{\Lambda(\omega) + \Lambda(\omega+\nu)} \Bigg\{ 1 - \frac{\tilde{\omega}(\omega)\tilde{\omega}(\omega+\nu) - \tilde{\Delta}(\omega)\tilde{\Delta}(\omega+\nu)}{\Lambda(\omega)\Lambda(\omega+\nu)} \Bigg\}$$
$$+ \frac{1}{\Lambda^*(\omega) - \Lambda(\omega+\nu)} \Bigg\{ 1 + \frac{\tilde{\omega}^*(\omega)\tilde{\omega}(\omega+\nu) - \tilde{\Delta}^*(\omega)\tilde{\Delta}(\omega+\nu)}{\Lambda^*(\omega)\Lambda(\omega+\nu)} \Bigg\} - \frac{2}{\tilde{\omega}_N^*(\omega) - \tilde{\omega}_N(\omega+\nu)} \Bigg] \tag{7.23}$$

where

$$\Lambda(\omega) = \sqrt{\tilde{\omega}^2(\omega) - \tilde{\Delta}^2(\omega)} \; . \tag{7.24}$$

Note that for all the frequencies in these two equations that an $i\delta$ should be added, but this notation has been dropped for convenience. The normal state renormalized frequencies, $\tilde{\omega}_N(\omega)$, can be evaluated using equation 6.26, from the last chapter. Using this formula, one can then evaluated the phonon self-energy difference purely on the real axis.

7.3 THEORETICAL RESULTS AND SOME COMMENTS ON EXPERIMENTS

In this section, we would like to determine what kind of results the real frequency axis formula, (7.23), will give us under various physical circumstances. To begin with, we would like to compare the BCS formula discussed in the previous section with what happens for strong coupling. In order to do this, we have used an $\alpha^2F(\omega)$ shape that is zero up to 24 meV and then is constant at finite value up until 100 meV, at which point it is cutoff, forming a box. This is somewhat similar to the $\alpha^2F(\omega)$ shape that Zeyher and Zwicknagl used in their work, except that, above 24 meV, they input data from the F(ω) of YBCO as obtained by Renker *et al.* [184]. In their model, they justify setting the lower part of the spectrum equal to zero by stating that the energy levels of Ba and Y are far away from the Fermi surface and consequently there should be very little electron-phonon coupling to the low lying phonon modes which these atoms contribute to. In preparing this thesis, several other spectral shapes were also tried. It was found that the actual spectral shape used has very little effect on the curves for $\Delta\Pi(\nu)/N(0)$. The most important property in determining these curves appears to be the overall electron-phonon coupling strength.

In Fig. 7.3, the real part of $\Delta\Pi(\nu)/N(0)$ is plotted vs. $\nu/2\Delta$ for three cases. The solid line represents the BCS result plotted in Fig. 7.2. The dotted line represents a situation where the $\alpha^2F(\omega)$ has been scaled so that, if $\mu^* = 0.0$, T_c would equal 50 K - this implies a mass enhancement of $\lambda = 0.83255$. However, for the actual run $\mu^*(\omega_c = 2000\text{meV}) = -0.096822$, which yields $T_c = 93$ K. The gap ratio that one obtains for this case is $2\Delta_o/k_BT_c = 4.25$.

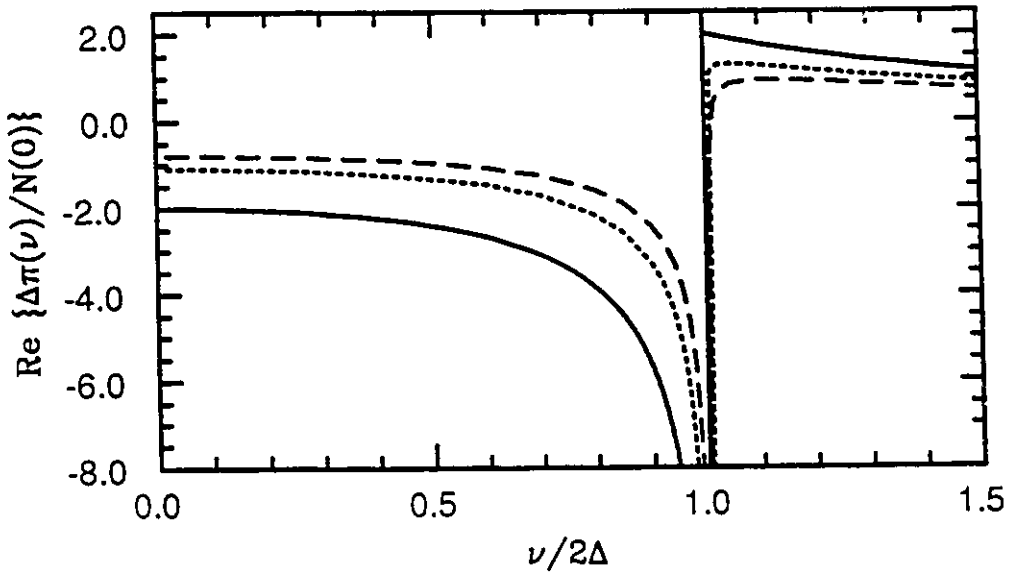

Figure 7.3 $\frac{\mathrm{Re}\{\Delta\Pi(\nu)\}}{N(0)\}}$ vs. $\nu/2\Delta$ is plotted. The solid line is the BCS limit, the dotted line is for $\lambda = 0.83255$ and the dashed line for $\lambda = 1.45373$.

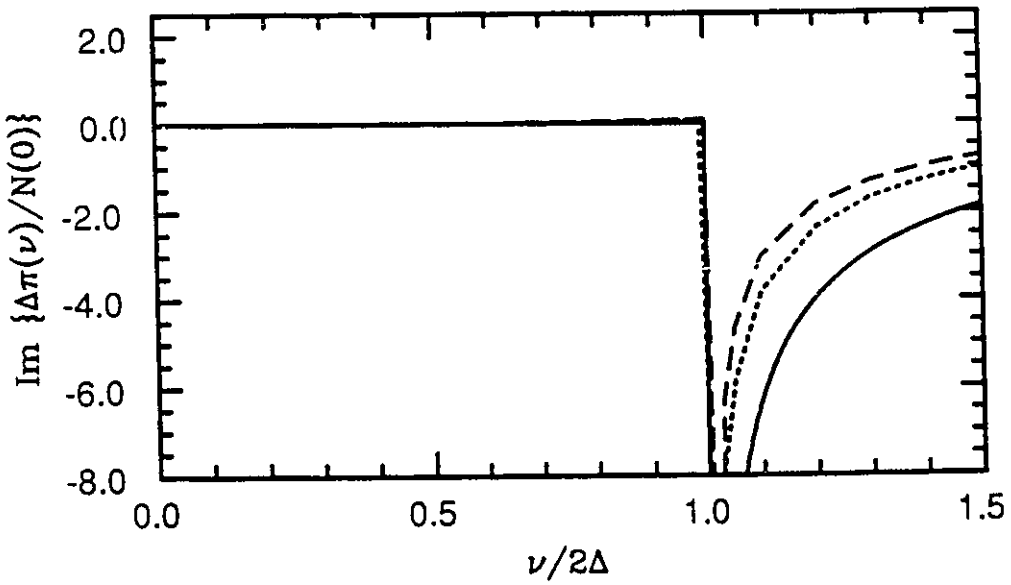

Figure 7.4 $\frac{\mathrm{Im}\{\Delta\Pi(\nu)\}}{N(0)\}}$ vs. $\nu/2\Delta$ is plotted. The solid line is the BCS limit, the dotted line is for $\lambda = 0.83255$ and the dashed line for $\lambda = 1.45373$.

The final case is represented by the dashed line. In this case, the electron-phonon spectrum is scaled so that it now accounts for the entire $T_c = 93$ K. This requires $\lambda = 1.45373$ and yields $2\Delta_o/k_BT_c = 4.61$. Again, it should be emphasized that the latter two curves were generated by using the real frequency axis formula, (7.23), after solving for $\Delta(\omega)$ and $Z(\omega)$ using Marsiglio *et al.* 's Eliashberg equations given in Chapter 2. The calculations were done at $T/T_c = 0.2$, low enough to simulate zero temperature. We see that all three curves have the same basic form and that going from BCS to strong-coupling should not change the qualitative effects - phonons below 2Δ should soften and phonons above 2Δ should harden. One important difference that does not show up in this figure is that $\mathrm{Re}\{\Delta\Pi(\nu)\}$ is no longer singular right at 2Δ. A deep depression is left in place of the singularity. The removal of this singularity can be traced back to the fact that the relevent quantities such as the gap function are complex because of quasiparticle damping effects in the strong coupling case. The situation is somewhat reminiscent of the case of the nuclear spin relaxation discussed in Chapter 5.

While qualitatively the curves are quite similar, there is a definite progression with coupling strength. The BCS curve appears to start at the lowest point - $\mathrm{Re}\{\Delta\Pi(\nu \sim 0)/N(0)\} = -2.0$. The strong coupling curves appear to start higher. The curve for $\lambda = 0.83255$ attains a value of ~ -1.1 for small frequencies while the $\lambda = 1.45373$ curve appears to be of the order of ~ -0.81 in this region. In fact, for low but not zero frequencies, $\mathrm{Re}\{\Delta\Pi(\nu)/N(0)\} \sim -2.0/(1+\lambda)$ in the neighbourhood of zero temperature. Right at zero frequency, it can be shown that $\mathrm{Re}\{\Delta\Pi(\nu)/N(0)\} = 0.0$, independent of temperature. This quantitative difference in the curves is maintained as the frequency is increased indicating that, for $\nu < 2\Delta$, the stronger the

electron-phonon coupling is, the less effective the system is in softening the phonon frequencies. Above $\nu = 2\Delta$, the BCS curve has the largest peak - $\mathrm{Re}\{\Delta\Pi(\nu \sim 2\Delta)/N(0)\} = 2.0$. As the coupling is increased, the peak drops to ~ 1.3 for $\lambda = 0.83255$ and ~ 0.5 for $\lambda = 1.45373$. Thus, for this frequency range, increasing the coupling strength appears to lower the systems effectiveness in hardening the phonon frequencies.

In Fig. 7.4, the imaginary part of $\Delta\Pi(\nu)/N(0)$ is plotted vs. $\nu/2\Delta$ for the same three cases as the previous figure. The solid line again refers to the BCS case. As was mentioned earlier, $\mathrm{Im}\{\Pi(\nu)/N(0)\} = 0.0$ up to $\nu = 2\Delta$, implying that, in the BCS case, the phonon line width is zero in this frequency range in the superconducting as well as normal state. While it is difficult to see in this figure, for the two finite λ cases, $\mathrm{Im}\{\Delta\Pi(\nu)/N(0)\}$, while small, is definitely greater than zero in this frequency range. The size of $\mathrm{Im}\{\Delta\Pi(\nu)/N(0)\}$ grows as $\nu = 2\Delta$ is approached and is slightly larger for the $\lambda = 1.45373$ case. These results indicate that phonons below 2Δ should sharpen if only slightly in the strong coupling case. This is due to the fact that, while $\mathrm{Im}\{\Pi_S(\nu)/N(0)\}$ remains essentially zero in this frequency range for strong coupling, $\mathrm{Im}\{\Pi_N(\nu)/N(0)\}$ is now finite and negative because the phonons can now decay via the electron-phonon interaction in the normal state. Above $\nu = 2\Delta$, the two curves for finite λ behave in a similar fashion as the BCS curve. However, the singularity at 2Δ is again removed. The BCS curve falls below the other two curves in this region. The $\lambda = 0.83255$ curve is next in sequence and falls below the $\lambda = 1.45373$ curve. Once again we have a situation where increasing coupling strength appears to reduce the effect - in this case the level of phonon linewidth broadening.

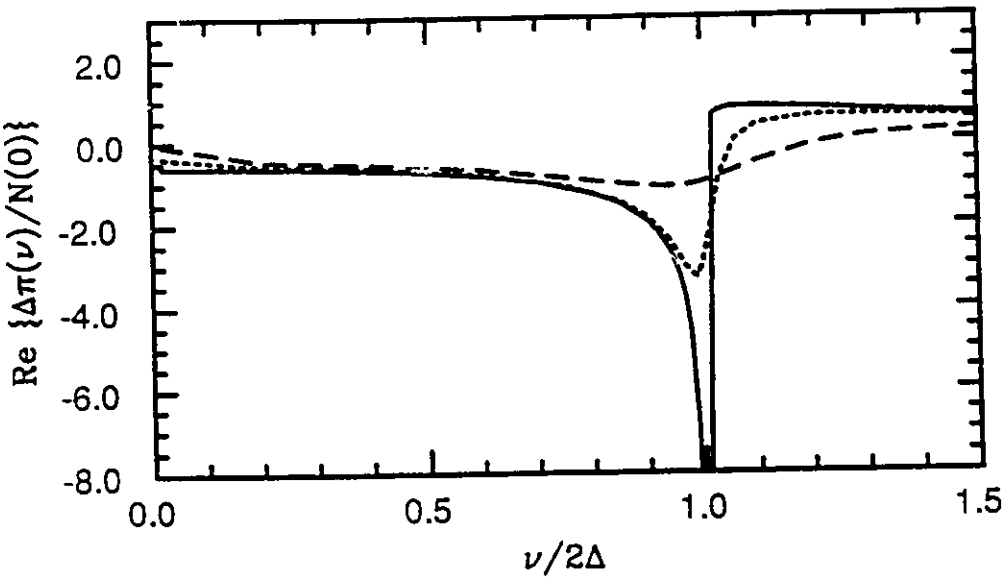

Figure 7.5 $\frac{\mathrm{Re}\{\Delta\Pi(\nu)\}}{N(0)}$ vs. $\nu/2\Delta$ is plotted. This time the temperature is varied. The curves are $T/T_c = 0.15$ (solid line), $T/T_c = 0.6$ (dotted) and $T/T_c = 0.8$ (dashed).

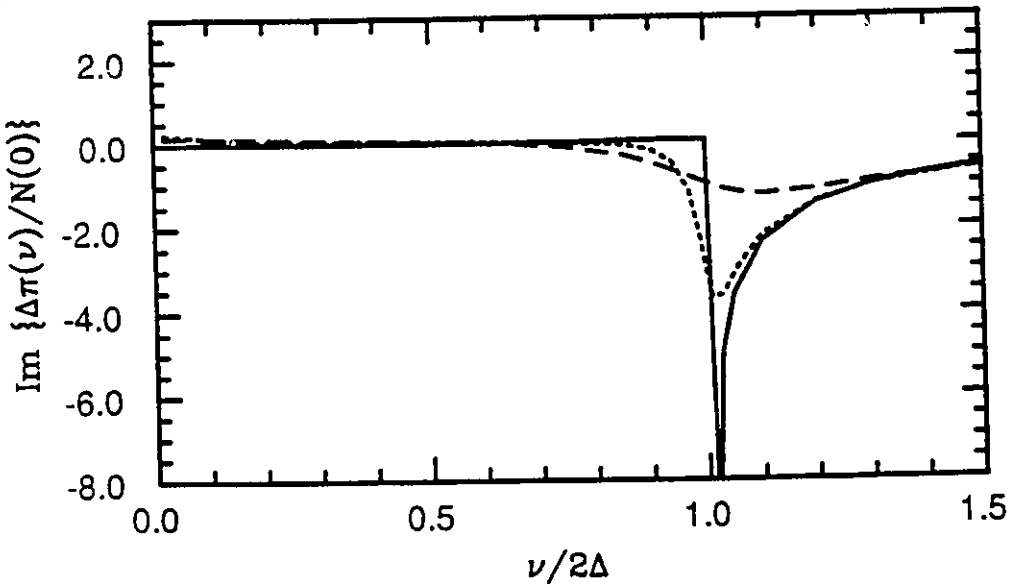

Figure 7.6 $\frac{\mathrm{Im}\{\Delta\Pi(\nu)\}}{N(0)}$ vs. $\nu/2\Delta$ is plotted for the temperatures $T/T_c = 0.15$ (solid line), $T/T_c = 0.6$ (dotted) and $T/T_c = 0.8$ (dashed).

Having established how strong coupling affects $\Delta\Pi(\nu)/N(0)$, it is of interest to see how some other factors influence this function. First of all, we consider the effect of temperature. In Fig. 7.5, $\mathrm{Re}\{\Delta\Pi(\nu)/N(0)\}$ is plotted vs. $\nu/2\Delta$ for several different temperatures - $T/T_c = 0.15$ (solid line), $T/T_c = 0.6$ (dotted) and $T/T_c = 0.8$ (dashed). To generate these curves, the box $\alpha^2F(\omega)$ of the previous calculations was again used. In this case, a finite μ^* was used, $\mu^*(\omega_c = 2000\mathrm{meV}) = 0.25$, and T_c again was fixed at 93 K. The λ that satisfied these parameters was 2.269 and the gap ratio was $2\Delta_o/k_bT_c = 4.99$, so this represents an even stronger coupling case than any of those shown in the previous figure. We see that as the temperature is increased, the depression in $\mathrm{Re}\{\Delta\Pi(\nu)/N(0)\}$ near 2Δ is reduced and the width of the depression becomes broader due to thermal smearing. Above 2Δ, the maximum is gradually reduced with temperature. Another interesting feature in this figure is what occurs at the lower frequencies. Earlier it was mentioned that $\mathrm{Re}\{\Delta\Pi(\nu = 0)/N(0)\} = 0$ independent of temperature. That this should be the case is not obvious looking at the lowest temperature curve because the upturn occurs at such a low frequency that it would not show up in this figure. For the two higher temperatures, however, the upturn at low frequencies is now quite visible. One other point that should be emphasized here is that as we near T_c, the value of Δ reduces with increasing rapidity, particularly above $T/T_c \sim 0.4$. If one was to replot these curves just as a function of ν, the curves at higher temperature would have their minima at lower and lower frequencies. This is an extremely important consideration if one is interested in what is happening at a particular frequency.

In Fig. 7.6, $\mathrm{Im}\{\Delta\Pi(\nu)/N(0)\}$ is plotted vs. $\nu/2\Delta$. We are again exploring the effect of temperature and the curves apply for the same parameter

sets as the previous figure. The effect of temperature on the imaginary part of $\{\Delta\Pi(\nu)/N(0)\}$ appears to be analogous to that on the real part. Perhaps the most interesting feature of these curves is how the sharp "corner" at 2Δ is gradually lost as the temperature is increased, giving a region where $\mathrm{Im}\{\Delta\Pi(\nu)/N(0)\}$ can be less than zero even for $\nu > 2\Delta$. Hence, at temperatures approaching T_c, phonons with frequencies significantly less that 2Δ can be broadened.

In Fig. 7.7, $\mathrm{Re}\{\Delta\Pi(\nu)/N(0)\}$ is again plotted vs. $\nu/2\Delta$ for the same case as the previous figure, except here the temperature is held fixed at $T/T_c = 0.15$ and now normal impurities are introduced. The impurity concentrations depicted on the figure are $t^+ = 0$ meV (solid line) , $t^+ = 6.37$ meV (dotted) and $t^+ = 12.74$ meV (dashed). Unlike the previous chapter, where the impurity dependence of the Lee *et al.* conductivity formula was made explicit, the impurity dependence of the real axis phonon self-energy formula here is hidden in the renormalized frequencies and gaps. In order to go from the pure to impure case, one must add the factors $\frac{i\pi t^+\omega}{\sqrt{\omega^2-\Delta(\omega)}}$ and $\frac{i\pi t^+\Delta(\omega)}{\sqrt{\omega^2-\Delta(\omega)}}$ to $\tilde{\omega}(\omega)$ and $\tilde{\Delta}(\omega)$, respectively. At lower frequencies, we see that the inclusion of impurities causes the curves to start smoothly from zero, rather than start at zero and then drop abruptly at a small frequency as the pure case does. For the dirtier case, $t^+ = 12.74$ meV, $\mathrm{Re}\{\Delta\Pi(\nu)/N(0)\} \sim 0$ for a significantly larger range of frequency than the $t^+ = 6.37$ meV case. In the region of $\omega \sim 2\Delta$, we see that the depth of the resonance is reduced by the inclusion of impurities. However, the resonance remains quite sharp even for $t^+ = 12.74$ meV. As was the case for increasing the temperature, the maximum above 2Δ is broadened out and reduced by increasing the impurity concentration.

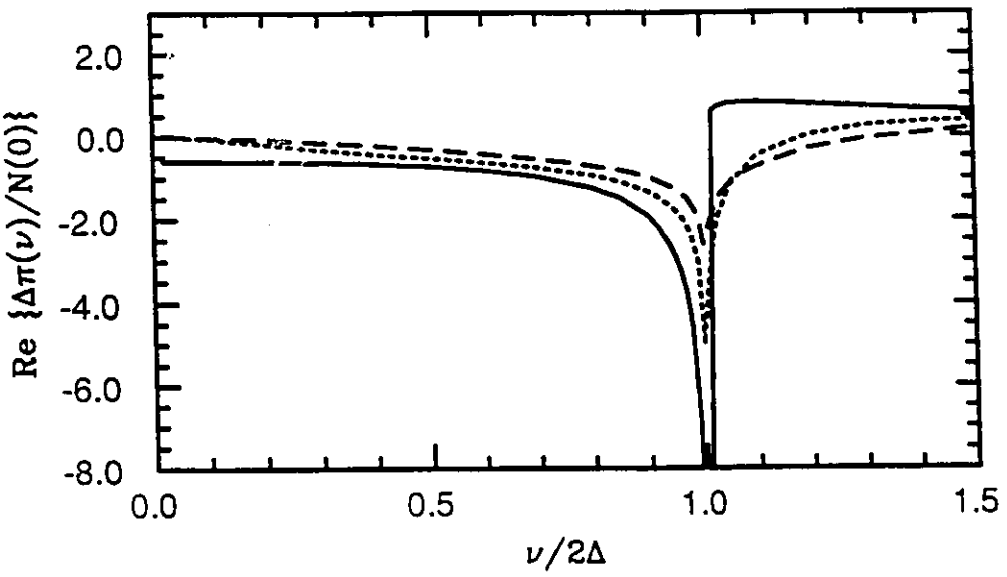

Figure 7.7 $\frac{\mathrm{Re}\{\Delta\Pi(\nu)\}}{N(0)\}}$ vs. $\nu/2\Delta$ is plotted. In this case, impurities are introduced. The curves are $t^+ = 0.0$ meV (solid line), $t^+ = 6.37$ meV (dotted) and $t^+ = 12.74$ meV (dashed).

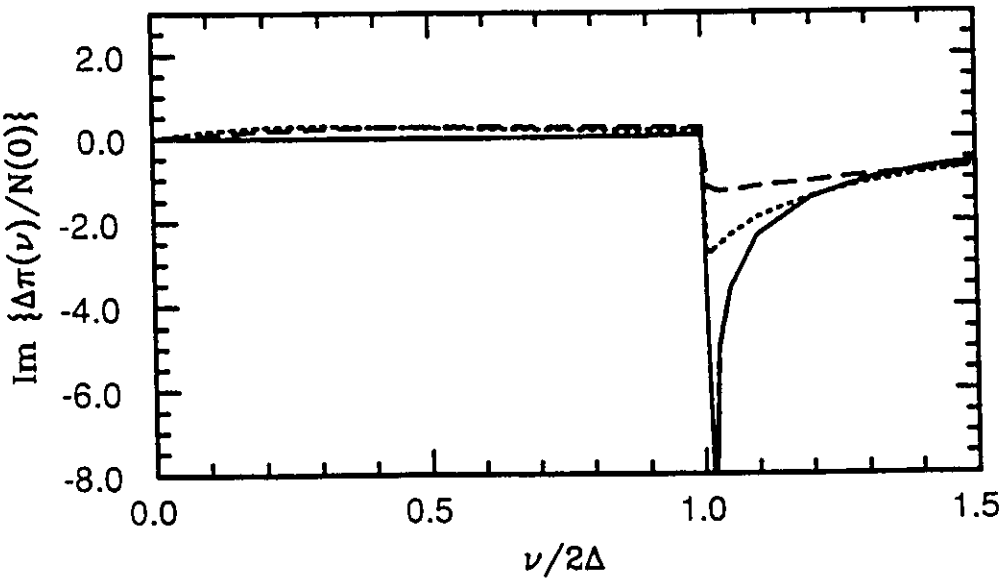

Figure 7.8 $\frac{\mathrm{Im}\{\Delta\Pi(\nu)\}}{N(0)\}}$ vs. $\nu/2\Delta$ is plotted for the impurity concentrations $t^+ = 0.0$ meV (solid line), $t^+ = 6.37$ meV (dotted) and $t^+ = 12.74$ meV (dashed).

In Fig. 7.8, $\mathrm{Im}\{\Delta\Pi(\nu)/N(0)\}$ is plotted vs. $\nu/2\Delta$ for the same impurity concentrations. In a similar manner as the previous figure, the minimum in $\mathrm{Im}\{\Delta\Pi(\nu)/N(0)\}$ is reduced by the presence of impurities, but the drop at $\nu = 2\Delta$ remains quite abrupt. Another significant feature of the impure curves is that they are significantly above zero in the region $\nu < 2\Delta$. This means that one should expect a more significant sharpening of the phonon linewidths in this frequency region in a dirty superconductor than in a clean one since the linewidths in the normal state are broader to begin with in this case.

Having shown some results obtained using the real axis formula for the phonon self-energy, it is now of interest to compare some of these results with those obtained from the imaginary axis formula of Zeyher and Zwicknagl, who, in their papers[177,179], sh[illegible]igures similar in content to all the figures shown so far in this section. In Fig. 7.9, $\mathrm{Re}\{\Delta\Pi(\nu)/N(0)\}$ is again plotted vs. $\nu/2\Delta$. The results shown here apply for the $\lambda = 2.269$ case used to generate the past few figures. The solid line corresponds to $T/T_c = 0.15$ and $t^+ = 0.0$ meV. The dotted line was generated by the same set of parameters but this time using Zeyher and Zwicknagl's formula and an analytic continuation with Padé approximants. In the lower and upper frequency regions of this figure, we see that the agreement is quite good and the curves basically fall on top of each other. However, in the region of 2Δ, there are some significant deviations. In particular, the minimum obtained from the imaginary axis technique is no where near as deep as that obtained from the purely real axis results. Just above 2Δ, the imaginary axis curve overshoots the real axis result. These two features are most likely artifacts due to the

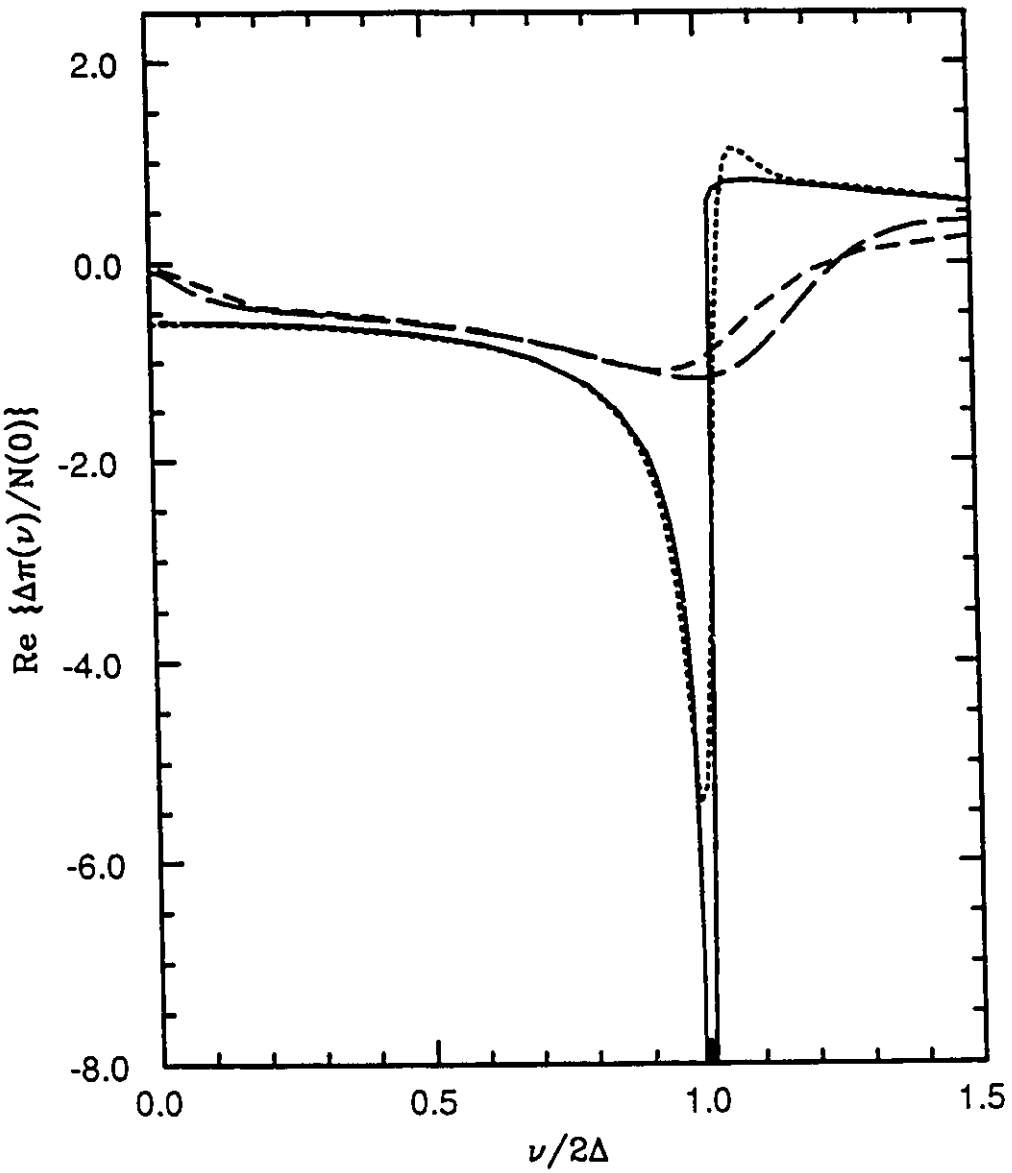

Figure 7.9 $\frac{\mathrm{Re}\{\Delta\Pi(\nu)\}}{N(0)}$ vs. $\nu/2\Delta$ is plotted. Real axis results are compared with the Zeyher and Zwicknagl formula for a case with $\lambda = 2.269$. The real axis and imaginary axis results for $T/T_c = 0.15$ and $t^+ = 0.0$ meV are represented by a solid line and a dotted curve respectively. For the remaining two curves, the reduced temperature is raised to $T/T_c = 0.8$. The short dashed curve gives the real axis result for this temperature and the long dashed curve was obtained using the Zeyher and Zwicknagl formula.

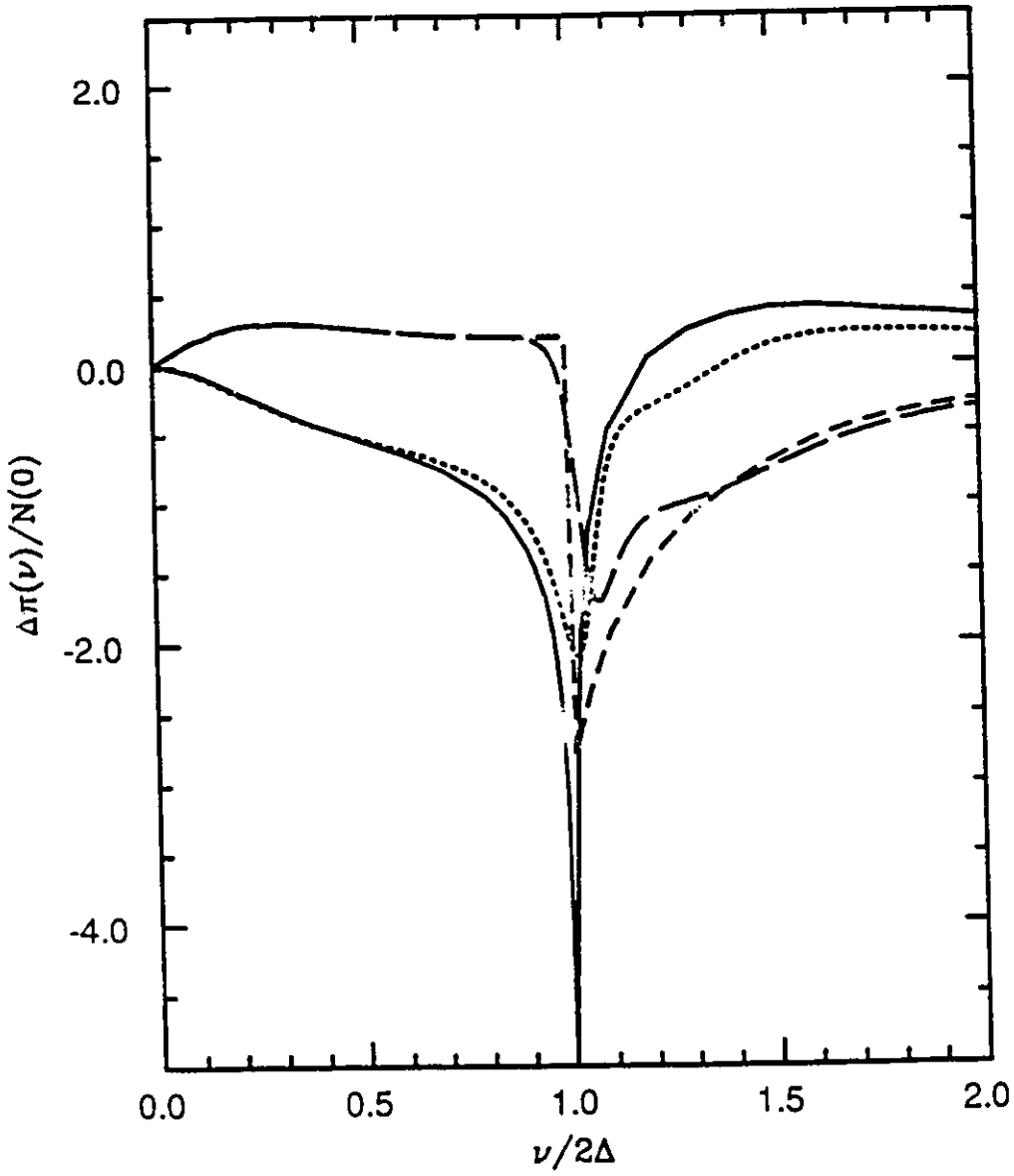

Figure 7.10 $\frac{\Delta\Pi(\nu)}{N(0)}$ vs. $\nu/2\Delta$ is again plotted to compare results of the real and imaginary axes. Unlike the previous figure, impurities are now included- $t^+ = 6.37$ meV. The solid line is $\frac{\mathrm{Re}\{\Delta\Pi(\nu)\}}{N(0)}$ as calculated on the real axis for $T/T_c = 0.15$. The dotted line is the same quantity calculated for the same set of parameters on the imaginary axis. The short dashed line is $\frac{\mathrm{Im}\{\Delta\Pi(\nu)\}}{N(0)}$ as calculated on the real axis for $T/T_c = 0.15$ and the long dashed line represents the same case obtained on the imaginary axis.

use of the Padé algorithm. Also shown are curves for the same set of parameters, except that the reduced temperature is raised to $T/T_c = 0.8$. Here, the short dashed curve represents the real axis results while the long dashed curve was obtained using the imaginary axis formulation. In this case, the imaginary and real axis curves give minima in the region of 2Δ that are about the same depth, and there is good agreement for frequencies less than 2Δ. At higher frequencies, while the curves are qualitively similar, there are significant quantitive differences.

In Fig. 7.10, the results of the real and imaginary axis formulations are again compared, this time for $T/T_c = 0.15$ and $t^+ = 6.37$ meV. The solid line depicts the real axis results for $\mathrm{Re}\{\Delta\Pi(\nu)/N(0)\}$ while the dotted line depicts the imaginary axis results for the same quantity.Once again, there appears to be good agreement at low frequency. However, at 2Δ, the imaginary axis formulation does not even come close in reproducing the sharp minimum obtained from the real axis formula. Above 2Δ, there is qualitative agreement but quantitative differences. In particular, it appears that the imaginary axis formulation would underestimate the degree of phonon hardening in this region. Results for the imaginary part of $\Delta\Pi(\nu)/N(0)$ are also displayed. As was the case for the real part, the agreement is good at low frequencies and the real axis solutions (short dashed line) fall on top of the imaginary axis solutions (long dashed curve) in this region. This is interesting because, as discussed earlier, $\mathrm{Im}\{\Delta\Pi(\nu)/N(0)\}$ is significantly positive in this region. In their original paper[179], Zeyher and Zwicknagl attempt to explain these deviations from zero as being artifacts of the Padé algorithm. Obviously, this is incorrect. As with the real part, $\mathrm{Im}\{\Delta\Pi(\nu)/N(0)\}$ in the region of $\nu = 2\Delta$ is somewhat smeared by using the Padé technique. The sharp

drop at 2Δ obtained using the real axis formula has been to some extent lost. The agreement between the two formulations for higher frequencies for this quantity appears to be quite good.

From the results depicted in Fig. 7.8 and Fig. 7.9, it appears that the imaginary axis formulation has a particular problem in trying to reproduce the minima of the real and imaginary parts of $\Delta\Pi(\nu)/N(0)$ obtained from the exact real frequency axis solutions. This appears to be especially true for situations where there is a finite impurity concentration. This is an extremely important point when one is trying to compare with experimental results. Obviously, the phonon frequency shifts and changes in phonon widths that one would predict for phonons in the neighbourhood of $\nu = 2\Delta$ using the imaginary axis formulation would probrably be quite significant underestimates.

Another extremely important point is that the the imaginary frequency axis results shown in the preceding two figures were calculated during the preparation of this thesis using the Zeyher and Zwicknagl formula. They were not taken from the papers of Zeyher and Zwicknagl. This is important because there are some difference between the imaginary frequency axis results as calculated here and those shown by Zeyher and Zwicknagl. By far the most major difference is where the minima in $\mathrm{Re}\{\Delta\Pi(\nu)/N(0)\}$ and $\mathrm{Im}\{\Delta\Pi(\nu)/N(0)\}$ occur. In the preceding two figures, we find that the resonance phenomena occurs right at or at least very close to $\nu = 2\Delta$ for both the real and imaginary axis formulations. Zeyher and Zwicknagl have shown curves[177] where the minima occur at a frequency closer to $\nu \sim 1.07 \times (2\Delta)$. This is most likely because Zeyher and Zwicknagl have used a value of the gap that is too small. They scale their $\alpha^2F(\omega)$ spectrum to give $T_c = 91$ K for

$\lambda = 2.9$ and then quote a gap ratio of $2\Delta_o/k_BT_c = 4.94$. When a similar spectral shape to theirs (*i.e.*, using Renkers data[83] for F(ω) for $\omega > 24$ meV) was used in our programs, a gap ratio of $2\Delta_o/k_BT_c = 5.38$ was obtained for the same value of λ, indicating that they may have underestimated the gap by about 10 percent. This is consistent with having the resonance effect occur at a point ~ 1.1 times higher than it should be, which is what they indeed find.

Up until now, the quantity that has been concentrated on in this section has been $\Delta\Pi(\nu)/N(0)$. However, normalized values for phonon shifts and linewidths that have the potential to be directly compared with experimental results can also be calculated. From chapter 2, recall that the electron-phonon spectral density $\alpha^2F(\omega)$ can be decomposed into a set of delta function bins centered at the frequencies ω_i, i=$1 \cdots N$, and having the coupling strengths a_i. For $\nu = \omega_i$, one can show that the following relationship holds between $\Sigma_\sigma(\nu)$ and $\Delta\Pi(\nu)/N(0)$:

$$\frac{\Sigma_\sigma(\nu)}{\nu} = \frac{\Delta\Pi(\nu)}{N(0)}\frac{a_i}{\nu} \; . \tag{7.25}$$

From this equation, it is obvious that the actual shift or linewidth change that one obtains will depend very strongly on the structure of the $\alpha^2F(\omega)$ at the particular frequency of interest because of the proportionality with a_i.

This capability to calculate relative shifts and widths will be exploited here. However, no specific fitting is done to the experiments. Instead, some general trends are illustrated for the shifts and linewidth changes as a function of temperature using the real axis formulation and the simple box model for $\alpha^2F(\omega)$ used previously with $\lambda = 2.269$ and $2\Delta_o/k_BT_c = 4.99$.

This was the same case used to generate the data in Fig. 7.5. In this case, $a_i = 0.7604$ for each $\alpha^2 F(\omega)$ bin above 24 meV.

In Fig. 7.11, $\delta\nu/\nu$ is plotted vs. T/T_c, for four different frequencies, namely $\nu = 55$ meV (solid line), $\nu = 42$ meV (dotted), $\nu = 39$ meV (dot-dashed) and $\nu = 35$ meV (dashed). No impurities have been added here. Note that the two curves corresponding to the two highest frequencies remain positive definite. So, for this particular model, one would expect positive shifts only for both these frequencies. This is understandable because $\nu > 2\Delta$ for all temperatures for these frequencies and so we are always in the region where $\mathrm{Re}\{\Delta(\nu)/N(0)\} > 0$. At zero temperature, $2\Delta_o = 41.3$ meV for this example. More interesting are the curves for the lower two frequencies, particularly for $\nu = 39$ meV. For this frequency, the curve starts at ~ -0.07 for $T/T_c = 0.15$ but, as the temperature is increased, goes through a minimum at $T/T_c \sim 0.47$ and then rises rapidly and becomes positive near T_c. What is happening here is that $\nu < 2\Delta$ for the lowest temperatures. However, as the temperature is increased, the value of 2Δ drops so that the frequency eventually passes through the minimum that occurs in $\mathrm{Re}\{\Delta(\nu)/N(0)\}$ at 2Δ. As the temperature continues to be increased, the frequency passes through the region where $\mathrm{Re}\{\Delta(\nu)/N(0)\}$ increases rapidly and finally becomes positive. Thus, by keeping the frequency fixed but changing the temperature, much of the features of the function $\mathrm{Re}\{\Delta(\nu)/N(0)\}$ have been traced out by this curve. The same thing occurs for $\nu = 35$ meV, but in this case the point where $\nu = 2\Delta$ is reached is much higher in temperature and so the minimum in $\delta\nu/\nu$ is reduced by thermal smearing.

In Fig. 7.12, $\delta\nu/\nu$ is again plotted vs. T/T_c, the curves corresponding to the same four frequencies. What is different in this case is that impurities

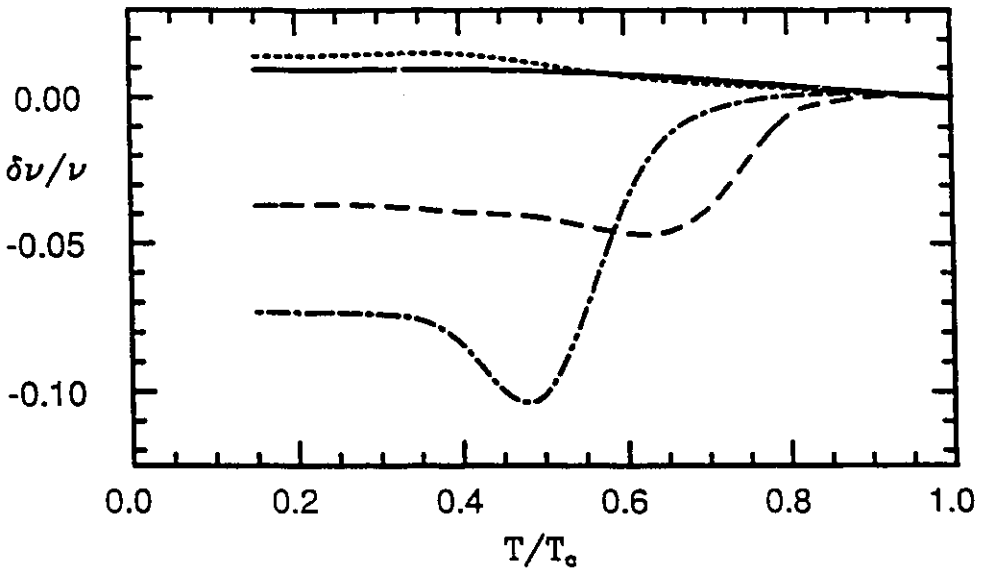

Figure 7.11 $\delta\nu/\nu$ is plotted vs. T/T_c, for the frequencies $\nu = 55$ meV (solid line), $\nu = 42$ meV (dotted), $\nu = 39$ meV (dot-dashed) and $\nu = 35$ meV (dashed). No impurities are included here.

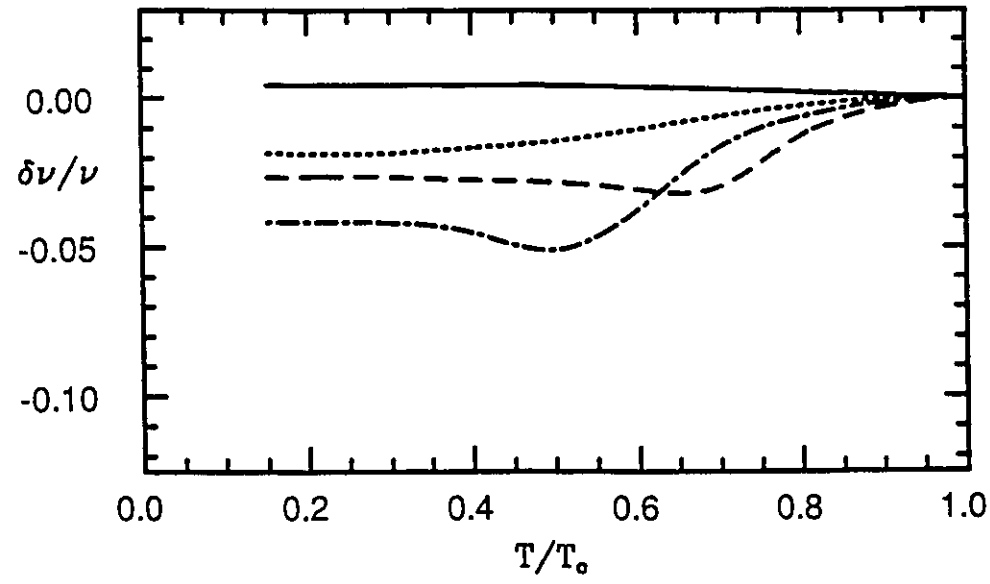

Figure 7.12 $\delta\nu/\nu$ is plotted vs. T/T_c for the frequencies $\nu = 55$ meV (solid line), $\nu = 42$ meV (dotted), $\nu = 39$ meV (dot-dashed) and $\nu = 35$ meV (dashed). This time, the impurity concentration is $t^+ = 6.37$ meV.

have been added - $t^+ = 6.37$ meV. The presence of impurities reduces the minima for the $\nu = 39$ meV and $\nu = 35$ meV curves but does not eliminate them completely. The $\nu = 55$ meV curve is still positive definite. However, the $\nu = 42$ meV curve has now becomes negative despite the fact that $\nu > 2\Delta$ for all temperatures. This behavior while puzzling at first is understandable from the results of Fig. 7.6. In that figure, one can see when impurities are introduced that $\mathrm{Re}\{\Delta(\nu)/N(0)\} < 0$ for frequencies a fair bit above 2Δ. So, here we have the presence of impurities changing the behavior of some phonons below T_c from hardening to softening.

In Fig. 7.13, $\delta\gamma/\nu$ is plotted vs. T/T_c. The curves correspond to the same set of frequencies as the previous two figures. No impurities are included here. What occurs here is reminiscent of what occurs for the normalized shifts, but is even more dramatic. The solid curve for $\nu = 55$ meV is the least interesting as this frequency is well enough above 2Δ so that it is in the region where $\mathrm{Im}\{\Delta(\nu)/N(0)\} < 0$ but is approaching zero. The frequency $\nu = 42$ meV occurs in the depression in $\mathrm{Im}\{\Delta(\nu)/N(0)\}$ for a large temperature range so one obtains what one expects - a large increase in linewidth. For the lower temperatures, $\nu = 39$ meV $\nu = 35$ meV lie in the region where $\mathrm{Im}\{\Delta(\nu)/N(0)\} \sim 0$. Of course, as the temperature is increased, they pass through the depression in $\mathrm{Im}\{\Delta(\nu)/N(0)\}$ and the result is the onset of a dramatic increase in linewidth shown in the curves here. Once again, the effect is less prominent for $\nu = 35$ meV since it occurs at a higher temperature.

In Fig. 7.14, $\delta\gamma/\nu$ is again plotted vs. T/T_c, but this time with $t^+ = 6.37$ meV. The curves are basically the same as in the previous figure, however the effect of the impurities seems to have lessened their magnitude. Also of

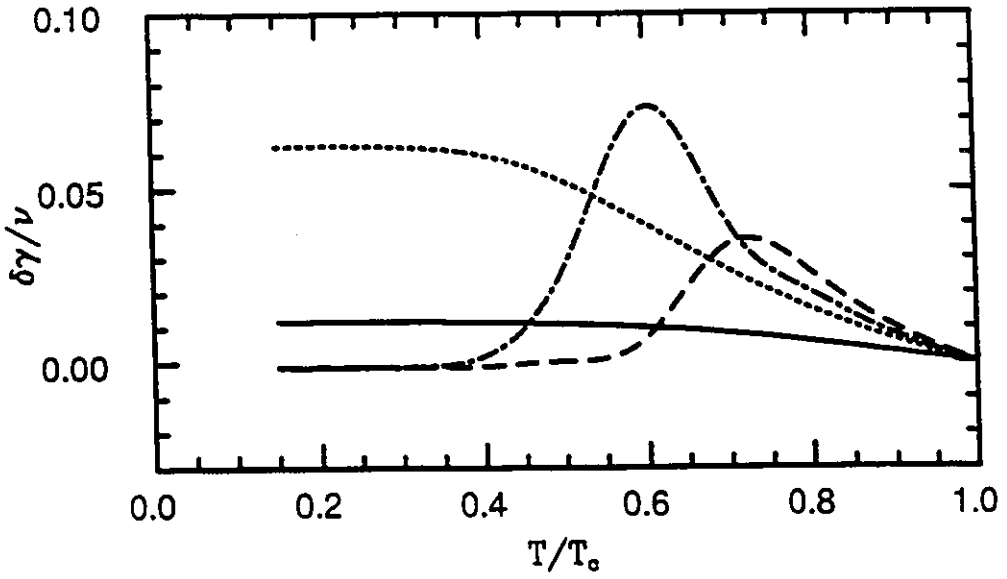

Figure 7.13 $\delta\gamma/\nu$ is plotted vs. T/T_c, for the frequencies $\nu = 55$ meV (solid line), $\nu = 42$ meV (dotted), $\nu = 39$ meV (dot-dashed) and $\nu = 35$ meV (dashed). No impurities are included here.

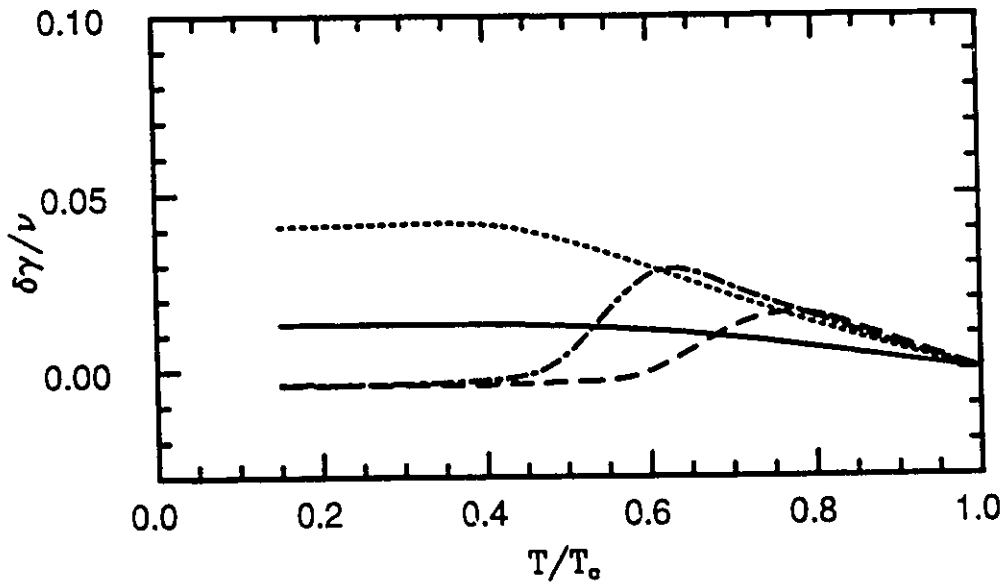

Figure 7.14 $\delta\gamma/\nu$ is again plotted vs. T/T_c for the frequencies $\nu = 55$ meV (solid line), $\nu = 42$ meV (dotted), $\nu = 39$ meV (dot-dashed) and $\nu = 35$ meV (dashed). This time, the impurity concentration is $t^+ = 6.37$ meV.

interest is that $\delta\gamma/\nu$ is now more significantly less than zero for $\nu = 35$ meV and $\nu = 39$ meV in the lower temperature range.

Curves similar to those shown in the previous four figures appear in papers by Zeyher and Zwicknagl[177,179,180]. Despite the fact that they were generated from the imaginary axis, most of the features observed here occur in their curves as well. One important feature they seem to have missed however is the minimum in $\delta\nu/\nu$ that should occur for frequencies just below $2\Delta_o$. They show curves for $\nu/2\Delta_o = 0.99$ which should show this feature quite strongly but do not. Oddly, the corresponding effect in $\delta\gamma/\nu$ is displayed.

As stated earlier, none of the curves shown in the preceeding four figures was generated to fit a particular set of experimental data. However, the frequencies that were used, 55 meV, 42 meV, 39 meV and 35 meV were chosen because some experiments on YBCO indicate that some interesting behaviour occurs around these frequencies.

As stated earlier, shifts in phonon frequency and changes in phonon width have been observed in some oxide materials using Raman scattering techniques. In particular, materials of the type $RBa_2Cu_3O_{7-y}$, where R≡ rare earth element, usually Y, have been investigated. The critical temperature of these materials seems to be relatively independent of the rare earth atom that used[185].

One phonon that has been singled out for displaying unusual behavior below T_c is one with a frequency of $\omega \sim 42$ meV in YBCO[186–191]. Between 100 K and 0 K, it has been observed to soften by about ~ 1 meV. In the meantime, it's linewidth has been observed[183] to increase from ~ 2 meV to ~ 3 meV going from 90 K to 10 K. Substituting different rare earths for Y, while not changing the T_c, does change the frequency of this mode. The actual

frequency appears to be related to the ionic radius of the rare earth atom. When this is done, it has been found[183] that the phonon can apparently be tuned to map out where $\omega = 2\Delta$ falls by observing at which frequency where the phonon changes from being softened to hardening. When this is done it has been determined that $2\Delta_o/k_BT_c \sim 5.2$. A similar determination has also been carried out using changes in the linewidth behavior. In this case, a value of $2\Delta_o/k_BT_c \sim 4.95$ was the result[191].

Another Raman active phonon that appears to show some anomolies is one with $\omega \sim 55$ meV. In this case, the phonon is observed to harden by ~ 0.5 meV[183]. In the meantime, it also broadens by about 0.6 meV.

It seems also that some shifts in phonon frequencies have been observed in infrared data[192]. Apparently modes in the neighbourhood of ~ 35 meV and ~ 39 meV show decreases in frequency below T_c.

There are of course other phonon modes that have been examined and many more experiments that can be cited. However, for the modes that we have discussed, they show behavior that is fairly consistent with the model used here with $\lambda = 2.269$ and $2\Delta_o/k_BT_c = 4.99$. This is not surprising as Zeyher and Zwicknagl, as well as the some of the experimentalists themselves, have used models with similar values for the gap ratio to try and fit them.

On the other hand, there are experimental indications that the theory as it stands may be oversimplified. The effect of introducing impurities such as Au, Pr, and Fe into YBCO has also been the subject of Raman studies[192]. It seems that introducing these impurities can change the phonon behaviour from broadening to sharpening. The experimenters have speculated that this is evidence of impurities causing the gap to become more

isotropic in an anisotropic material. Experiments[194] have recently been performed on $YBa_2Cu_4O_8$, a material with $T_c \sim 72$ K. In this case, the authors claim to observe two distinct gap values: $2\Delta_2/k_BT_c \sim 6.5$ and $2\Delta_1/k_BT_c \sim 2.3$, with these results apparently confirmed by the appropriate softenings and hardenings of various phonon modes. Obviously, it would seem that the inclusion of anisotropy into the theory would be an appropriate next step.

7.4 CONCLUSIONS

A new formula for the phonon self-energy, written directly on the real frequency axis, has been derived. Using this new formula, some results obtained using the imaginary axis formulation have been reconfirmed. In particular, going from BCS to strong coupling does not cause any profound changes in the qualitative behaviour of the phonon self-energy. Even when there are some quantitative changes due to coupling strength, the $\alpha^2F(\omega)$ shape that is used appears to be relatively unimportant. Increasing the temperature and adding impurities have similar effects - the minima of the real and imaginary parts of $\Delta\Pi(\nu)/N(0)$ are reduced in depth. Comparing results of a real frequency axis formulation with an imaginary axis formulation one finds agreement for the most part but the Padé approximants appear to have some difficulty reproducing the sharp behaviour that occurs in the region around 2Δ. Knowing the phonon self-energy, phonon shifts and changes in phonon width can be calculated and tracked as a function of temperature.

Chapter 8

Summary

In this thesis, we have investigated many superconducting properties, all within the context of strong coupling Eliashberg theory. With many of these properties, attempts were made to see whether or not results from experiments on the high-T_c oxides could be fitted into the strong coupling framework. These attempts met with varying degrees of success.

As discussed in chapter 3, the high T_c's of the oxides by themselves do not provide much of a problem for Eliashberg theory, at least on mathematical grounds. Somewhat more difficult to reconcile are the relatively small isotope effects that have been observed in the oxides. However, two models, one where a strong electron-phonon coupling is combined with a very large coulomb repulsion and the other combining an additional high-energy boson mechanism with phonons, were found to be able to explain the small isotope effects seen in experiments. On the other hand, there are additional experiments that show that the isotope effect can change radically with the

composition of the material. These experiments may require models with more flexibility in order to explain them.

In Chapter 4, the electronic specific heat in superconductors was discussed. Two features were concentrated on - the slope of the specific heat jump at T_c and the temperature where $\Delta C(T) = 0$, which was referred to as the crossover temperature. Using functional derivative techniques, maxima for these quantities, that should not be violated by strong coupling superconductors, were established. Unfortunately, a comparison with some experiments on the oxides indicated that these materials may indeed violate these maxima, in some cases radically.

In Chapter 5, the primary focus was on the spin-lattice relaxation rate. In this quantity, BCS predicts the appearance of a coherence peak below T_c. However, it was shown that strong coupling can remove this peak so that even in some conventional materials the peak may be absent, as it appears to be in the oxides. Anisotropy, which is expected to be important in the oxides, was also included in an approximate way. Using a combination of strong coupling, anisotropy and the antiferromagnetic Fermi liquid corrections of Monien and Pines, some rough fits to some experimental data on YBCO were made. The agreement was fairly reasonable, though it was difficult to fit the entire temperature range.

In Chapter 6, the conductivity was examined. The problem of extracting the superconducting gap from optical data was studied extensively. It was shown that there are various physical circumstances where determining the gap in this manner may be unreliable. The low frequency conductivity, which in some ways behaves like the spin lattice relaxation, was also studied. Whether or not one observes a coherence peak in this property was shown to

depend strongly on such factors as coupling strength, impurity concentration and frequency. The oxides, while not showing any peak in the spin-lattice relaxation rate, do appear to show a peak in the low frequency conductivity. This result may be difficult to explain in the strong coupling scenario.

Finally, in Chapter 7, the phonon self-energy was studied. A new formula for this quantity, written on the real frequency axis, was derived and compared with an earlier formula derived on the imaginary axis. The results of these formulas showed fairly good agreement with each other, but it was evident that the imaginary axis formula did have some problems, particularly with reproducing the sharp structure at 2Δ. Knowing the phonon self-energy, one can calculate phonon shifts and changes in phonon width that are comparable to experiment and this has been done by other authors in the past using the imaginary axis formulation. They have determined that the experimentally observed values for these quantities may be consistent with strong electron-phonon coupling. Switching to a real axis formulation is unlikely to change this conclusion. On the other hand, some experiments have also indicated that anisotropy may have to be taken into account.

Bibliography

1. H.K Onnes, *Lieden Comm.* **1206**, 1226 (1911), Suppl. 34 (1913).
2. W. Meissner and R. Ochsenfeld, *Naturwiss.* **21**, 787 (1933).
3. E.L. Wolf and G.B. Arnold, *Phys. Reports* **91**, 32 (1982).
4. J.R. Gavaler, *Appl. Phys. Lett.* **23**, 480 (1973).
5. C.J. Gorter and H.B.G. Casimer, *Phys. Z.* **35**, 963 (1934).
6. G. Rickayzen, Theory of Superconductivity, (Wiley, New York, 1965)
7. J. Bardeen, L.N. Cooper, J.R. Schreiffer, *Phys. Rev.* **108**, 1175 (1957).
8. J.P Carbotte, *Physics in Canada* **31**, 131 (1975).
9. G.M. Eliashberg, *Sov. Phys. (JETP)* **11**, 696 (1960).
10. J.G. Bednorz and K.A. Müller, *Z. Phys. B* **64**, 189 (1986).
11. C.W. Chu, P.H. Hor, R.L. Meng, L. Gao, Z.J. Huang and Y.Q. Wang, *Phys. Rev. Lett.* **58**, 405 (1987).
12. R.J. Cava, R.B. van Dover, B. Batlogg and E.A. Reitman *Phys. Rev. Lett.* **58**, 408 (1987).
13. M.L. Wu, J.R. Ashburn, C.J. Torng, P.H. Hor, R.L. Meng, L. Gao, Z.J. Huang, Y.Q. Wang and C.W. Chu *Phys. Rev. Lett.* **58**, 908 (1987).
14. R.J. Cava *et al.* , *Phys. Rev. Lett.* **58**, 1676 (1987).
15. P.M. Grant *et al.* , *Phys. Rev. B* **35**, 7242 (1987).
16. H. Maeda, Y. Tanaka, M. Fakutomi, T. Asano, *Jpn. J. Appl. Phys.* **27**, L209 (1988).

17. Z.Z. Sheng and A.M. Herman, *Nature* **332**, 55 (1988).

18. Z.Z. Sheng and A.M. Herman, *Nature* **332**, 138 (1988).

19. R.M. Hazen, L.W. Finger, R.J. Angel, C.T. Prewitt, N.L. Ross, C.G. Hadidiacos, P.J. Heaney, D.R. Veblen, Z.Z. Sheng, A. Ali and A.M. Herman, *Phys. Rev. Lett.* **60**, 1657 (1988).

20. J.J. Schooley, W.R. Hosler and M.L. Cohen, *Phys. Rev. Lett.* **12**, 474 (1964).

21. A. Santaro in High Temperature Superconductivity, edited by J.W. Lynn (Springer-Verlag, New York, 1990), p. 84.

22. J.C. Phillips, Physics of High-T_c Superconductors,(Academic Press. San Diego, 1989).

23. M. Reedyk, Master's thesis, McMaster University, 1988 (unpublished).

24. M.B. Salamon in Physical Properties of High Temperature Superconductors I, edited by D.M. Ginsberg (World Scientific, Singapore, 1989), p. 39.

25. J.E. Crow and N. Ong in High Temperature Superconductivity, edited by J.W. Lynn (Springer-Verlag, New York, 1990), p. 203.

26. A.I. Braginski in Novel Superconductivity, edited by S.A. Wolf and V.Z. Kresin (Plenum, New York, 1987), p. 935.

27. J.R. Schrieffer, Theory of Superconductivity, (Addison Wesley, Redwood City, 1964).

28. G.D. Mahan, Many-Particle Physics, 2nd Edition, (Plenum,New York, 1990)

29. A.A. Abrikosov,L.P. Gorkov and I.E. Dzyaloshinski, Methods of Quantum Field Theory in Statistical Physics, (Dover, New York, 1963)

30. Y. Nambu, *Phys. Rev.* **117**, 648 (1960).

31. L.P. Gorkov, *Sov. Phys. (JETP)* 7, 505 (1958).

32. D. J. Scalapino, in Superconductivity, edited by R.D. Parks (Marcel Dekker, Inc., New York, 1969), Vol. 1, p.449.

33. A.B. Migdal, *Sov. Phys. (JETP)* **34**, 996 (1958).

34. G. Grimvall, The Electron-Phonon Interaction in Metals, North-Holland, New York, 1981.

35. P. Morel and P.W. Anderson, *Phys. Rev.* **125**, 1263 (1962).

36. D. Rainer and G. Bergmann, *J. Low Temp. Phys.* **14**, 501 (1974).

37. F. Marsiglio, M. Schossman and J.P. Carbotte, *Phys. Rev. B* **37**, 4965 (1988).

38. F. Marsiglio, Ph.D thesis, McMaster University, 1988 (unpublished).

39. H.J. Vidberg and J.W. Serene, *J. Low Temp. Phys.* **29**, 179 (1977).

40. B. Mitrović, H.G. Zarate, and J.P. Carbotte, *J. Low Temp. Phys.* **43**, 263 (1981).

41. R. Blaschke and R. Blocksdarf, *Z. Phys. B* **49**, 99 (1982).

42. C.R. Leavens and D.S. Ritchie, *Solid State Comm.* **53**, 137 (1985).

43. J.P Carbotte, *Rev. Mod. Phys.* **62**, 1027 (1991).

44. W.L. McMillan and J.M. Rowell, in Superconductivity, edited by R.D. Parks (Marcel Dekker, Inc., New York, 1969), Vol. 1, p.561.

45. R.C. Dynes, Ph.D thesis, McMaster University, 1968 (unpublished).

46. W.L. McMillan, *Phys. Rev.* **167**, 331 (1968).

47. R.C. Dynes, *Solid State Comm.* **10**, 615 (1972).

48. P.B. Allen and R.C. Dynes, *Phys. Rev. B* **12**, 905 (1975).

49. B. Mitrović, H.G. Zarate, and J.P. Carbotte, *Phys. Rev. B* **29**, 184 (1984).

50. F. Marsiglio and J.P. Carbotte, *Phys. Rev. B* **33**, 6141 (1986).

51. J.M. Coombes and J.P. Carbotte, *J. Low Temp. Phys.* **63**, 431 (1986).

52. J.M. Coombes, Ph.D thesis, McMaster University, 1987 (unpublished).

53. C.R. Leavens and J.P. Carbotte, *J. Low Temp. Phys.* **14**, 195 (1974).

54. C.R. Leavens and J.P. Carbotte, *Ferroelectrics* **16**, 295 (1977).

55. C.M. Varma, in Superconductivity in d- and f- Band Metals, edited by W. Buckel and W. Weber (Kernforschungszentrum Karlsruhe, Karlsruhe, West Germany, 1982), p.603.

56. M. Cohen and P.W. Anderson, in Superconductivity in d- and f-Band Metals, edited by D.H. Douglass (AIP, New York, 1972), p.17.

57. J. Ruvalds, *Phys. Rev. B* **35**, 8869 (1987).

57. V. Kresin, *Phys. Rev. B* **35**, 8716 (1987).

59. D. Allender, J. Bray and J. Bardeen, *Phys. Rev. B* **7**, 1020 (1973).

60. C.M. Varma, S. Schmitt-Rink and E. Abrahams, *Solid State Comm.* **62**, 681 (1987).

61. F. Marsiglio, R. Akis and J.P. Carbotte, *Solid State Comm.* **64**, 905 (1987).

62. F. Marsiglio, R. Akis and J.P. Carbotte, *Physica C* **153-155**, 227 (1988).

63. R. Akis, Master's thesis, McMaster University, 1988 (unpublished).

64. R. Akis and J.P. Carbotte, *J. Low Temp. Phys.* **76**, 65 (1989).

65. F. Marsiglio, *Physica C* **165-166**, 1453 (1990).

66. F. Marsiglio, in Proceedings of the First Cinvestav-Superconductivity Symposium, edited by R. Baquero (World Scientific, Singapore, 1991) p. 167.

67. R. Akis and J.P. Carbotte, submitted to *The Bulletin of Materials Science.*

68. J.W. Garland Jr., *Phys. Rev. Lett.* **11**, 114 (1963).

69. J.P. Carbotte in Proceedings of the First Cinvestav-Superconductivity Symposium, edited by R. Baquero (World Scientific, Singapore, 1991) p. 98.

70. P.B. Allen, *Nature* **335**, 396 (1988).

71. B. Batlogg *et al.* , *Phys. Rev. Lett.* **58**, 2333 (1987).

72. L.C. Bourne *et al.* , *Phys. Rev. Lett.* **58**, 2337 (1987).

73. K.J. Leary *et al.* , *Phys. Rev. Lett.* **59**, 1236 (1987).

74. E. Morris, R.M. Kuroda, A.G. Markelz, J.H. Nickel, and J.T. Wei, *Phys. Rev. B* **37**, 5936 (1988).

75. E.L. Benitez *et al.* , *Phys. Rev. B* **38**, 5025 (1988).

76. P.J. Yvon *et al.* , *Phys. Rev. B* **39**, 6690 (1989).

77. L.C. Bourne, A. Zettl, T.W Barbee III and M.L. Cohen, *Phys. Rev. B* **36**, 3990 (1987).

78. Lin Quan *et al.* , *Solid State Comm.* **65**, 869 (1988).

79. B.V. Vasiliev and V.I. Luschikov, *Physica C* **153-155**, 261 (1988).

80. B.V. Vasiliev, V.I. Luschikov and V.V. Sikolenko, *JETP Lett.* **48**, 252 (1988).

81. T. Hidaka, T. Matsui and X. Nakagawa, *Jpn. J. Appl. Phys.* **27**, L553 (1988).

82. R. Akis and J.P. Carbotte, *Phys. Rev. B* **41**, 11661 (1990).

83. B. Renker *et al.* , *Z. Phys. B* **71**, 437 (1988).

84. J. Rammer. in Studies of High Temperature Superconductors, edited by A. Narlikar (Nova Science Publishers, New York, 1988), Vol. 1, p. 116.

85. S. Hoen *et al.* , *Phys. Rev. B* **39**, 2269 (1989).

86. P.C. Pattnaik and, D.M. Newns, *Physica C* **157**, 13 (1989).

87. D. Rainer and F.J. Culetto, *Phys. Rev. B* **19**, 2540 (1979).

88. T.A. Faltens *et al.* , *Phys. Rev. Lett.* **59**, 915 (1987).

89. L.C. Bourne *et al.* , *Solid State Comm.* **67**, 707 (1987).

90. H.C. zur Loye *et al.* , *Science* **238**, 1558 (1987).

91. Ashauer, B.W. Lee, D. Rainer, and J. Rammer *Physica B* **148**, 243 (1987).

92. W. Weber, *Phys. Rev. Lett.* **58**, 1371 (1987). See also W. Weber, *Phys. Rev. Lett.* **58**, 2154(E) (1987).

93. J.P. Franck, J. Jung, M.A.K. Mohamed, S. Gygax and G.I. Sproule, *Physica B* **169**, 697 (1991).

94. J.P. Carbotte, M. Greeson and A. Perez-Gonzalez, *Phys. Rev. Lett.* **66**, 1789 (1991).

95. B. Mitrović, Ph.D thesis, McMaster University, 1981 (unpublished).

96. B. Mitrović and J.P. Carbotte, *Can. J. Phys.* **61**, 784 (1983).

97. S.G. Lie and J.P. Carbotte, *Solid State Comm.* **34**, 599 (1980).

98. E. Schachinger, M.G. Greeson and J.P. Carbotte, *Phys. Rev. B* **42**, 406 (1990).

99. C.C. Tsuei, D.M. Newns, C.C. Chi and P.C. Pattnaik, *Phys. Rev. Lett.* **65**, 2540 (1990).

100. J.P. Carbotte and R. Akis, submitted to *Phys. Rev. B.*

101. J.P. Carbotte and E.J. Nicol submitted to *Physica C.*

102. M.K. Crawford, M.N. Kunchur, W.E. Farneth, E.M. McCarron III and S.J. Poon, *Phys. Rev. B* **41**, 283 (1990).

103. J.C. Phillips, *Phys. Rev. B* **43**, 3305 (1991).

104. S.L. Dreschsler and N.M. Plakida, *Physica C* **153-155**, 206 (1988).

105. R.A. Fisher, J.E. Gordon and N.E. Phillips, *J. of Superconductivity* **1**, 231 (1988).

106. A. Junod in Physical Properties of High Temperature Superconductors II , edited by D.M. Ginsberg (World Scientific, Singapore, 1990), p. 13.

107. A. Junod, A. Bezinge, D. Eckhart, T. Graf and J. Muller, *Physica C* **152**, 495 (1988).

108. V.I. Voronin *et al.* in Novel Superconductivity, edited by S.A. Wolf and V.Z. Kresin (Plenum, New York, 1987), p. 375.

109. J. Loram and K.A. Mirza, *Physica C* **153-155**, 1020 (1988).

110. B.A. Aleksashin *et al.* , *Soviet Physics (JETP)* **95**, 678 (1989).

111. B.A. Aleksashin, *et al.* , *Physica C* **153-155**, 339 (1988).

112. A. Schilling, H.R. Ott and F. Hulliger, *Physica C* **161**, 626 (1989).

113. N.E. Phillips, *Phys. Rev.* **114**, 676 (1954).

114. G. Chanin and J.P. Torre, *Phys. Rev. B* **5**, 4357 (1972).

115. J. Bardeen and M. Stephen, *Phys. Rev.* **136**, A1485 (1964).

116. J.W. Blezius and J.P. Carbotte, *Phys. Rev. B* **36**, 3622 (1987).

117. J.W. Blezius, Ph.D thesis, McMaster University, 1987 (unpublished).

118. F. Marsiglio, J.P. Carbotte and E. Schachinger, *J. Low Temp. Phys.* **65**, 305 (1986).

119. G. Bergman and D. Rainer, *Z. Phys.* **263**, 59 (1973).

120. J.M. Daams and J.P. Carbotte, *J. Low Temp. Phys.* **43**, 263 (1981).

121. R. Akis, F. Marsiglio, E. Schachinger and J.P. Carbotte, *Phys. Rev. B* **37**, 9318 (1988).

122. J.P. Carbotte in Proceedings of the ITCTPS '90 Conference on Transport Properties of Superconductors, edited by R. Nicolsky (World Scientific, Singapore, 1990), p. 435.

123. P.J Williams and J.P. Carbotte, *Phys. Rev. B* **39**, 2722 (1989).

124. P.J. Williams, Ph.D thesis, McMaster University, 1990 (unpublished).

125. S.E. Inderhees *et al.* , *Phys. Rev. Lett.* **60**, 1178, 1988 and **60**, 2245, 1988.

126. J.F. Annett, N. Goldenfeld and S.R. Renn in Physical Properties of High Temperature Superconductors II, edited by D.M. Ginsberg (World Scientific, Singapore, 1990), p. 571

127. L.N. Bulaevskii and O.V. Dolgov, *Physica C* **153-155**, 242 (1988).

128. L.N. Bulaevskii and O.V. Dolgov, *Solid State Comm.* **67**, 63 (1988).

129. C. Kittel, Introduction to Solid State Physics, 5th Edition, (Wiley, New York, 1976).

130. H. Monien and D. Pines, *Phys. Rev. B* **41**, 6297 (1990).

131. R. Akis and J.P. Carbotte, *Solid State Comm.* **78**, 393 (1991).

132. R. Akis C. Jiang, and J.P. Carbotte, *Physica C* **176**, 485 (1991).

133. K. Yosida, *Phys. Rev.* **107**, 901 (1957).

134. L.C. Hebel and C.P. Slichter, *Phys. Rev.* **113**, 1504 (1959).

135. D.E. MacLaughlin in Solid State Physics , edited by H. Ehrenreich, F. Seitz and D. Turnbull (Academic Press, New York, 1976), Vol. 31, p. 1.

136. L.C. Hebel and C.P. Slichter, *Phys. Rev.* **107**, 901 (1957).

137. M. Fibich, *Phys. Rev. Lett.* **14**, 561, 1965 and **14**, 621, 1965.

138. P.B. Allen and D. Rainer, *Nature* **349**, 396 (1991).

139. T.T. Chen, J.T. Chen, J.D. Leslie and H.J.T. Smith, *Phys. Rev. Lett.* **22**, 526 (1969).

140. K.E. Killstrom, *Phys. Rev. B* **32**, 2891 (1985).

141. J.R. Clem, *Annals of Physics* **50**, 268 (1966).

142. J.M Daams, Ph.D thesis, McMaster University, 1977 (unpublished).

143. M.A. Biondi, M.P. Garfunkel and W.A. Thompson, *Phys. Rev.* **136**, A1471 (1964).

144. D. Markowitz and L.P. Kadanoff, *Phys. Rev.* **121**, 563 (1963).

145. T. Schneider, H. de Raedt and M. Frick, *Z. Phys. B* **76**, 3 (1989).

146. B.W. Statt, *Phys. Rev. B* **42**, 605 (1990).

147. B.W. Statt, *Physica B* **165-166**, 1059 (1990).

148. C. Jiang, private communication

149. C.H Pennington and C.P. Slichter in Physical Properties of High Temperature Superconductors II , edited by D.M. Ginsberg (World Scientific, Singapore, 1990), p. 269.

150. S.E. Barrett, D.J. Durand, C.H. Pennington, C.P. Slichter, T.A. Freidmann, J.M. Rice and D.M. Ginsberg *Phys. Rev. B* **41**, 6283 (1990).

151. H. Seidel, F. Hentsch, M. Mehring, J.G. Bednorz and K. A. Muller *Europhysics Letters* **5**, 647 (1988).

152. M. Mehring *IBM J. Res. Dev.* **33**, 342 (1989).

153. M. Takigawa, P.C. Hammel, R.H. Heffner and Z. Fisk *Phys. Rev. B* **39**, 7371 (1989).

154. P.B. Littlewood and C.M. Varma, *J. App. Phys. B* **69**, 4979 (1991).

155. N.W. Ashcroft and N.D. Mermin, Solid State Physics , (HRW, Philadelphia, 1976).

156. T. Timusk and D.B. Tanner, in Physical Properties of High Temperature Superconductors I, D.M. Ginsberg, editor (World Scientific, Singapore, 1989) p.339.

157. F. London, Superfluids Vol. II. Macroscopic Theory of of Superfluid Helium, (Wiley, New York, 1954).

158. D.C. Mattis and J. Bardeen, *Phys. Rev.* **111**, 412 (1958).

159. N.E.Bickers, D.J.Scalapino, R.T.Collins, and Z.Schlesinger, *Phys. Rev. B* **42**, 67 (1990).

160. W.Lee, D.Rainer, and W.Zimmermann, *Physica C* **159**, 535 (1989).

161. F.Marsiglio, submitted to *Phys. Rev. B*..

132. R. Akis C. Jiang, and J.P. Carbotte, *Physica C* **176**, 485 (1991).

133. K. Yosida, *Phys. Rev.* **107**, 901 (1957).

134. L.C. Hebel and C.P. Slichter, *Phys. Rev.* **113**, 1504 (1959).

135. D.E. MacLaughlin in Solid State Physics , edited by H. Ehrenreich, F. Seitz and D. Turnbull (Academic Press, New York, 1976), Vol. 31, p. 1.

136. L.C. Hebel and C.P. Slichter, *Phys. Rev.* **107**, 901 (1957).

137. M. Fibich, *Phys. Rev. Lett.* **14**, 561, 1965 and **14**, 621, 1965.

138. P.B. Allen and D. Rainer, *Nature* **349**, 396 (1991).

139. T.T. Chen, J.T. Chen, J.D. Leslie and H.J.T. Smith, *Phys. Rev. Lett.* **22**, 526 (1969).

140. K.E. Killstrom, *Phys. Rev. B* **32**, 2891 (1985).

141. J.R. Clem, *Annals of Physics* **50**, 268 (1966).

142. J.M Daams, Ph.D thesis, McMaster University, 1977 (unpublished).

143. M.A. Biondi, M.P. Garfunkel and W.A. Thompson, *Phys. Rev.* **136**, A1471 (1964).

144. D. Markowitz and L.P. Kadanoff, *Phys. Rev.* **121**, 563 (1963).

145. T. Schneider, H. de Raedt and M. Frick, *Z. Phys. B* **76**, 3 (1989).

146. B.W. Statt, *Phys. Rev. B* **42**, 605 (1990).

147. B.W. Statt, *Physica B* **165-166**, 1059 (1990).

148. C. Jiang, private communication

149. C.H Pennington and C.P. Slichter in Physical Properties of High Temperature Superconductors II , edited by D.M. Ginsberg (World Scientific, Singapore, 1990), p. 269.

150. S.E. Barrett, D.J. Durand, C.H. Pennington, C.P. Slichter, T.A. Freidmann, J.M. Rice and D.M. Ginsberg *Phys. Rev. B* **41**, 6283 (1990).

151. H. Seidel, F. Hentsch, M. Mehring, J.G. Bednorz and K. A. Muller *Europhysics Letters* **5**, 647 (1988).

152. M. Mehring *IBM J. Res. Dev.* **33**, 342 (1989).

153. M. Takigawa, P.C. Hammel, R.H. Heffner and Z. Fisk *Phys. Rev. B* **39**, 7371 (1989).

154. P.B. Littlewood and C.M. Varma, *J. App. Phys. B* **69**, 4979 (1991).

155. N.W. Ashcroft and N.D. Mermin, Solid State Physics , (HRW, Philadelphia, 1976).

156. T. Timusk and D.B. Tanner, in Physical Properties of High Temperature Superconductors I, D.M. Ginsberg, editor (World Scientific, Singapore, 1989) p.339.

157. F. London, Superfluids Vol. II, Macroscopic Theory of of Superfluid Helium, (Wiley, New York, 1954).

158. D.C. Mattis and J. Bardeen, *Phys. Rev.* **111**, 412 (1958).

159. N.E.Bickers, D.J.Scalapino, R.T.Collins, and Z.Schlesinger, *Phys. Rev. B* **42**, 67 (1990).

160. W.Lee, D.Rainer, and W.Zimmermann, *Physica C* **159**, 535 (1989).

161. F.Marsiglio, submitted to *Phys. Rev. B*..

162. E.H.Brandt, M.Bauer, E.Seider, and L. Genzel, in, Proceeding of the USSR-FRG Bilateral Seminar "Investigation of High Temperature Superconductors - Modern Spectroscopic and Microscopic Methods" held Oct.30.1989 in Tallinn, USSR.

163. S.L.Cooper *et al.* , *Phys. Rev. B* 40, 11358 (1989).

164. Z.Schlesinger, R.T.Collins, F.Holtzberg, C.Field, G.Koren, and A.Gupta, *Phys. Rev. B* **41**, 11237 (1990).

165. Z.Schlesinger, R.T.Collins, F.Holtzberg, C.Field, N.E.Bickers, and D.J.Scalapino, *Nature* **343**, 242 (1990).

166. K.Kamarás *et al.* *Phys. Rev. Lett.* **64**, 84 (1990).

167. M. Reedyk *et al.* , *Phys. Rev. B* **38**, 11981 (1988).

168. E.Nicol, J.P.Carbotte and T.Timusk, *Solid State Comm.* **76**, 937 (1990).

169. E.Nicol, J.P.Carbotte and T.Timusk, *Phys. Rev. B* **43**, 473 (1991).

170. G.A. Thomas *et al.* , *Phys. Rev. Lett.* **61**, 1313 (1988).

171. S.B. Nam, *Phys. Rev.* **156**, 470 (1967).

172. H.-M. Cheah, A. Porch and J.R. Waldram, *Physica B* **165-166**, 1195 (1990).

173. M.C. Nuss, P.M. Mankiewich, M.L. O'Malley, E.H. Westerwick and P.B. Littlewood, *Phys. Rev. Lett.* **66**, 3305 (1991).

174. D.B. Tanner *et al.* , to be published in Proceedings of the Miami Workshop on Electronic Structure and Mechanisms for High Temperature Superconductivity, G. Vezoli *et al.* , editors (Plenum, New York , 1991).

175. D.A. Bonn, P. Dosanjh, R. Liang, W.N. Hardy, submitted to *Phys. Rev. Lett.*.

176. K. Holczer, L. Forro, L. Mihály and G. Grüner, *Phys. Rev. Lett.* **67**, 152 (1991).

177. R. Zeyher and G. Zwicknagl, *Z. Phys. B* **78**, 175 (1990).

178. S.M. Shapiro, G. Shirane and J.D. Axe, *Phys. Rev. B* **12**, 4899 (1975).

179. R. Zeyher and G. Zwicknagl, *Solid State Comm.* **66**, 617 (1988).

180. R. Zeyher and G. Zwicknagl, *Physica C* **162-164**, 1709 (1989).

181. H.G. Schuster *Solid State Comm.* **13**, 1559 (1973).

182. P.B. Littlewood and C.M. Varma, *Phys. Rev. B* **26**, 4883 (1982).

183. C. Thomsen *et al.* *Solid State Comm.* **75**, 219 (1990).

184. B. Renker *et al.* , *Z. Phys. B* **73**, 309 (1988).

185. P.H. Hor *et al.* , *Phys. Rev. Lett.* **58**, 1891 (1987).

186. R.M. MacFarlane, H. Rosen and H. Seki *Solid State Comm.* **63**, 831 (1987).

187. A. Wittlin *et al.* *Solid State Comm.* **64**, 477 (1987).

188. C. Thomsen *et al.* *Solid State Comm.* **65**, 219 (1987).

189. M. Krantz, H.J. Rosen, R.M. MacFarlane and V.Y. Lee. *Phys. Rev. B* **38**, 4992 (1988).

190. C. Thomsen and M. Cardona in Physical Properties of High Temperature Superconductors I , edited by D.M. Ginsberg (World Scientific, Singapore, 1989), p. 409.

191. B. Freidl, C. Thomsen and M. Cardona, *Phys. Rev. Lett.* **65**, 915 (1990).

192. L. Genzel *et al.* , *Phys. Rev. B* **40**, 2170 (1990).

193. C. Thomsen, B. Freidl, M. Cieplak and M. Cardona, *Solid State Comm.* **78**, 727 (1991).

194. E.T. Heyen, M. Cardona, J. Karpinski, E. Kaldis, and S. Rusiecki, *Phys. Rev. B* **43**, 12958 (1991).